ADAPTATION OF ADVANCED MRI AND NMR TECHNIQUE FOR LOW MAGNETIC FIELD MRI SYSTEM

A DISSERTATION

SUBMITTED TO THE FALCUTY OF THE GRADUATE SCHOOL

OF THE UNIVERSITY OF MINNESOTA

BY

YUN LI

IN PARTIAL FULFILMENT OF THE REQUIREMENTS

FOR THE DEGREE OF

DOCTOR OF PHILOSOPHY

ADVISOR: ROGER RUAN

JULY 2012

ACKNOWLEDGEMENTS

I wish to express my deep appreciation to my advisor Dr. Roger Ruan for his guidance, support and encouragement throughout my whole PhD research. He has been a truly excellent advisor.

I also wish to express my sincere appreciation to my other graduate advisory committee members, Dr. Wei Chen, Center for Magnetic Resonance Research, Dr. Vance Morey and Dr. Jun Zhu, for their valuable advice and guidance during my research.

I wish to acknowledge other faculty and staffs in Department of Bioproducts and Biosystems Engineering, especially, Dr. Paul Chen and Dr. Jinning Qi for their friendship and help.

Finally, I wish to express my special thanks to my parents, Guoqiang Li and Meixia Qi and my sister Wei Li for their love, encouragement and support.

ABSTRACT

Nuclear magnetic resonance techniques, including nuclear magnetic imaging (MRI) and nuclear magnetic resonance (NMR) relaxometry are increasingly gaining interest and acceptance by food scientists and engineers. These techniques are being used to study moisture and fat content, water mobility, and distribution of water, fat, and temperature in foods. They are also used to determine freezing front and viscosity of foods. A unique advantage of NMR techniques is their non-invasive and non-destructive nature, making analysis faster and more reliable than conventional techniques. MRI work in the food area is primarily conducted using expensive and hard to operate large MRI systems. Most food companies, especially small companies, are not willing to use or cannot afford such large systems. Therefore, developing small systems specifically for food samples is an urgent need.

NMR relaxometry has been used by food scientists for decades. However, only recently food scientists began to realize that the technique has more to offer. Research on the relationship between NMR relaxation times and physiochemical properties of foods is emerging.

A suite of techniques were developed for the acquisition of reliable data and high quality images using low field MRI machines. My research has helped solve some key

technical problems by improving the hardware configuration, pulse sequences, and data analysis techniques.

In my research, advanced pulse sequences were adapted to our low field MRI machines for MRI imaging work and NMR relaxation work. Pulse sequences were tuned to obtain high quality images. New hardware was developed to accommodate unique samples.

New NMR data acquisition schemes and data analysis techniques were developed to obtain additional information for the analysis of food stability. Models were designed for state diagrams. Coding programs were developed to calculate and analyze state diagram related parameters.

My work involved both hardware and software improvements to facilitate adaptation and implementation of advanced techniques. It is my hope that these low field MRI machines be improved through my study so that they become an affordable, easy-to-operate, and relatively maintenance free analytical tool for food research and development and quality control labs.

TABLE OF CONTENTS

PAGE

LIST OF TABLES

LIST OF FIGURES

CHAPTER 1. INTRODUCTION

1.1 Rationale and Objectives

NMR (Nuclear Magnetic Resonance) and MRI (Magnetic Resonance Imaging) are non-destructive and non-invasive techniques which have been used to monitor dynamic processes and quality changes in food processing and storage in the last twenty years (Simoneau et al., 1993; Hills, 1995; Divakar, 1998). NMR is commercially used for determination of moisture and fat content of foods, especially oil seeds. NMR is often used to study the water related properties of foods, drugs, and biological materials and their relationships to sensory quality and stability (Charlton, 2010; Guojonsdottir et al., 2009; Ruan and Chen, 1998). MRI is used to study spatial distribution of water, fat, and temperature in foods. Spatial information on water, fat, and temperature provided by MRI also allows us to study heat and mass transfer in foods and biological materials during dynamic processes such as drying/dehydration, soaking, heating, freezing, and storage (Shyh-Shin et al., 2009; Regier et al., 2007; Ghosh et al., 2007; Ramos-Cabrer et al., 2006; Ghosh et al., 2006; Yi-Lin and Hsi-Mei, 2004; Ruan et al., 1989).

Nuclear magnetic resonance techniques, including nuclear magnetic imaging (MRI) and nuclear magnetic resonance (NMR) relaxometry are increasingly gaining interest and acceptance by food scientists and engineers. These techniques are being used to study moisture and fat content, water mobility, and distribution of water, fat, and temperature in

foods. They are also used to determine freezing front and viscosity of foods. A unique advantage of NMR techniques is their non-invasive and non-destructive nature, making analysis quick and reliable. MRI work in the food area is primarily conducted using expensive and hard to operate large MRI systems. Most food companies, especially small companies, are not willing to use or cannot afford such large systems. Therefore, developing small systems specifically for food samples is an urgent need. NMR relaxometry has been used by food scientists for decades. However, only recently food scientists began to realize that the technique has more to offer. Research on the relationship between NMR relaxation times and physiochemical properties of foods is emerging.

MRI offers many attractive advantages for food researchers: 1) it is noninvasive and nondestructive; 2) in addition to structural information, it provides other valuable information, such as proton density related to moisture or fat concentration, chemical shift, internal structure, chemical shift, diffusion, flow and temperature; and 3) data acquisition time is extremely short compared with optical and electronic microscopy techniques.

Many food processes also require frequent measurement of moisture contents of materials and products. The advantages of NMR technique are: 1) it is rapid and efficient; 2) it is noninvasive and nondestructive; 3) it requires less sample preparation than other techniques; 4) it can provide valuable information such as the amount of different

fractions of water having different mobility; and 5) it has the possibility of automation because the data acquisition can be real-time and data are electronic signals.

Objectives

Our lab is equipped with two low field MRI machines which can be used to conduct relaxometry and imaging. They are inexpensive and easy to operate and therefore have the potential to become routine tools in food analytical labs. The overall objective of this study was to develop a suite of techniques which allow acquisition of reliable data and high quality images using these low field MRI machine systems. In addition, new data acquisition schemes and data analysis were developed for the study of food stability. The specific aims of my study were to:

1) Adapt advanced pulse sequences to our low field MRI machines;
2) Tune the pulse sequences to obtain high quality images;
3) Develop new hardware to accommodate unique samples; and
4) Develop new NMR data acquisition and analysis techniques enabling researchers to obtain additional information.

1.2 Principle of Magnetic Resonance Imaging

1.2.1 Basic Principles of Nuclear Magnetic Resonance (NMR)

NMR basics

As we know from quantum mechanics, any nucleus with a non-zero spin quantum number, when placed in a magnetic field, can absorb and emit energy through electromagnetic radiation, which can be detected by NMR spectroscopy. Most of the elements in the Periodic Table have at least one isotope capable of nuclear magnetic resonance but a number of abundant isotopes such as ^{12}C, ^{16}O, ^{32}S, have zero quantum number and therefore cannot be detected by NMR spectroscopy. However, some nuclei do have non-zero spin quantum number and they can be considered as spinning about an axis. Such spinning can generate a small magnetic field, which is called magnetic moment (μ) representing the strength and direction of the magnetic field surrounding the nucleus. The magnitude of the spinning is measured by the angular momentum that the nucleus possesses. Spin angular momentum is quantized. They are always integer or half integer multiples of $h/2\pi$, where h is Plank's constant. The proton (^1H nucleus), which has an angular momentum of $(1/2)\times(h/2\pi)$ or a spin of ½, is by far the most commonly used nucleus in NMR spectroscopy and NMR imaging or MRI (magnetic resonance imaging), because of the ease of observation, its high natural abundance and its presence in majority of samples, especially in biological samples. Besides ^1H, ^{13}C, ^{17}O, ^{19}F, ^{23}N, ^{31}P, are also used in NMR studies because they are present in many compounds which medical and biological scientists are interested in. In this research, only proton is the target for NMR and MRI studies.

When the nucleus with non-zero quantum number is placed in a static external magnetic field, two phenomena usually occur. One phenomenon is that its magnetic moment will interact with the static magnetic field and tend to align with the field. The other phenomenon is that its spin will precess around the axis of the static magnetic field, as shown in Figure 1.2.1, at a rate defined by the Larmor relationship

$$f = \omega / 2\pi = \gamma B_0 / 2\pi \qquad (1.1)$$

Where f is the resonance frequency in Hz, ω is the angular frequency in radians per second, B_0 is the strength of the static magnetic field in Tesla, γ is termed the geromagnetic ratio and has a precise value characteristics of each nuclear species. For example, proton has a γ of 42.6 MHz/Tesla.

In addition, when placed in a static magnetic field at absolute temperature T, each nucleus can be in two possible states, i.e., the state where its spin points in the direction of the static magnetic field or the state where its spin points in the opposite direction of the static magnetic field as shown in Figure 1.2.2. A nucleus which has its spin aligned with the field will have the lower energy level than when it has its spin aligned with the opposite field direction as shown in Figure 1.2.3.

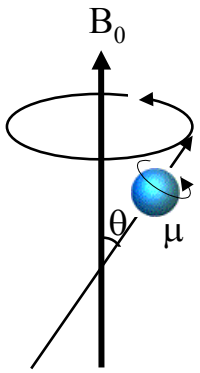

Figure 1.2.1 Magnetic moment precesses about the external magnetic field B_0 with an angle θ.

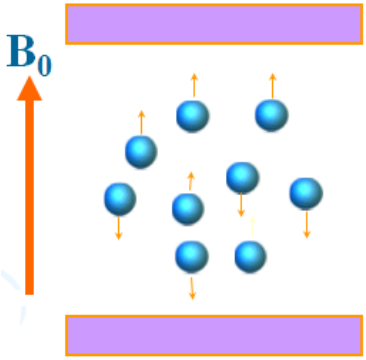

Figure 1.2.2 Spin orientations when placed in a static magnetic field.

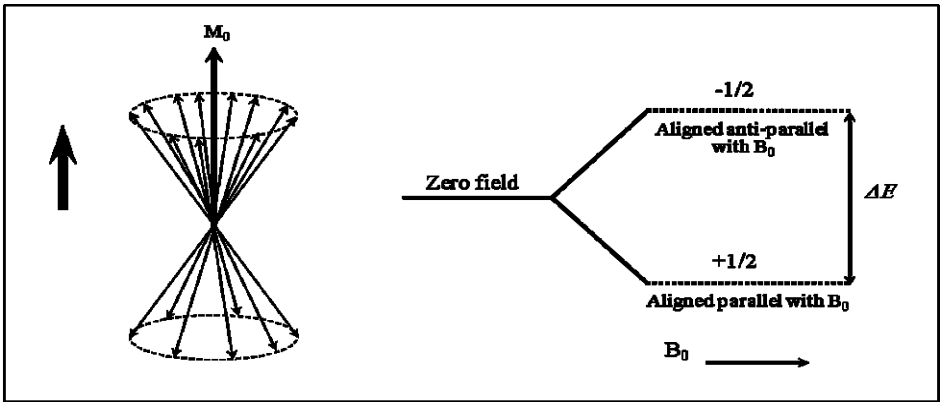

Figure 1.2.3 Spin orientations and energy levels when placed in a static magnetic field for spins with quantum number ½.

The lower energy state is more stable than the higher energy state. Therefore there are more nuclei in the lower level than in the upper level, creating a population difference. Each energy level follows $E=-\mu_z B_0$, where μ_z is the z component of the nuclear magnetic moment which is defined as $\mu_z = m\gamma\hbar$, where m is the nuclear magnetic quantum number (1/2 or -1/2 for protons) and $\hbar$ is the Planck's constant divided by 2π. The energy difference ΔE of the two levels is proportional to the strength of the static magnetic field and the population difference

$$\Delta E = \gamma\hbar B_0 \qquad (1.2)$$

and

$$\frac{N_{upper}}{N_{lower}} = e^{-\Delta E/kT} \qquad (1.3)$$

where N_{upper} and N_{lower} represent the population of nuclei in the upper and lower energy levels respectively, and k is the Boltzmann constant and T is the absolute temperature. Equation (1.3) is also called Boltzmann's law describing the thermal equilibrium of the nuclear spins.

The NMR experiment is to induce transition between neighboring energy levels by absorption or emission of a photon with the necessary energy. A nucleus in the lower energy state absorbs a photon and ends up in the upper energy state. The energy of this photon must exactly match the energy difference between the two states. The energy, E, of a photon which is exactly ΔE described above has the following equation

$$\Delta E = h \nu \qquad (1.4)$$

where ν is the required frequency, h is the Plank's constant ($h = 6.626 \times 10^{-34}$ J s). In NMR and MRI, ν is called the resonance frequency. From equation (1.2) and (1.4), we have the famous Larmor eqution

$$\nu = \gamma B_0 / 2\pi \qquad (1.5)$$

Therefore, for any particular nucleus in a given static magnetic field, such resonance frequency is also termed as Larmor frequency.

Magnetic resonance is achieved by inducing a radiofrequency (RF) field B_1 at the Larmor frequency in the direction perpendicular to the static external magnetic field. The application of such a radio frequency (RF) field of Lamor frequency with an energy of

ΔE to the system will cause lower energy level nuclei to absorb energy and get excited to upper energy level. This process is called nuclear magnetic resonance. The RF field B_1 will force a torque onto the macroscopic magnetization and rotate it about the RF field while it is precessing about the main static magnetic field B_0. Such rotation can be considered as a flipping action, meaning that the net magnetization along B_0 direction has been flipped down to an angle α, as shown in Figure 1.2.4. The value of the angle depends on different RF pulses. If the angle is 90°, then the magnetization will be flipped down right onto the transverse plane as shown in Figure 1.2.5. The angle α is determined by $\alpha = \gamma B_1 t$, where B_1 is the amplitude of the RF field and t is the duration of the RF pulse. We can manipulate pulses by controlling its corresponding amplitude and applying time.

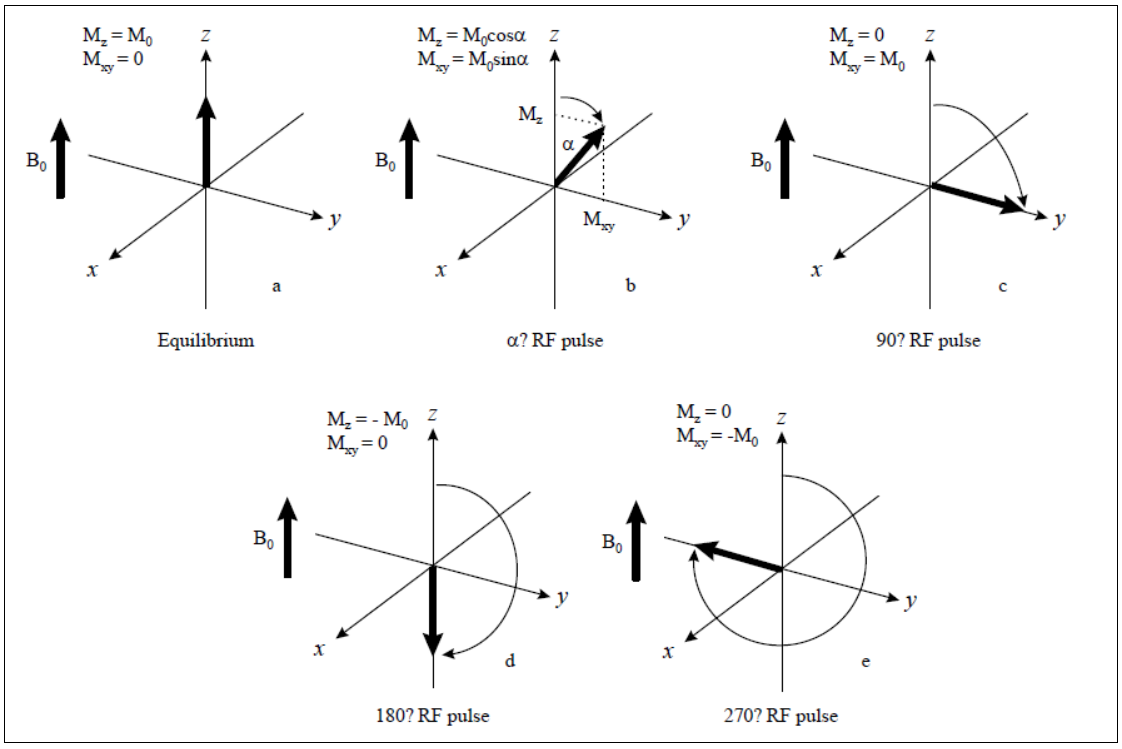

Figure 1.2.4. Interactions between RF pulses and net magnetization.

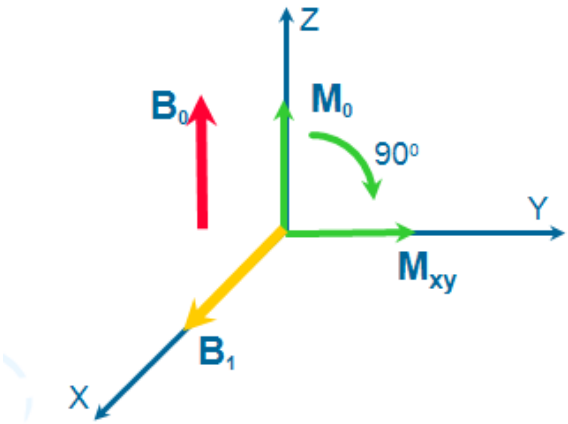

Figure 1.2.5. Interactions between 90° RF pulse and net magnetization.

Relaxation Processes

Removal of the RF field following the resonant absorption of energy will allow the excited nuclei to return to their equilibrium energy states. The majority upward transition population, that is the originally lower level population, returns to its equilibrium by losing energy in the form of an RF wave via various radiationless transition processes termed "relaxation". The RF signal is characterized by the Lamor frequency of the nucleus, and can be received and recorded by the NMR instrument.

After the RF pulse is turned off, the recorded signal of recovery, denoted by Mz, will increase gradually from zero to the equilibrium maximum while the recorded signal of decay, denoted as Mxy, will decrease gradually from equilibrium maximum to zero, as shown in Figure 1.2.6. These two relaxation processes are termed as spin-lattice (or longitudinal) relaxation and spin-spin (or transverse) relaxation. The time constants describe these relaxation processes and are termed as relaxation times. The spin-lattice relaxation time is designated by T_1 and the spin-spin relaxation time is designated by T_2. Relaxation time is a function of the spin species and the chemical and physical environments surrounding the spins. Or we can say that relaxation time constants are a fundamental property of the sample. Therefore, the analysis of T1 and T2 give us indications of physical and chemical properties of the samples. Specifically, the spin-lattice relaxation is related to the process of dissipating the excess energy to the surroundings by the spins at excited state when returning to the lower energy state.

Therefore, only frequencies at Larmor frequency affect T_1. Since Larmor frequency is proportional to B_0, T_1 will therefore vary as a function of magnetic field strength. In general, T_1 is inversely proportional to the number of molecular motions at Larmor frequency. During the relaxation process, in addition to energy dissipation to lattice, spins in the excited and equilibrium state also exchange with each other. In such a process, magnetic moments lose phase coherence and transverse magnetization decays to zero with a time constant T_2. Therefore the net magnetization starts to dephase because each of the spin packets making it up is experiencing a slightly different magnetic field and rotates at its own Larmor frequency. The longer the time elapses, the greater the phase difference becomes. Unlike spin-lattice relaxation, spin-spin relaxation is inherent to the property of food materials and biological tissue and is less susceptible to external fields than T_1.

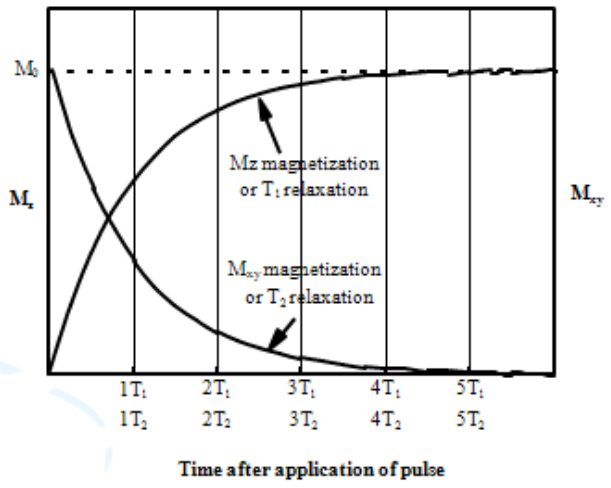

Relaxation of NMR signals after a 90° RF pulse.

Figure 1.2.6. Relaxation process: recovery process and decay process.

The relaxation properties can be conveniently related to the states of the proton-containing chemicals such as water and lipids as explained in the literature review section. By analyzing the states of water and lipids in a material using NMR techniques, we can learn the quantity of water and lipids and stability of the material. More discussion on development and application of "relaxometry" for study of food stability will also be provided in the literature review section.

1.2.2 Magnetic Resonance Imaging (MRI)

The MRI system is designed to record signals from a single point, or a line, or a plane, or a three dimensional volume in a sequential manner. And how to record the differences among each point in the sample is the key concern. The idea is to superimpose magnetic field gradients onto the main magnetic field and expand the magnetic field gradients for many other uses in MRI image acquisitions.

Magnetic Field Gradient and Frequency Encoding

We know that the Larmor frequency of a spin is proportional to the magnetic field that it is experiencing, $\omega = \gamma B_0$. If three tubes of water are placed in the same field, there will be only one frequency, and one peak in the NMR spectrum (Figure 1.2.7). If a linear field gradient, G, is superimposed on the main magnetic field, B_0, water tubes in different horizontal locations will be experiencing different field strength because the field strength varies with horizontal location in this case. Therefore, there will be two

frequencies, and two peaks will appear in the NMR spectrum. The amplitude of the signal is proportional to the number of water tubes or spin density.

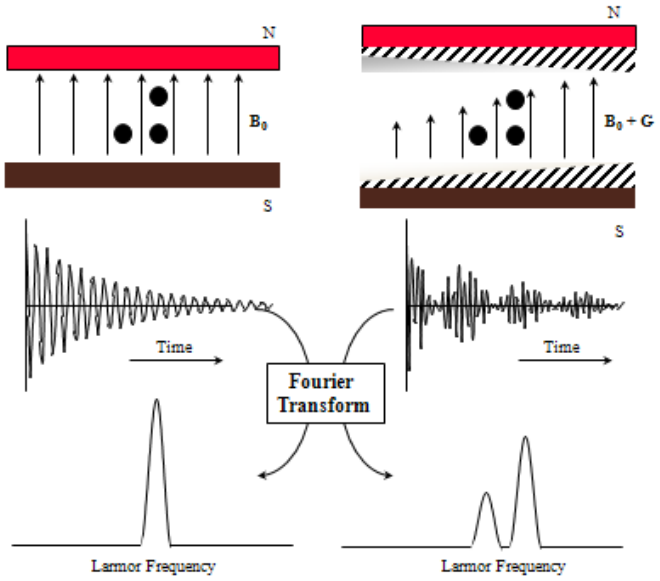

Figure 1.2.7. Application of a field gradient in order to encode signals from different spatial positions. Three spots represent three tubes water in the sample.

Because Larmor frequency is proportional to the field strength and field strength is a function of position, we can establish a relationship between frequency and spatial position of the spins by an equation similar to Equation $\omega = \gamma B_0$,

$$\omega = \gamma (B_0 + xG_x) = \omega_0 + \gamma x G_x \qquad (1.6)$$

or,

$$x = \frac{w - w_0}{\gamma G_x} \qquad (1.7)$$

where x is the position in x axis direction and Gx is the field gradient applied in the x axis direction. Here we say the frequency is spatially encoded. Field gradients can be applied in all three directions. The symbols for a magnetic field gradient in the y and z directions are Gy and Gz. Similarly we have

$$\omega = \gamma(B_0 + yGy) \qquad (1.8)$$

$$\omega = \gamma(B_0 + zGz) \qquad (1.9)$$

Equation (1.6) forms the basis for all magnetic resonance imaging methods. The back projection reconstruction imaging method will be presented in the next section to illustrate how the MR image is produced.

Fourier Transform Imaging

Fourier transform (FT) imaging is currently the most widely used MRI technique. A Fourier transform (FT) is an mathematical operation which converts functions from time to frequency domains. An inverse Fourier transform (IFT) converts from the frequency domain to the time domain, as shown in Figure 1.2.8.

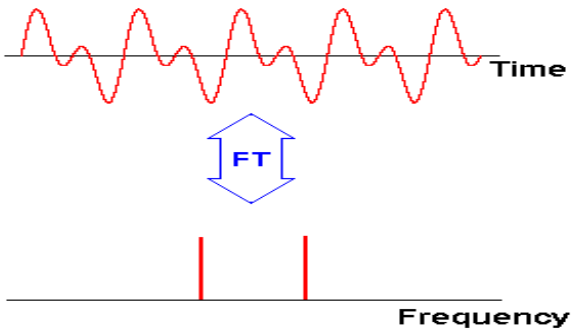

Figure 1.2.8. Fourier transform process

The first two dimensional Fourier transform image was proposed in 1974 by Kumar et al. (Kumer, et al. 1975). In FT imaging, both the amplitude information and phase information are acquired to spatially encode the signal. The amplitude information (frequency encoding) is obtained by using the original field gradient, *Gx* from which *x* can be calculated. Phase encoding is achieved by applying a phase encoding gradient just before the original field gradient is turned on, and at the right angle to the original gradient, normally in *y* direction, and is denoted by *Gy* or *G*φ. The phase encoding gradient is raised from zero in a series of small successive steps (time duration *t*). Phase angle φ is given by

$$\phi = \gamma y \int_0^t Gy(t)dt \qquad (1.10)$$

φ can be determined through experiment (Chen and Hoult 1989). Knowing the phase change, −γ, *Gy,* and *t*, we will be able to calculate *y*. Data collected after the original gradient *Gx* will contain both the frequency and phase encoded information, and the

number of the data *n* is the set sampling points. If we increment *Gy* and repeat the procedure m times, we will get a data set containing *m* rows and *n* columns. By using Fourier transform, we can produce an $m \times n$ image.

Slice Selection

Data for production of MR images are collected from spins of a plane through an object. This plane will have certain thickness, and is therefore termed a slice. An MRI instrument is capable of selecting a slice of certain spatial location and thickness. Slice selection is of great importance to signal to noise ratio and image resolution. The principle behind slice selection is explained by the resonance equation. Slice selection is achieved by applying a one-dimensional, linear magnetic field gradient during the period that the RF pulse is applied. A 90° pulse applied in conjunction with a magnetic field gradient will rotate spins, which are located in a slice or plane through the object. Picture what this would look like if we had a cube of small net magnetization vectors. To understand this we need to examine the frequency content of a 90° pulse. A 90° pulse contains a band of frequencies. This can be seen by employing the convolution theorem. The frequency content of a square 90° pulse is shaped as a *sinc* pulse. The amplitude of the *sinc* function is largest at the frequency of the RF which was turned on and off. This frequency will be rotated by 90° while other smaller and greater frequencies will be rotated by lesser angles. The application of this 90° pulse with a magnetic field gradient in the *x* direction will rotate some of the spins in a plane perpendicular to the *x* axis by

90°. The word *some* was used because some of the frequencies have a $B1$ less than that required for a 90° rotation. As a consequence the selected spins do not actually constitute a slice. The slice thickness Δz is determined by $\Delta z=\Delta \nu /(2\pi\gamma G_z)$.

Pulse Sequences

The basic procedure for production of a two-dimensional MR image can be summarized into four steps. Excite the spins of selected slice first; then apply a phase encoding gradient for a fixed period of time; apply a frequency encoding or read gradient and collect *n* data point; and then increment the value of phase encoding gradient and repeat steps 1 to 3 *m* times perform two dimensional Fourier transform on the data to produce an *m* by *n* image. Therefore, pulses are applied in a sequential order. A schematic diagram of a typical MRI pulse sequence is shown in Figure 1.2.9.

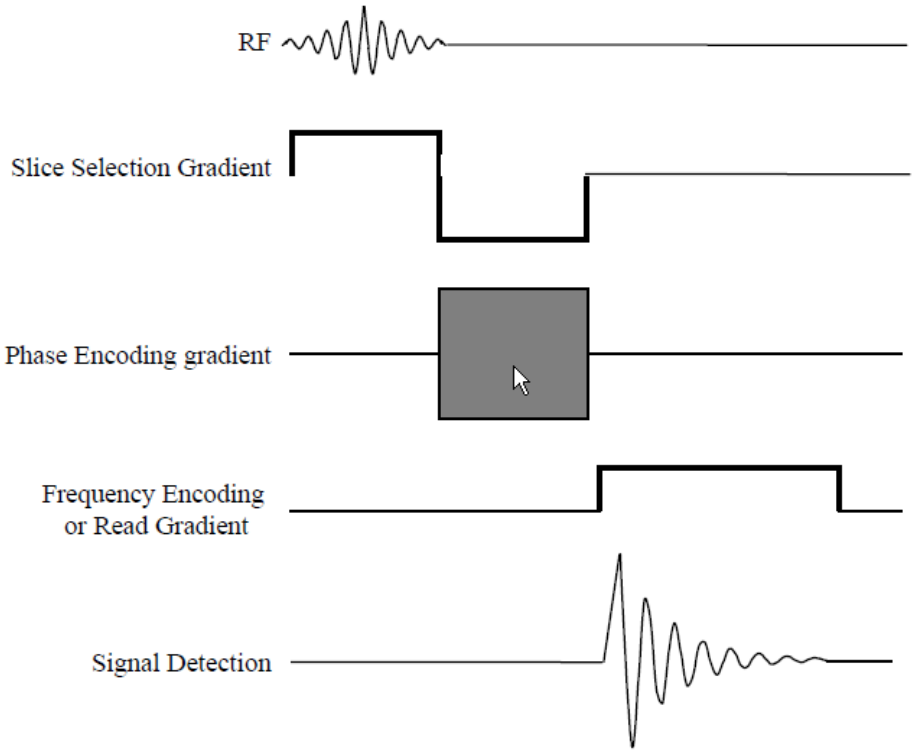

Figure 1.2.9. A two-dimensional FT imaging sequence.

Many NMR properties can be regarded as contrast agents which are used to construct images. When these contrast agents are very low in detectable quantity, for example in the case of materials with very low moisture and lipid contents, producing high quality MR images is challenging as discussed in next section. Therefore, contrast enhancement must be conducted for low moisture foods through hardware and pulse sequence improvements, which was one of the key objectives of this study.

1.3 Literature Review

1.3.1 Water and food stability

Water is a key component in foods. It affects the quality attributes, shelf stability, and processing (Levine and Slade, 1991). For example, if we want to extend the shelf life of a food product, its natural moisture content should be reduced to a level at which microbiological and biological activities which cause safety and spoilage issues, are under control. Change in moisture content during storage and transportation could affect the stability and quality of food products, and therefore monitoring water in foods is of great interest to food processors.

NMR techniques have been used for measurement of moisture contents in different systems, such as foods, seeds, wood, etc (Nanassy, 1973; Nanassy, 1976; Brosio et al., 1978; Sharp et al., 1979; Di Dola and Brosio, 1983; Renou et al., 1987; Chambers et al., 1989; Tollner and Hung, 1992; Hartley et al., 1994). More NMR based methods for study of water were developed later when pulsed NMR became available. The proton density of proton-containing compounds can be quantified with NMR and MRI. Since the proton density is proportional to the concentration of the proton-containing compounds, it is possible to quantitatively determine the concentration of these proton-containing compounds such as water and fat via NMR and MRI techniques.

Moisture content alone is not an adequate indicator of shelf stability of food products. The water activity concept was used to measure the availability of water in foods, which is not only a function of water content, but also the environments in which water molecules are embedded. “Availability” of water is a measure of how “freely”

water molecules can participate in reactions or how easily water molecules diffuse to the reaction sites to participate in or facilitate the reactions. Many researchers have found that the mobility of water, as measured by NMR and other techniques, is related to the "availability" of water in complex systems (Richardson et al., 1986; Richardson et al., 1987; Mora-Gutierrez and Gaianu, 1989; Kakalis et al., 1990; Lai and Schmidt, 1990; Hills, 1991; Schmidt and Lai, 1991; Lai and Schmidt, 1993). Relaxometry is an excellent NMR technique for the measurement of water mobility, and provides useful information on the biological and physiochemical stability and water migration in food systems (Ghosh *et al.,* 2006). In the case of high protein food bars firming processes, Lin *et al.* (2006) found that these high protein food bars firmed without significant changes in moisture content or water activity, suggesting that bar hardening was not due to moisture loss and that water activity was not sensitive enough to reflect the physicochemical changes likely associated with the properties of water. Ruan and Chen (1998) reported other cases where the physical properties of foods changed (i.e. hardness) without fluctuations in moisture content or water activity during storage; these changes were accompanied by alterations in the profiles of water mobility within the products. Because water mobility is a function of the physical and chemical environments in which the water molecules are embedded, any changes to these environments, such as those which occur during storage, will result in a change in the mobility profile of water molecules (Ruan and Chen, 1998).

1.3.2 Water distribution and structure of foods

Many processes require the knowledge of water and temperature distribution during the processes so that suitable methods can be designed to control heat and mass transfer. Undesirable moisture redistribution in food materials may cause severe quality and stability deterioration. Most of the conventional techniques for the study of water distribution and morphology of foods require substantial preparation work; sometimes thin sections are needed. Obviously, these techniques are, to different degrees, destructive or invasive, which inevitably disrupt the nature of the sample, and alter the processes being observed; the validity of the data obtained using these techniques is questionable. Moreover, they do not allow continuous, non-interrupting monitoring of moisture migration in a sample undergoing either processing or storage and transport. MRI, on the other hand, can be used to obtain quantitative images of moisture content and other NMR properties of protons of water. The image itself allows researchers not only to visualize the distribution of moisture but also to develop new mathematical models or validate existing models. The most attractive features of MRI in this context are its non-destructive and non-invasive nature, rapidity, and no requirement for sample preparation. Additionally, MRI offers live or real-time observation of moisture migration during a process that can be incorporated into the MRI instrument (Gonzalez et al., 2000; Thybo et al., 2002; Galed et al., 2003; Clark and MacFall, 2003; Granizo et al., 2005; Kotyk et al., 2005; Goetz et al., 2007).

Many applications of MRI in the study of moisture and fat distribution, moisture migration, temperature distribution in foods have been reported (Hills, 1995; Schrader et

al., 1992; Schmidt and Lai, 1990; Shyh-Shin et al., 2009; Regier et al., 2007; Ghosh et al., 2007; Ramos-Cabrer et al., 2006; Ghosh et al., 2006; Yi-Lin and Hsi-Mei, 2004; Ruan et al., 1989). Figure 1.3.1 shows a series of MR images of a barley kernel taken at different steeping times (Ruan and Chen 1998). The steeping process began with a rapid water uptake by the regions just bellow the hull followed by redistribution of the water to internal tissues. The regions just below the outermost layers of the hull have a greater amount of water than the surface of the grain. This may be due to the hull's ability to act as a selective membrane, allowing water below its surface for retention. It appears that initially all outer tissues (pericarp and hull) imbibe water at about the same rate until a mechanism (metabolic or vascular) within the seed redistributes the surface water to the embryo (McEntyre et al., 1997). The same study also illustrates the pathways of water movement during steeping and difference in water absorption characteristics among different cultivars (Goodman et al., 1992; Clark et al., 1997; Kuo et al., 2003; Lammertyn et al., 2003; Nguyen et al., 2005).

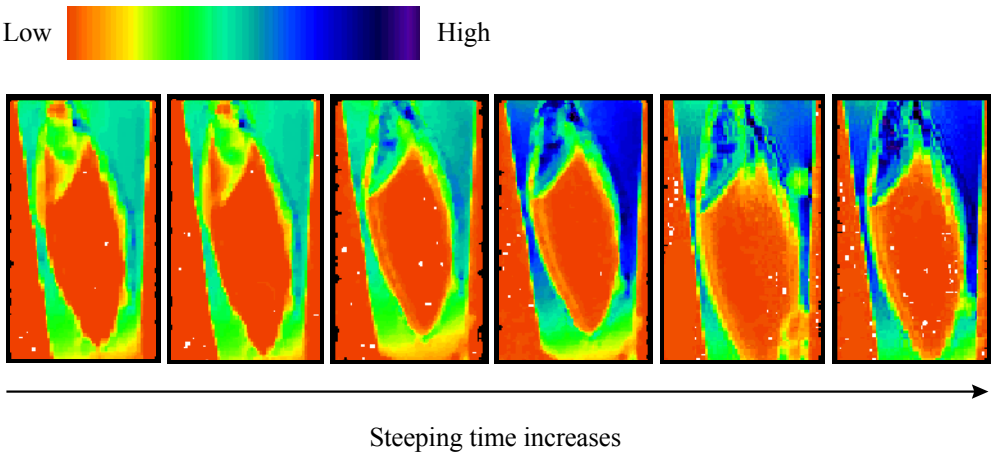

Figure 1.3.1. MR images of barley kernel obtained at different steeping times (1,2,8,12,24,48 hours) with color bar showing signal intensities.

However, use of MRI in research involving food and biological systems is rather limited compared with that in clinical fields. The reasons may be:

- Many food and biological systems are very low in moisture content compared with the human body. Thus, the signal to noise ratio often is a serious problem with MRI of food and biological systems.
- Many dynamic processes occurring in food and biological systems are very fast, and observation of these processes requires the techniques to have a comparable speed, while in the clinical field, MRI is used for diagnosis purposes, and imaging time usually is not an issue. Rapidity of MRI is one of the key issues in MRI on-line sensing applications.
- Food products are typically small in size and have complex structure and composition. Observation of structural, textural, and flow properties of certain foods and biological materials requires high resolution.
- MRI experiments on food and biological systems may be performed in extreme conditions such as high or low temperature, high flow rate, etc.
- Few food and biological scientists have sufficient knowledge of and/or access to MRI instrumentation, while most of MRI experts are in the medical field and

they are reluctant to explore the less familiar systems such as foods and biological materials.

As can be seen, MRI technique development has been essentially oriented towards clinical applications; without further advancing MRI technology, the use of MRI in food and biological systems will be hindered.

1.3.3 The NMR state diagram

1.3.3.1 NMR state diagram concept

State transition, also known as glass transition (from glassy state to rubbery state), is a unique property of polymers when they experience changes in temperature. The physiochemical properties change dramatically during state transition. Food scientists borrowed this polymer science theory and considered food materials as polymers. Close relationships between glass transition and stability and quality of low moisture foods have been established (Roos et al., 1996; Slade and Levine 1993, Rahman 2006). Transition from glassy state to rubbery state due to temperature rise or increase in water (water is a good plasticizer) will cause the mobility of the system to increase dramatically. In theory, relaxation times (T1 and T2) show a phase transition when temperature is changed gradually (Figure 1.3.2a). Our previous work showed that T2-temperature curves of maltodextrins of different moisture contents were characterized by a sharp transition point (Figure 1.3.2b). Based on these observations, we developed an NMR technique in which NMR experiments are conducted to determine relaxation times at

different temperatures. An NMR state diagram is obtained by plotting relaxation times against corresponding temperatures. From the NMR state diagram, a transition temperature may be identified.

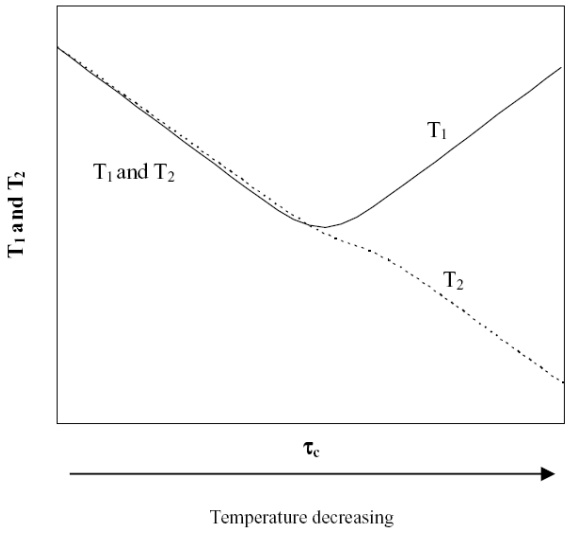

Figure 1.3.2a. A generalized schematic diagram showing the relationships between relaxation time constants and correction time.

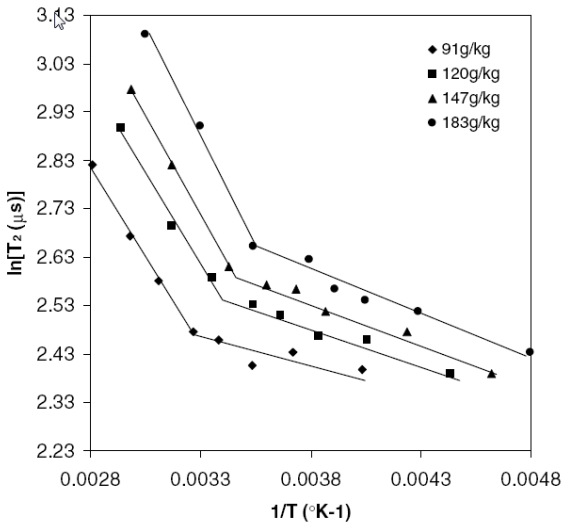

Figure 1.3.2b. Relationship between spin–spin relaxation time (*T*2) and temperature (*T*) in maltodextrins (DE15). The legend indicates the grams of water in 1 kg maltodextrins.

1.3.3.2 Applications of state diagram concept

The state diagram concept was used to predict the shelf life stability of a number food systems (Noel et al. 1990, Buera and Karel 1995, Roos et al. 1996, Kilcast and Subramaniam 2000) A study on protein bar will be discussed next to demonstrate the applications of the concept.

After a decade of rapid growth, the nutrition bar market has been gradually increasing since 2003, with major market trends including fortification with protein and/or fiber and inclusion of organic or all natural ingredients (Lockwood and Dornblaser 2007). High protein bars are composed primarily of powdered proteins from soy or dairy sources and sugar- or polyol-based syrups, with the addition of soy protein allowing for lower cost formulations and placement of heart health claims on the product label. The physicochemical characteristics and interactions of proteins and syrups are thought to influence the hardening of high protein bars over time, but the exact mechanism is not yet well understood.

Lin *et al.* (2006) showed that high protein food bars firmed without significant changes in moisture content or water activity, suggesting that bar hardening was not due to moisture loss and that water activity was not sensitive enough to reflect the physicochemical changes likely associated with the properties of water. Moisture migration will occur when regions of different moisture content are brought in contact with each other, but the direction of moisture migration is not necessarily from higher moisture content to lower moisture content. Instead, the migration of water takes place from regions of higher water activity to those of lower water activity (Ghosh *et al.* 2004).

In the case of high protein food bars, the migration of water will occur from the higher water activity syrups to the lower water activity powders, with the magnitude and speed of migration influencing the degree and rate of bar hardening. Ruan and Chen (1998) found other cases where the physical properties of foods changed (i.e. hardness) without fluctuations in moisture content or water activity during storage; these changes were accompanied by alterations in the profiles of water molecule mobility within the products. Because water mobility is a function of the physical and chemical environments in which the water molecules are embedded, changes to that environment, such as those which occur during storage, will result in a change in the profile of water molecules (Ruan and Chen 1998). Since the physicochemical properties of water and solid ingredients (i.e. proteins and carbohydrates) are key factors of high protein bar firming, nuclear magnetic resonance (NMR) techniques, including NMR state diagrams, lend themselves best to the study of these issues (Ruan and Chen 1998, Davenel and Schuck 2002, Chung *et al.* 2003).

Water can exist in three states in food bars—bound water, free water, and intermediate water, with the amount of intermediate water acting as a plasticizer and having the greatest influence over the softness of the bar. It has been hypothesized that bar hardening occurs when some of the water from the syrups migrates to the proteins during storage, causing molecular linkages to form (Gallo-Torres 2003). This causes the amount of bound water in the product to increase, thereby reducing the amount of water available to act as a plasticizer. An increase or a reduction in the amount of plasticizer

available could cause a glass transition to take place (Lin *et al.* 2006). The relationships between food stability and glass transition phenomena have been extensively studied in the food science and technology community (Slade and Levine 1993, Rahman 2006). The glass transition temperature (T_g) can be estimated using a NMR state diagram, which is a curve describing NMR relaxation time as a function of temperature (Lin *et al.* 2006). Greater differences between T_g and storage temperatures above T_g are expected to be associated with more rapid deterioration or reaction.

NMR measures the relaxation characteristics of protons, which can be related to the mobility of the proton-containing compounds, such as water, proteins, carbohydrates, and lipids. Spin-spin relaxation time (T_2) is commonly used as an indication of proton mobility, with higher T_2 values being indicative of a more mobile system (Lin *et al.* 2006). In the context of high protein food bars, the mobility has two significant implications: (1) higher T_2 may be associated with a softer bar texture; (2) higher T_2 may indicate that the ingredient or the bar is more susceptible to physicochemical changes that may lead to quality changes.

Previous research with dry soup powders suggests that powdered ingredients can be classified into four different types (A, B, C, and D) based on the shape of the NMR state diagram curve, with each type demonstrating distinct stability characteristics. Preliminary studies using powdered proteins found that proteins fell into three of the four types (A, B, or D), with the hypothesis that a better understanding of the grouping of proteins based on their stability could lead to improved ingredient selection (Lin *et al.*

2006). Manufacturers are continuously looking for effective ways to inhibit the migration of water in nutrition bars, with the most common method focusing on proper choice of ingredients (Gottschalk 2006, Wade 2005, Gerdes 2005). In order to make ingredient selection more straightforward and less of a "trial-and-error" process, a practical approach needs to be established to aid in the selection of appropriate proteins and carbohydrates for improved texture and shelf life of nutritional food bars.

1.3.4 Current technical challenges

Expensive and complicated high field superconducting NMR and MRI machines were used until low cost benchtop NMR and small MRI machines became available in recent years. These low cost NMR and MRI machines have the potential of making routine monitoring and analysis of processes and products possible in industry environments. However, these machines' capabilities are limited due to their low magnetic field strength. Furthermore, implementation of existing advanced NMR and MRI techniques are met with challenges and difficulties. For example, many foods and drugs have very low moisture (proton) contents and hence the signal/noise ratios seen by NMR and MRI machines are very low, making acquisition of reliable data and high quality images difficult. Field inhomogeneity is another issue. All these contribute to the low resolution of MR images. Furthermore, current NMR studies of foods fail to connect the NMR properties with fundamental physiochemistry associated with changes in foods. We need to explore the interconnection between the glass transition and water because water is the most effective plasticizer in foods and biological materials and has a

profound impact on the motional characteristics of the food system (Micklander et al., 2002; Bertram et al., 2005; Granizo et al., 2007; Hernandez-Sanchez et al., 2007).

1.3.4.1. Hardware issues

As described earlier, the basic hardware of a MRI system includes: a permanent magnet, gradient coils, radio frequency coils, computer systems, etc. The performance qualities of hardware are crucial to the quality of MRI images. Therefore, development of hardware components to fit various imaging requirements has been a constant research and development topic. Imaging probes can be generally divided into two categories: surface coils and volume coils. Since the amount of noise is related to the mass volume of the materials contained within the sensitive field of the probe, i.e., the filling factor (Stark and Bradley, 1989), surface coils will give a better *S/N* ratio for samples close to the surface of an extended volume. However, in most of the food and biological applications, it is advantageous to use a volume coil for more uniform excitation and easier image quantification (Haacke et al., 1999).

The gradient coil is also a key to the quality of MRI images, especially to the resolution of MRI images. It is crucial to have a highly linear magnetic field gradient in order to obtain high resolution images, which is a key requirement for most food and biological materials (Ruan and Chen, 1998).

The maximum theoretical resolution of an image (l) is a function of both the NMR signal line width (d) and the linear magnetic field gradient (G):

$$l = d / \gamma G \qquad (1.11)$$

where l is the resolution (in cm), d is the line width (in Hz), and G is the gradient strength (in G/cm). γis 42.67 Hz/G for protons. Most foods and biological samples usually have very short T2 values (solid-like NMR characteristics) which lead to rapid signal decay and broad signal line width. Equation (1.11) shows that a stronger gradient can improve resolution (Haacke et al., 1999). T2 is the spin-spin relaxation time.

Another hardware related issue is that foods have different states (solid, gel, liquid) and shapes. Special coils may be necessary for unique samples in order to compensate for the noise and variations arising from samples (Constantinesco et al., 1997; Grimault et al., 2004; Goloshevsky et al., 2005; Epstein and Magland, 2006).

1.3.4.2 Pulse sequences

The spin-echo pulse sequence (Hahn, 1950) has been the most widely used MRI imaging sequence. Early spin-echo sequences consisted of relatively simple components. As high field MRI technique developed, much more complex pulse or gradient components were added or modified in the sequence to satisfy specific imaging requirements. For example, T1weighted or T2 weighted MRI images are widely used in medical examinations due to the unique properties of relaxation time parameters in

human body tissues (Pui and Fok, 1995; Melhem et al., 1996; Schmalbrock et al., 1998; Lee et al., 2000; Li and Mirowitz, 2003; Both et al., 2004). T1 is the spin-lattice relaxation time and T2 is the spin-spin relaxation time. These relaxation times are commonly used as an indication of proton mobility. However, such sequences may not to be necessary for food materials because of different relaxation characteristics and they usually take relatively longer acquisition time compared to other imaging sequences although the signal to noise ratio is relatively higher.

The gradient-echo pulse sequence eliminates the 180° rephrasing pulses used in spin-echo sequences. This sequence simply uses reversals of the readout gradient to form the echo so that fast imaging with small tip-angle excitations (<90°) as the initial pulse in each sequence can be performed. Such changes can reduce acquisition time dramatically and can be applied in the fast imaging area. However, eddy currents due to gradient switching are also introduced and thus this sequence requires a good linear shape of the magnetic field gradient (Haacke et al., 1999).

Deka et al. (2005) used a centric scan SPRITE sequence to acquire good density profiles with pure phase encoding and 1D gradient. Although the experiments were applied in a 2.4 Tesla magnetic field, which is much higher than the magnetic field in this study, it still shows that such sequence can be used to image extremely dry foods such as solid materials and still be able to obtain density contrast rather than relaxation parameters weighting which provides feasibility to adapt to food materials at low magnetic field (Fang et al., 2001; Gruwell et al., 2004; Deka et al., 2005).

CHAPTER 2. ADAPTATION OF ADVANCED MRI TECHNIQUES FOR FOOD AND NON-FOOD APPLICATIONS

The adaptation of advanced MRI techniques to the low field MRI machines is one of the primary tasks of this study. Through the successful adaptation of the MRI techniques, good quality images could be obtained, which thus provide a basic platform as well as useful tools for analysis of the properties of water and the physicochemical characteristics in foods and other biological materials. The objective of this MRI work was to develop imaging techniques for the evaluation of properties of water in foods and non-food materials with low moisture contents. In this part of the study, spin-echo sequences, gradient-echo sequences and SPI sequences were adapted onto both the DRX and DRX2 MRI systems and validated using model foods. The application of these sequences in the studies of several food and non food materials is then demonstrated.

2.1. MRI Techniques Development and Validation

2.1.1. Pulse sequence development

2.1.1.1 Instruments

All experiments were carried out using two low field MRI machines housed in our lab in the Department of Bioproducts and Biosystems Engineering at the University of

Minnesota. One of them is a Maran DRX Benchtop (Resonance Instruments Ltd, UK) with a 21.4 MHz permanent magnet which can accommodate samples up to 25 mm in diameter (Figure 2.1). The other MRI system (Yuyao, China) is equipped with a 12.9 MHz permanent magnetic field and can accommodate samples up to 180 mm in diameter (Figure 2.2). More specifications of the two systems are listed in Table 2.1.

Figure 2.1. Maran DRX Benchtop low field MRI system.

Figure 2.2. Maran DRX2 low field MRI System.

Table 2.1. Specifications of our MRI machines

Specification	**Maran DRX benchtop MRI system**	**Maran DRX2 large horizontal bore MRI system**

Manufacturer	Resonance Instruments Ltd	Yuyao
Field strength	21.4 MHz	12.9 MHz
Coil configuration (vertical, horizontal)	Vertical	Horizontal
Bore size	25mm in diameter	220 mm in limiting height
Gradient	116, 121, 199 G/cm for XYZ directions	11, 15, 18 G/cm for XYZ three directions correspondingly
Preloaded pulse sequences installed	Basic NMR and basic MRI sequences	Basic NMR and basic MRI sequences
FOV	20cm×20cm	20cm×20cm
Imaging mode	Single and multi slice 2D images, 3D images	Single and multi slice 2D images, 3D images

Operation of the imagers is performed through a PC with IDL5.6 software installed. The software allows users to select pulse sequence, experiment parameters, image mode, etc.

2.1.1.2 Sequences development

Several commonly used pulse sequences were adapted onto our low magnetic field MRI systems. These sequences were modified in order to satisfy imaging requirements in food research. In addition, post-acquisition data processing models and methods were developed to analyze data more efficiently and to provide additional and meaningful information. Images of different samples were obtained. The following results indicate that the pulse sequences work reasonably well with our low field system.

Spin-echo sequence development

Spin-echo sequences are widely used in imaging. A simple spin-echo sequence can be developed into different sequences according to the imaging requirements. In applications in food materials, high resolution images are required within a relatively shorter acquisition time. The sequence diagrams are designed as shown in Figure 2.1.1.2a and 2.1.1.2b. Spin echo sequences can be used for different purposes. In food research studies, an image for one single slice usually cannot provide enough information. Therefore, images for several slices or the entire sample are more meaningful for food researchers. Sequences shown in Figure 2.1.1.2a and 2.1.1.2b can be used for acquisition of multi-slice images or complete 3D slice images. Parameters of each sequence are shown in the figures.

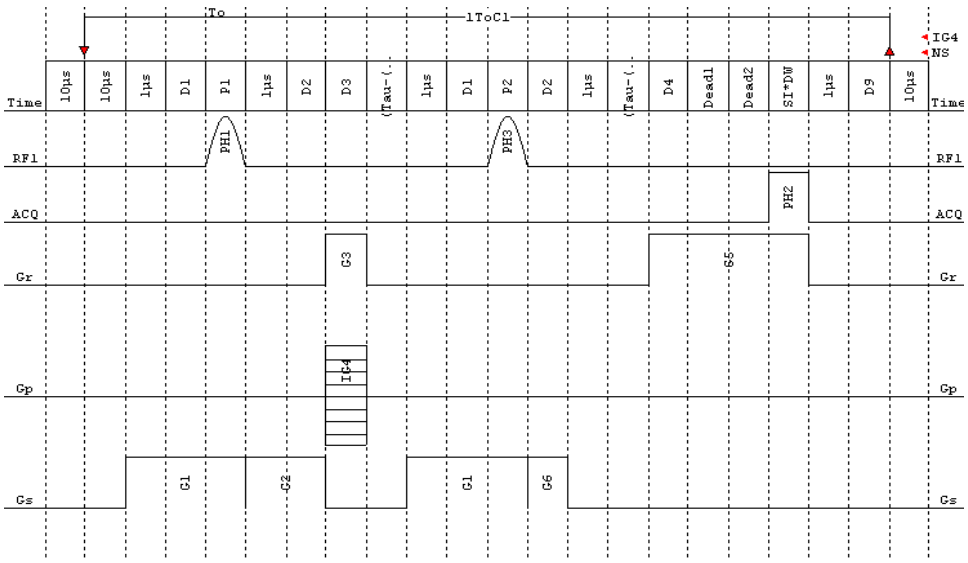

Figure 2.1.1.2a Spin echo sequence diagram for multi-slices

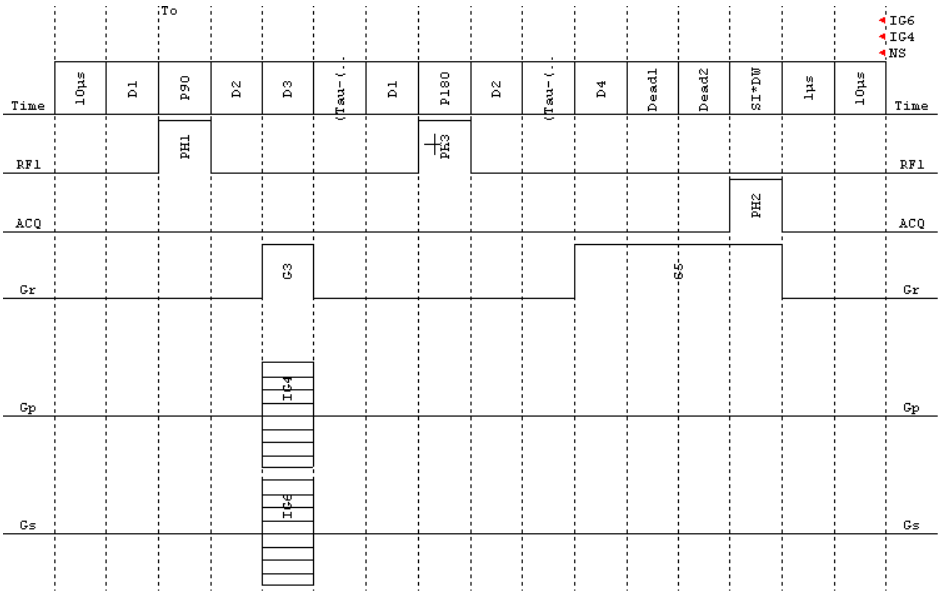

Figure 2.1.1.2b Spin echo sequence diagram for whole sample 3D slices

Examples of MRI images acquired with these adapted and modified spin-echo sequences for different specific purposes are shown in Figures 2.2.1.3a-e. 3D imaging is used most often in food research. Food scientists always want to see clear images of the internal structure of food materials. Figures 2.2.1.3a-b show two typical food examples. With a 3D spin-echo sequence (shown in Figure 2.2.1.2b), the whole 3D images and individual slices of the materials can be presented very clearly. The moisture distribution in these slice images are illustrated through color gradients. Two-D images acquired using spin-echo sequence are shown in Figures 2.2.1.3c-e. A vertical noise strip in the left image was noticed in Figure 2.2.1.3c. Such noise is thought to be caused by a specific disturbance frequency which might be close to the center frequency of this low field MRI system.

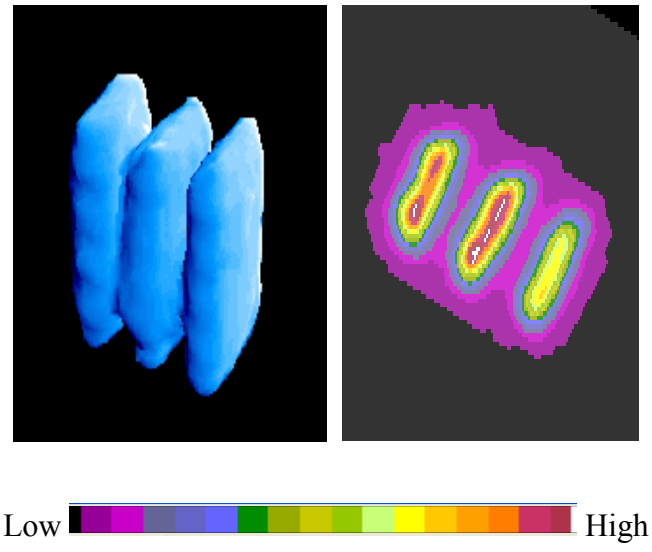

Figure 2.2.1.3a. 3D images and 2D images for sandwich samples processed by software IDL5.6 using the sequence shown in Figure 3.3b with color bar showing signal intensities.

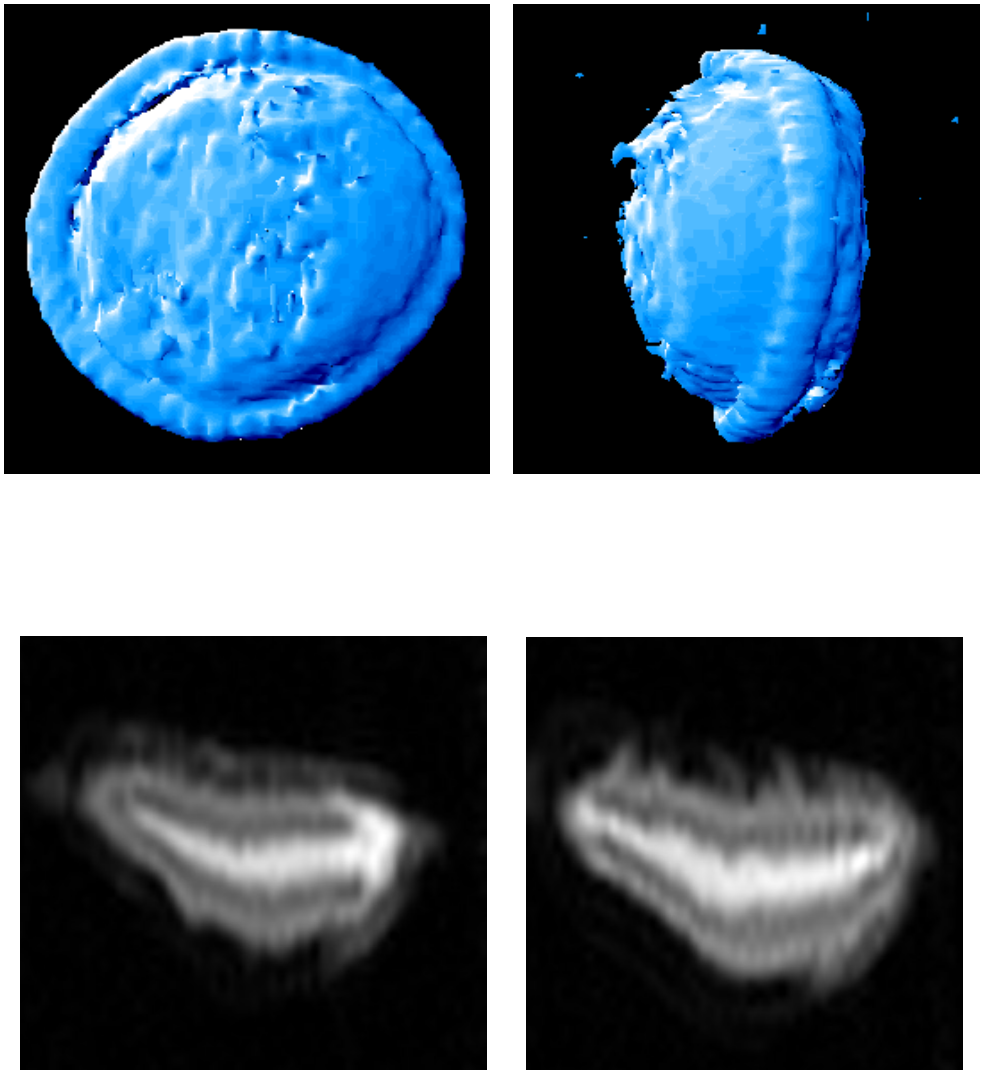

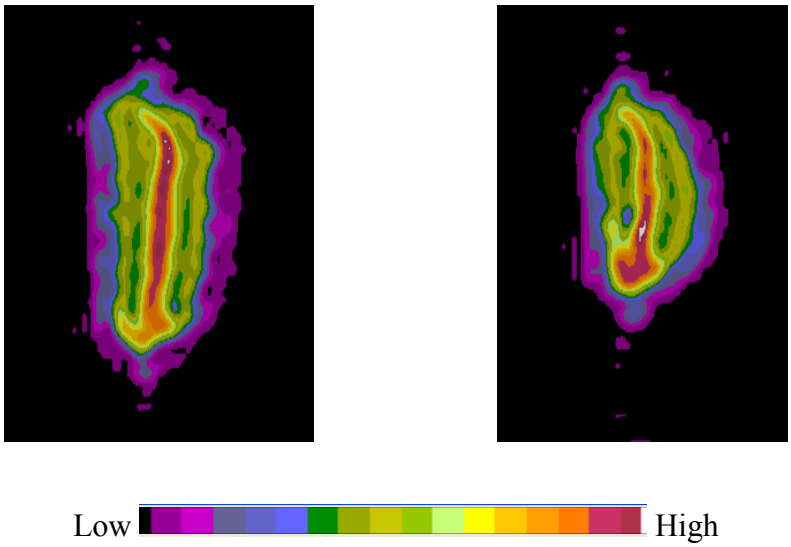

Figure 2.2.1.3b. 3D images and 2D images for sandwich samples processed by software IDL5.6 using sequence in Figure 3.3b with color bar showing signal intensities.

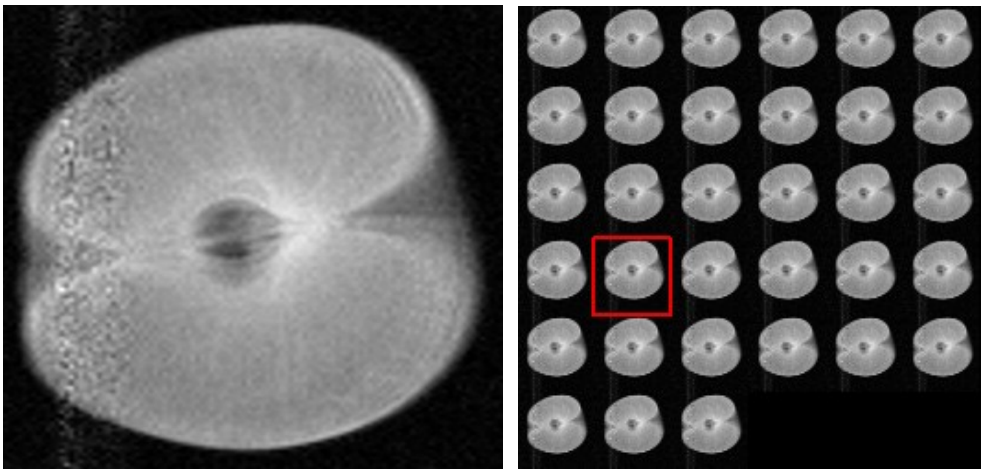

Figure 2.2.1.3c. An apple was used as the sample. The left image is selected from the right image group with a resolution of 128×128 using sequence in Figure 3.3a.

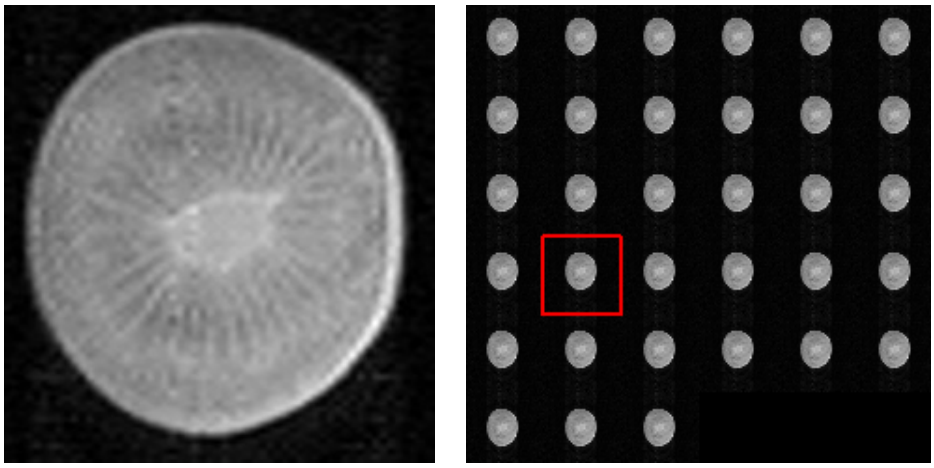

Figure 2.2.1.3d. A kiwi was used as the sample. The left image is selected from the right image group with a resolution of 128×128 using sequence in Figure 3.3a.

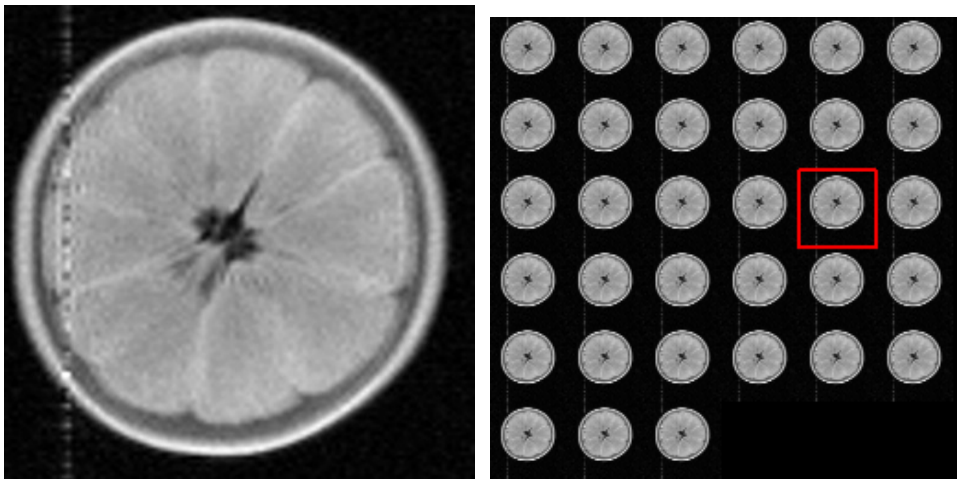

Figure 2.2.1.3e. An orange was used as the sample. The left image is selected from the right image group with a resolution of 128×128 using sequence in Figure 3.3b.

Gradient-echo sequence development

Gradient echo sequences do not apply the 180◦ rephrasing pulses which are the key components in spin-echo sequences. Instead, this sequence uses reversals of the readout gradient to form the echo. In addition, small flip-angle pulse excitations (<90◦) were applied several times to lead the spins into saturation state very quickly. These changes can reduce acquisition time very efficiently and thus a grad-echo sequence can be developed into a fast imaging sequence. The sequence diagram is designed as shown in Figure 2.1.1.4.

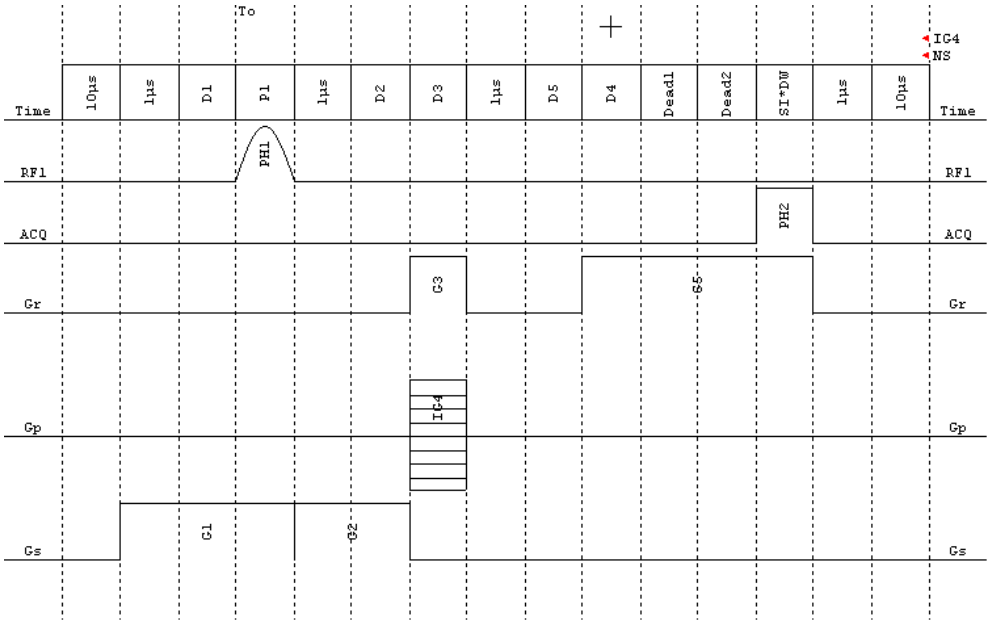

Figure 2.1.1.4. Gradient echo sequence diagram

Examples of MRI images acquired with Gradient echo sequence are shown in Figure 2.1.1.5. We can see from the image that the quality of this image can be compared to the image acquired with the spin echo sequence and the noise appeared to be more apparent in this gradient echo image has been reduced, suggesting that the magnetic field homogeneity in this low field MRI system was improved for gradient echo applications. Gradient echo sequence is believed to be an efficient fast imaging technique.

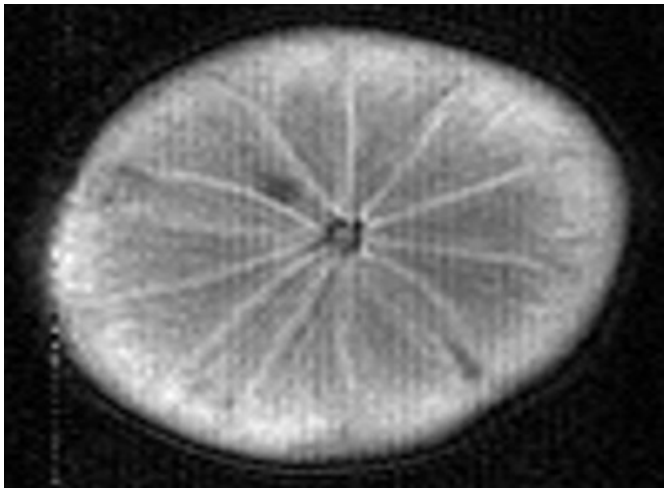

Figure 2.1.1.5. An orange was used as the sample with resolution of 128×128 using gradient echo sequence.

SPI sequence development

Single point imaging sequence (also called SPI sequence) is a 3D phase encoding MRI sequence (Emid and Cryghton, 1985) which can be used to acquire images for solid state materials with extremely low moisture content and very short T2 values (<50 μs). The sequence diagram was designed as shown in Figure 2.1.1.6.

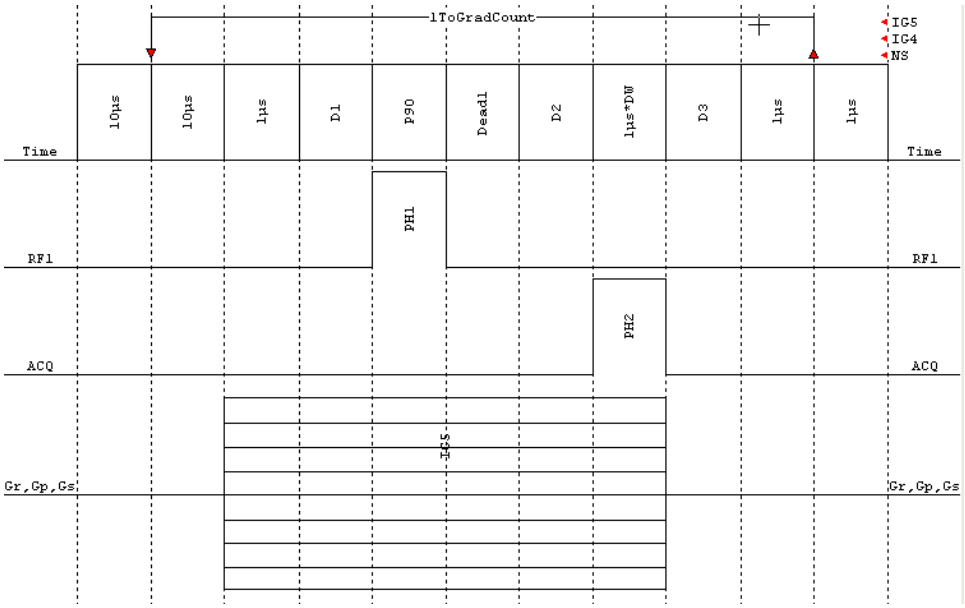

Figure 2.1.1.6. SPRITE sequence diagram

Samples were prepared for the two low magnetic systems respectively. Each sample contained two pieces of materials. Sample-1 had one small piece of dry wood (whole cubic), with dimensions of 1.4cm×1.6cm×2.8cm and one small piece of plastic (formed by two cylinders, hollow inside), with dimensions of diameter 2.0cm; height 0.5cm (lower part); and diameter 1.2cm; height 0.8cm (upper part). The gradient strengths for smaller low magnetic field MRI system were: 116, 121, 199 G/cm for XYZ

directions shown in Figure 2.1.1.7a. The resolution of the images was 64×64. Sample position information was as follows: Project XZ plane to Y direction,

For wood, x=1.4cm, y=2.8cm, z=1.6cm;

For plastic, XZ plane diameter=2.0 & 1.2cm, z=0.5 & 0.8cm, respectively.

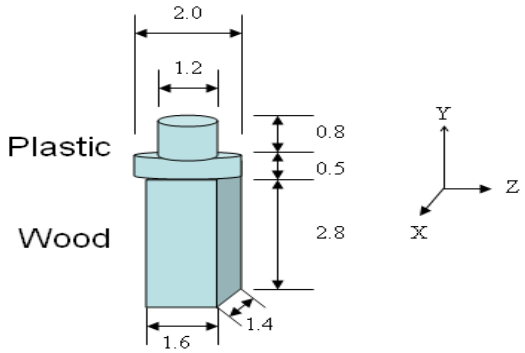

Figure 2.1.1.7a. Sample structure with dimensions for benchtop MRI system

Similarly, sample-2 for the larger low field MRI system contained one piece of dry wood (whole cubic), with dimensions of 3.8cm×8.8cm×8.8cm and one piece of plastic (formed by three cylinders, hollow inside), with dimensions of diameter 5.0cm, height 2.5cm; diameter 7.5cm, height 3.0cm; diameter 5.0cm, height 2.5cm shown in Figure 2.1.1.7b. The gradient strengths for larger low magnetic field MRI system were: 11, 15, 18 G/cm for XYZ directions. The resolution of the images was 64×64. Sample position information was as follows: Project YZ plane to X direction,

For wood, x=3.8cm, y=8.8cm, z=8.8cm;

For plastic, XY plane diameter=5.0, 7.5 & 5.0cm, z=2.5, 3.0 & 2.5cm, respectively.

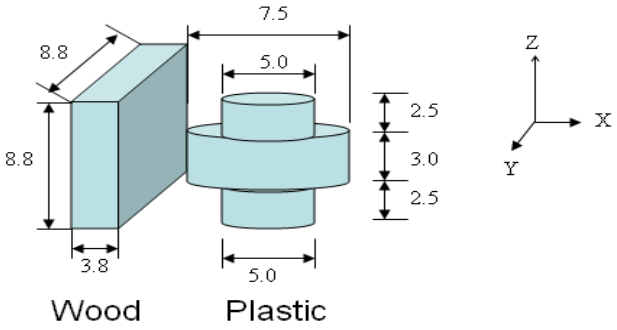

Figure 2.1.1.7b. Sample structure with dimensions for MRI system

The 1D profiles of SPI sequence are shown in Figure 2.1.1.7c and Figure 2.1.1.7d. We found that these 1D profiles showed the basic shapes and relative dimension proportions of the samples. The edges of the samples, especially the plastic ones are a bit steeper compared with their real shape, but they still can provide useful information of the samples and full 3D SPI images will be acquired in further studies.

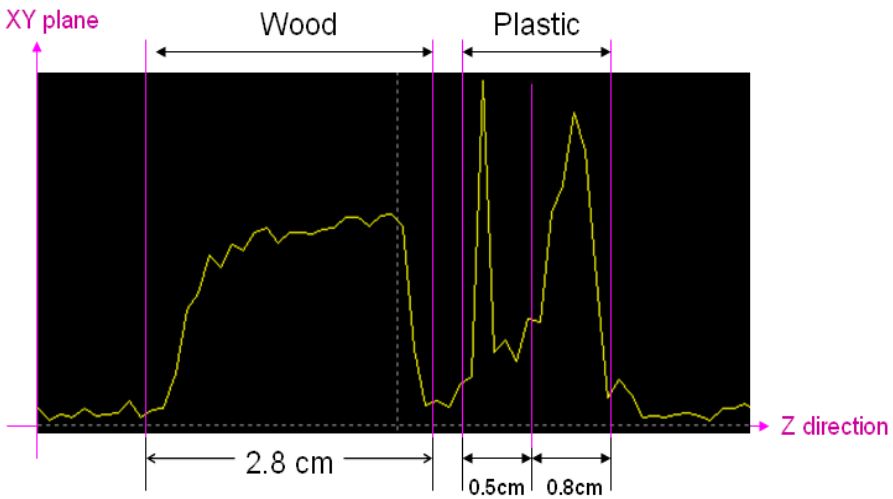

Figure 2.1.1.7c. SPI 1D profile in benchtop MRI system.

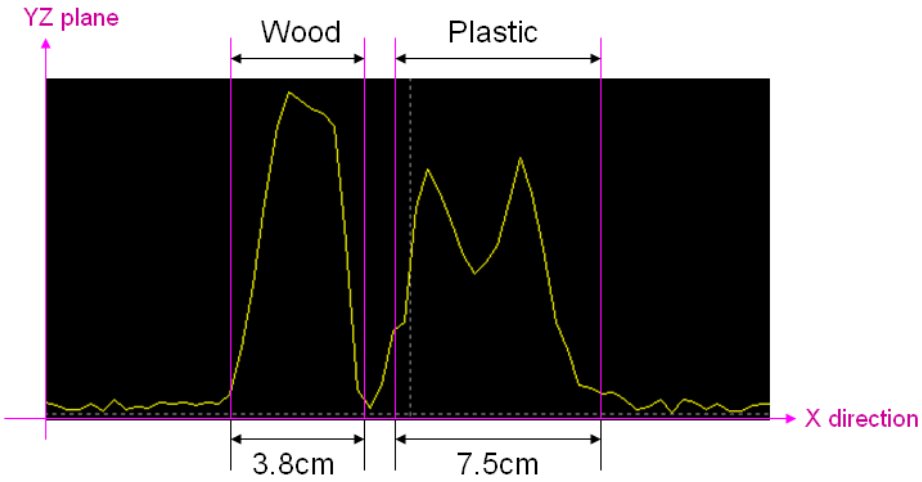

Figure 2.1.1.7d. SPI 1D profile in MRI system.

Hardware Design for Food Applications

A gradient coil (2.1.1.8 a-c) was designed, constructed, and tested for its feasibility..

A 1D profile was acquired and is shown in Figure 2.1.1.9. A regular cylinder shaped

bottle of CuSO4 solution was used as a phantom sample. The edges of the samples look steeper compared with the actual shape of the sample, but the images still can provide useful information in the sample.

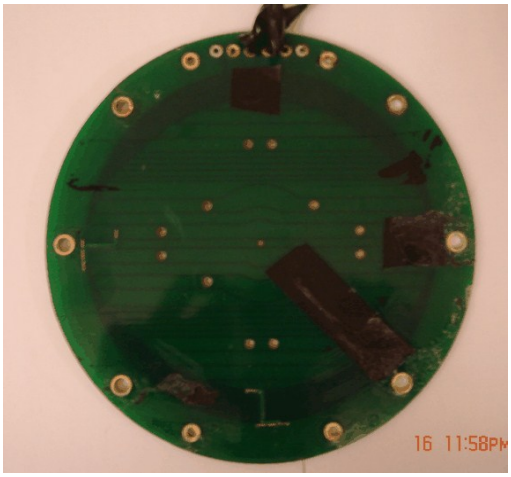

(a)

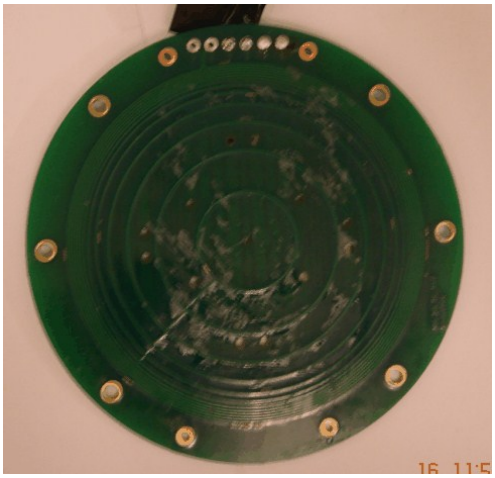

(b)

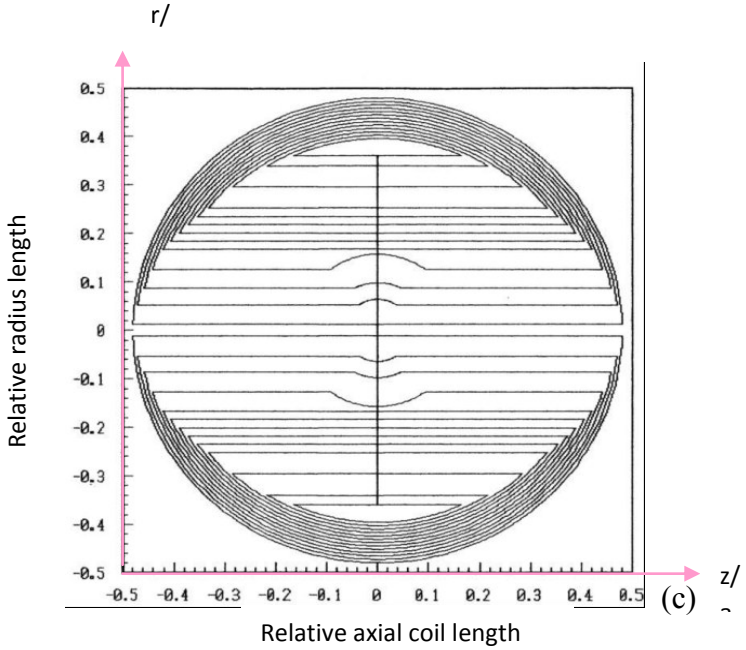

(c)

Figure 2.1.1.8. (a) Front side of the gradient coil; (b) Back side of the gradient coil; (c) wire layout of the gradient coil.

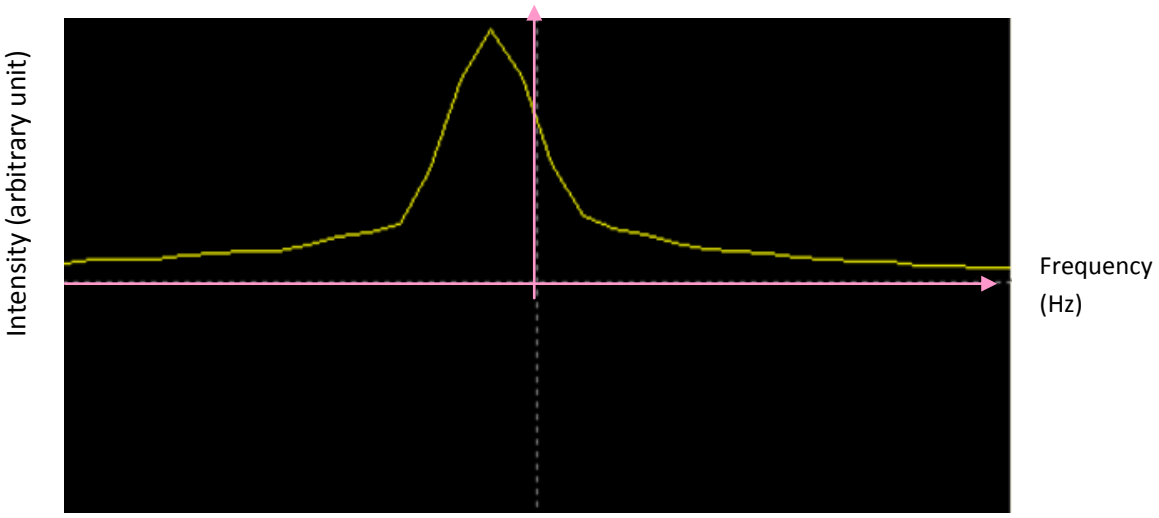

Figure 2.1.1.9. 1D profile acquired by the self-designed coil.

2.1.2. Validation of moisture mapping techniques

Sandwich samples from major food processing company under different conditions, Control, Leaky, and Soggy, were prepared for mapping moisture distributions. MRI experiments were conducted at 25°C using an MRI system with a 12.9 MHz permanent magnet. Three pieces of sandwiches, one each type, were piled together and MRI 3D images of matrix 64*64*64 were obtained using the 3D spin echo sequence implemented on the MRI machine. The 3D images were constructed using IDL 5.6RI advanced image software. The moisture distributions were presented using Matlab6.5 software.

Figure 2.1.2.1 shows a 3D MR image of a single sandwich. The glace layer is visible. Figure 2.1.2.2 shows the 3D and 2D images of the three sandwiches when imaged

together. The 2D slice shows clearly the soggy and leaky samples had much higher mobility and moisture content in the filling than control sample. Control sample is more uniform. Figures 2.1.2.3 and 2.1.2.4 clearly confirm the observation from Figure 2.1.2.2 that control sample had much lower mobility as well as moisture content in the filling compared with soggy and leaky samples while leaky sample obviously had highest water mobility. This also agrees with our common sense that control sample was supposed to hold up more water than the leaky and soggy and to keep a more intact and more uniform structure. Therefore by using such MRI imaging technique, these images and processed figures are able to clearly show the inside structure and moisture distribution for further analysis such as comparing and finding the differences among samples without doing any damage to the samples such cutting them into pieces for testing crust and fillings separately. (More NMR related details are shown in Chapter 3 section 3.2.1)

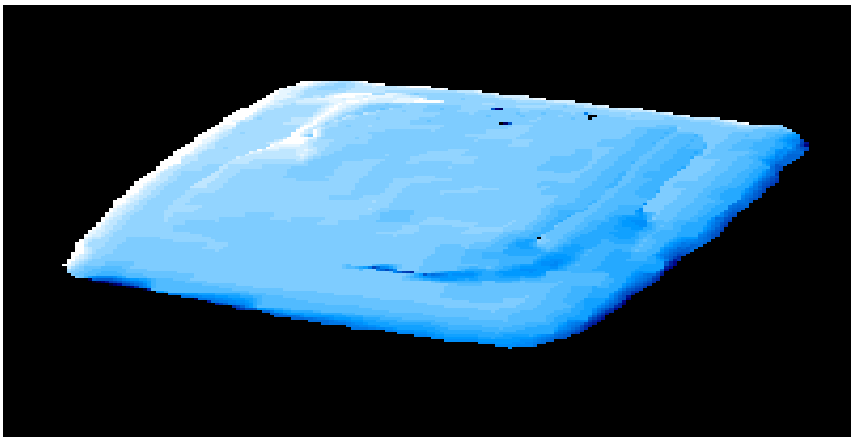

Figure 2.1.2.1. 3D MR image of sandwich.

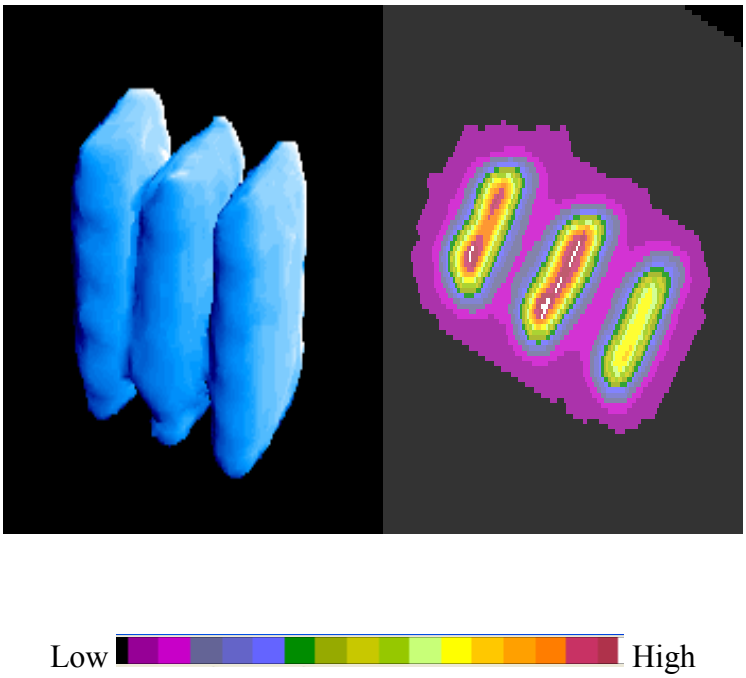

Figure 2.1.2.2. 3D images and 2D images for sandwich samples in the order of from left to right: Soggy, leaky, and control, processed by software IDL5.6 with color bar.

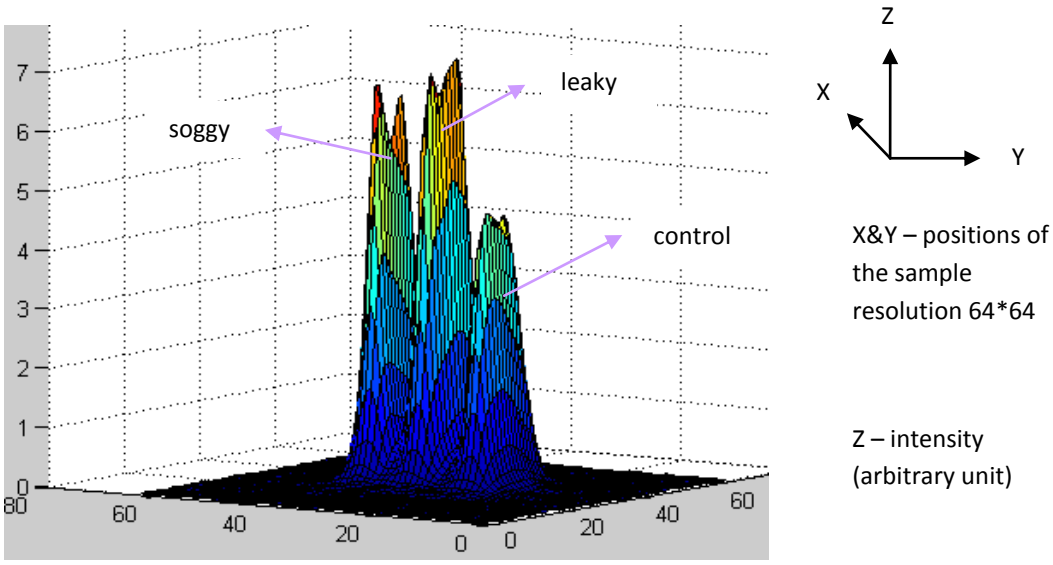

Figure 2.1.2.3. Surface plot of selected slice image shown in Figure 2.1.2.2 from left to right: Soggy, leaky, and control, processed by MatLab(Horizontal plane represents positions in the 64*64 resolution image slice and vertical axis represents signal intensity).

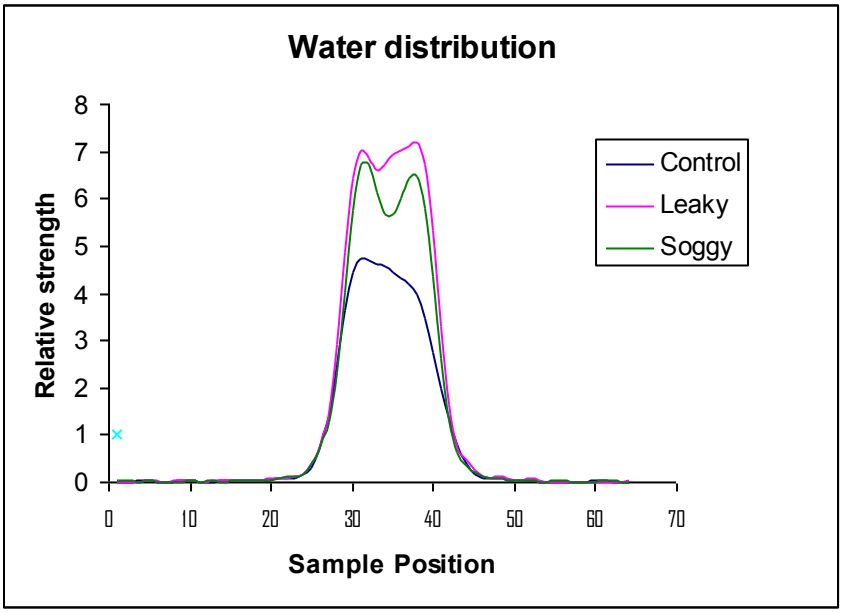

Figure 2.1.2.4. Profiles of the three sandwiches shown in Figure 2.1.2.2.

2.1.3. Validation of T2 mapping techniques

Model design and data processing for T2 mapping

The MRI machines came with limited number of preloaded pulse sequences. In order to make our machines suitable for the study of food and biological materials, especially those with low moisture content, the pulse sequences must be customized and new ones must be developed. Furthermore, new data processing schemes must be developed to extract additional information from the raw data in order to relate nuclear resonance dependent properties to the physiochemical characteristics and stability of foods and biological materials.

The relaxation parameter T2 has the following equation:

$$S = A e^{-\frac{Tau}{T_2}} \qquad (2.1)$$

where S is arbitrary NMR signal intensity, A is a constant, and Tau is the echo time duration in sequences. The formula can then be converted to:

$$\ln(S) = \ln(A) - Tau / T2 \qquad (2.2)$$

Therefore, ln(S) and Tau have a linear relationship. T_2 can be calculated from the slope of equation (2.2). A coding program will be written in MatLab to construct T2 mapping (attached in the Appendix).

Moisture mapping data can be further processed using MatLab software, which gives more options on presenting data, such as discarding noise, presenting revolving or colorful figures, etc. In addition, Matlab provides a coding platform for users to create different programs to process data to satisfy different purposes. New programs were created in order to obtain more mapping results and provide more analysis methods.

T2 mapping

Two filters, denoted as A and B, were prepared for mapping localized T2 distributions. These filters, composed of fibers and pores, with 2 cm in diameter and 0.1 cm in thickness, were first fully soaked in CuSO4 and then depleting the soaked liquid. MRI experiments were conducted at 25°C using an MRI system with a 21.4 MHz permanent magnet. Three pulse sequences, 90 degree pulse, CPMG sequence and INVREC sequence were used to obtain the NMR relaxation data. The data obtained with the 90 degree pulse were fitted into a mathematical model to produce T2* values. The CPMG data were fitted to a continuous model to produce T2 values. The INVREC data were fitted to produce T1 values. T2 mapping was carried out using a spin-echo imaging sequence. Different TE values were tested and then five suitable TE values were selected

to acquire a set of five T2-weighted images in order to fit each T2 mapping. MRI images had the resolution of 32*32*32. Then MRI data were further processed using MatLab software. Scripts were written for special treatment of our data based on previous model designed for T2 mapping specifically. For example, data fitting software was developed to obtain the T2 value for each pixel from a set of T2-weighted images to construct the T2 mapping. 3D images were constructed using IDL 5.6 RI Advanced Image. Data are presented in table and as 3D proton image, 2D surface plot, 1D profile, for both moisture and T2 mapping images and T2 mapping histogram.

T2 mapping results

Due to the limitation of the MRI imaging resolution, in these tests, the filter samples had a diameter of 2 to 2.5 cm and the resolution size was 32*32. Therefore, the size of each pixel in the MRI images was around 0.06 cm, almost 10 to 100 times larger than the real pore size in the samples. So from our MRI images, it is not quite possible to see very detailed structures, but we can obtain some basic information. The results are shown in Figures 2.1.3.1- 2.1.3.12. Specifically, Figures 2.1.3.1-2.1.3.6 show the results from Filter A and Figures 2.1.3.7-2.1.3.12 show the results from Filter B.

From Figure 2.1.3.6 and Figure 2.1.3.12 and their corresponding T2 mean values, we found that filter A has a slightly larger T2 mean value than filter B; filter A has a

wider T2 distribution and filter B has a more skewed T2 distribution. Figure 2.1.3.5 and 2.1.3.11 show that filter B has a more homogeneous T2 distribution than filter A for a single slice, which may indicate a more homogeneous structure of the filter and may also give some hints on the distribution of the fibers and pores. And such structure differences could directly affect the filtering efficiency of the filters. Large pores could always hold more amount of water around indicating a larger amount of relatively mobile water compared with small pores. While fibers could always capture water tightly surrounded and thus decreasing the water mobility. Therefore, filters with small pores and more fibers, leading to a tighter structure, will do a better filtering job of holding water. For example, if filter B has more small fibers or more relatively small pores than filter A, it may capture water more easily, thus leading to a less mobile water state, and smaller T2 values and larger percentage of shorter T2 component could be expected which could be verified by NMR tests and analysis.

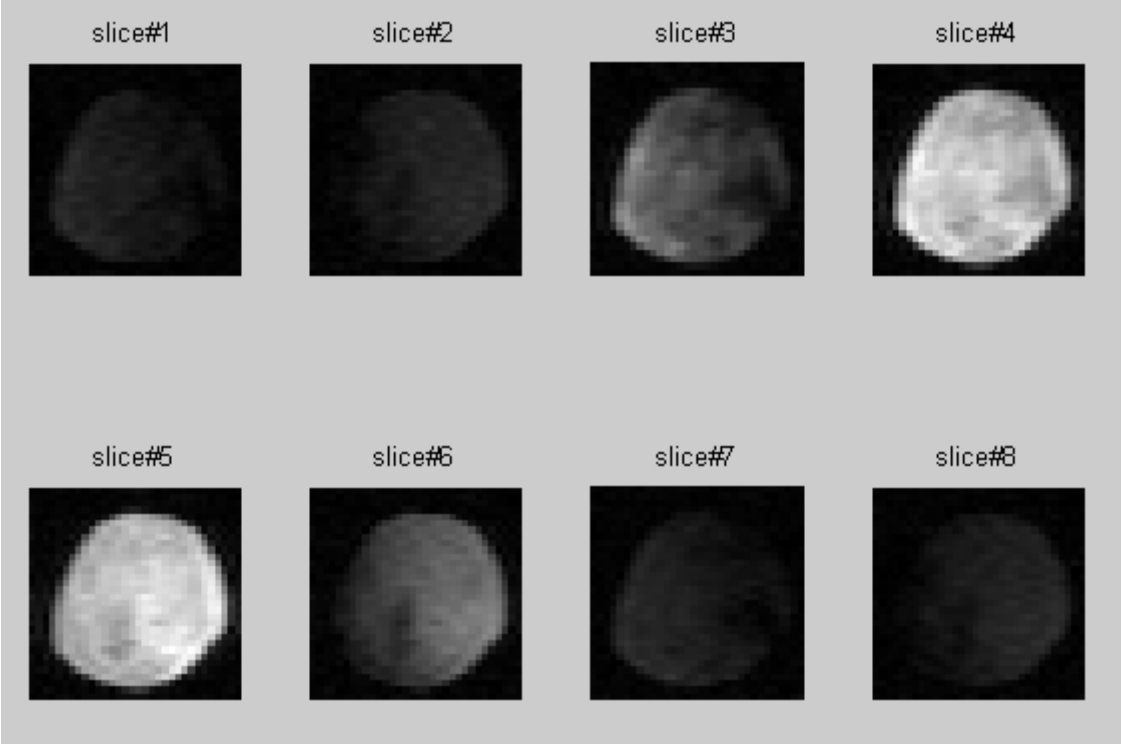

Figure 2.1.3.1. MRI images of the selected 8 slices of Filter A

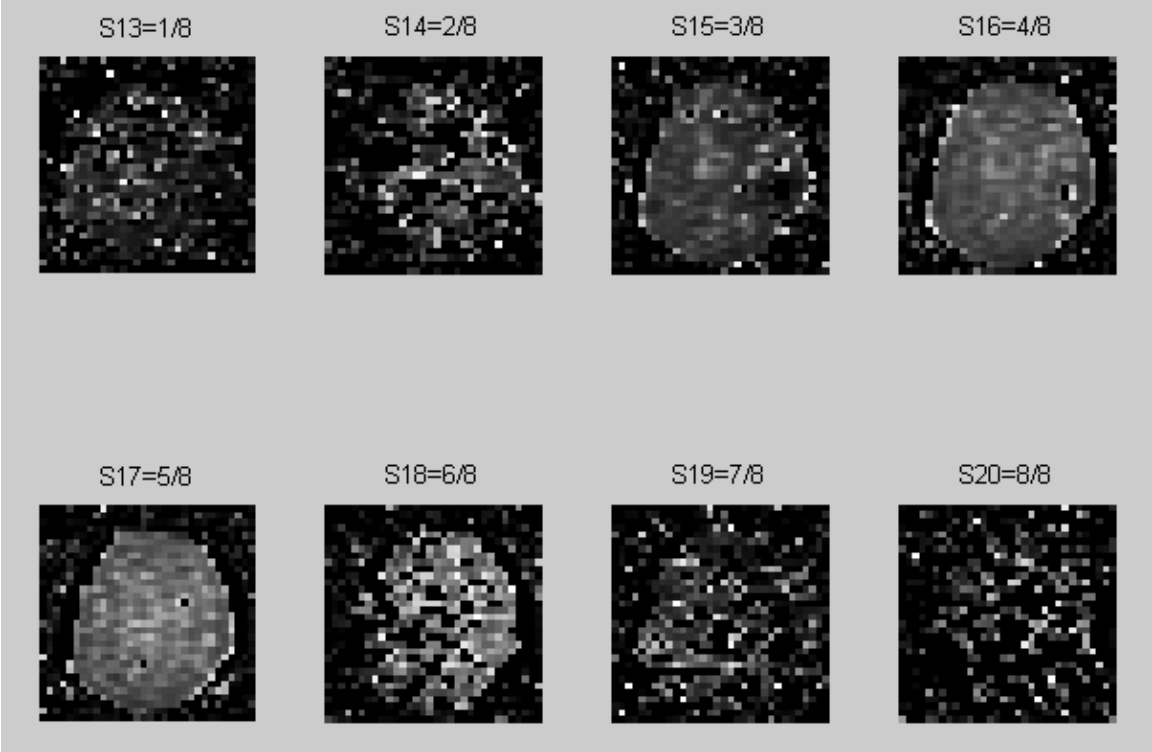

Figure 2.1.3.2. T2 mapping of the selected 8 slices of Filter A

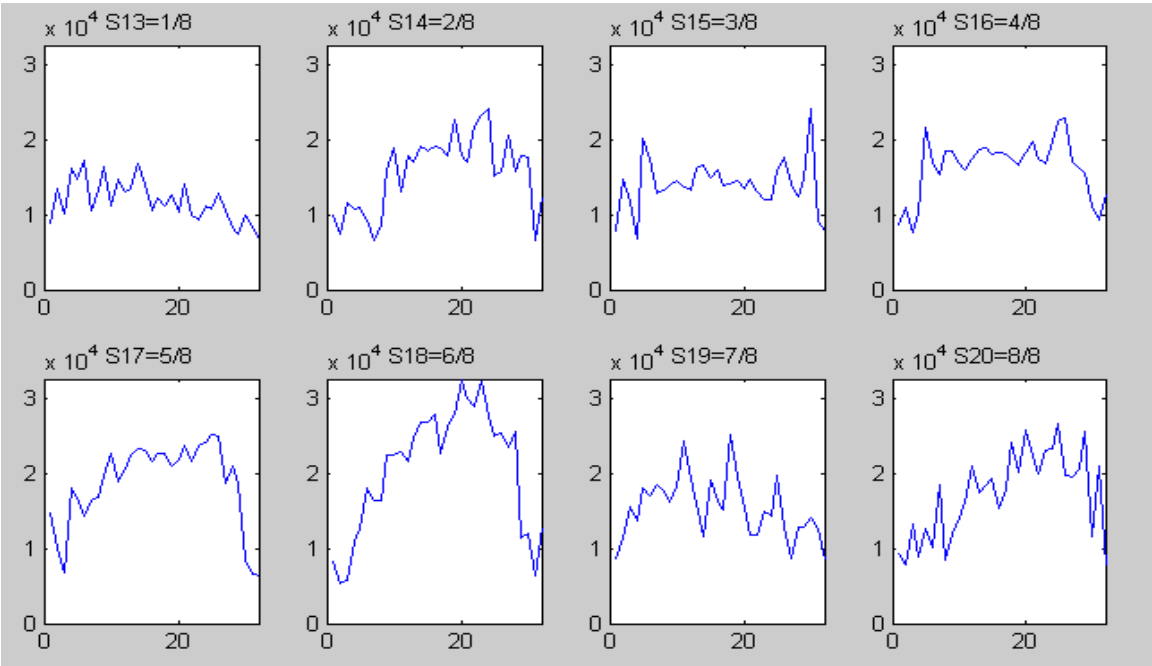

Figure 2.1.3.3. T2 mapping average 1D profile along horizontal direction for 8 selected slices

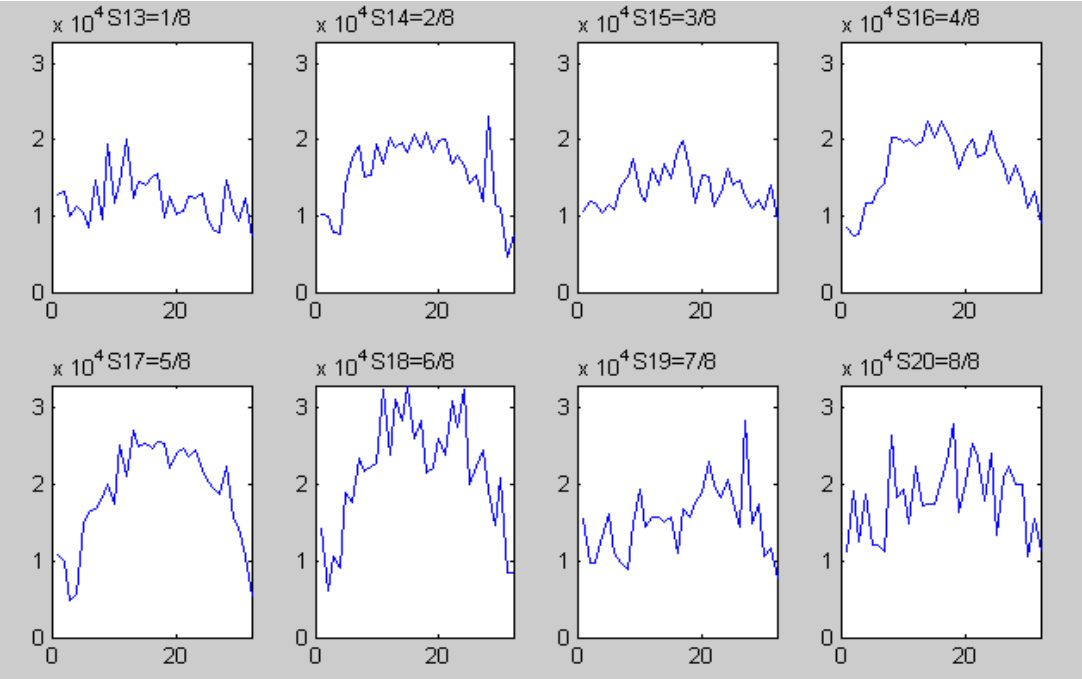

Figure 2.1.3.4. T2 mapping average 1D profile along vertical direction for 8 selected slices

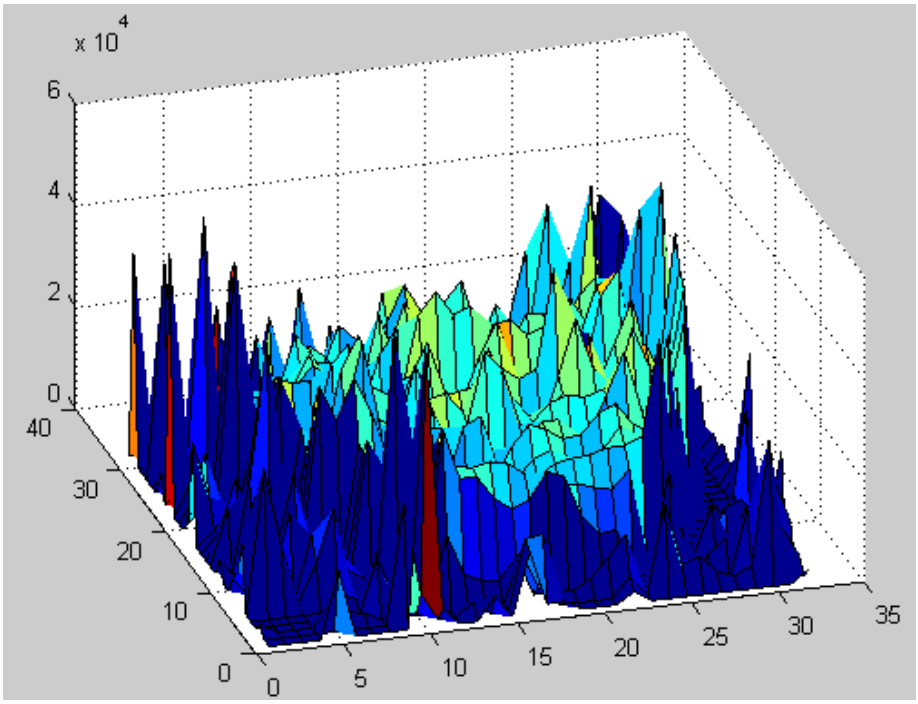

Figure 2.1.3.5. T2 mapping of one selected slice for Filter A

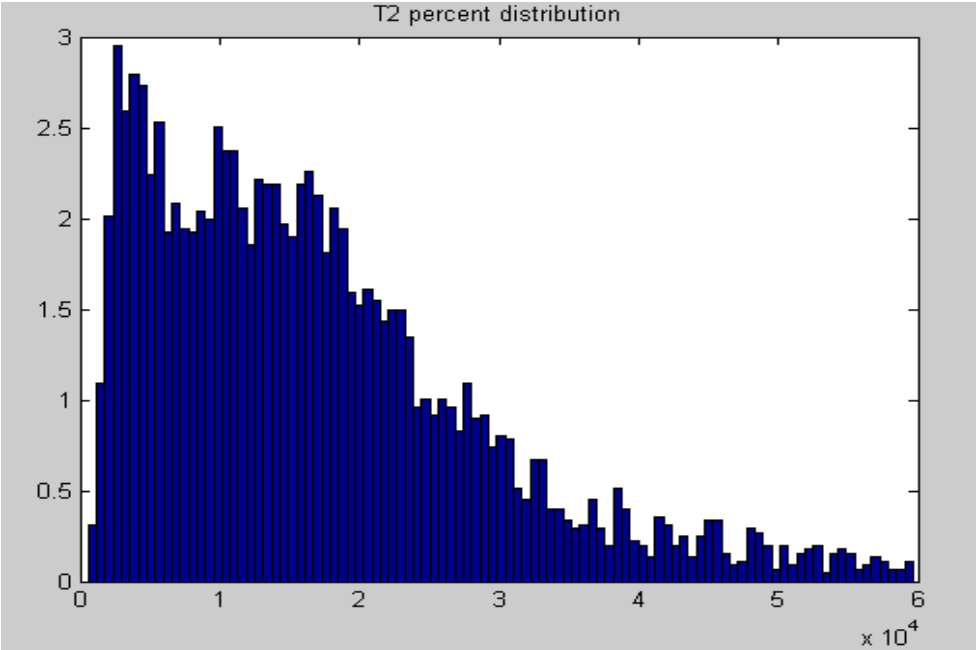

Filter A: T2 mean = 1.6910e+004 μs, T2 standard deviation = 1.1903e+004 μs;

Figure 2.1.3.6. T2 percent distribution for Filter A

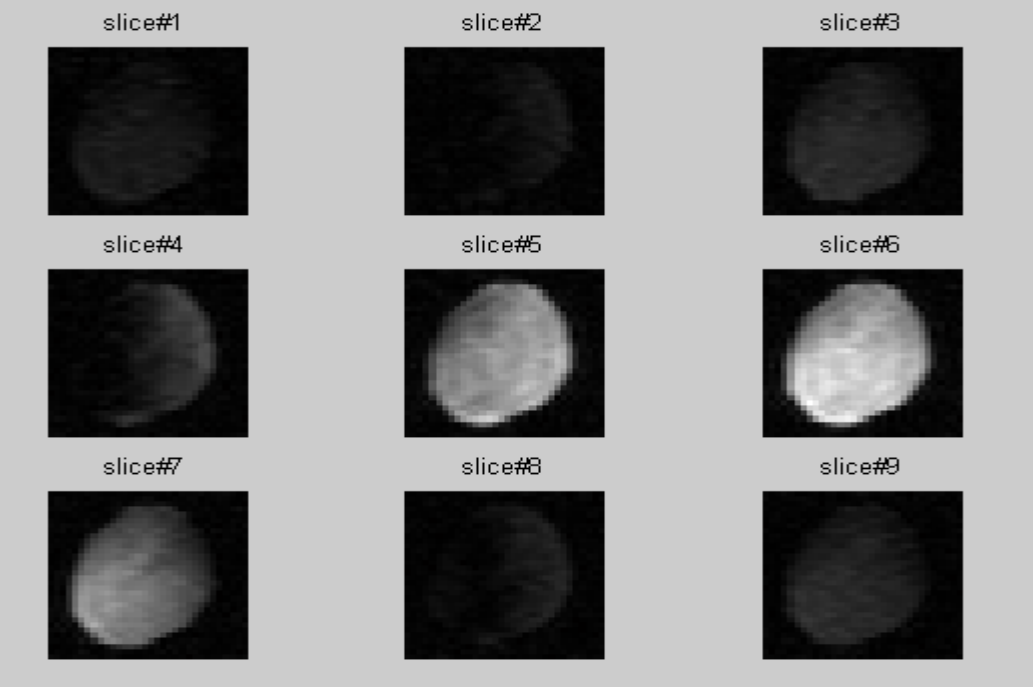

Figure 2.1.3.7. MRI images of the selected 9 slices of Filter B

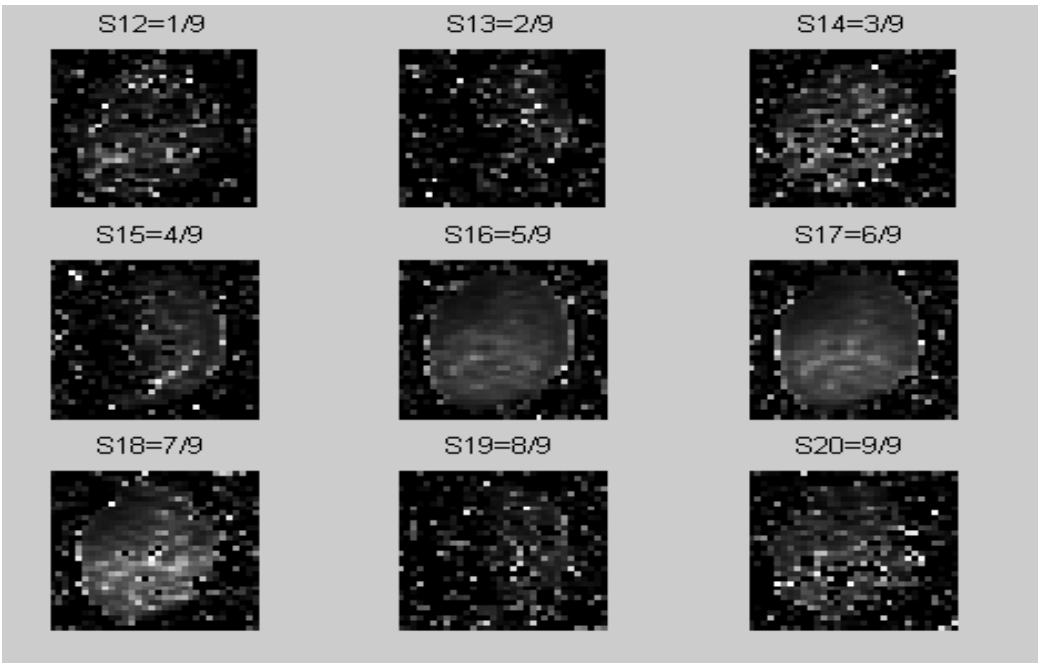

Figure 2.1.3.8. T2 mapping of the selected 9 slices of Filter B

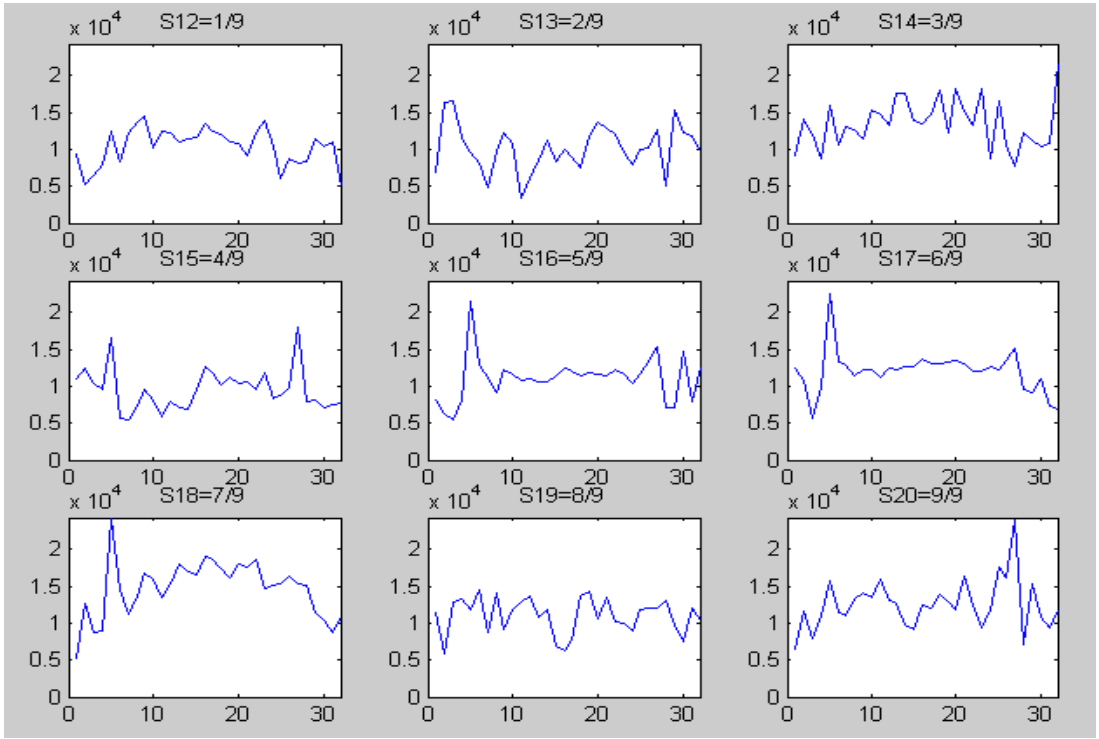

Figure 2.1.3.9. T2 mapping average 1D profile along horizontal direction for 9 selected slices

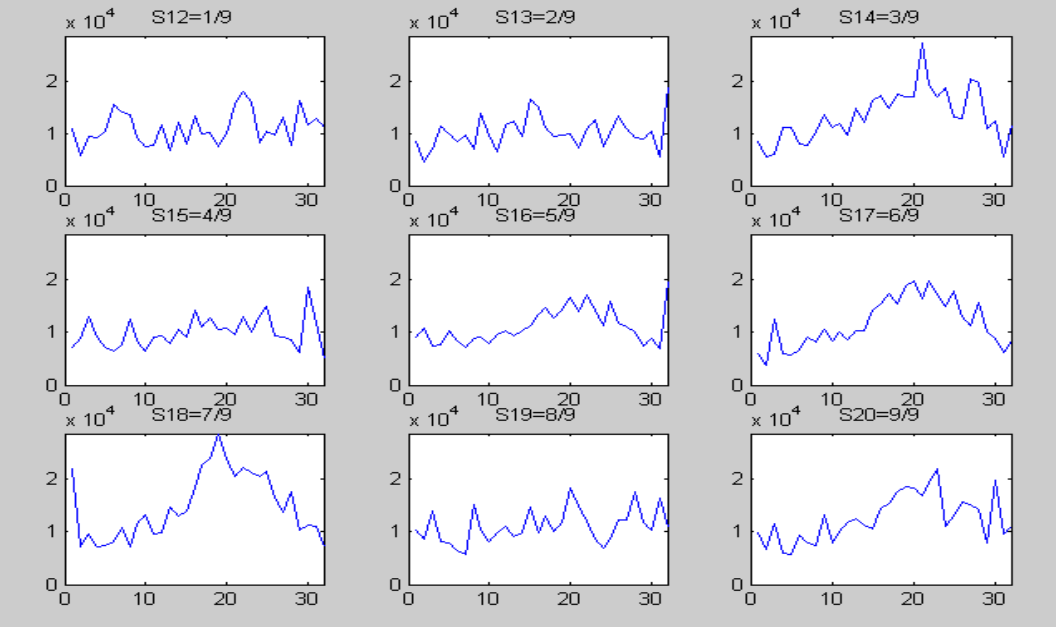

Figure 2.1.3.10. T2 mapping average 1D profile along vertical direction for 9 selected slices

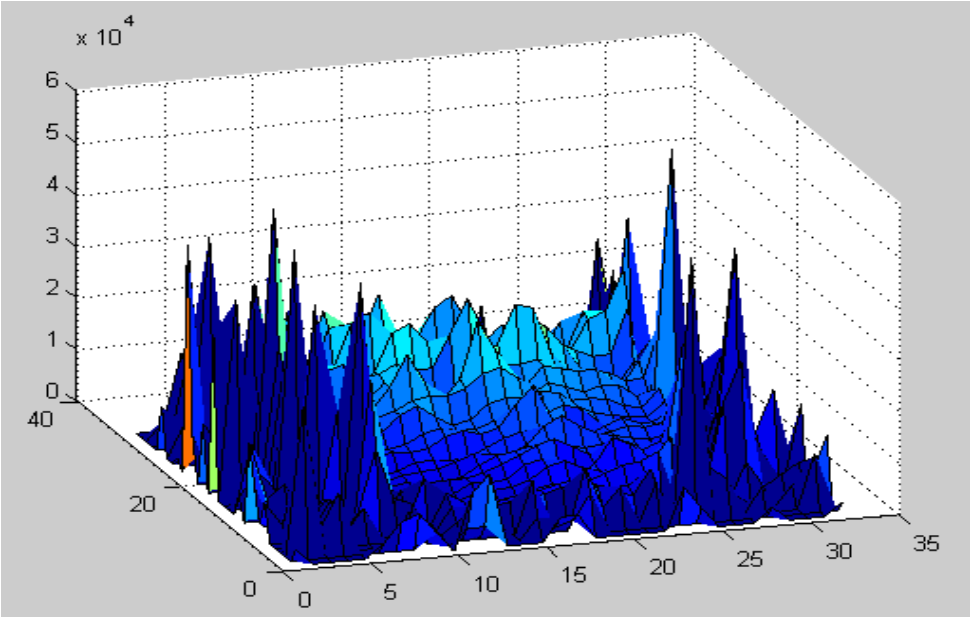

Figure 2.1.3.11. T2 mapping of one selected slice for Filter B

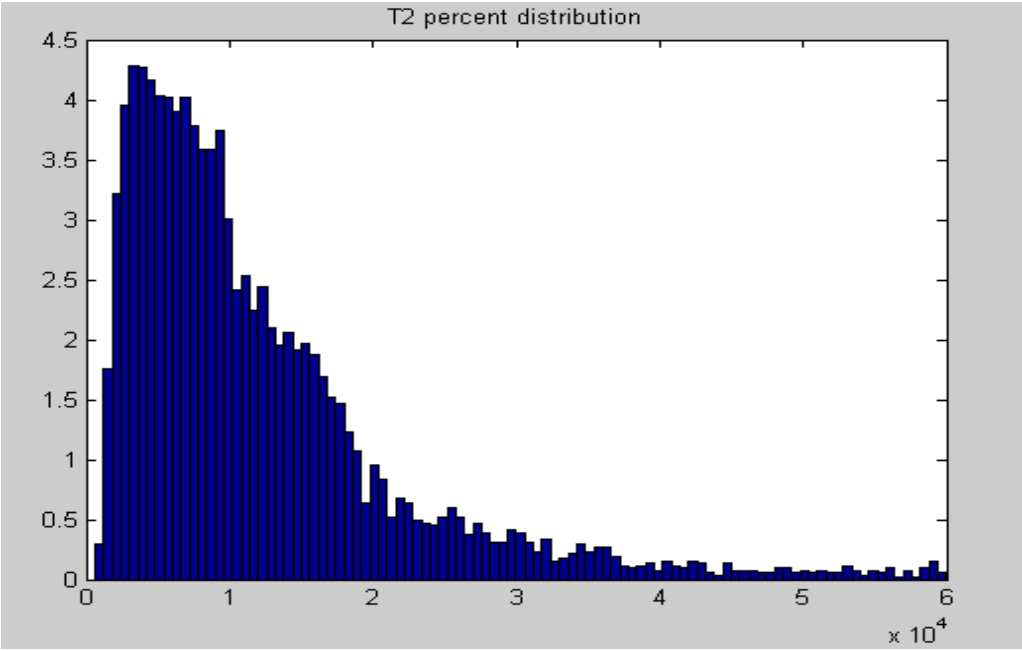

Filter B: T2 mean = 1.2079e+004 μs, T2 standard deviation = 9.9670e+003 μs;

Figure 2.1.3.12. T2 histogram for Filter B

2.2. Application of the MRI Techniques in Food Research – Case Studies

In this section, studies of actual food systems using the MRI techniques developed will be presented. Specifically, distribution and migration of water in two- and multi-components food systems during storage and processing (cooking) were monitored using the MRI techniques. The relationships among physiochemical properties of foods, relaxation time, and moisture distribution/migration will be discussed.

2.2.1 Study of moisture migration in foods with two components

Samples

Sandwiches with two components, bread and cheese were used as sample foods in this study. The sandwich breads had two types - high density and low density, which were both equilibrated to water activity of 0.75. Each bread sample of 1.5 cm long and 2 cm diameter was interfaced with equal size commercial cheese (Velveeta, Kraft Foods Global, Inc., Glenview, IL). Both sandwiches were assembled and stored at refrigerated temperature for 1 week and 3 weeks. Sandwiches were sealed in a pouch and stored at refrigerated temperature for 1 week and 3 weeks. Each binary system was tested at week 1 and week 3 using a MRI instruments. When a measurement was conducted, the sample was withdrew from the refrigerator and kept at room temperature for 1 hour. After testing, the sample was put back. Duplicate measurements for each sample were performed.

The objective of this preliminary study was to use MRI technique to monitor the change in water content, mobility and distribution in these sandwich samples. The spatial moisture distributions were presented by the proton intensity images acquired using MRI. T2 mapping results were shown to indicate the moisture migration characteristics.

MRI Tests and Data processing

NMR and MRI measurements were conducted at 25°C using an MRI system with an 12.9 MHz permanent magnet. Two pulse sequences, 90 degree FID pulse and CPMG pulse, were used to obtain the NMR relaxation data. The data obtained with the 90 degree pulse were fitted into a mathematical model to produce T2* and amplitude values. The CPMG data were fitted to a continuous model to produce T2-amplitude spectra and mulit-component model to yield two to three component T2 values. T1 was measured using an INVREC sequence. Moisture and T2 mapping was carried out using a spin-echo imaging sequence with MRI 3D images of matrix 32*32*32. Five TE values were used in this spin-echo imaging sequence to acquire a set of five T2-weighted images in order to fit each T2 mapping.

The 3D images were constructed using software IDL 5.6RI advanced image. MRI data were further processed using MatLab software. Scripts were written for special treatment of our data. For example, a data fitting software was developed to obtain the T2 value for each pixel from a set of T2-weighted images to obtain the T2 mapping. 3D images were constructed using IDL 5.6 RI Advanced Image. Data are presented in table and as 3D proton image, 2D surface plot, 1D profile, for both moisture and T2 mapping images and T2 mapping histogram.

Results and Discussion

From T2 mapping results, the T2 values of different locations of the sample could be clearly shown. Thus the differences between T2 values of bread and cheese could be

easily recognized and distinguished. Figures 2.2.1.1.1-2.2.1.1.4 show that the overall T2 values of the sandwiches including both bread and cheese decreased over storage time. And T2 values of cheese are generally longer than T2 values of bread. It is worth pointing out that the higher mobility in cheese does not necessarily indicate moisture content changes because protons in fat should have longer T2 than those in water. Although no significant difference between low and high density breads was observed from T2 maps shown in Figures 2.2.1.1.5 – 2.2.1.1.10 and from histograms shown in Figures 2.2.1.2.1 – 2.2.1.2.10 and from 2D profiles shown in Figures 2.2.1.3.1- 2.2.1.3.12, we can still tell that difference in proton density distribution between the two storage times for high density bread systems are more obvious compared with low density bready systems at the same storage time point. However, there are obvious gradients near the interfacial regions between bread and cheese in Wk1 and such gradients between bread and cheese become less in Wk3. Cheese has higher moisture content than bread. For the binary sandwich systems, the free water in the cheese continually migrated into the bread until certain equilibrium arrived. Some of the migrating water interacted with some molecules in the bread, such as starch (or some active sites) and became structural water. Some continued to move after most of the active sites were occupied. The structural water has smaller T_2 values than free water. So, the decrease in T_2 values means the formation of the structural water, and migration of water. It was also observed that moisture migrated out of the binary sandwich systems and condensed on the walls of wrapping paper as evidenced by the high peaks around the edges of the moisture and T2 maps. Similar trends are also found from the later moisture mapping results.

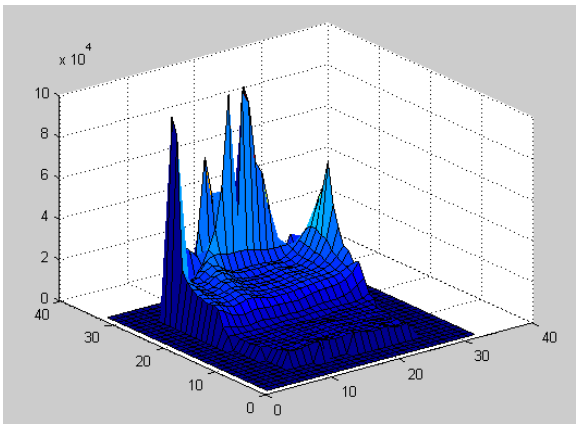

Figure 2.2.1.1.1. T2 map of Cheese-bread (high density), Wk1

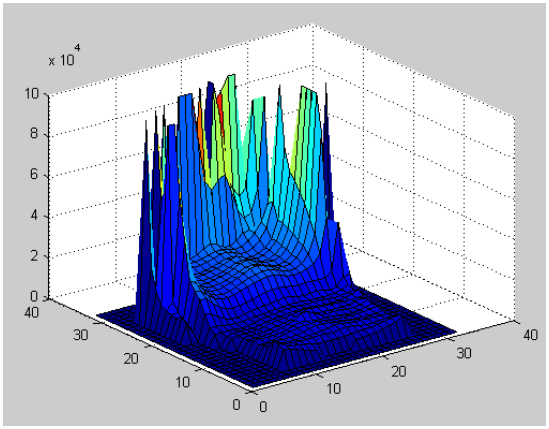

Figure 2.2.1.1.2. T2 map of Cheese-bread (high density), Wk3

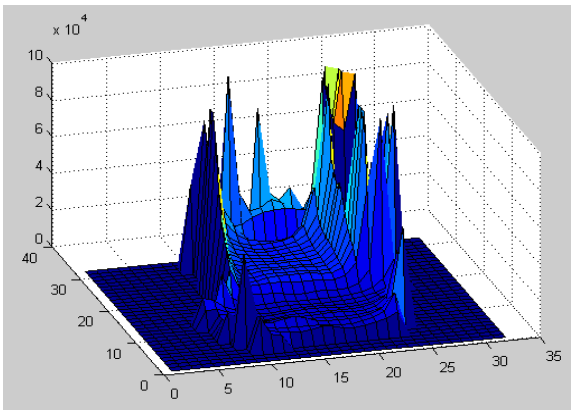

Figure 2.2.1.1.3. T2 map of Cheese-bread (low density), Wk1

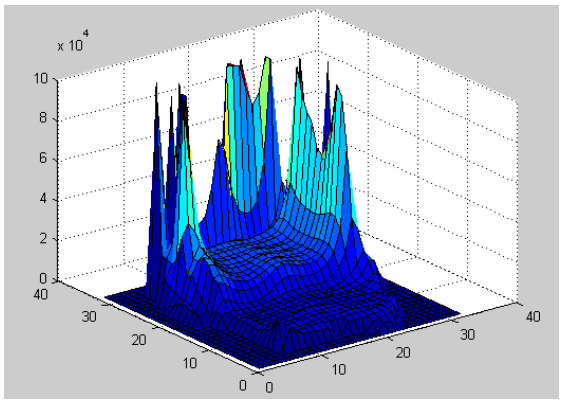

Figure 2.2.1.1.4. T2 map of Cheese-bread (low density), Wk3

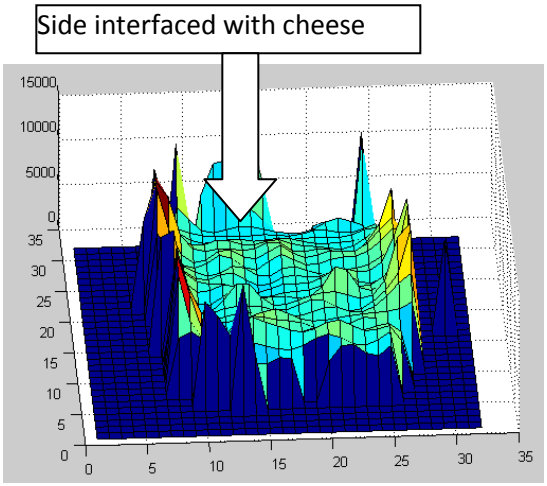

Figure 2.2.1.1.5. T2 map of bread only (high density), wk1

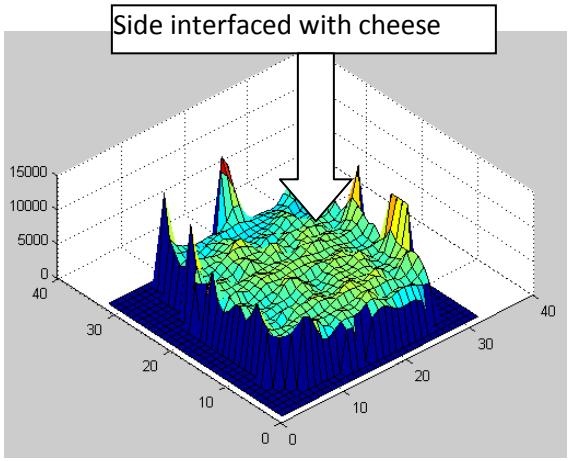

Figure 2.2.1.1.6. T2 map of bread only (high density), Wk3

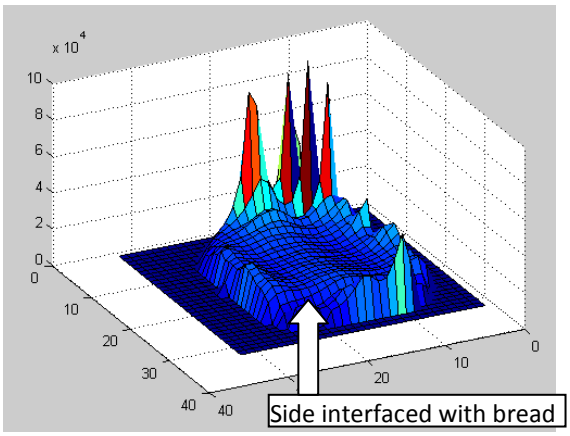

Figure 2.2.1.1.7. T2 map of Cheese only in contact with high density bread, wk1

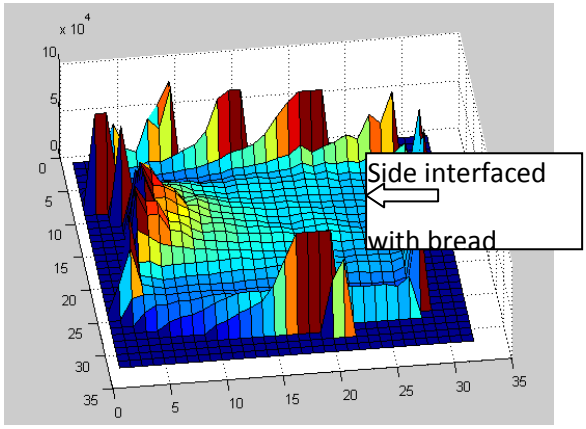

Figure 2.2.1.1.8. T2 map of Cheese only in contact with high density bread, Wk3

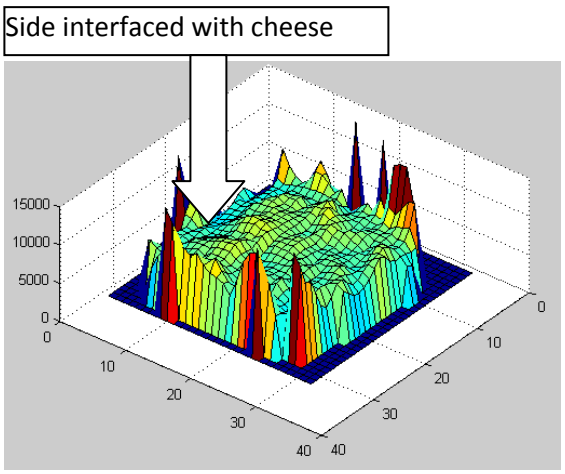

Figure 2.2.1.1.9. T2 map of bread (low density), Wk3

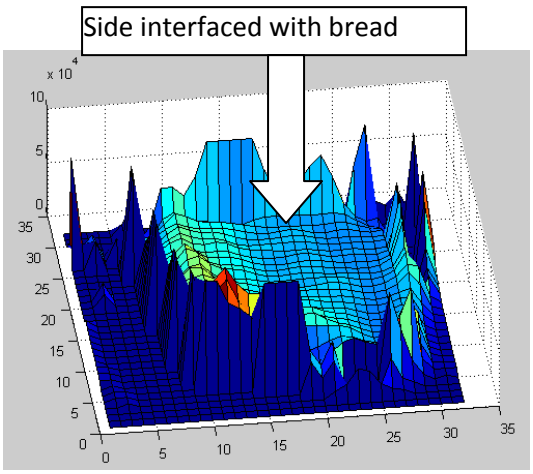

Figure 2.2.1.10. T2 map of Cheese in contact with low density bread, Wk3

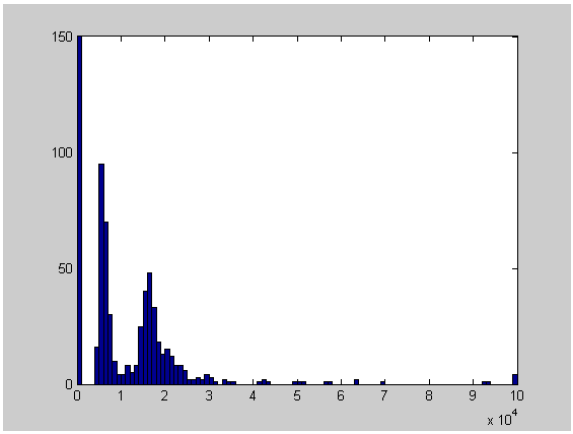

Figure 2.2.1.2.1. Histogram of T2 map for Cheese-bread (high density), Wk1;

(mode is the highest value in histogram)

bread region: mean=6268µs, std=1191µs for range 4000 to 11000µs, mode=6000 µs

cheese region: mean=17994µs, std=3603 for mode=20000µs

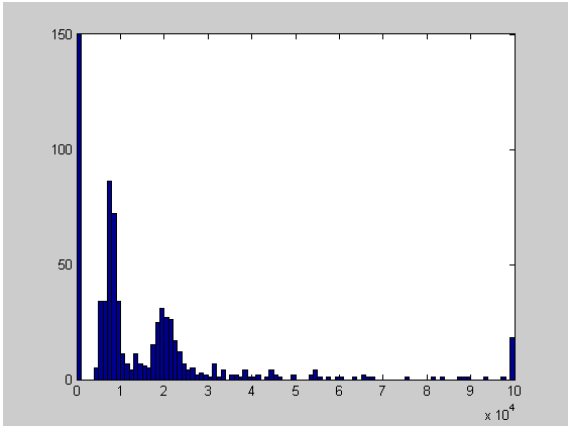

Figure 2.2.1.2.2. Histogram of T2 map for Cheese-bread (high density), Wk3;

bread region: mean=7918µs, Std=1469 for range 5000 to 13000 µs, mode=8000 µs

Cheese region: mean=20127µs, std=3397 for range 13000 to 30000µs,

range 12000 to 30000µs, mode=17000µs

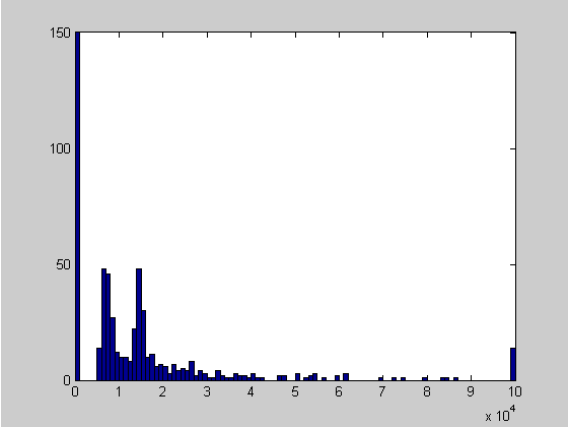

Figure 2.2.1.2.3. Histogram of T2 map for Cheese-bread (low density), Wk1

Bread region: mean=7749µs, std=1707 for the range 6000 to 12000 µs, mode=7000 µs

cheese region: mean=17708µs, std=4482 for std=3546 µs the range 13000 to 30000 µs,

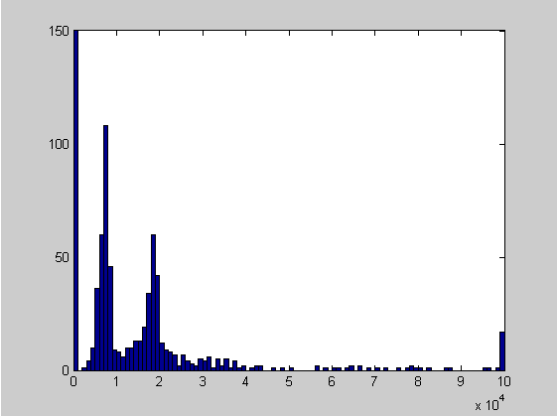

Figure 2.2.1.2.4. Histogram of T2 map for Cheese-bread (low density), Wk3

Bread region: mean=7231µs, std=1503µs for the range 2000 to 12000µs,

Cheese region: mean=18775µs, mode=15000µs for range 1200 to 30000µs, mode=19000 µs

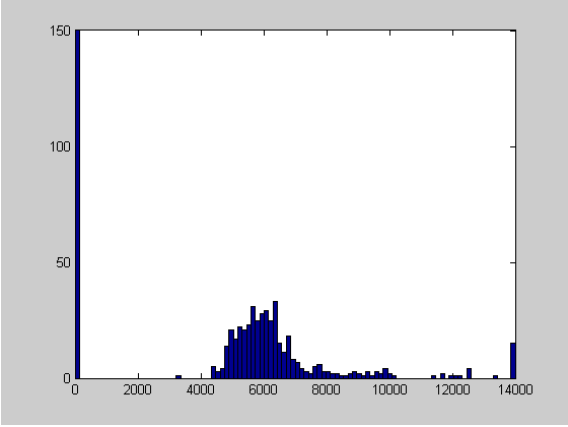

Figure 2.2.1.2.5. Histogram of T2 map for

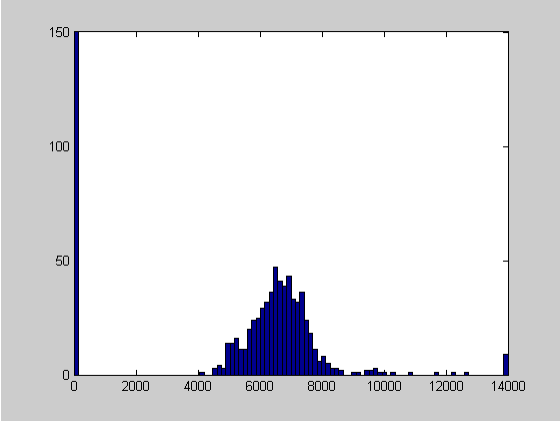

Figure 2.2.1.2.6. Histogram of T2 map for

bread only (high density), wk1

bread only: mean=6151µs, std=1094µs for range 4000 to 10000µs, mode=6700 µs

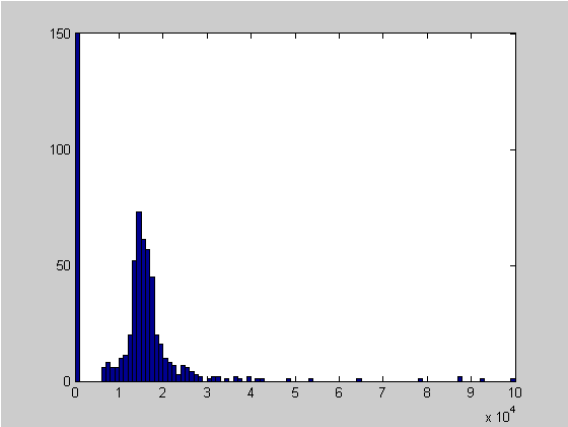

Figure 2.2.1.2.7. Histogram of T2 map for Cheese only in contact with high density bread, wk1

cheese only: mean=15806µs, std=3907µs for range 5000 to 30000µs, mode=15000 µs

bread only (high density), Wk3

bread only: range=4000 to 1e4 µs, mean=6595µs, std=930, mode=6800 µs

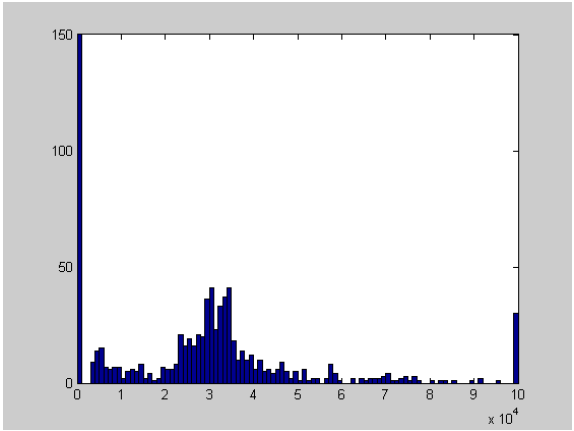

Figure 2.2.1.2.8. Histogram of T2 map for Cheese only in contact with high density bread, Wk3

cheese only: range=4000 to 55000µs, mean=28994 µs, std=10916 µs, mode=31000 µs

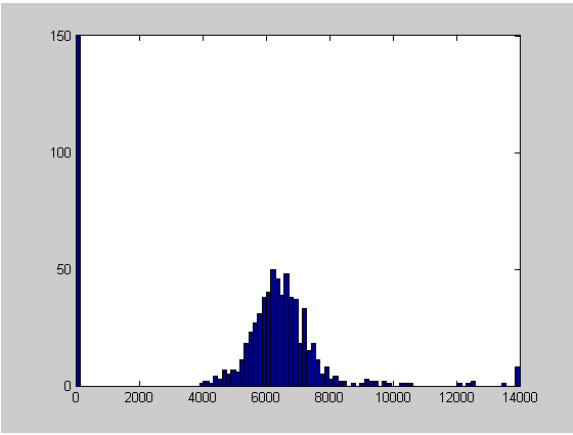

Figure 2.2.1.2.9. Histogram of T2 map for

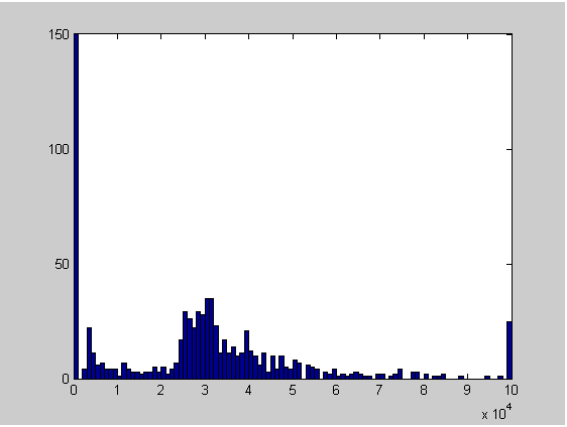

Figure 2.2.1.2.10. Histogram of T2 map for

bread only (low density), Wk3

bread only: range=4000 to 1e4 µs, mean=30213, std=12913,

Cheese only in contact with low density bread, Wk3

mean=6425µs, std=904, mode=6500 µs

cheese only: range=2000 to 60000µs, mode=31000µs

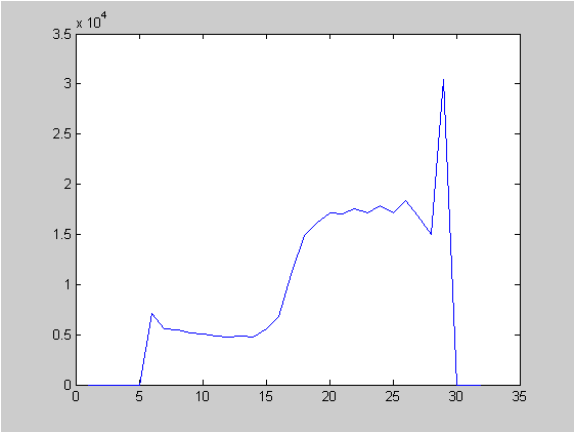

Figure 2.2.1.3.1. 2D profile of T2 map for for Cheese-bread (high density), wk1

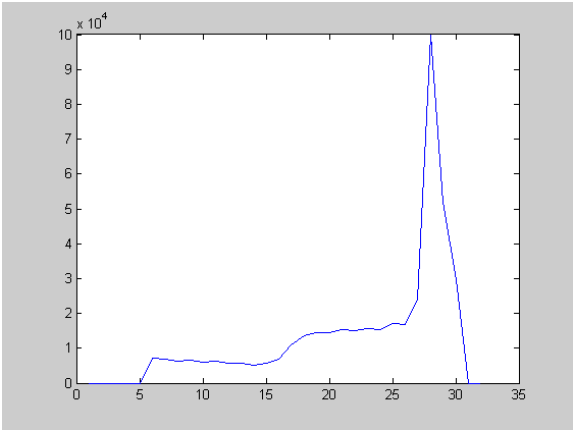

Figure 2.2.1.3.2. 2D profile of T2 map Cheese-bread (high density), wk1

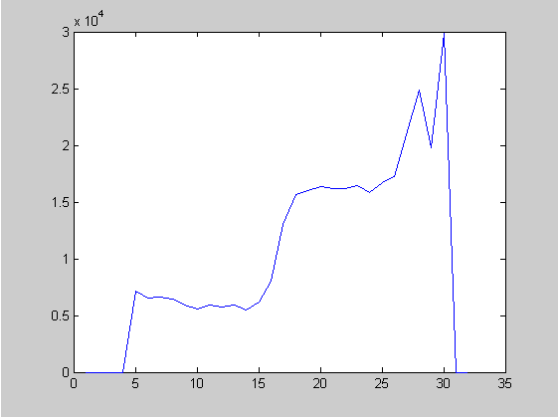

Figure 2.2.1.3.3. 2D profile of T2 map for Cheese-bread (high density), wk1

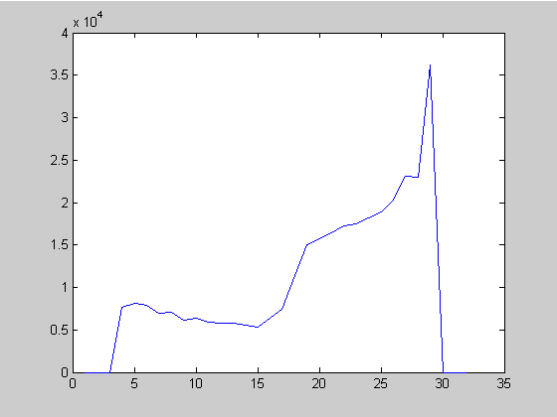

Figure 2.2.1.3.4. 2D profile of T2 map for Cheese-bread (high density), Wk3

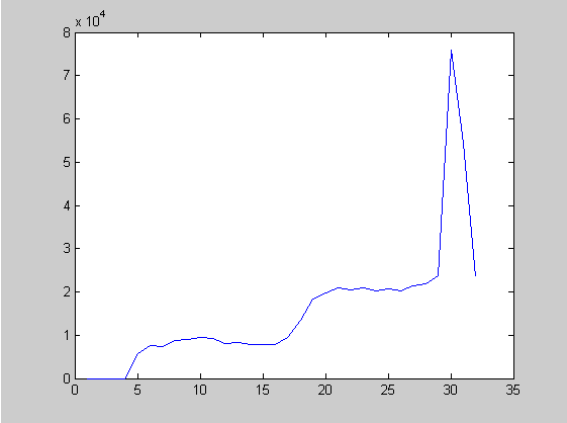

Figure 2.2.1.3.5. 2D profile of T2 map for Cheese-bread (high density), Wk3

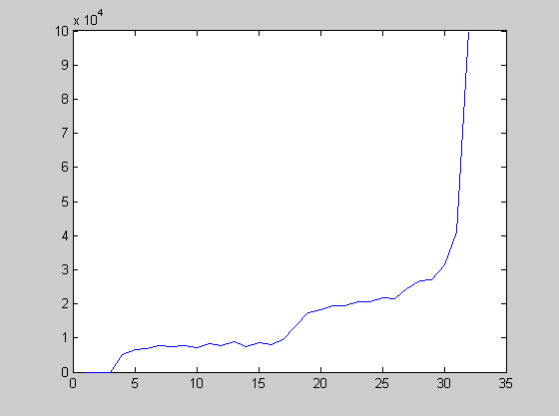

Figure 2.2.1.3.6. 2D profile of T2 map for Cheese-bread (high density), Wk3

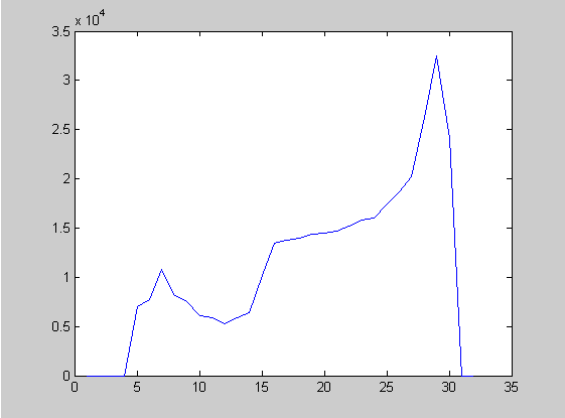

Figure 2.2.1.3.7. 2D profile of T2 map for Cheese-bread (low density), wk1

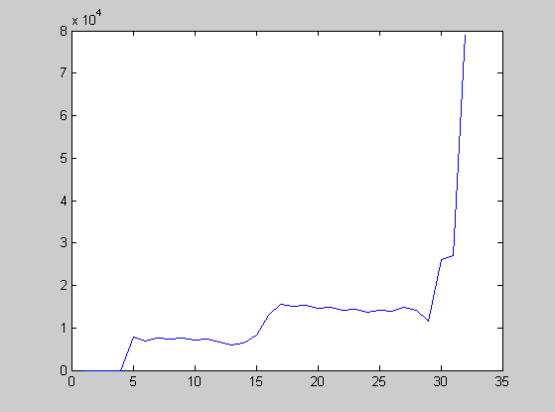

Figure 2.2.1.3.8. 2D profile of T2 map for Cheese-bread (low density), wk1

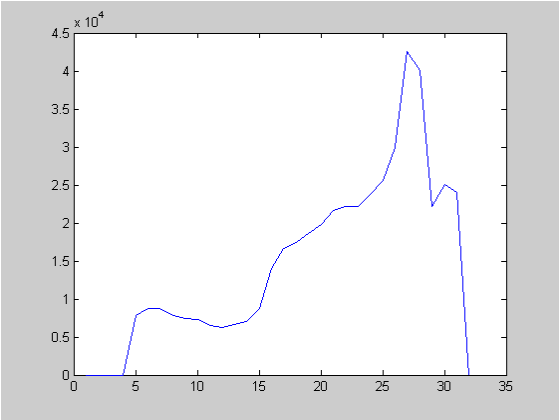

Figure 2.2.1.3.9. 2D profile of T2 map for Cheese-bread (low density), wk1

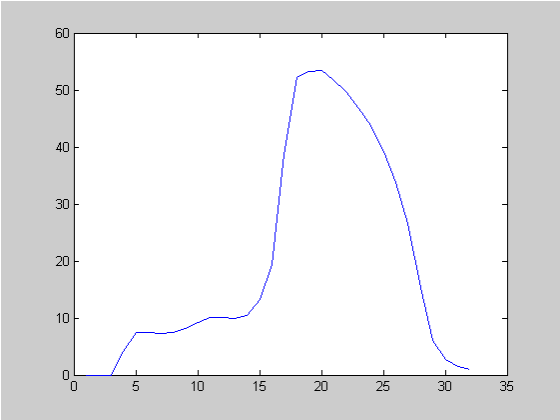

Figure 2.2.1.3.10. 2D profile of T2 map for Cheese-bread (low density), Wk3

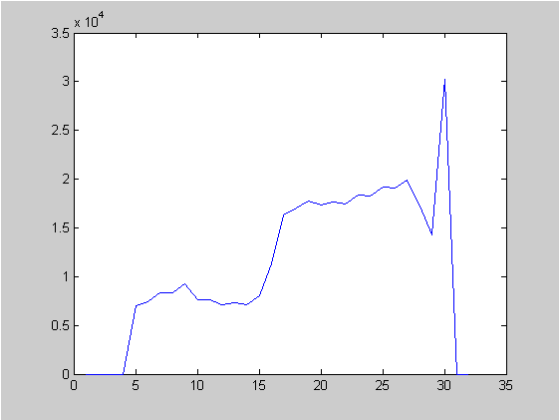

Figure 2.2.1.3.11. 2D profile of T2 map for Cheese-bread (low density), Wk3

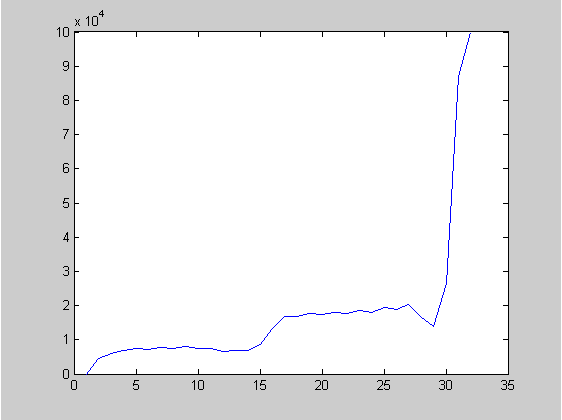

Figure 2.2.1.3.12. 2D profile of T2 map for Cheese-bread (low density), Wk3

Figures 2.2.1.4.1-2.2.1.4.16 present the moisture mapping results in color scales. And these figures show the 2D slice images and 3D surface images for the bread and cheese sandwiches measured at Wk1 and Wk3. Figures 2.2.1.4.1-2.2.1.4.16 also show the

cross-section slice images for the bread and cheese sandwiches measured at Wk1 and Wk3. The higher density shown in the cheese part could be attributed to the fat presence in the system. It is found that the slice images obtained from the binary systems do not show significant difference in proton density distribution between the two storage times for high density bread systems compared with low density bready systems at the same storage time point. However, there are obvious gradients near the interfacial regions between bread and cheese in Wk1 and such gradients between bread and cheese become less in Wk3. Figure 2.2.1.5.1 show the moisture mapping results of two sandwiches placed and imaged together. This mapping result indicates that the moisture densities in cheese parts for both low and high density samples are nearly the same, while the moisture density in bread part of low density sample is a little larger than that in the high density sample. This agrees with previous color scale image analysis.

Low intensity High intensity

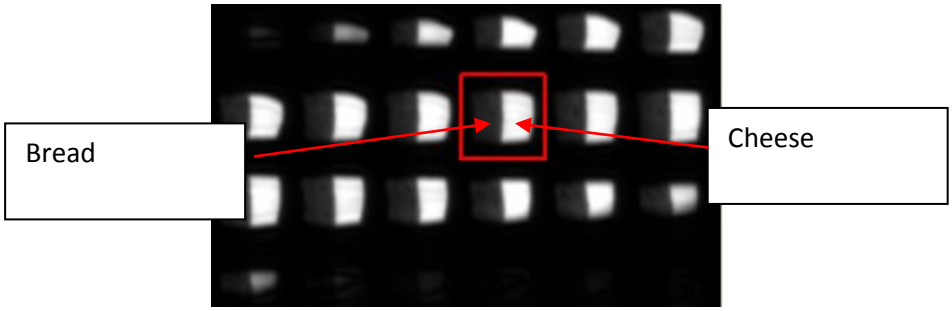

Figure 2.2.1.4.1. 2D slices, cheese-bread (high density), Wk1

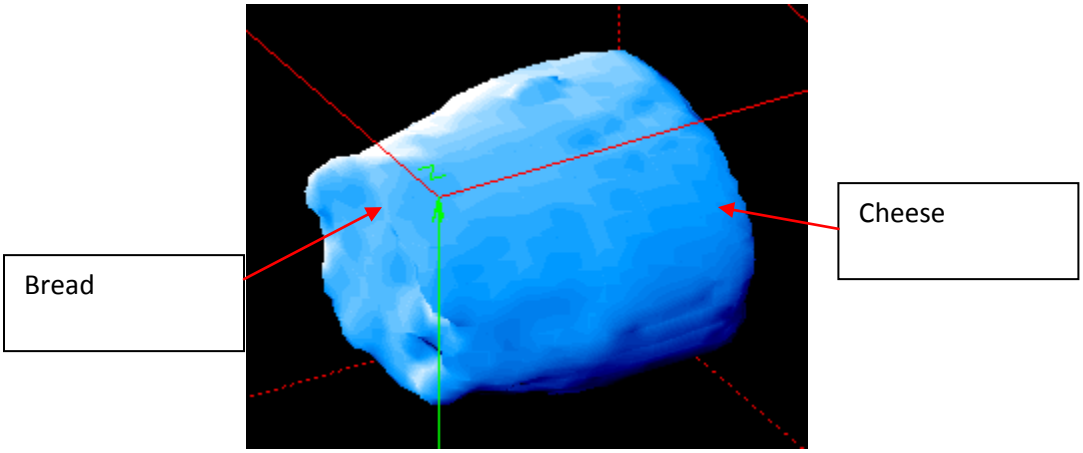

Figure 2.2.1.4.2. 3D image, cheese-bread (high density), Wk1

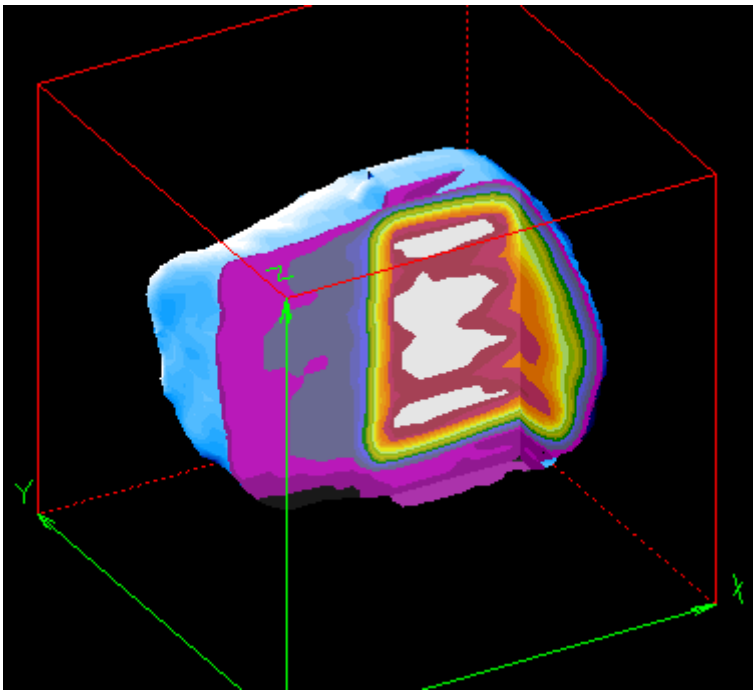

Figure 2.2.1.4.3. Cross intersection, cheese-bread (high density), Wk1

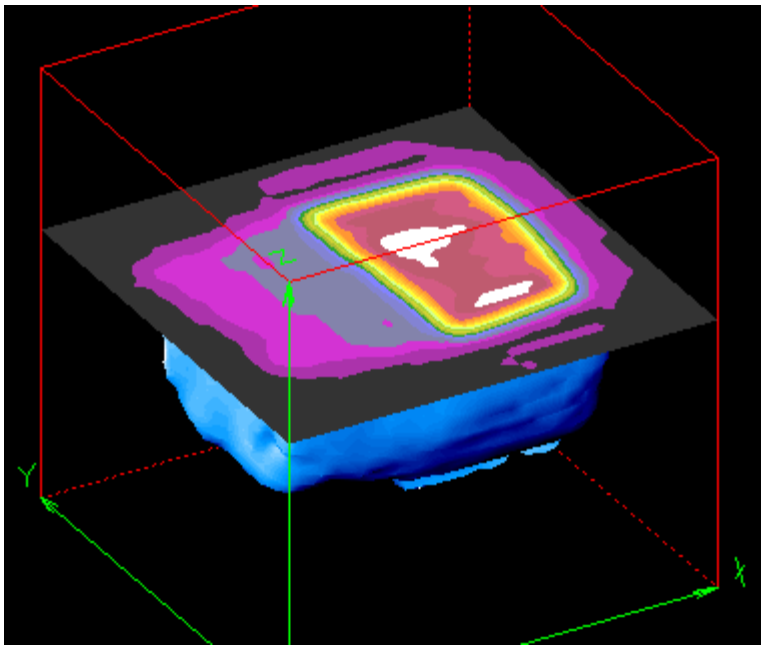

Figure 2.2.1.4.4. Slice, cheese-bread (high density), Wk1

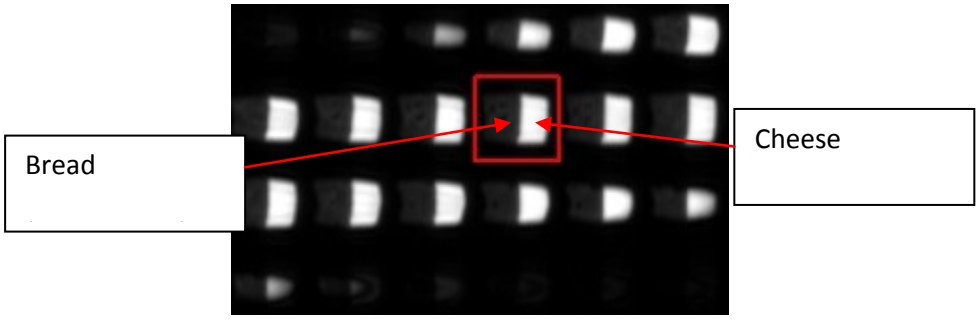

Figure 2.2.1.4.5. 2D slices, cheese-bread (high density), Wk3

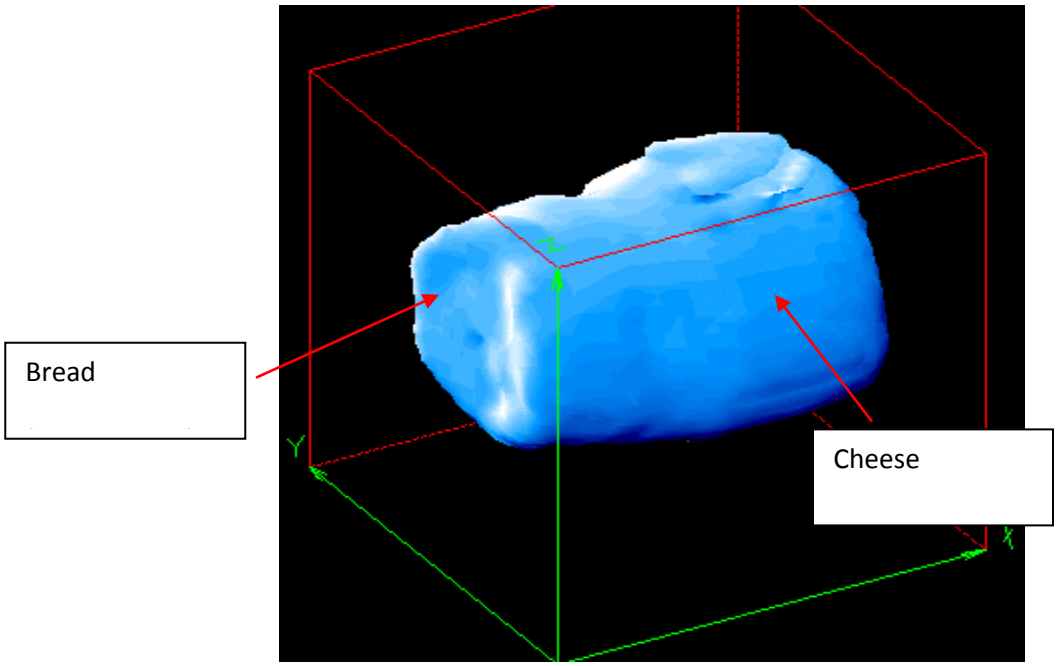

Figure 2.2.1.4.6. 3D image, cheese-bread (high density), Wk3

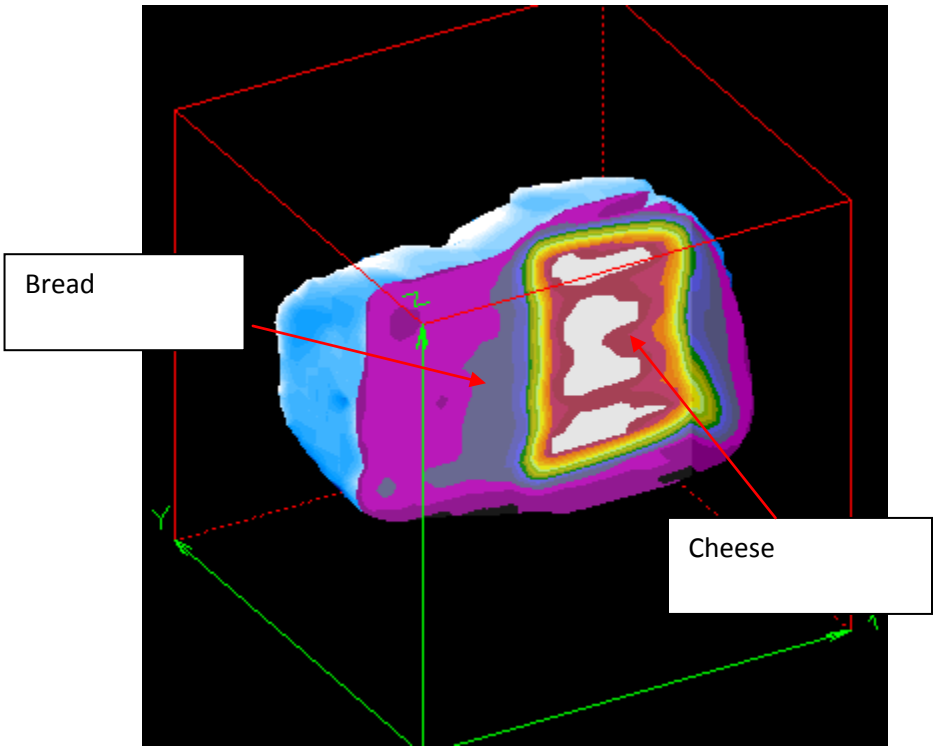

Figure 2.2.1.4.7. Cross intersection, cheese-bread (high density), Wk3

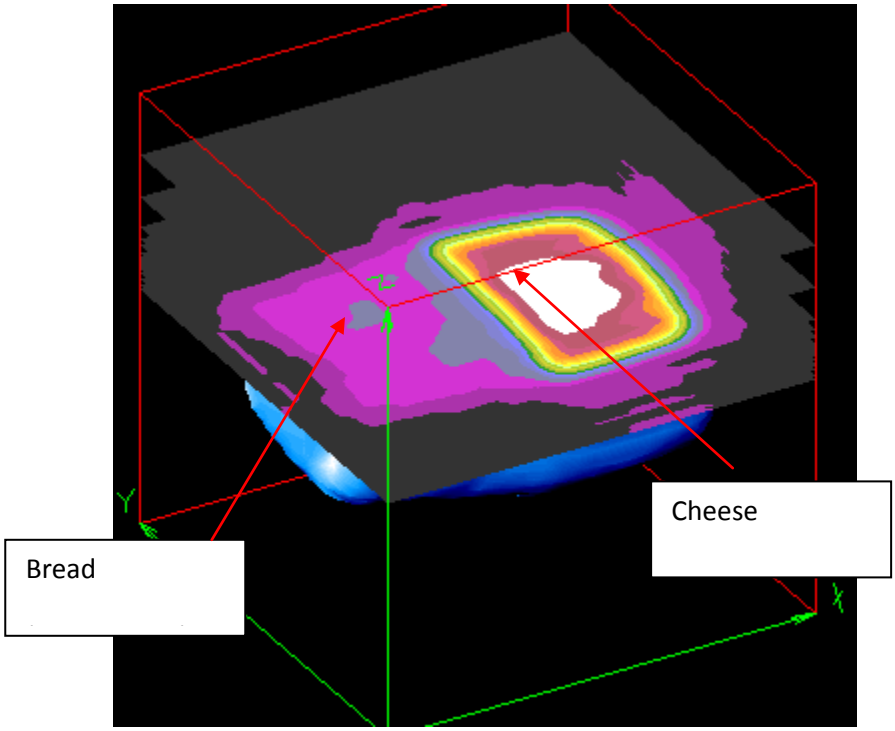

Figure 2.2.1.4.8. Slice, cheese-bread (high density), Wk3

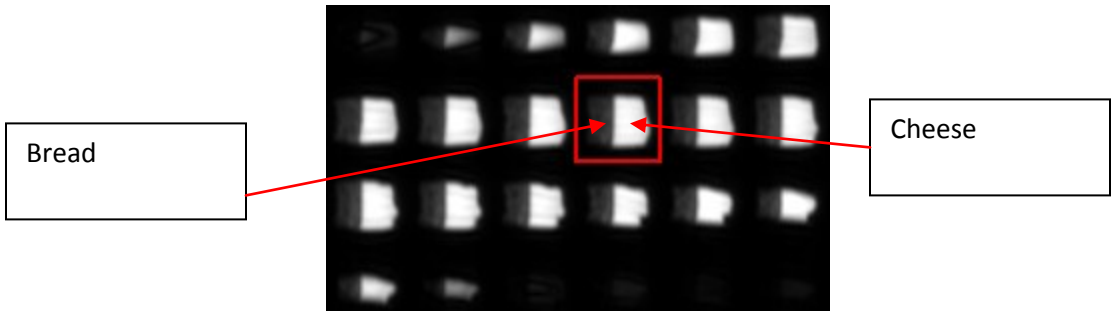

Figure 2.2.1.4.9. 2D slices, cheese-bread (low density), Wk1

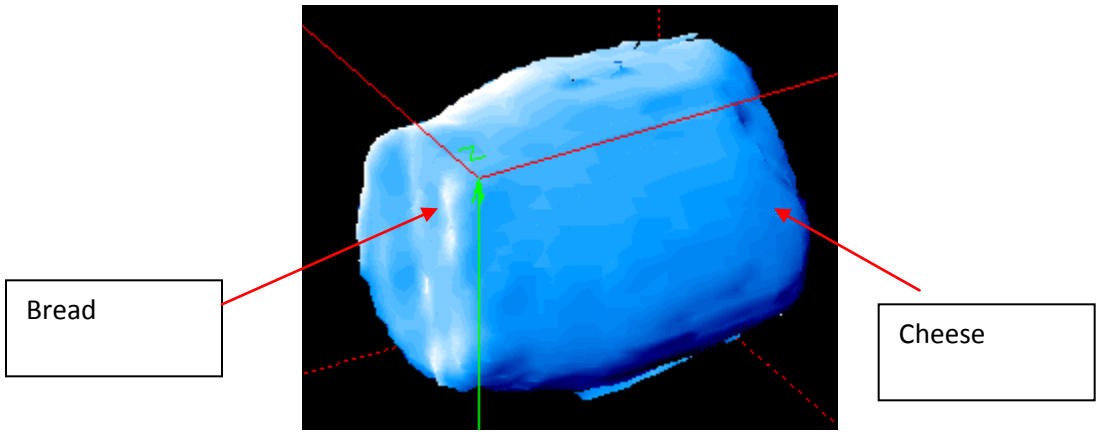

Figure2.2.1.4.10. 3D image, cheese-bread (low density), Wk1

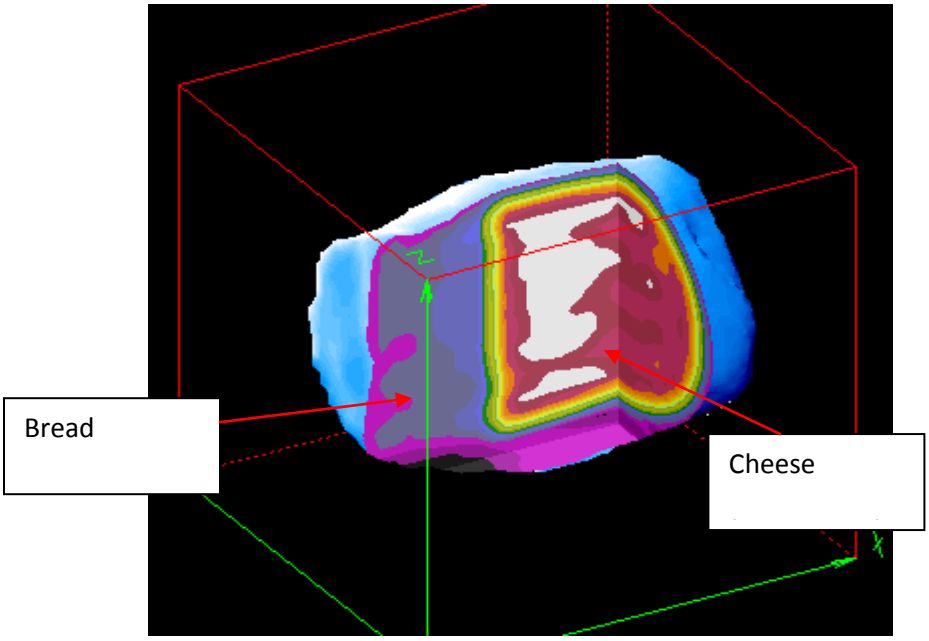

Figure 2.2.1.4.11. Cross intersection, cheese-bread (low density), Wk1

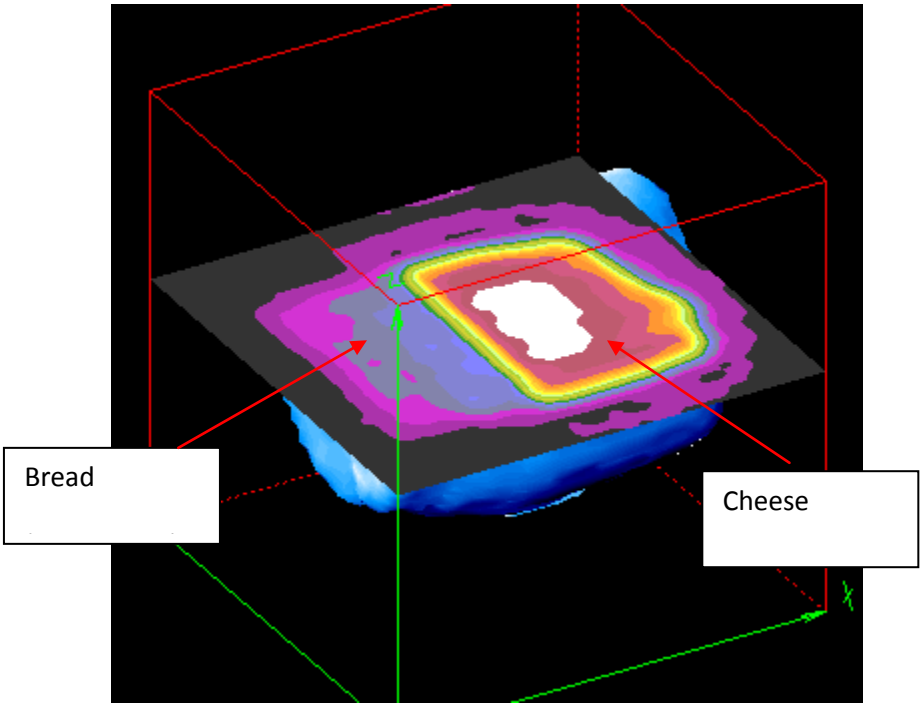

Figure 2.2.1.4.12. Slice, cheese-bread (low density), Wk1

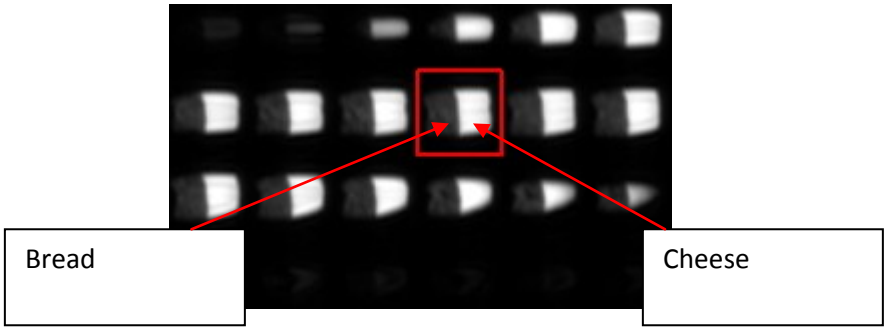

Figure 2.2.1.4.13. 2D slices, cheese-bread (low density), Wk3

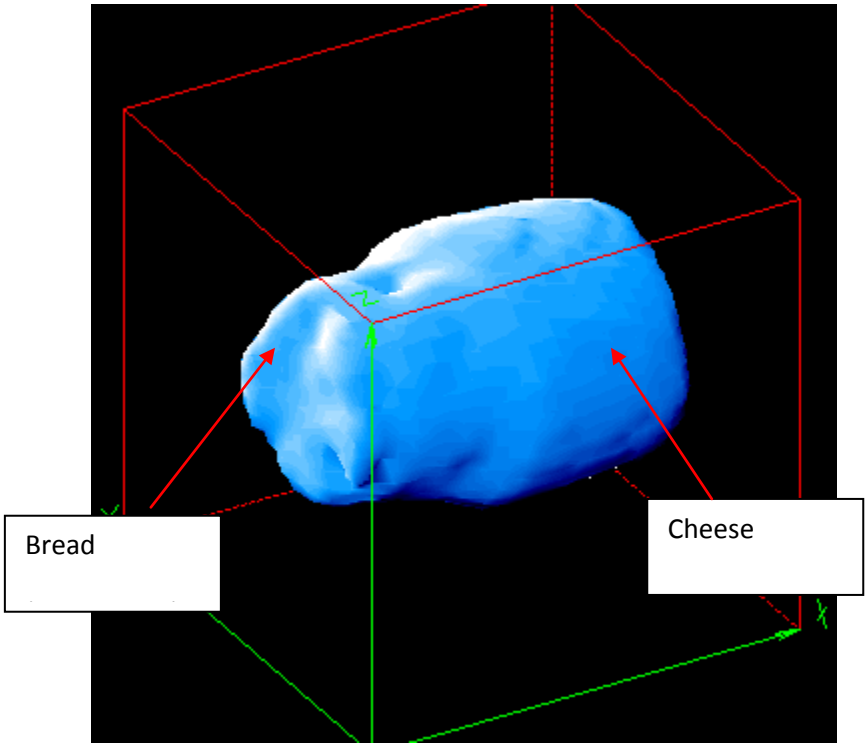

Figure 2.2.1.4.14. 3D image, cheese-bread (low density), Wk3

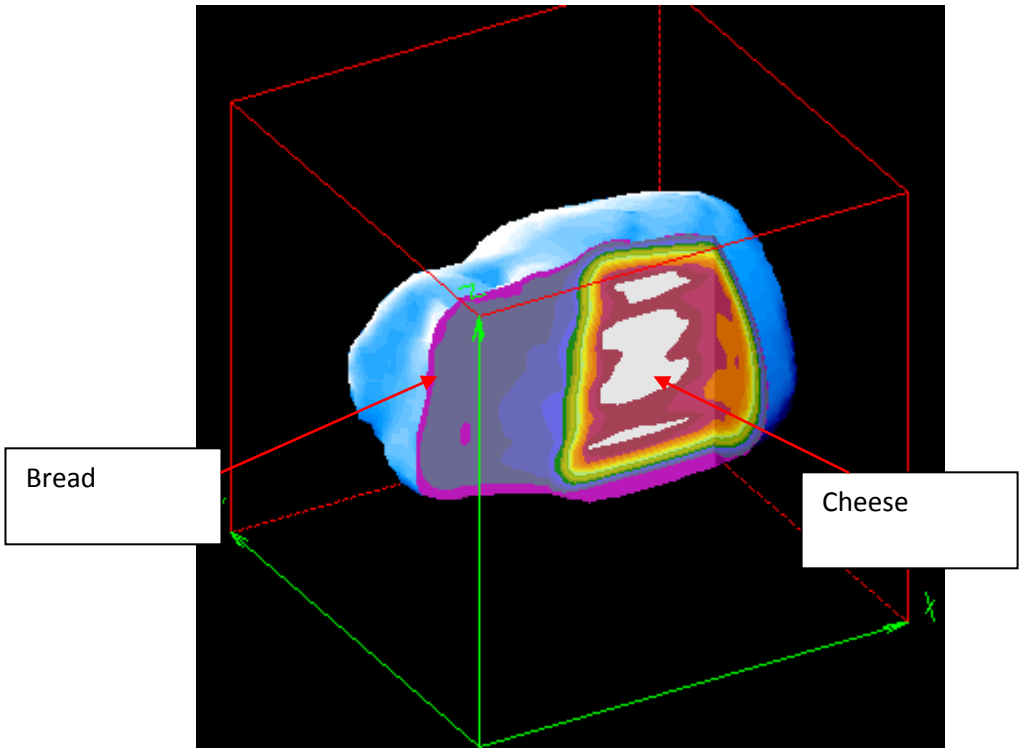

Figure 2.2.1.4.15. Cross intersection, cheese-bread (low density), Wk3

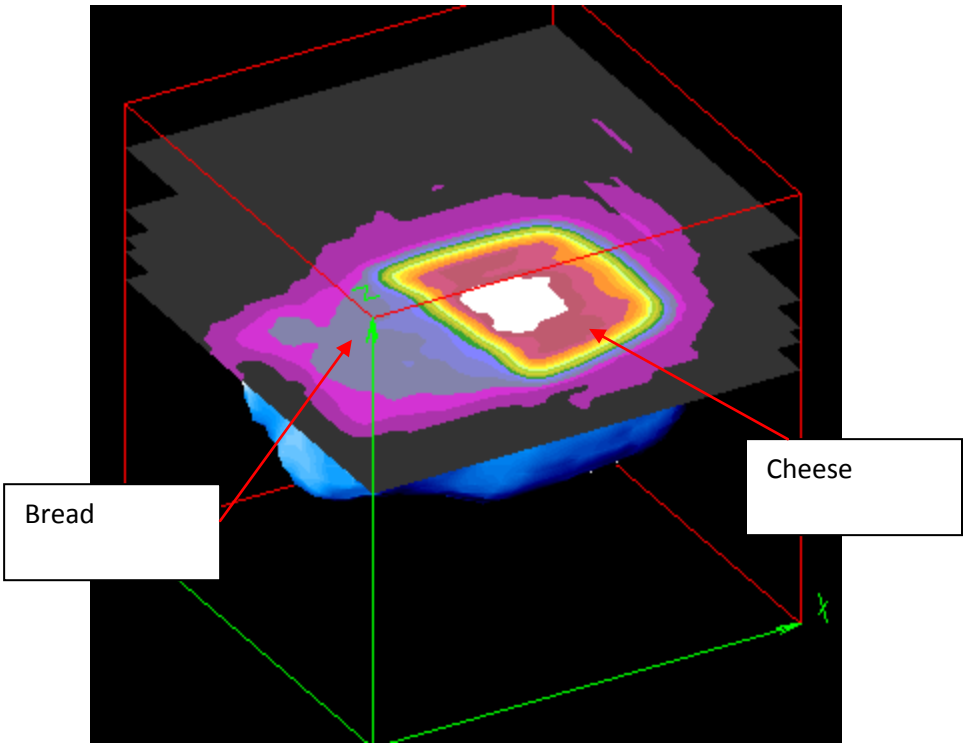

Figure 2.2.1.4.16. Slice, cheese-bread (low density), Wk3

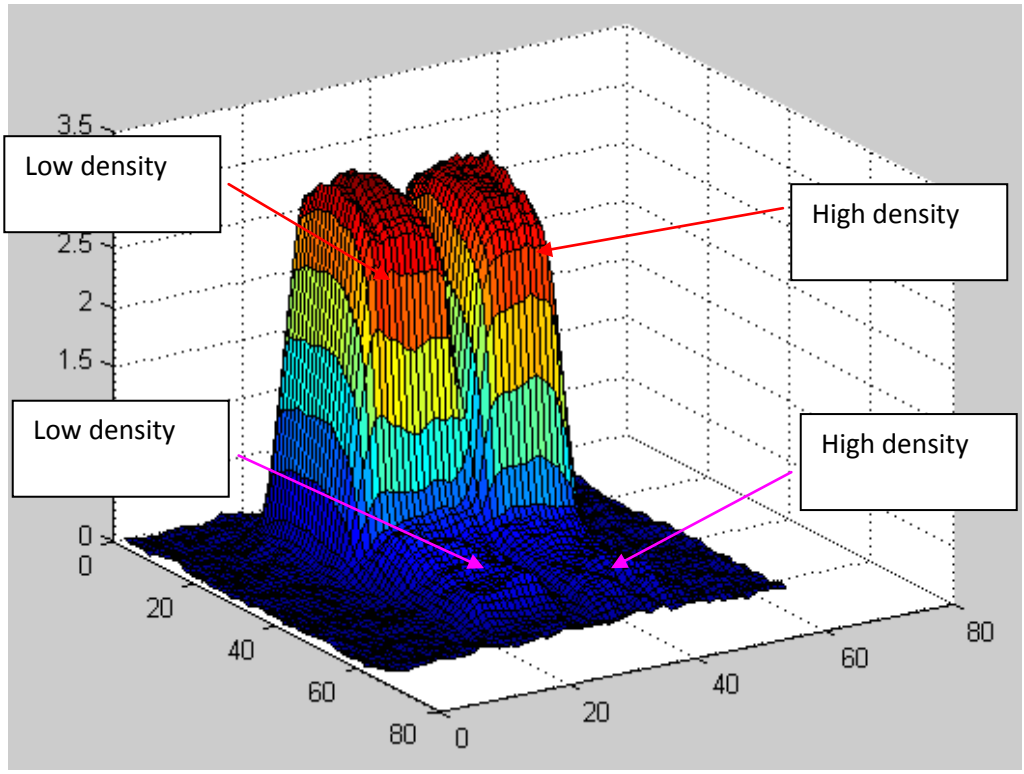

Figure 2.2.1.5.1. cheese-bread (both low and high density), Wk3

The moisture densities in cheese parts for both low and high density samples are nearly the same, while the moisture density in bread part of low density sample is a little larger than that in the high density sample.

2.2.2 Study of moisture migration in foods with multiple components

Samples

Sandwiches with three different treatments were used for tests in this study: Control treatment, Cycling treatment and Migration treatment. Two replications were

assigned to each treatment. There are totally six sandwiches. Bread, peanut butter and jam are the three major components of each sandwich. All sandwiches were stored in the non-defrosting walk-in freezer before experiments. Control and cycling ones were thawed 30 minutes on each side before tests; migration ones were thawed 24 hours before tests.

MRI Tests and Data processing

NMR and MRI measurements were performed using the RI NMR/MRI spectroscope equipped with temperature control device and a large bore NMR/MRI system. FID, CPMG and INVREC sequences were used to measure T2*, T2 and T1 values, respectively. Five 64*64*64 MRI 3D images with five different Tau values were obtained using a 3D spin echo sequence for each sandwich to get T2 mapping results. Each slice image was enlarged in order to see the detailed information.

The NMR relaxation parameter values were calculated from the raw data using software WINFIT. The continuous distributions of these parameters were obtained using software WINDXP. The 3D images were constructed using software IDL 5.6RI advanced image. T2 mapping results were processed using MatLab software.

Results and Discussion

Since the sandwiches have three major components: strawberry jam, peanut butter and bread, we will analyze them respectively. For the jam, we found that the controlled sandwiches had the strongest signal intensity among all three treatments shown by the MRI images (Figure 2.2.2.1). Meanwhile, T2 values of jam in controlled sandwiches were shorter than the other two treatments shown by T2 mapping results (Figure 2.2.2.3&2.2.2.4). These results indicate that jam in controlled sandwiches remains the best quality or stable water state. After different treatments (cycling and migration), water in jam changes its state and turns to be more mobile, leading to longer T2 value. Such a change in water state can easily induce quality changes of the jam and accelerate moisture migration to other components in the sandwiches.

For the peanut butter, we divide it into two portions: top level and bottom level (jam in the middle). We found that cycling sandwiches had the highest signal intensity among all three treatments shown in Figure 2.2.2.2, indicating that more water might be transferred to peanut butter from jam. We saw a special layer of peanut butter next to the bread portion in both levels of peanut butter which has darker color than regular from the real samples. Our MRI T2 mapping results showed that peanut butter next to the jam had lower T2 values than peanut butter next to bread. This was more obvious in cycling sandwiches than in migration sandwiches, shown in Figure 2.2.2.5(a). Since the dark layer positions farthest from the center jam, according to the T2 maps, it should have higher T2 values than regular peanut butter. Therefore, we speculate that this dark layer

of peanut butter has more mobile water but less oil, leading to its harder texture than regular peanut butter.

For the bread, we found that cycling sandwiches and migration sandwiches had stronger signal intensity than controlled sandwiches. One interesting observation was that some of the bottom bread and bottom peanut butter of migration sandwiches were combined together (like melting) in the T2 maps shown in Figure 2.2.2.2, 2.2.2.3 and 2.2.2.4. We speculate that there is more migration between bottom peanut butter and bottom bread in the migration sandwiches than in the other two treatments, such as oil transfer and moisture migration processes.

From T2 maps shown in Figure 2.2.2.4, we found that generally for all three treatments, T2 values of the interface between jam and top peanut butter were much higher than interface between jam and bottom peanut butter; specifically, T2 values of the interface between jam and peanut butter of migration sandwiches were higher than the other two treatments; T2 values of the interface between bottom peanut butter and bottom bread were higher than the other two treatments as well. These indicate that more migration processes occurred in the top interface inside migration sandwiches.

Another observation is that the cycling sandwiches had more scattered signals from outside the sandwich area than the other two treatments shown in Figure 2.2.2.5. We speculate that these signals are from the ice cubes or other extra moisture sources such as the package.

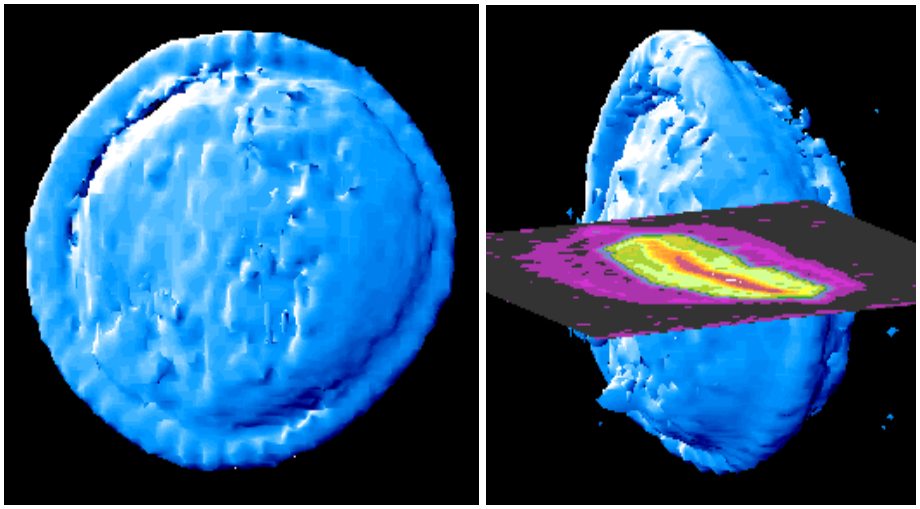

Low High

Figure 2.2.2.1 3D images and 2D image for a sandwich sample with bread crust and peanut butter coated strawberry jam fillings, processed by software IDL5.6 with color bar.

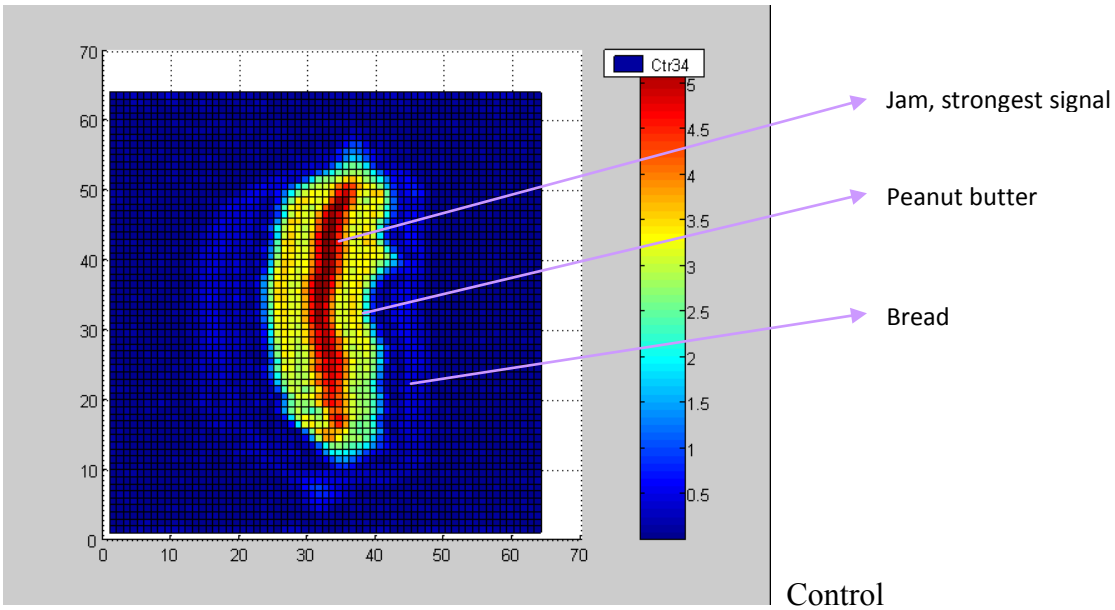

Control

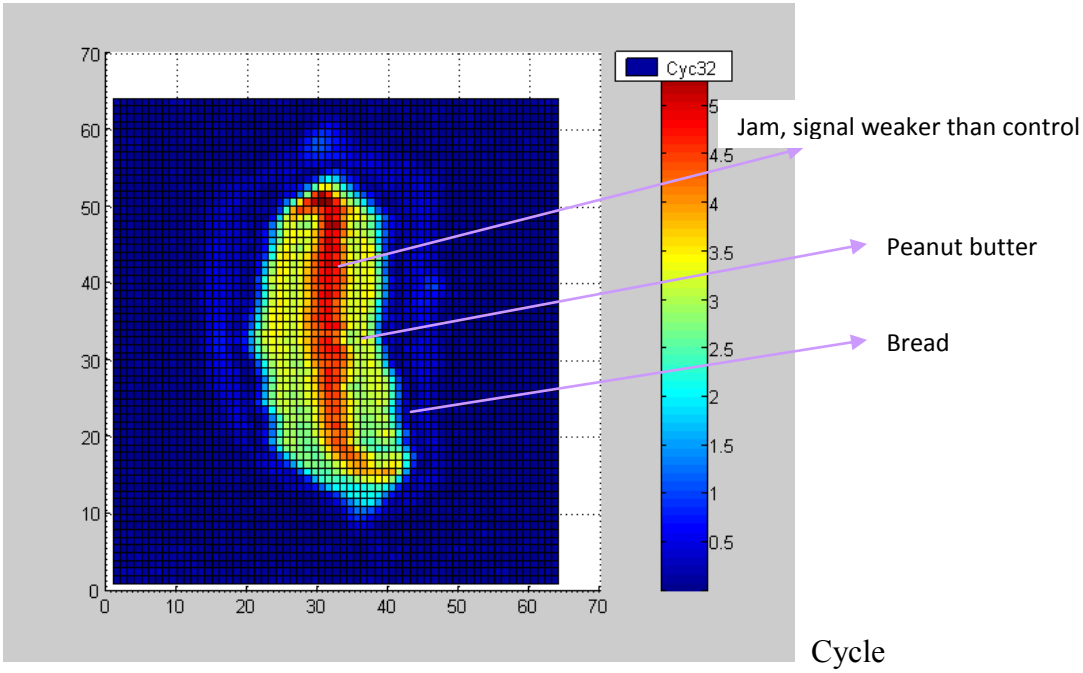
Cyc32
Jam, signal weaker than control
Peanut butter
Bread
Cycle

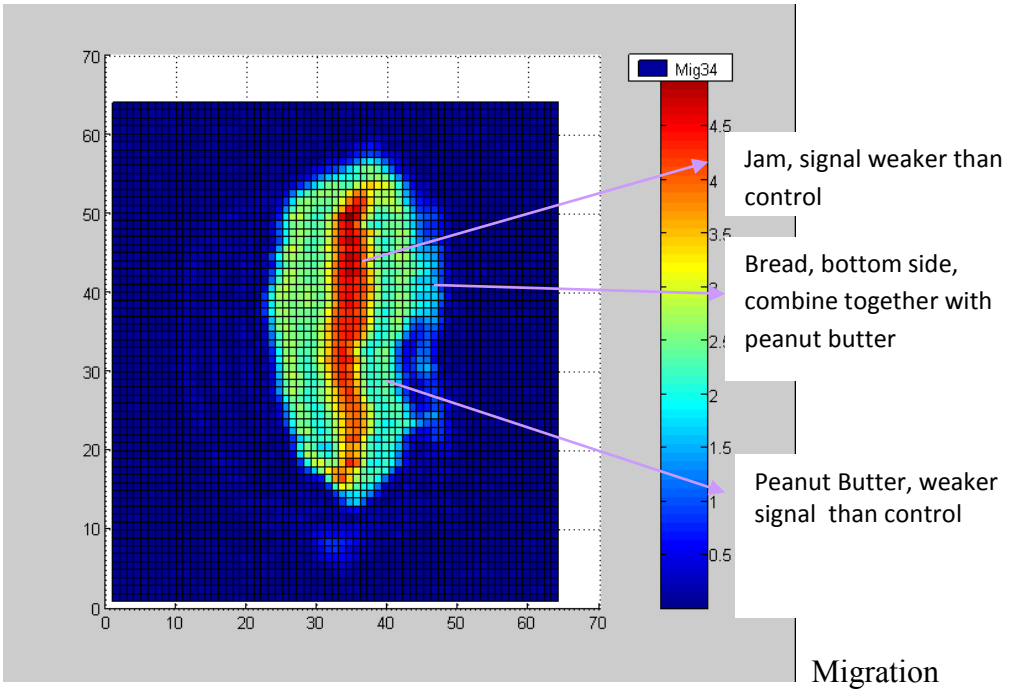

Figure 2.2.2.2. MRI slice images of sandwiches

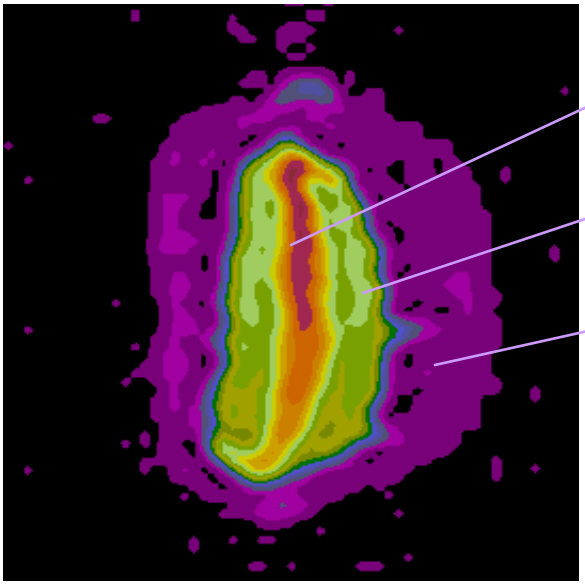

Control

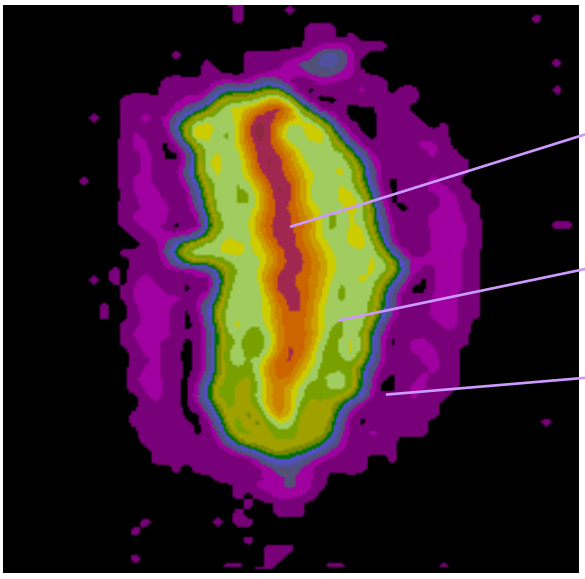

Cycle

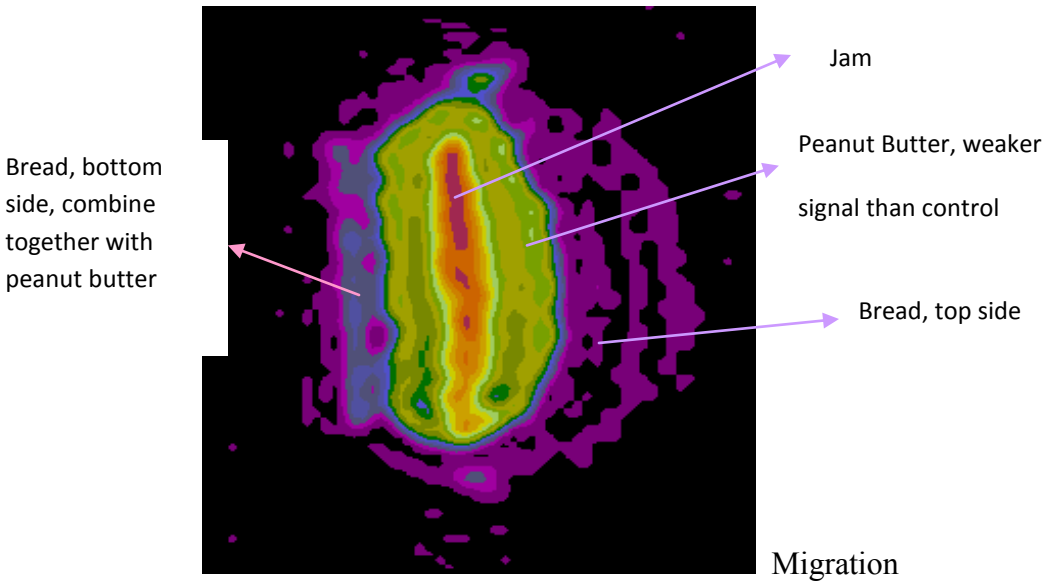

Figure 2.2.2.3. MRI slice images of sandwiches in color scale

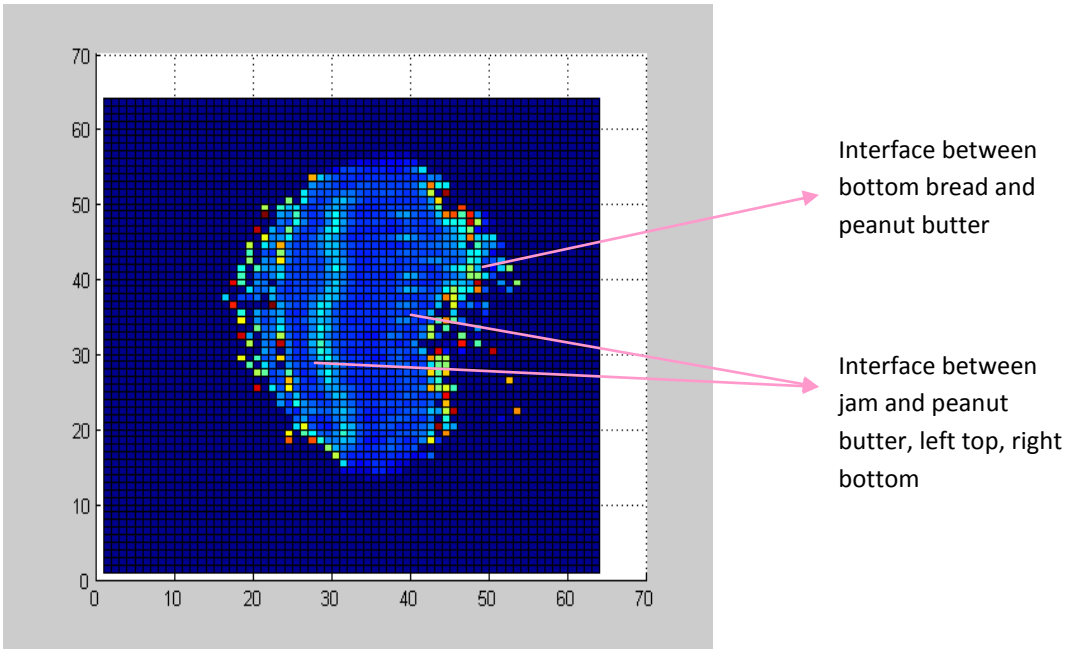

Figure 2.2.2.4(a). T2 map of one slice --- one colored example from the following Figure 2.2.2.4(b)

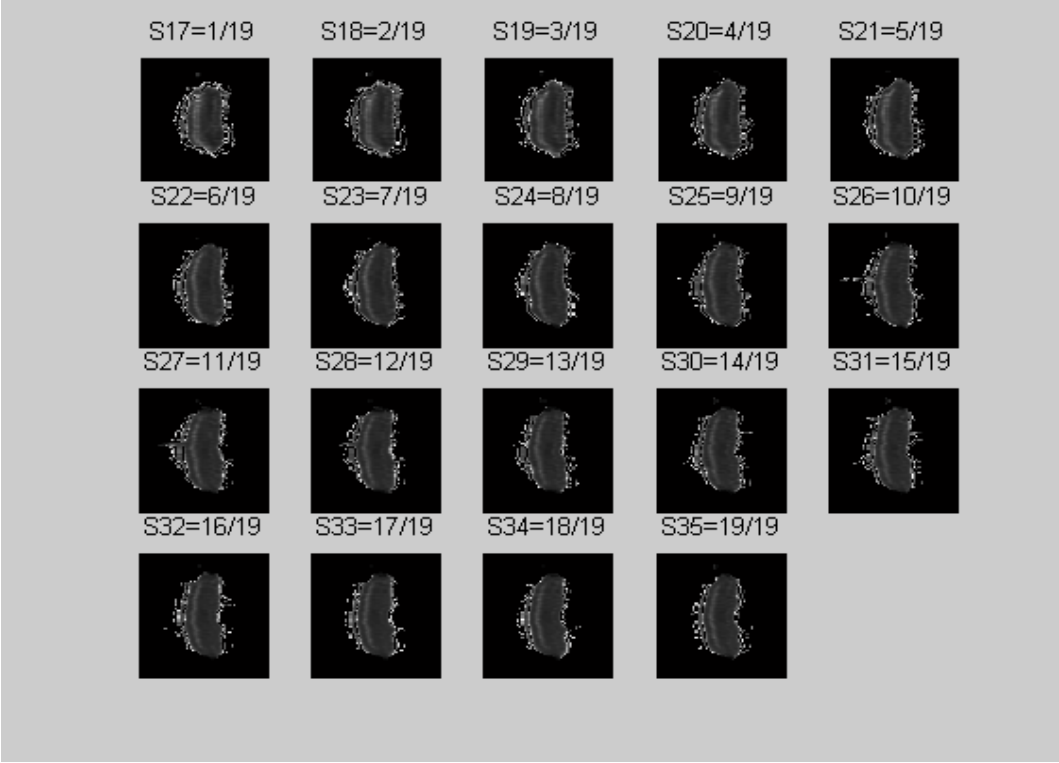

Control

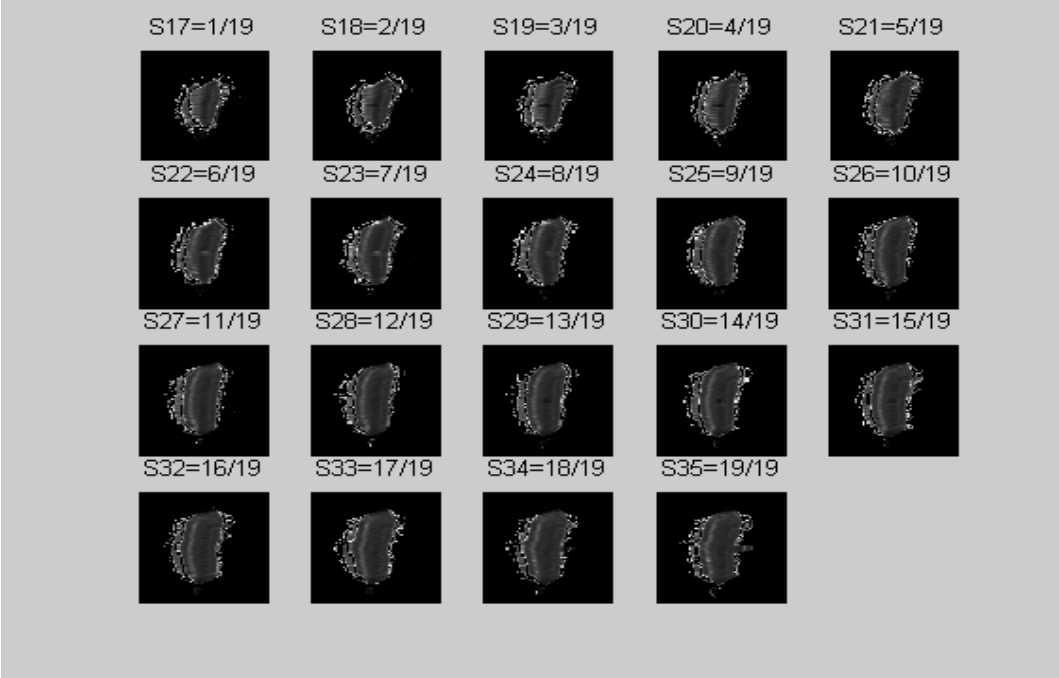

Cycle

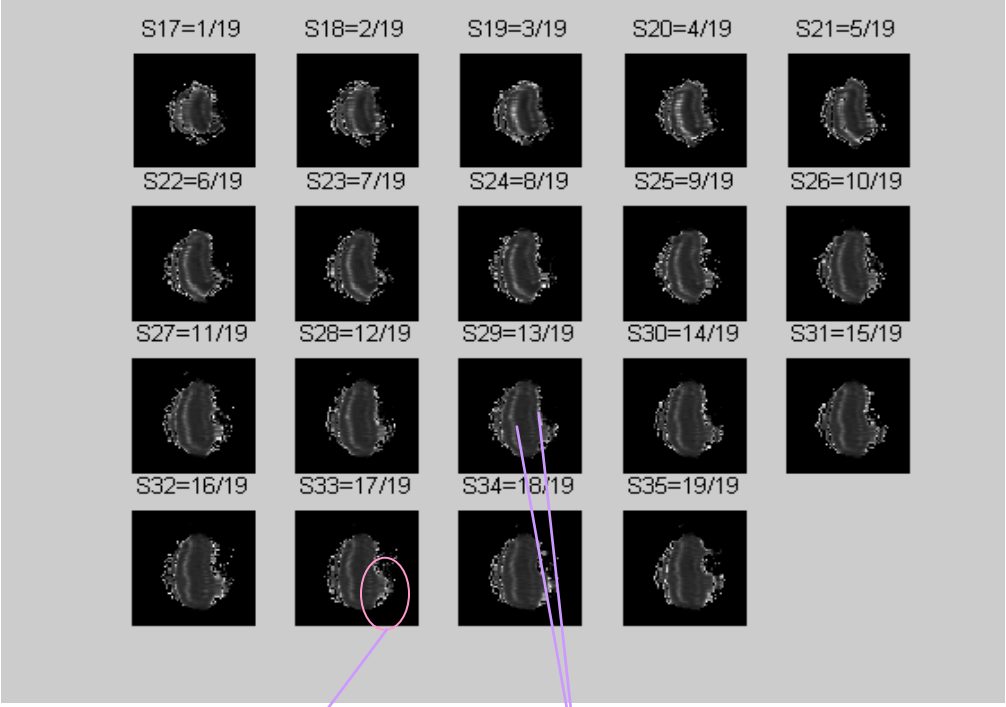

Migration

Bottom bread, combined with bottom peanut butter

Interface between jam and peanut butter

Figure2.2.2.4(b). T_2 maps on different slices of the sandwich shown in the above figures.

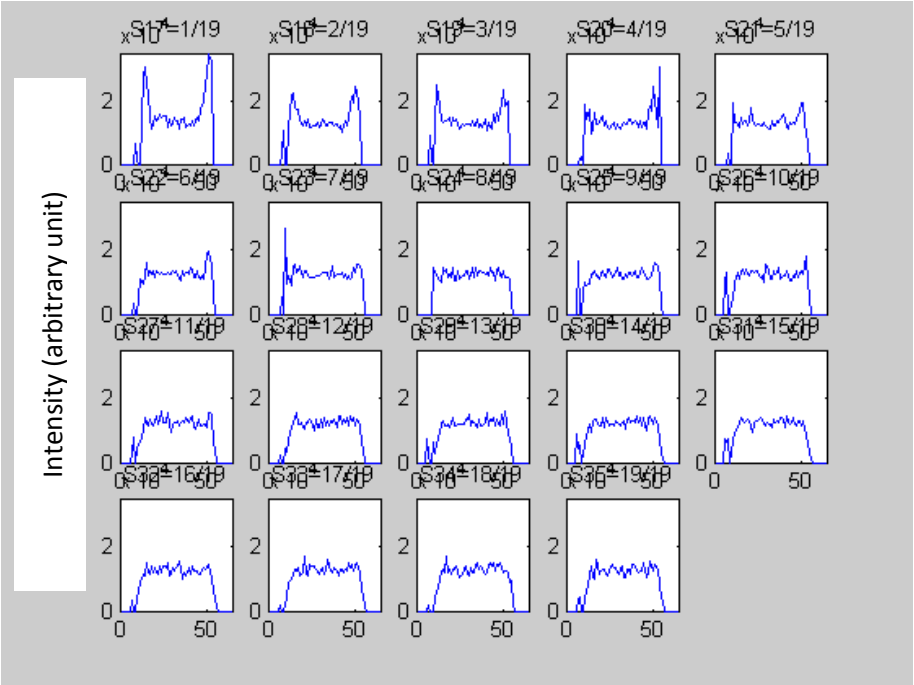

Control

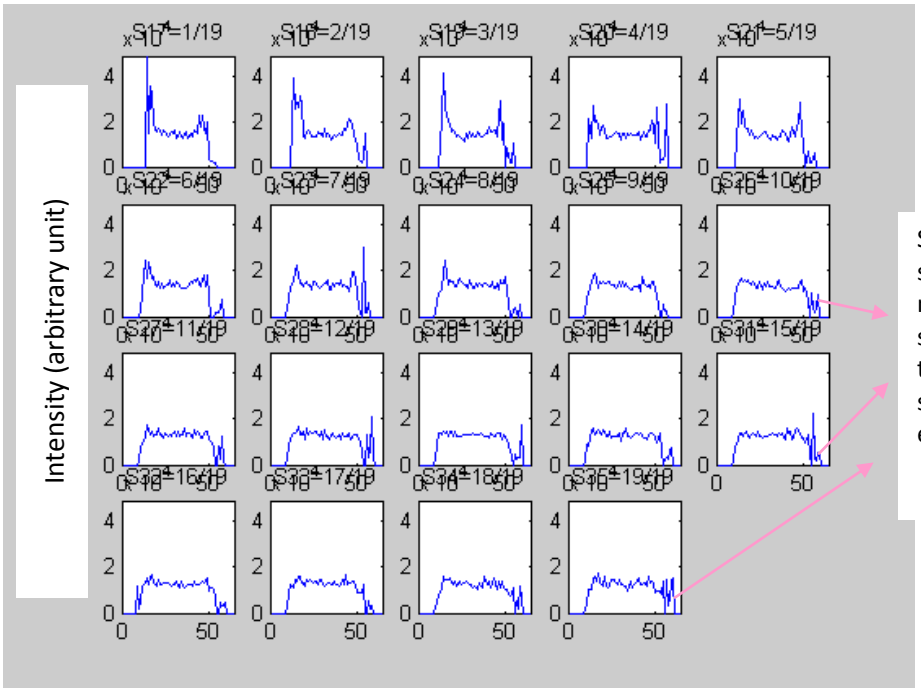

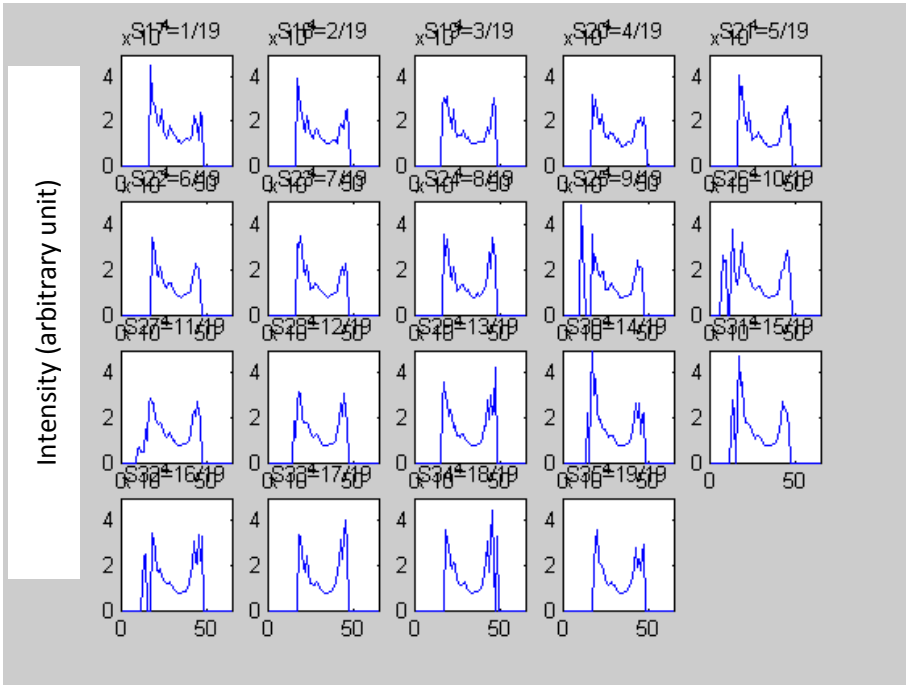

Positions of the sample slice on 1D profile

Figure 2.2.2.5(a). T2 values averaged to one direction from the 2D planes shown in Figure 2.2.2.4 (Horizontal axis represents positions in the 64*64 resolution image slice and vertical axis represents T2 values).

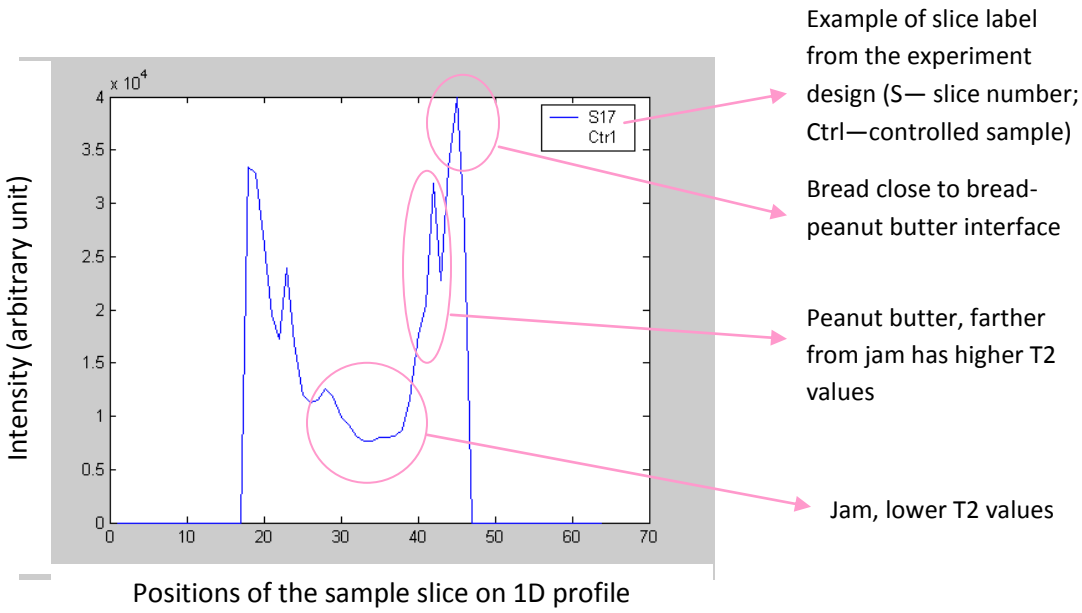

Figure 2.2.2.5(b). An enlarged T2 map example from Figure 2.2.2.5(a) (Horizontal axis represents positions in the 64*64 resolution image slice.).

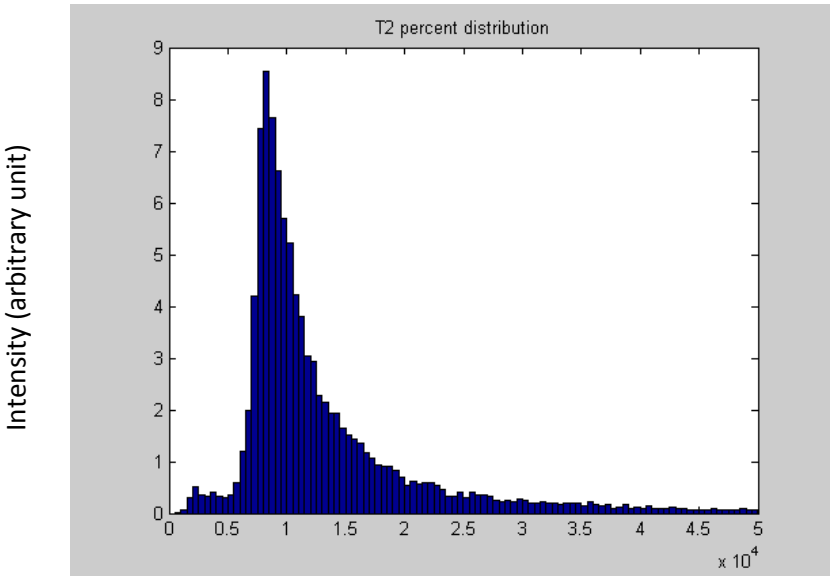

T2mean = 1.2970e+004; T2std = 7.6864e+003 calculated in µs

Figure 2.2.2.6. T2 distribution for the sandwich shown in above figures.

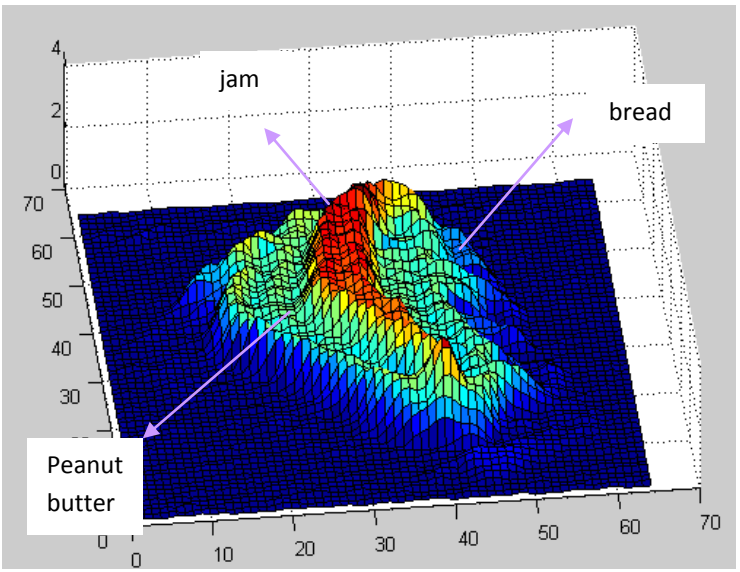

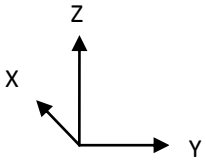

X&Y – positions of the sample resolution 64*64

Z – intensity (arbitrary unit)

Figure 2.2.2.7. Surface plot of selected slice image shown in Figure 2.2.2.1 processed by MatLab, showing three layers of different color signals from jelly, peanut butter and bread, respectively(Horizontal plane represents positions in the 64*64 resolution image slice and vertical axis represents signal intensity).

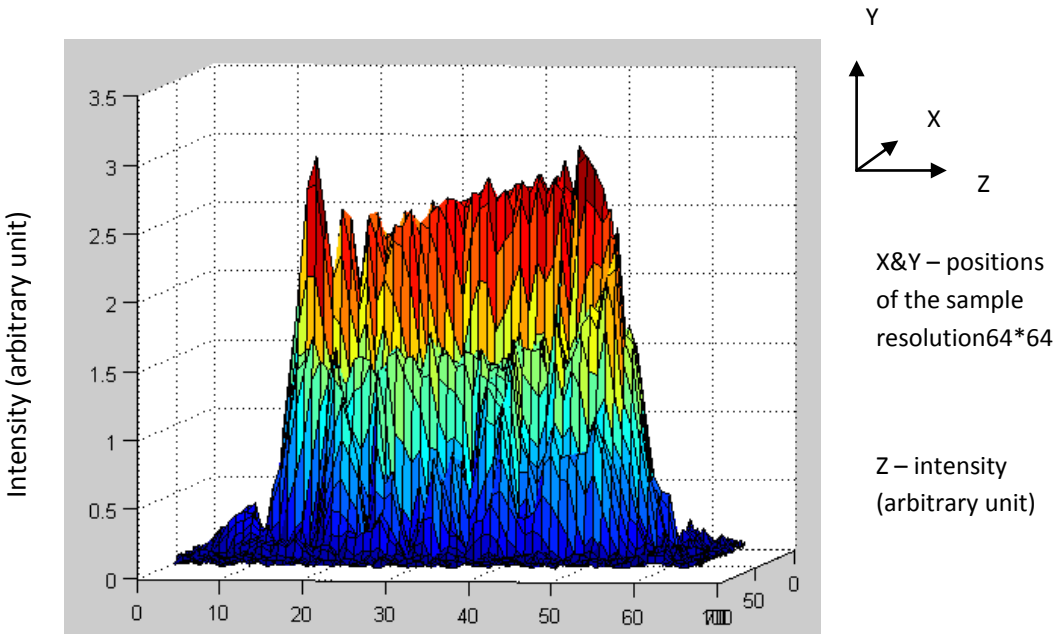

Figure 2.2.2.8. Further processed surface plot of the same slice image shown in Figure 2.2.2.2 processed by MatLab (Horizontal plane represents positions in the 64*64 resolution image slice and vertical axis represents signal intensity).

2.2.3 Relationship between water properties and temperature of foods in gel and liquid states

Samples

Two types of materials, denoted as A and B, were individually made into two kinds of frozen food. A was in jelly state and B was in liquid state. Both materials were put into 4 separate bottles, sealed and used for NMR and MRI tests. The objective of this study was to use MRI technique to monitor the change in water content, motion and distribution in two materials and two frozen food samples. The T1, T2 and T2* values were measured to illustrate the differences of moisture states using NMR technique. The T2 value mapping was calculated to show the spatial moisture distribution in different materials and samples.

MRI Tests and Data processing

NMR and MRI experiments were conducted using a MRI system with a 12.9 MHz permanent magnet. FID, CPMG and INVREC sequences were used to measure T2*, T2 and T1 values respectively. MRI 3D images of matrix 32*32*32 were obtained using a 3D spin echo sequence. Material A and Material B were taken NMR tests at 25°C and were each taken 4 MRI imaging series to map out T2 value distribution. Sample A and Sample B were taken NMR tests separately at 5°C and 25°C and were taken MRI images together in the controlled temperature decreasing process at 5°C, -5°C, -15°C, -25°C, -35°C respectively.

The NMR relaxation parameter values were calculated from the raw data using software WINFIT. The continuous distributions of these parameters were obtained using software WINDXP. The 3D images were constructed using software IDL 5.6RI advanced image. The T2 mapping images were constructed using Matlab software.

Results and Discussion

T2 mapping of Material A and Material B

T2 mapping results are shown in Figures 2.2.3.1-2.2.3.4. From 3D T2 mapping (Figures 2.2.3.1, 2.2.3.2 and 2.2.3.3), we found that T2 was more evenly distributed in Material A than in Material B. From T2 histogram (Figure 2.2.3.3), we are able to calculate the mean value of T2 in two materials, which showed that T2 mean value for B was much greater than A. This agrees with the discussion above. Because of the structural difference of the two materials, Material B had more bubbles inside, which are illustrated as the holes in the T2 mapping images below. Therefore, the structure was not tight enough to interact with water molecules strongly, and this is why there was more "free" water in B than in A, leading to a larger T2 value.

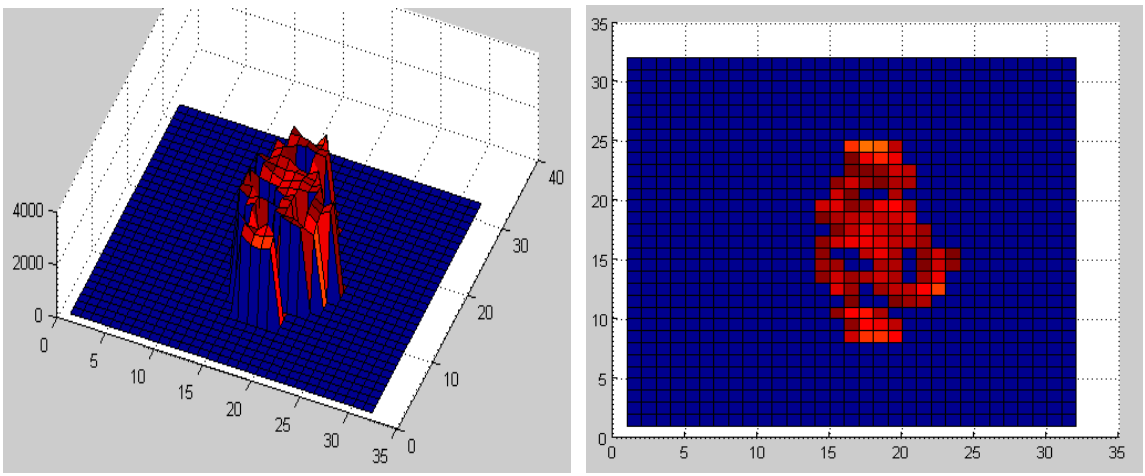

Figure 2.2.3.1. 3D and 2D T2 mapping for the center slice of Material A

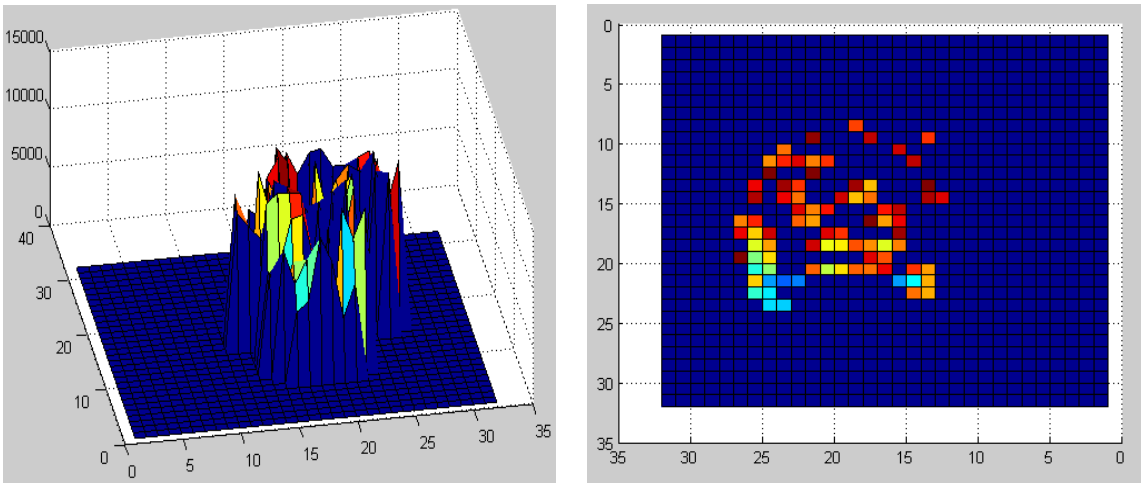

Figure 2.2.3.2. 3D and 2D T2 mapping for the center slice of Material B

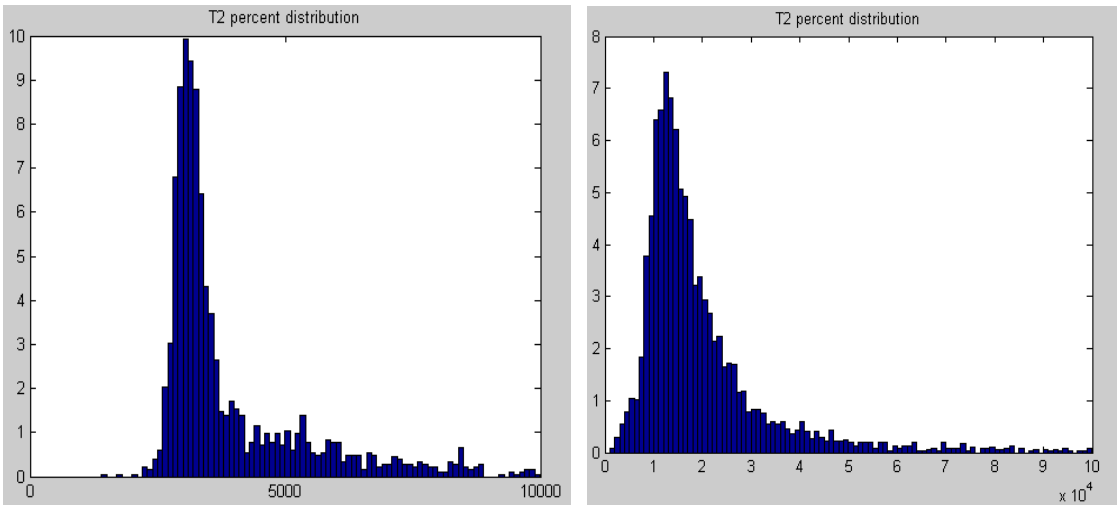

T2mean = 3.9113e+003 T2mean = 1.9635e+004

Figure 2.2.3.3. T2 distribution histogram for Material A (left) and B (right)

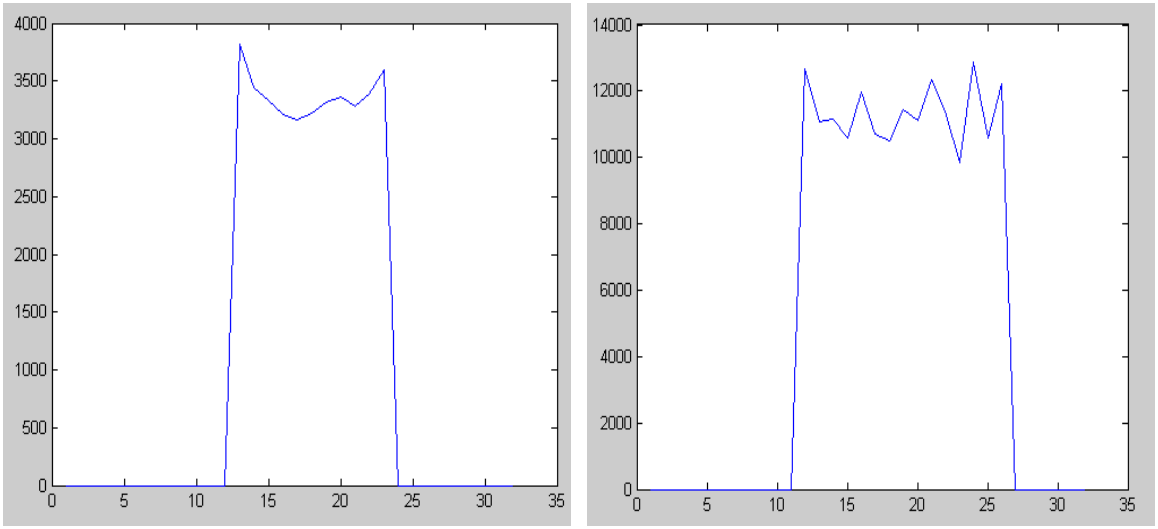

Figure 2.2.3.4. 1D T2 distribution for Material A (left) and B (right)

Moisture Distribution for Sample A and B together

MRI images were acquired from 5°C to -35°C. The purpose of doing this was to find the critical temperature points of two samples (left A, right B) when no image could be obtained, which means that "free" water was frozen and became totally "bound" and hence no signal was at detectable level. Figure 2.2.3.5 shows the 3D moisture distribution at different temperatures. We found that at around -25°C, the image of B almost disappeared. Images could still be taken from Sample A until around -35°C. Therefore, we speculate that the critical temperature point might be -25°C for B and –35°C for A. This agrees with our earlier discussion. As temperature decreases, the longer T2 component (T22) decreases much faster in B than in A. Thus the "free" water in B was frozen at higher temperature compared with that in A.

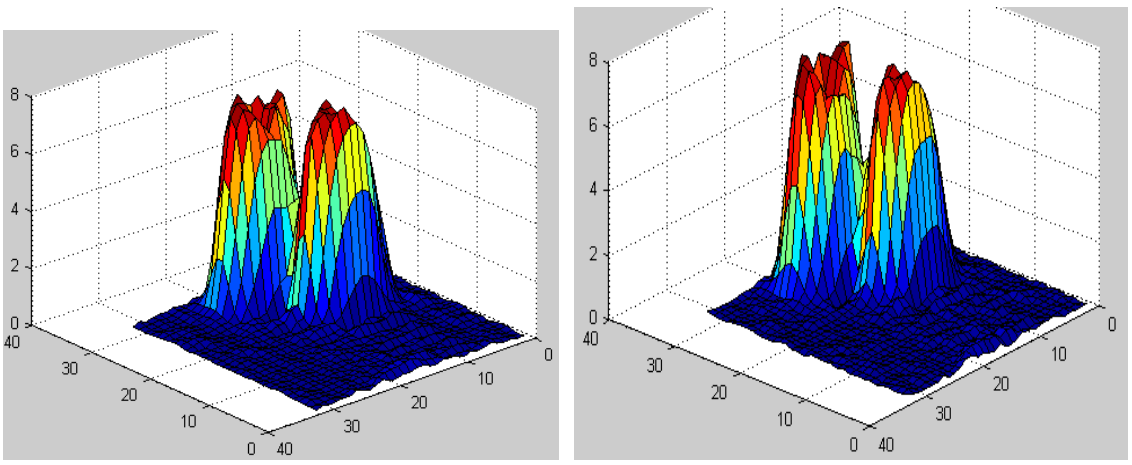

at 5 °C

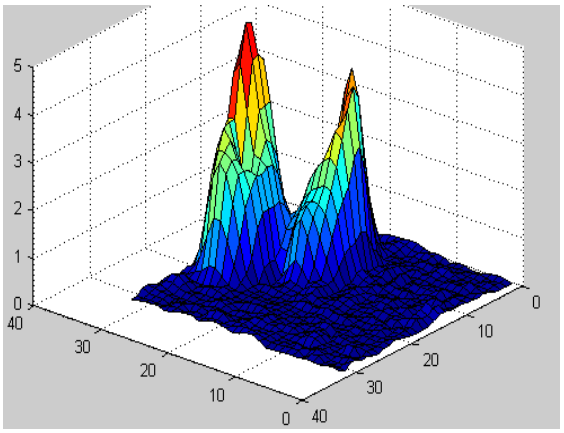

at -5°C

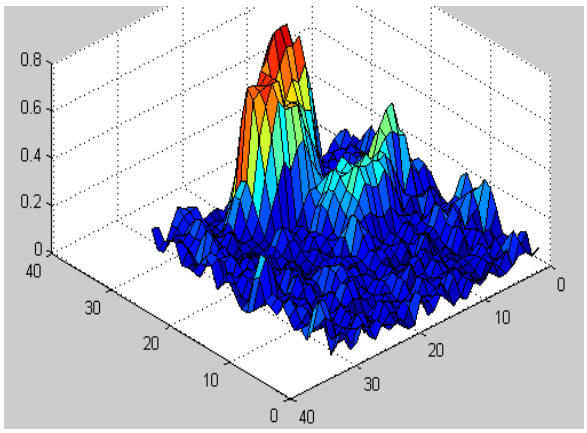

at -15°C

at -25°C

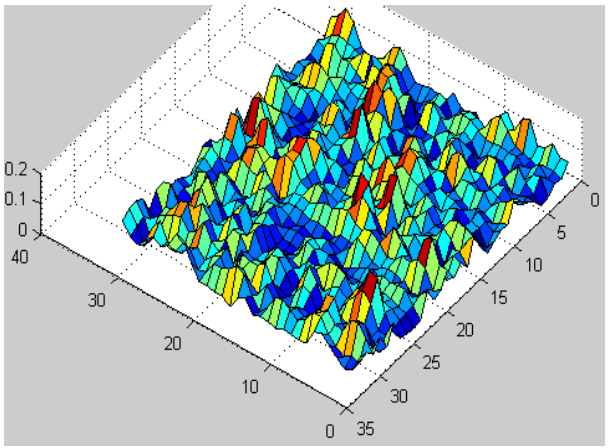

at -35°C

Figure 2.2.3.5. MRI images at different temperatures

2.2.4 Study of water diffusion properties in grains during cooking processes

Samples

Medium grain and long grain samples were prepared for NMR tests. For the soaking process, around 50 grams of each type of grain were weighted in two glass containers at room temperature. 5 grams of each grain were taken out for tests at initial time (before adding water) and at 10 minutes, 30 minutes, 60 minutes, 180 minutes after adding water. For the cooking process, around 50 grams of each type were put into a water bath to keep the cooking temperature at 95°C after boiling. 5 grams of each grain were taken out for tests at 5 minutes, 10 minutes, 15 minutes, 20 minutes, 30 minutes after boiling. During both processes, 2 grams of each grain were also taken out at each time point for moisture content measurement using oven drying method. During cooking process, one kernel of each grain was taken out for MRI test at each time point.

It was found that medium grain was more difficult to cook than long grain but how water moves differently between two types of grain during cooking process was not quite understandable. The objective of this study was to use NMR/MRI technique to illustrate the water mobility and distribution in the rice during cooking.

MRI Tests and Data processing

NMR and MRI experiments were conducted at 35°C using MRI system with a 21.4 MHz permanent magnet system (Resonance, UK). FID, CPMG and INVREC sequences were used to measure T2*, T2 and T1 values respectively. MRI 3D images of matrix 32*32*32 were obtained using a 3D spin echo sequence.

NMR experiments were conducted at 25°C using a MRI system with an 12.9 MHz permanent magnet. FID, CPMG and INVREC sequences were used to measure T2*, T2 and T1 values, respectively. The NMR relaxation parameter values were calculated from the raw data using software WINFIT.

Confocal Microscope Tests

One kernel of each grain was taken at initial time for Microscope tests using Nikon C1 spectral imaging confocal microscope system.

Results and Discussion

Moisture Content analysis

Moisture contents during both soaking and cooking process are summarized in Figures 2.2.4.1 and 2.2.4.2. Generally, moisture contents increased during both processes for both medium grain and long grain. But long grain had a faster moisture content

increasing rate between 10 and 50 minutes and higher moisture content after 30 minutes than medium grain in the soaking process. Differences also appeared in cooking process. During the first 15 minutes, there was no big moisture content difference for the two types of grain. However, long grain had a slightly faster moisture content increasing rate between 15 and 20 minutes and absorbed more water after 15 minutes cooking than medium grain. It is highly possible that these 5 minutes (between 15 and 20 minutes) play a key role in determining the actual time for grains to be fully cooked. It also indicates that medium grain needs more time to reach the certain moisture content in order to be ready for use.

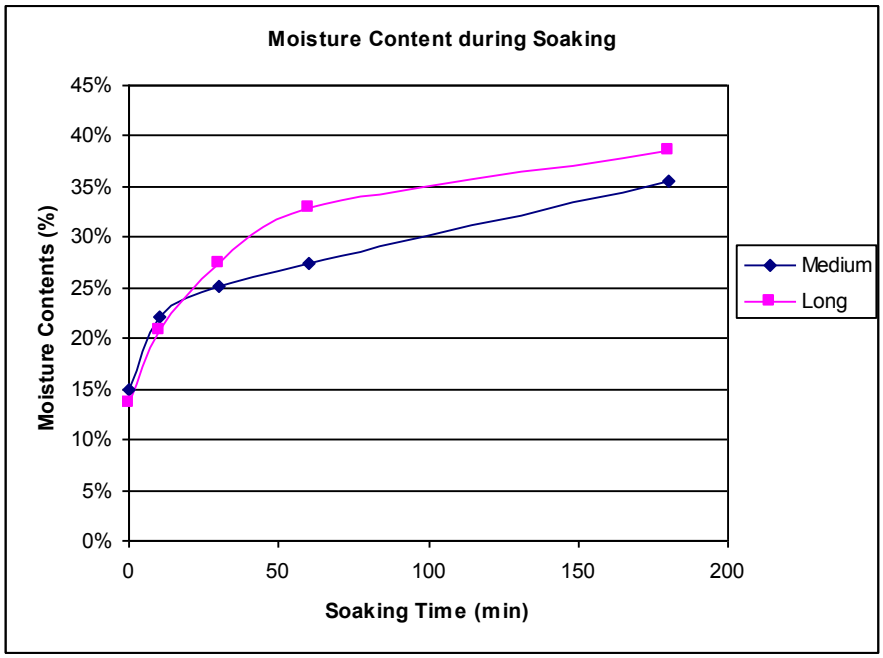

Figure 2.2.4.1. Moisture contents during soaking

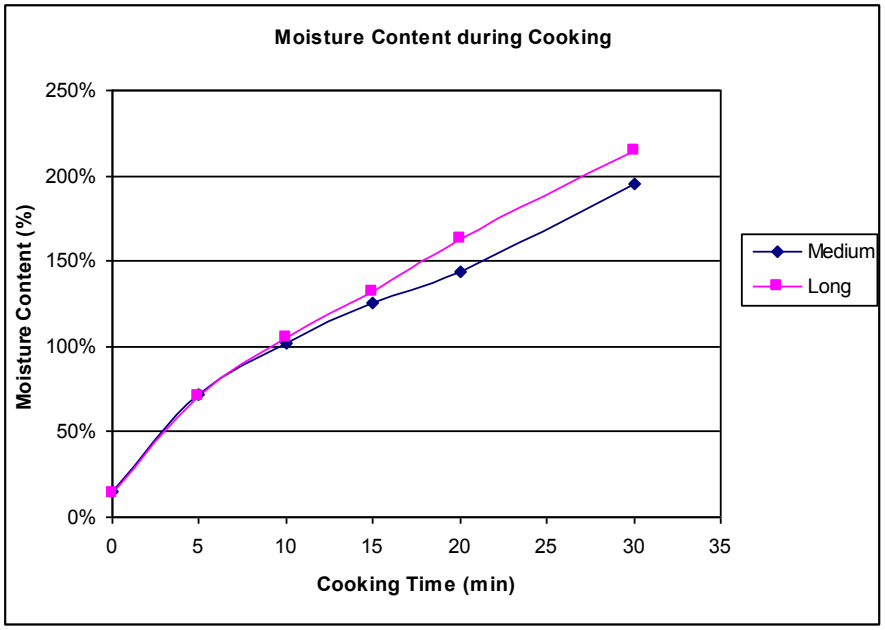

Figure 2.2.4.2. Moisture contents during Cooking

Table 2.2 and Figures 2.2.4.3-2.2.4.7 summarize the relaxation times (T2*, T2, T1) for long and medium grain obtained by discrete model fitting. We can clearly see the similar trend as we find in the moisture content analysis above. During soaking process, T2 values of long grain increased faster than T2 values of medium grain between 10 and 50 minutes. Moreover, T2 values of long grain were larger than T2 values of medium grain after 30 minutes of soaking. During cooking process which is the key process in this study, T2 values of long grain increased faster than T2 values of medium grain between 15 and 20 minutes. Furthermore, T2 values of long grain were higher than T2 values of medium after 15 minutes of cooking. We also found it interesting that T1 curve

in cooking process has a very similar increasing pattern and correlates quite well with the moisture content curve in soaking process. In addition, Figures 5&6 indicate that NMR relaxation times (such as T2 values) show a more obvious difference in the increasing pattern than moisture contents during cooking.

Table 2.2. Relaxation times (T2* and T1) during soaking

	T2* (μs)		T1 (ms)	
Time (min)	Medium	Long	Medium	Long
0	430	380	55	54
10	335	476	48	44
30	352	493	48	44
60	363	444	48	46
180	441	358	52	51

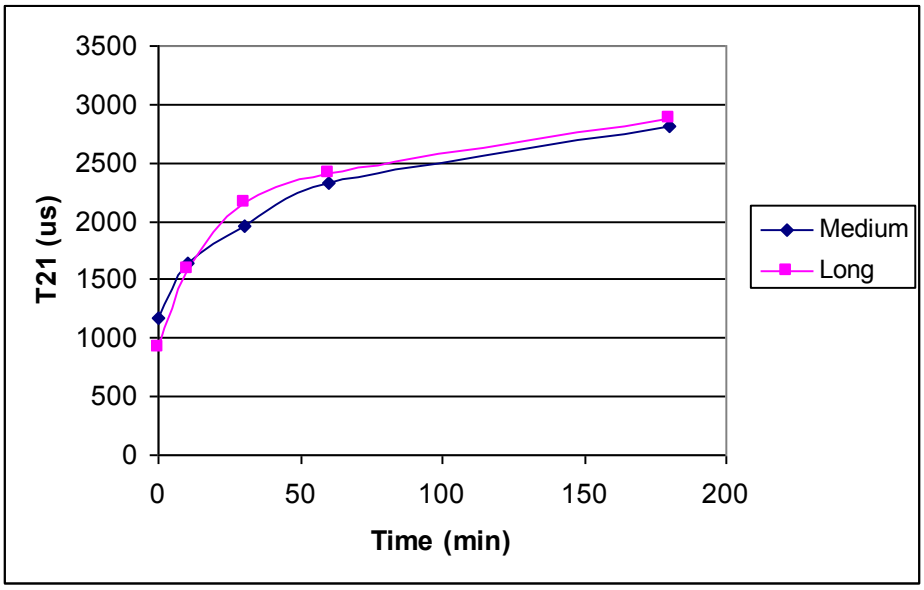

Figure 2.2.4.3. T21 (short T2 component) during soaking

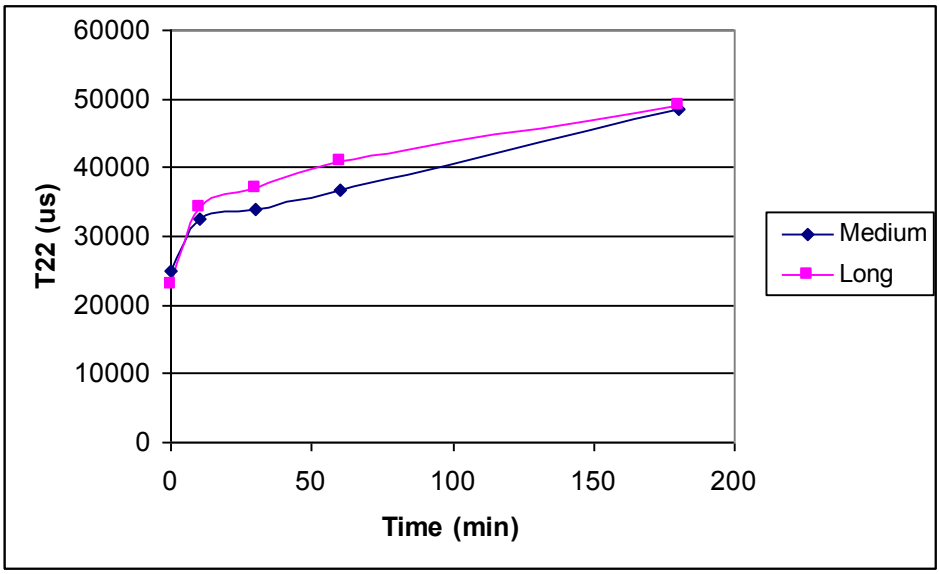

Figure 2.2.4.4. T22 (long T2 component) during soaking

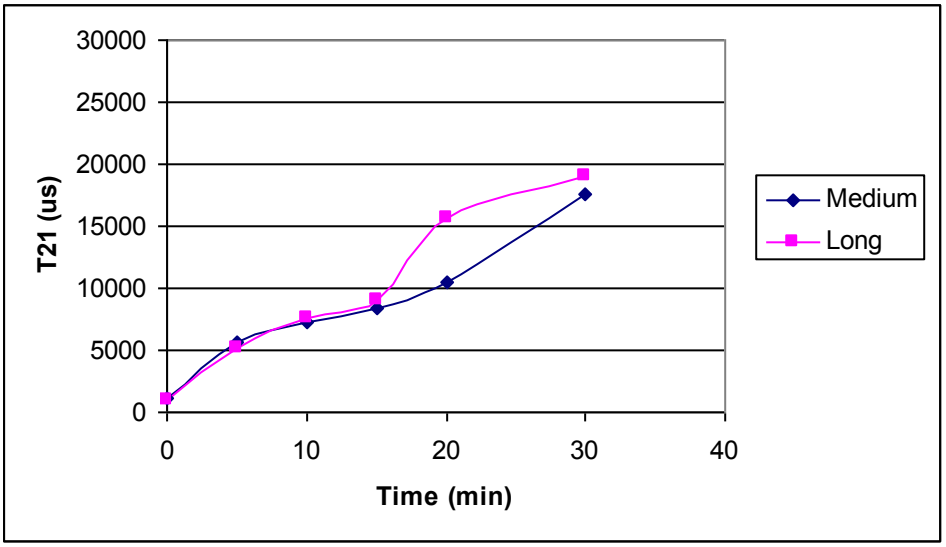

Figure 2.2.4.5. T21 (short T2 component) during cooking

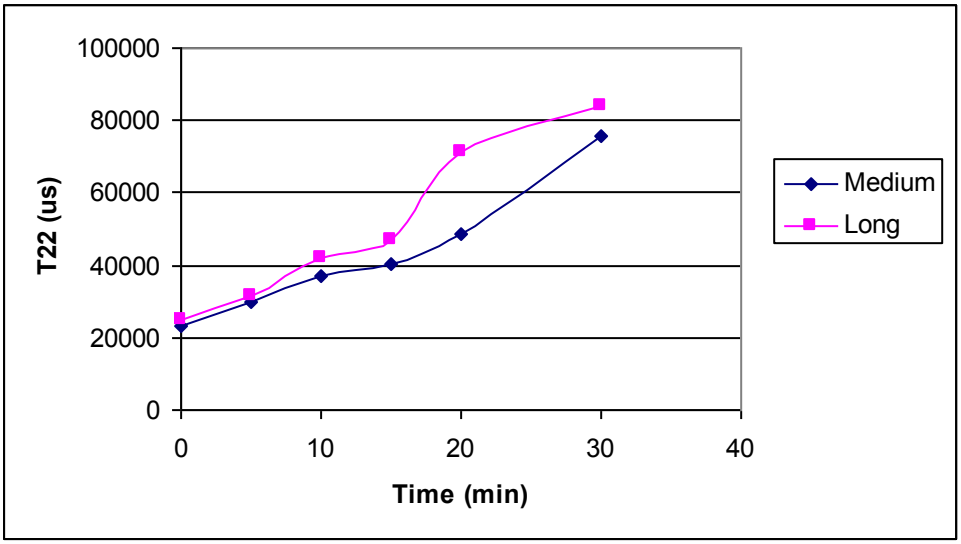

Figure 2.2.4.6. T22 (long T2 component) during cooking

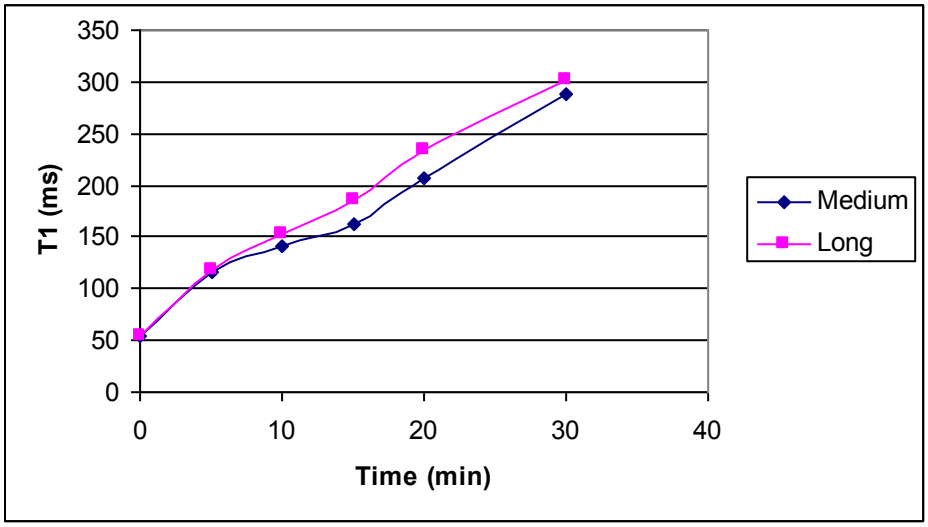

Figure 2.2.4.7. T1 during cooking

Continuous Results

Continuous results are shown in Figures 2.2.4.8.1- 2.2.4.8.12. We can see that the continuous distribution patterns for both grains are quite different. CPMG distributions showed that long grain had an obvious peak shifting to the right of the figure after 15 minutes indicating that more free water appears in the rice after 15 minutes of cooking. But medium grain had similar continuous distribution from 10 minutes to 20 minutes and did not have obvious peak shifting until cooking after 20 minutes. We also found it interesting that the distribution changing pattern of medium grain between 10 and 20 minutes is quite similar to the changing pattern of long grain between 15 and 20 minutes,

which means medium grains take more time than long grains to reach the same cooking state. This actually indicates that medium grain has a slower changing rate than long grain during a certain cooking time interval.

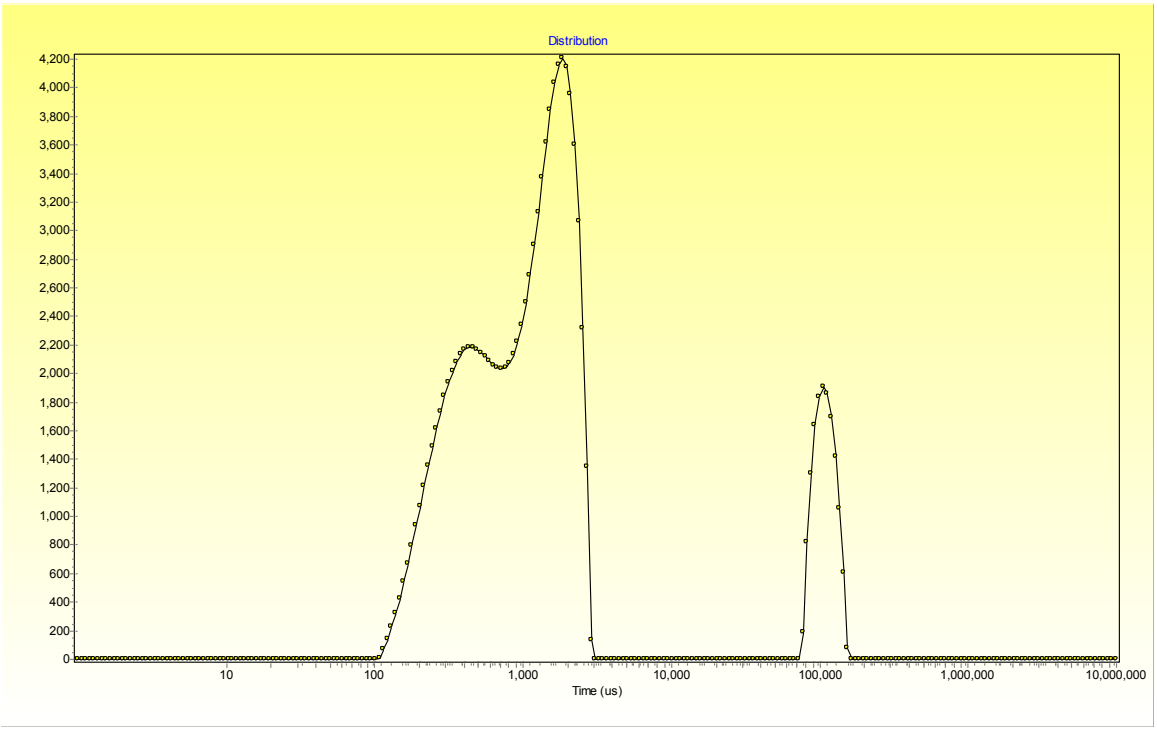

Figures 2.2.4.8.1. Medium grain, CPMG, 0 minute

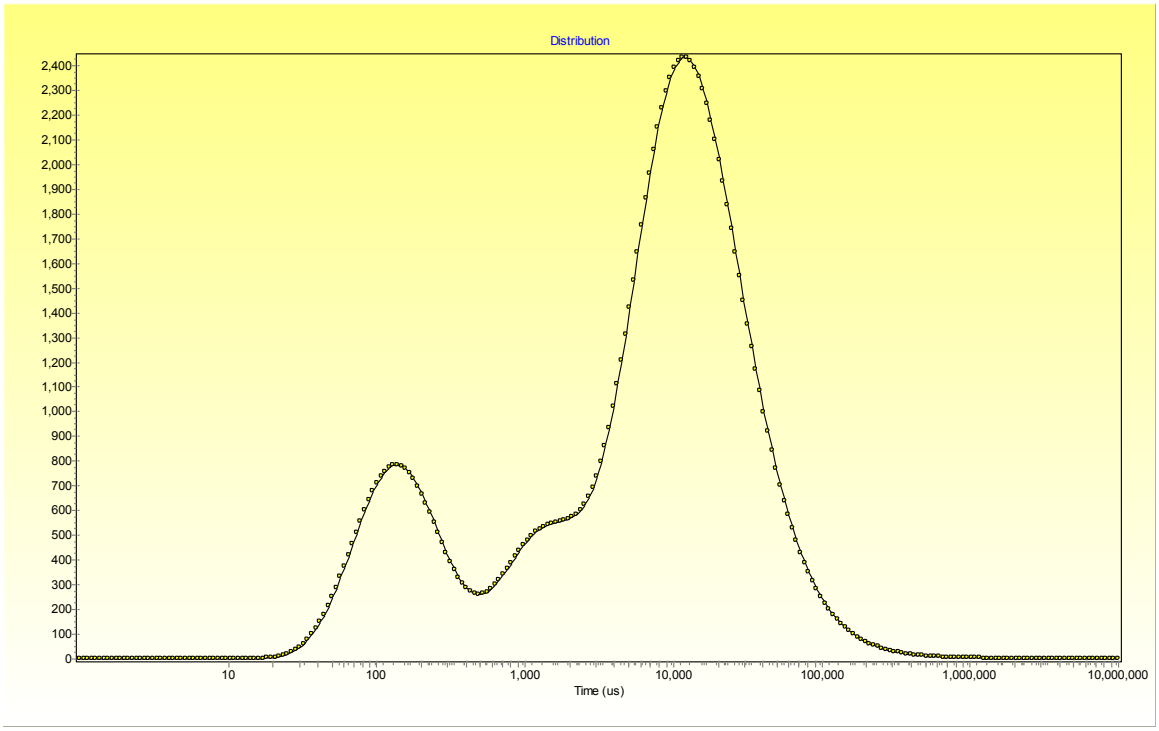

Figures 2.2.4.8.2. Medium grain, CPMG, 5 minute

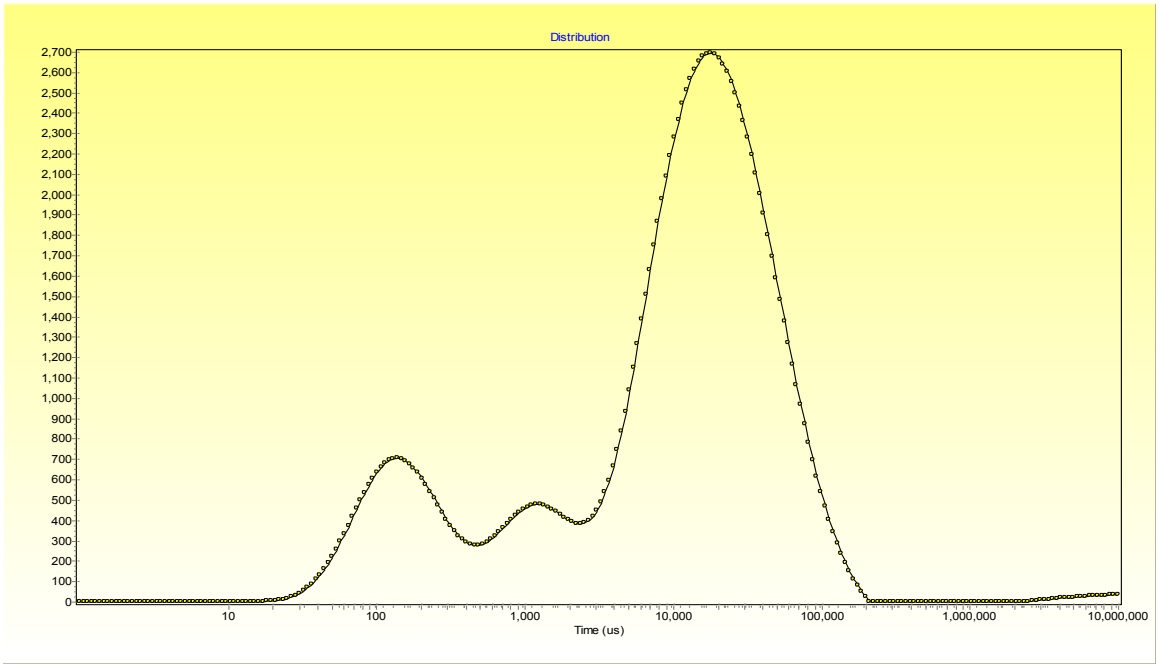

Figures 2.2.4.8.3. Medium grain, CPMG, 10 minute

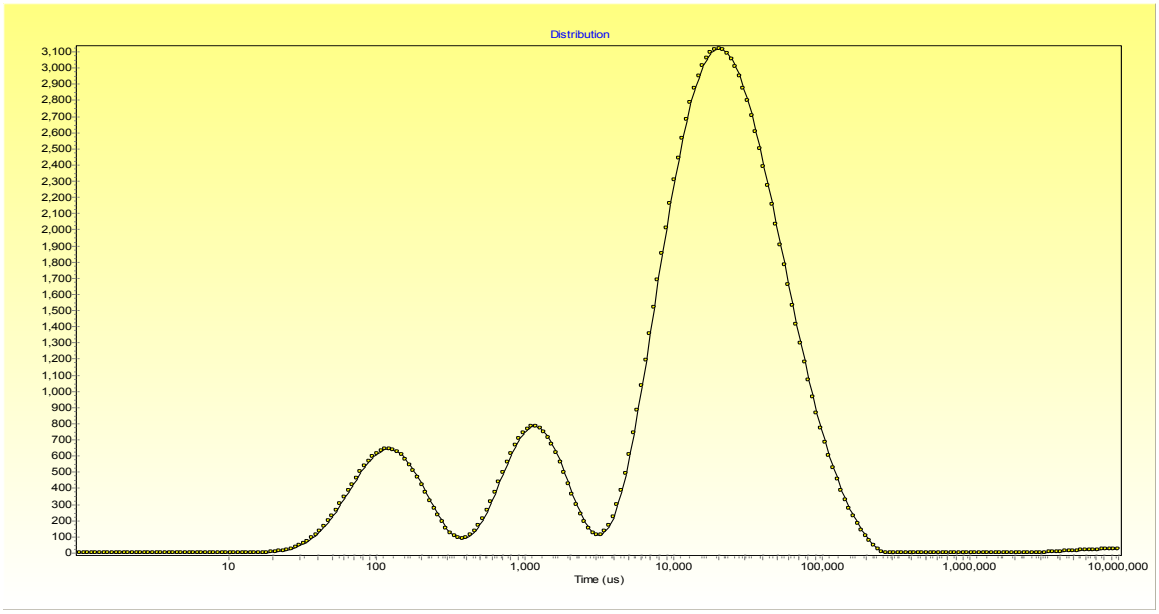

Figures 2.2.4.8.4. Medium grain, CPMG, 15 minute

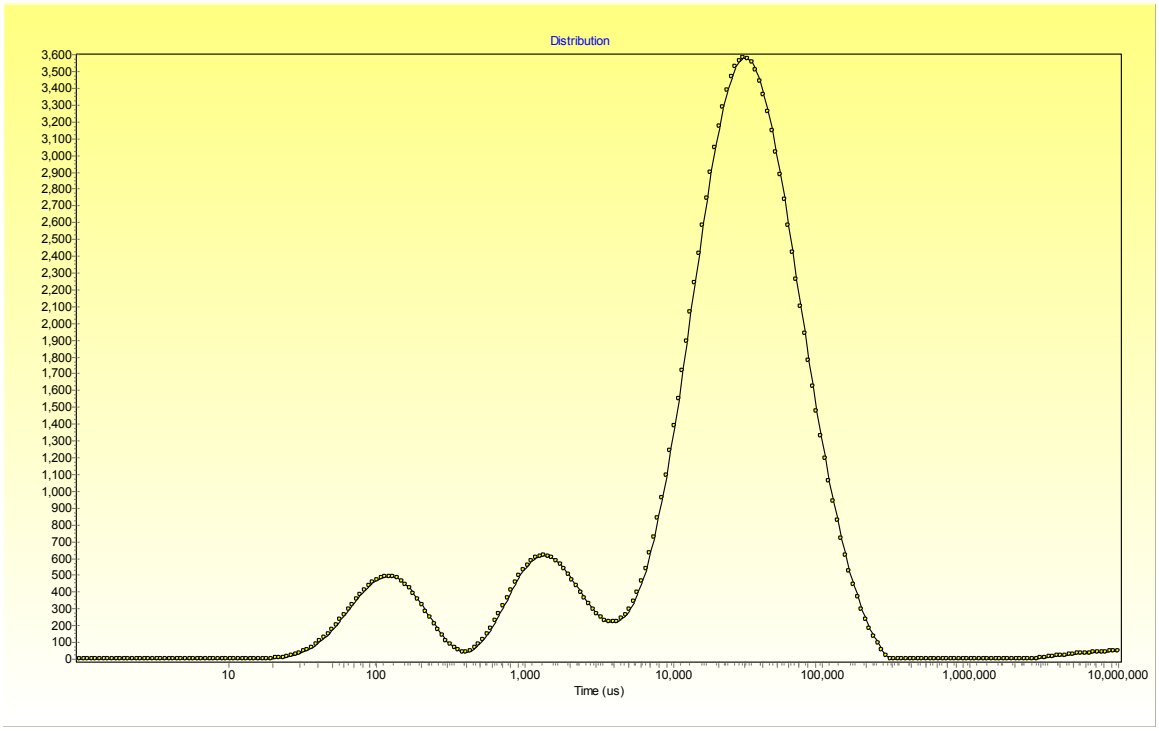

Figures 2.2.4.8.5. Medium grain, CPMG, 20 minute

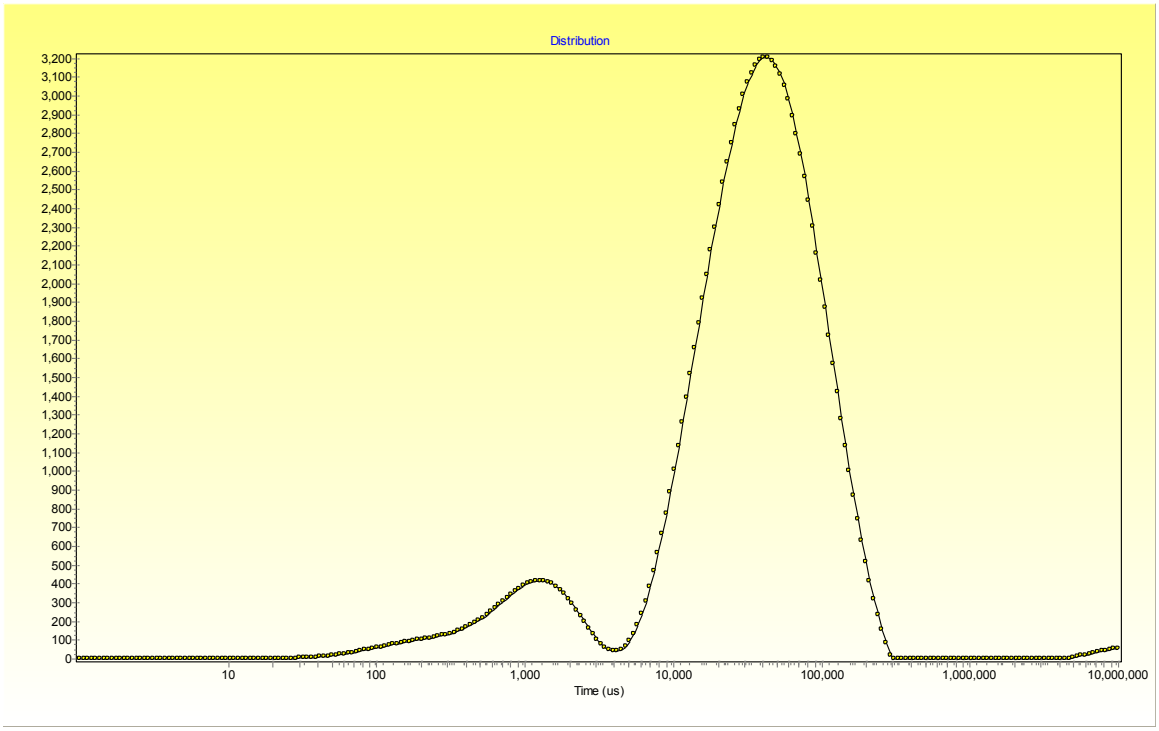

Figures 2.2.4.8.6. Medium grain, CPMG, 30 minute

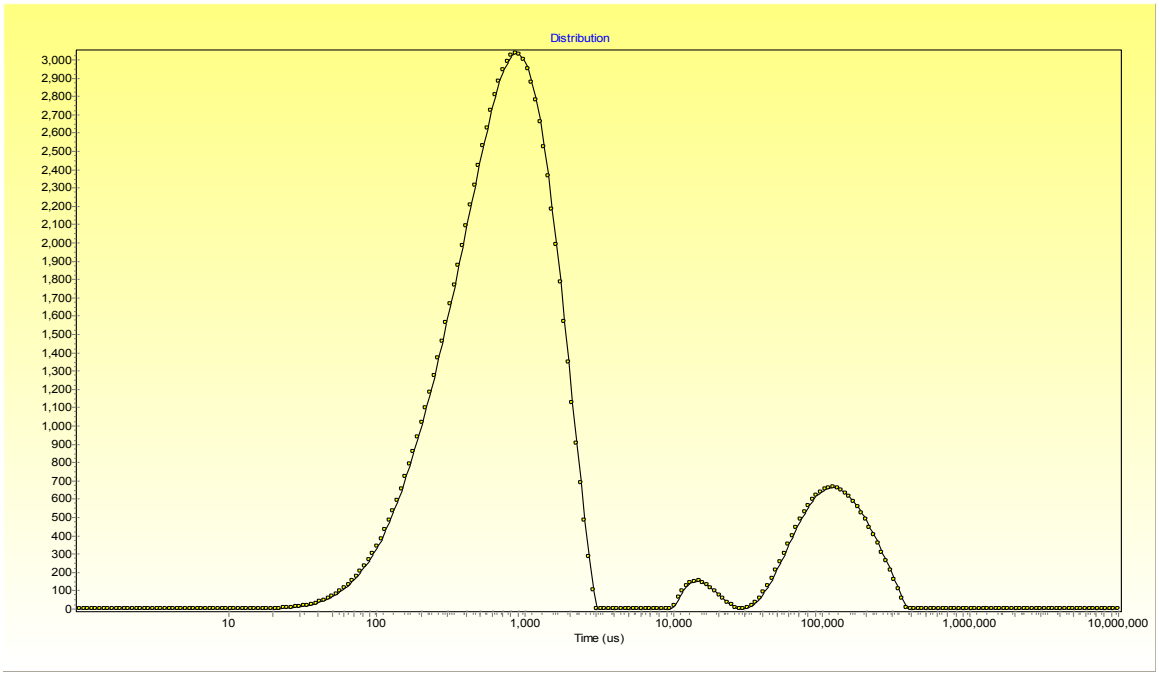

Figures 2.2.4.8.7. Long grain, CPMG, 0 minute

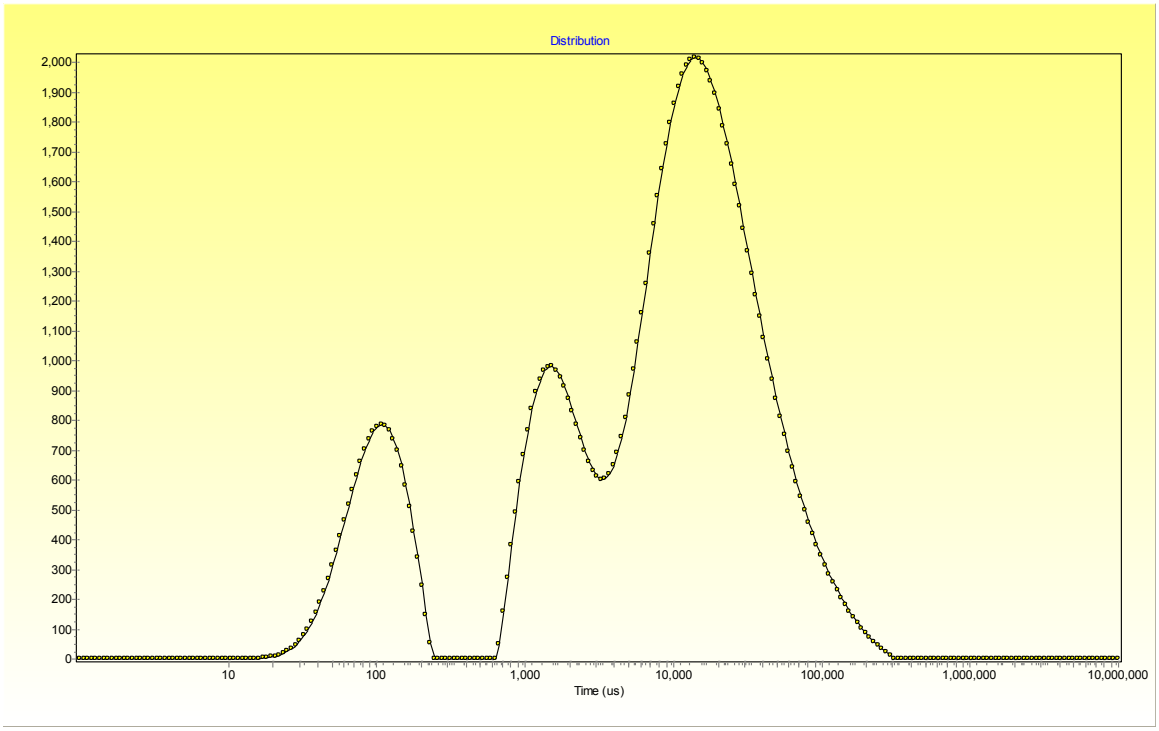

Figures 2.2.4.8.8. Long grain, CPMG, 5 minute

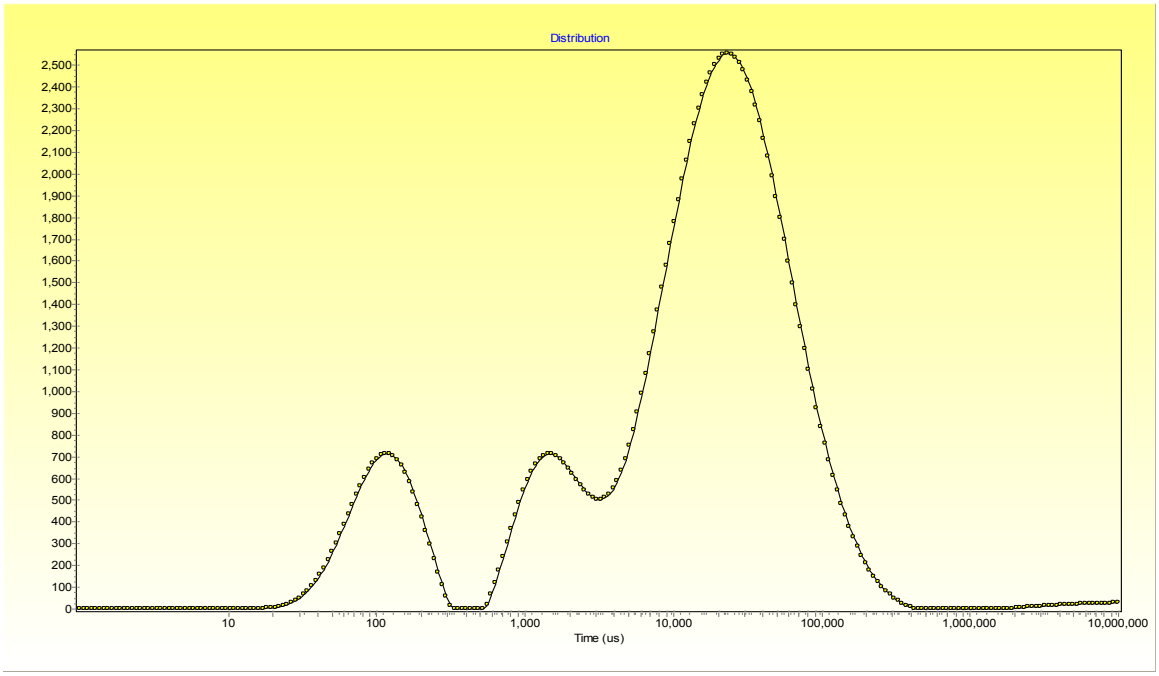

Figures 2.2.4.8.9. Long grain, CPMG, 10 minute

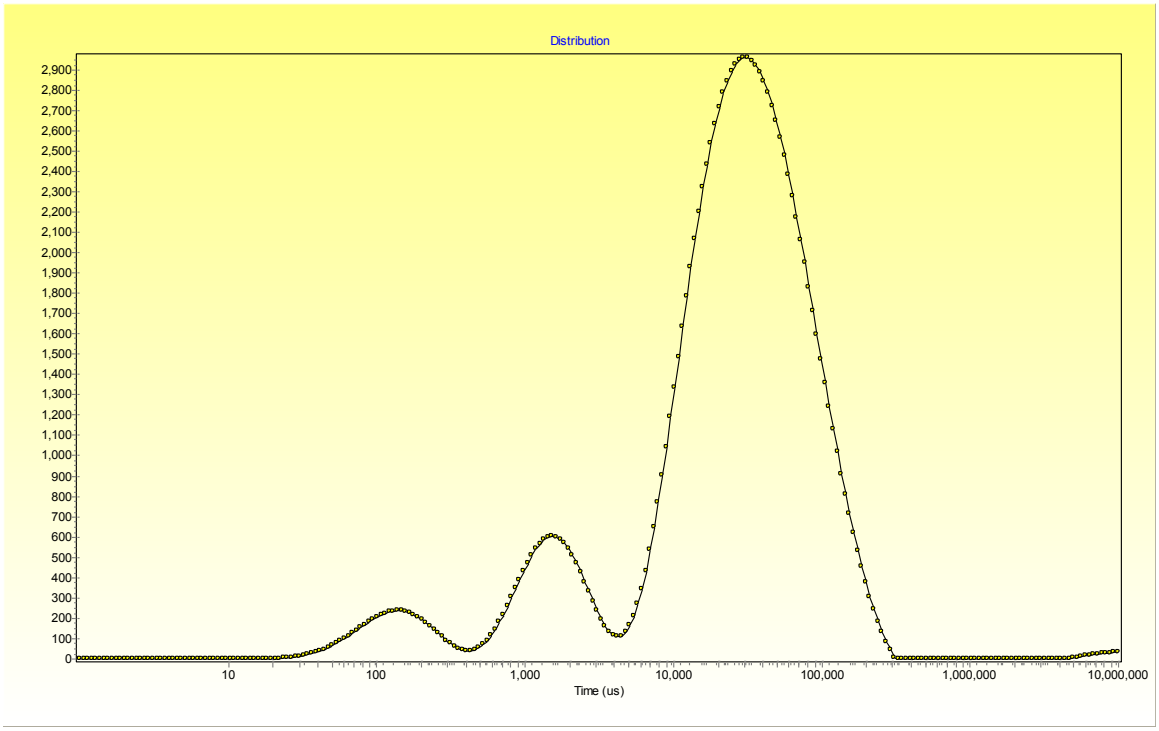

Figures 2.2.4.8.10. Long grain, CPMG, 15 minute

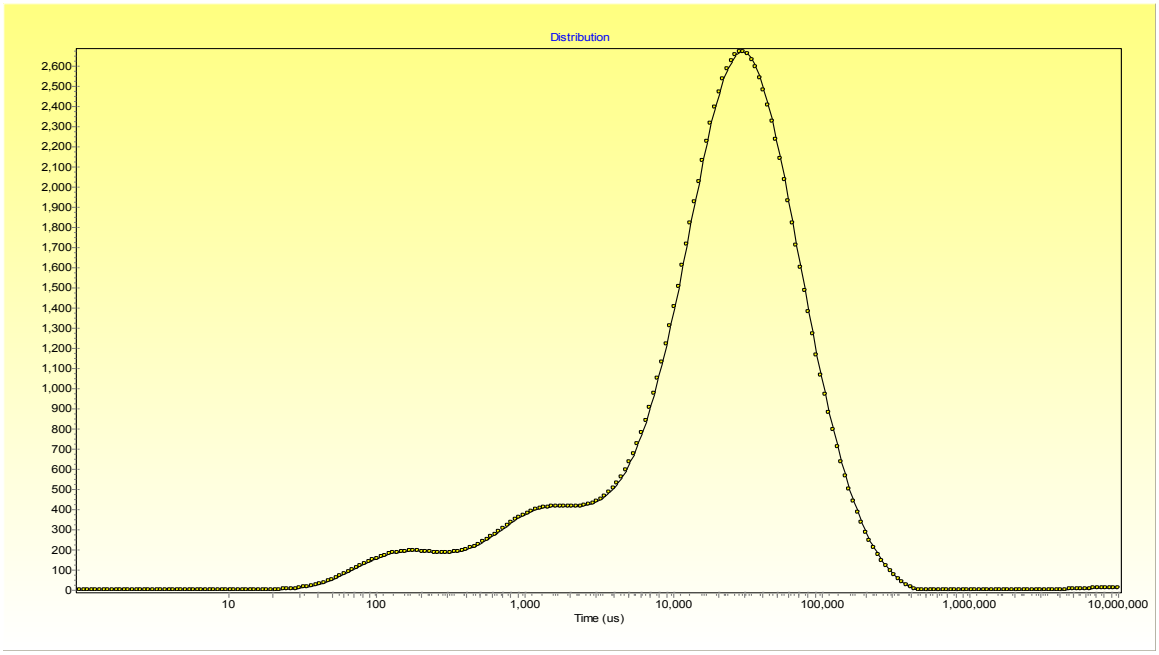

Figures 2.2.4.8.11. Long grain, CPMG, 20 minute

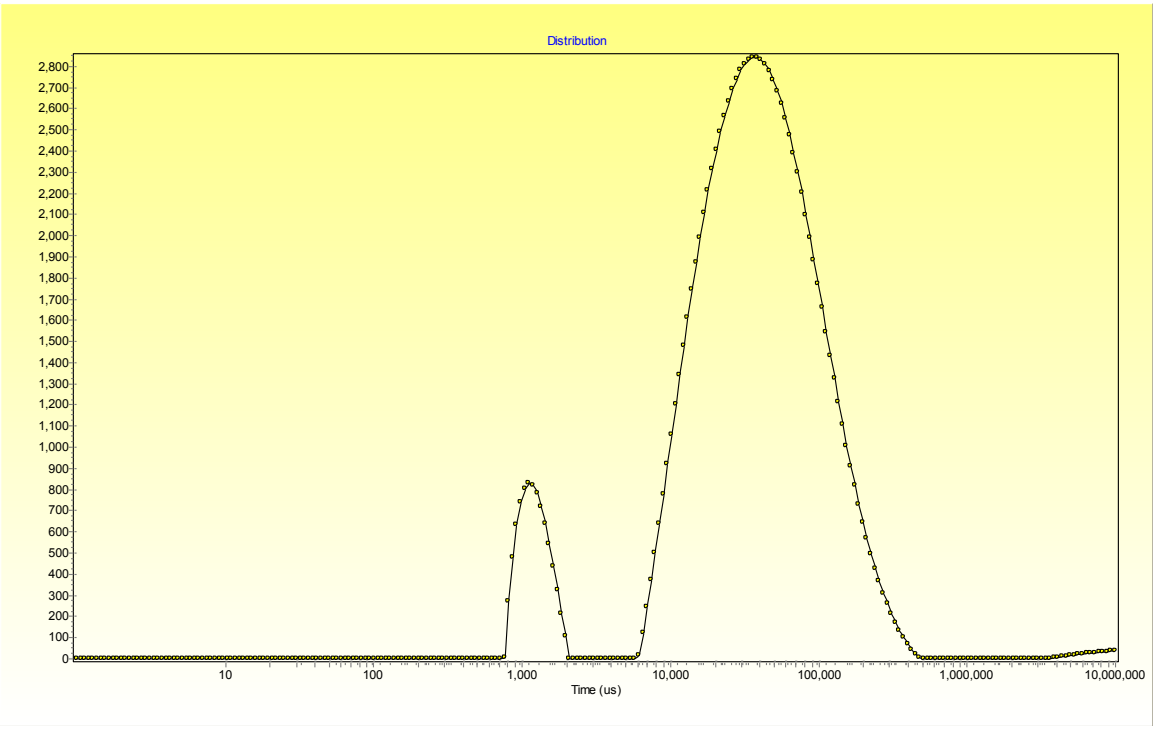

Figures 2.2.4.8.12. Long grain, CPMG, 30 minute

MRI analysis

MRI images are shown in Figures 2.2.4.9 and 2.2.4.10. We can monitor how water moves during the cooking process from these image series. Generally speaking, water migrates into the rice kernel from outside part to inner part. During the first 5 minutes of cooking, there was no big difference in the moisture distribution and we only observed some red spot which showed a little bit stronger signal in the outside area of the rice (red

signal layer). For long grain, after comparing with 10 minutes image with 15 minutes image, we noticed that more free water started to gather from outside area and penetrated into the central area after 10 minutes of cooking. After 20 minutes of cooking, the signal intensity in the inner area of rice kernel was very strong. However, for medium grain, during the first 10 minutes, water did start to move into the inner area, but the whole process was slow and became obvious after 15 minutes of cooking. The signal intensity of medium grain at 20 minutes were lower than signal intensity of long grain, which indicates that medium may not be as fully cooked as long grain after 20 minutes of cooking. Moreover, we can still find the difference in cooking rate by comparing the changing pattern from 10 minutes for long grain with changing pattern from 15 minutes for medium grain.

T2 mapping results are shown in Figures 2.2.4.11 – 2.2.4.14. At 20 minutes cooking time, long grain shows a larger T2 average value and more long T2 components than medium grain, which indicates that there is more free water in long grain than in medium grain. T2 maps and 1D profiles also show that long grain has more free water component in the inner area while medium grain has more free components concentrated in the outside area. These also agree with our discussions above, which suggests that the outside layer of medium grain may have stronger ability than long grain to block water to move inside in order to complete the cooking process. It is highly possible that during the first 10 minutes of cooking, water starts to gather around the outside layer which has an ability to slow down water migration due to thickness property. After 10 minutes, water

movements are different for two types of grains: long grain starts a faster process around 10 minutes while medium grain starts this process after 15 minutes of cooking.

Low intensity High intensity

A series of rice image slices:

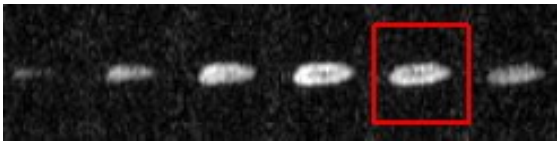

Rice slice image:

3D rice image:

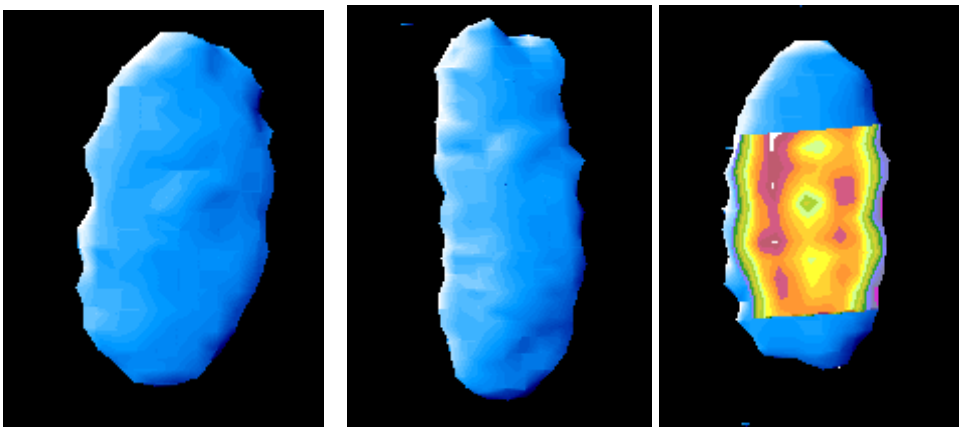

Medium grain **long grain** **cut inside**

Figures 2.2.4.9. 2D and 3D images of medium grain and long grain before cooking

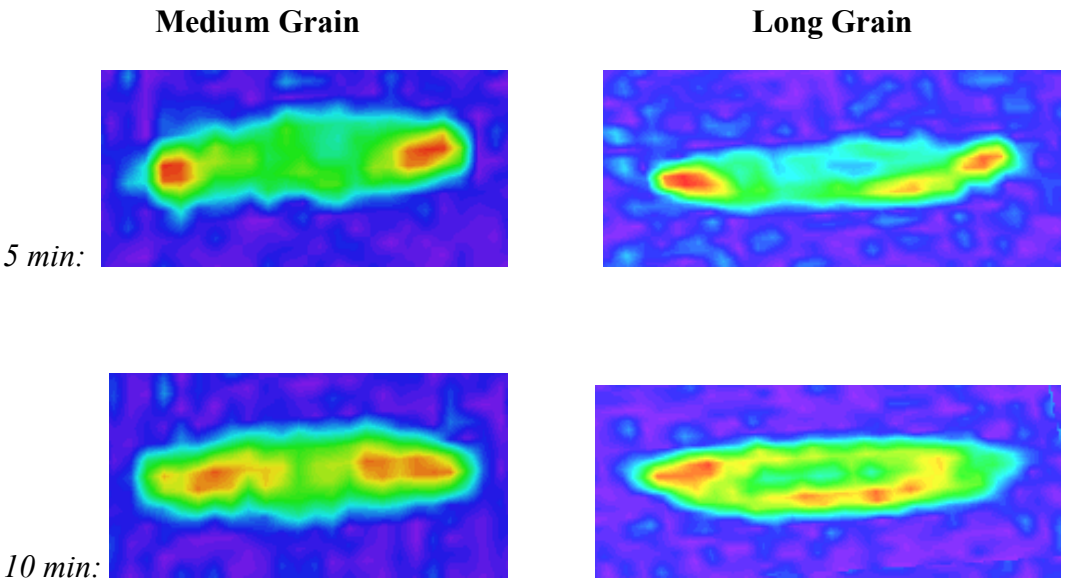

15 min:

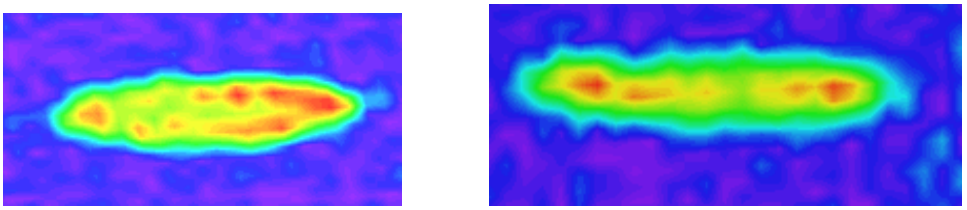

20 min:

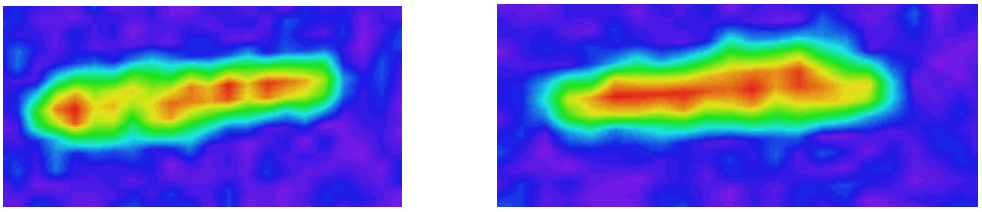

Figures 2.2.4.10. 2D slice images of medium grain and long grain during cooking process

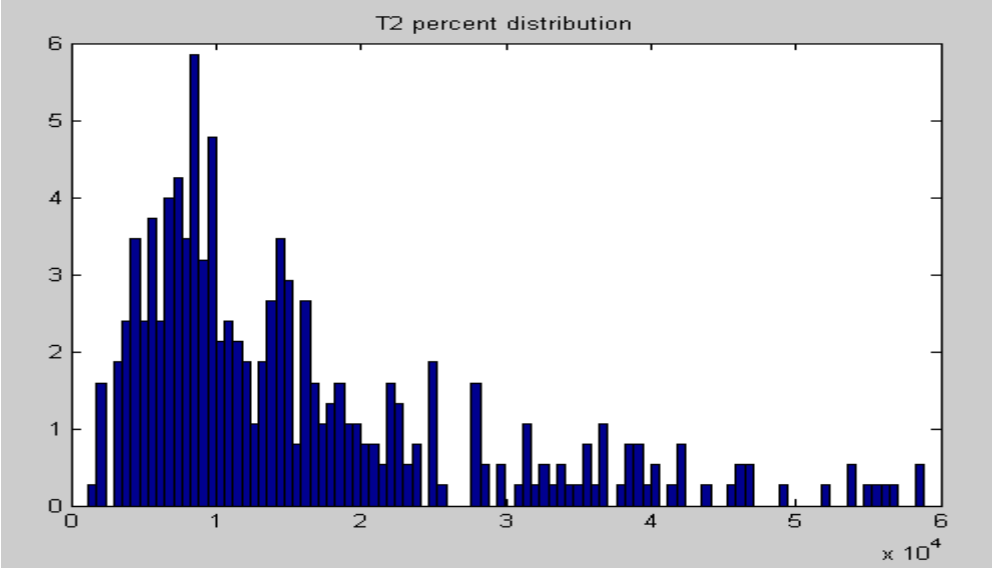

T2mean =1.5790e+004; T2std =1.2061e+004

Figures 2.2.4.11. Histogram of T2 map for medium grain at 20minutes cooking

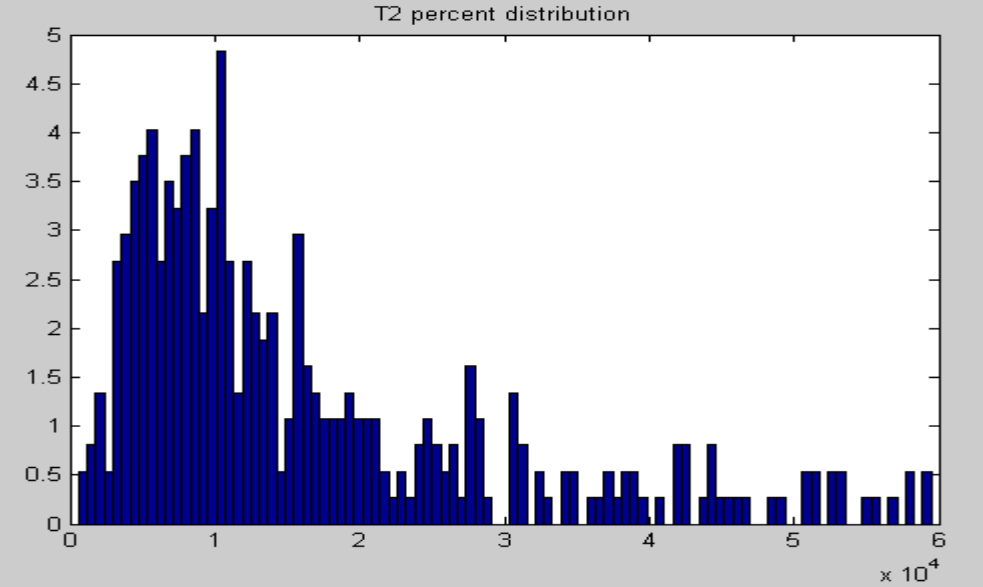

T2mean =1.6270e+004; T2std =1.3302e+004

Figures 2.2.4.12. Histogram of T2 map for long grain at 20minutes cooking

Medium grain Long grain

Figures 2.2.4.13. 2D T2 mapping result for medium and long grain at 20minutes cooking

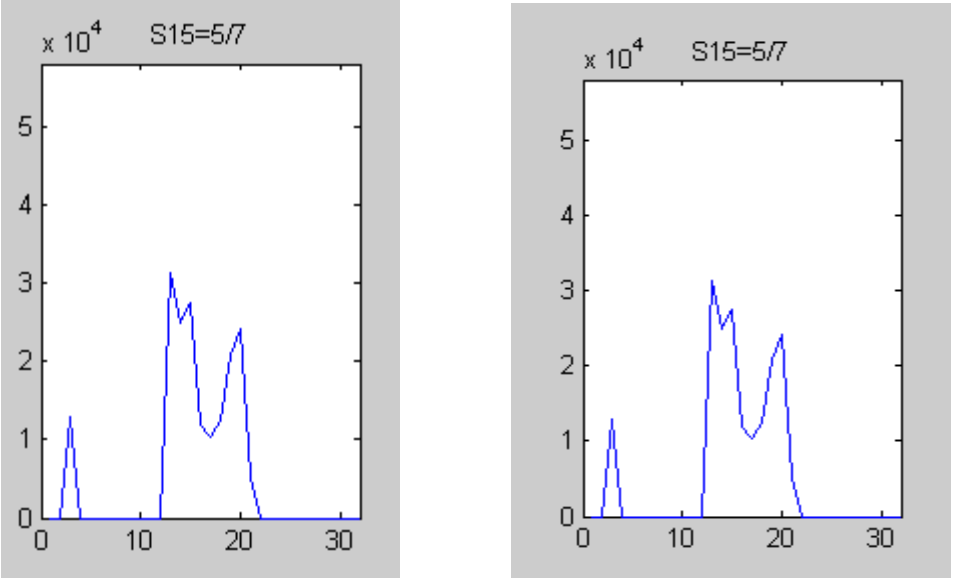

Medium grain Long grain

Figures 2.2.4.14. 1D T2 mapping profiles for medium and long grain at 20minutes cooking

Confocal Microscope

Confocal microscope results are shown in Figures 2.2.4.15. The thickness of the aleurone layer of two types of grain is indeed different, around 30 μm for long grain and around 40 μm for medium grain. It is possible that the thicker aleurone layer of medium grain was responsible for the slower water uptake and longer cooking time compared with the long gain. Thus confirmed previous MRI and NMR analysis.

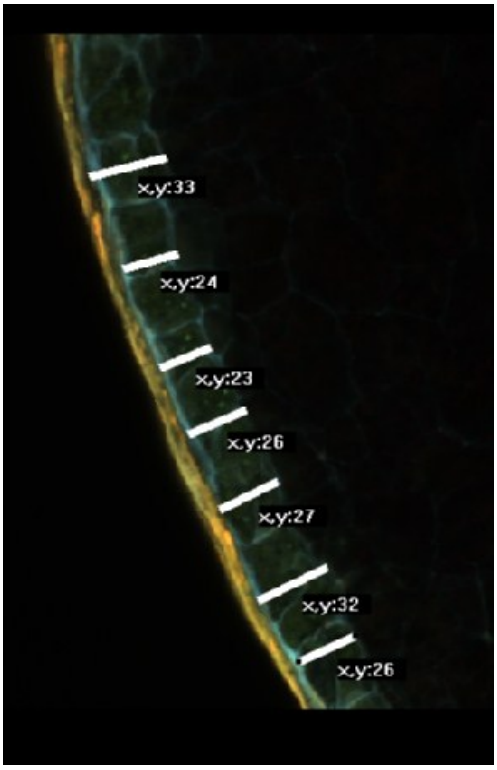

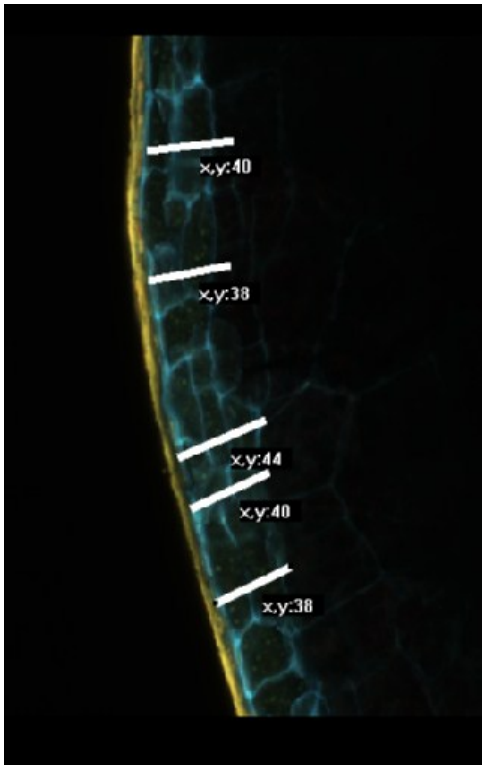

Long grain Medium grain

Figures 2.2.4.15. Confocal microscope images of medium and long grain before cooking process

2.2.5 Relationship between water diffusion in bread and the distance from the interface with cheese

Samples

Four sandwich bread samples containing 0, 5, 10 and 15% lipid contents, respectively, were tested. Each bread sample of 1.5 cm long and 2 cm diameter was interfaced with equal size commercial cheese (Velveeta, Kraft Foods Global, Inc., Glenview, IL). They were assembled snuggly, sealed in a pouch, and stored at

refrigerated temperature for 1 week and 3 weeks. Each binary system was tested at initial time, week 1 and week 3 using MRI instruments. A sample was taken from the refrigerator and kept at room temperature for 1 hour prior to MRI measurement. After the measurement, the sample was returned to the refrigerator. Duplicate measurements for each sample were performed.

Previous research data showed the increase in moisture content in the bread as a function of distance from the interface with the cheese after storage periods of 0-4 weeks. Therefore we need to get T2 measurements as a function of distance from the interface (eg, at 0.5, 1. 1.5, and 2.0 cm distance from the interface), and collect this data at 1 and 3 weeks of storage.
The objective of this study was to apply MRI techniques to study moisture migration/distribution in a binary system consisting of both cheese and bread of various lipid contents during storage. T_2 mapping of the systems was calculated to map out the mobility of water molecules during storage to model the relationship between water diffusion in bread and the distance from the interface with the cheese.

MRI Tests and Data processing

MRI measurements were conducted at 25 °C using a micro-image probe with a bore of 25 mm diameter, which was mounted in a MARAN DRX bench-top NMR

imager with a 21.4 MHz high quality permanent magnet (Resonance Instruments Inc., Witney, UK). MRI 3D images of matrix 32x32x32 were obtained using a 3D spin echo sequence. Each pixel in the images corresponds to an elementary volume of 1x 1 x 1 mm^3 in the sample.

3D images were constructed using IDL 5.6 RI Advanced Image software. MRI data were further processed using a T2-mapping software home-programmed using MatLab 5.6 software. The software were functioned to reconstruct the 3D T2 mapping images, 2D T_2 mapping plots for both single slice and averaging multiple slices, and average T2 mapping 1D profiles, and T_2 mapping histograms. The average T_2 mapping 1D profiles along the direction perpendicular to the interface of bread and cheese is taken as the longitudinal distribution of T_2 for the binary systems.

Results and Discussion

Figures 2.2.5.1 to 2.2.5.4 show the longitudinal distribution of T_2 values for the identical binary systems of sandwich bread and cheese at different storage times. Scale 0 in the figures indicates the interface position where the surfaces of a block of bread and an equal-size of cheese intimately in contact with each other. This scale is also applicable to other similar figures. Figures 2.2.5.1 to 2.2.5.4 indicate that the values of T_2 for cheese are higher than for bread. During three-week storage duration the T_2 values in cheese part decreased a little while those in bread part experienced complicated changes.

At Week 0 or immediately after assembling, the straight lines in Figures 2.2.5.1 to 2.2.5.4 show that the average T_2 values along longitudinal slices for both bread and cheese are uniform. At Week 1 and 3, as shown in Figures 2.2.5.1 to 2.2.5.4, a convex parabola and a line for the curve in the bread part can be elucidated. Cheese has higher moisture content than bread. For the binary systems, the free water in the cheese continually migrated into the bread until an equilibrium arrived. Some of the migrating water may interact with some molecules in the bread, such as starch (or some active sites) and became structural water. Some continued to move after most of the active sites were occupied. The structural water has smaller T_2 values than free water. So, the decrease in T_2 values means the formation of the structural water, and migration of water. This process exhibited the convex parabola pattern for the distribution of the T_2 values. The line segments at the end of bread part resulted from the diffusion of the water present in the bread. Therefore, the concept of the transition point where the parabola and the line meet, may be adopted here, and it indicated the distance of the migration of the water in the bread part from the cheese part (It does not indicate the amount of water that migrates). The transition points in Figures 2.2.5.1 to 2.2.5.4 listed in Table 2.3 indicates some water migrated faster in the bread containing higher lipid.

Table 2.3. Transition points (± 0.1 cm) for T_2 distribution in bread interfaced with cheese

Lipid content in Bread interfaced with cheese	0%	5%	10%	15%
Transition points (cm) at week 1	0.4	0.7	0.7	0.7

Transition points (cm) at week 3	0.9	1.0	1.1	1.2

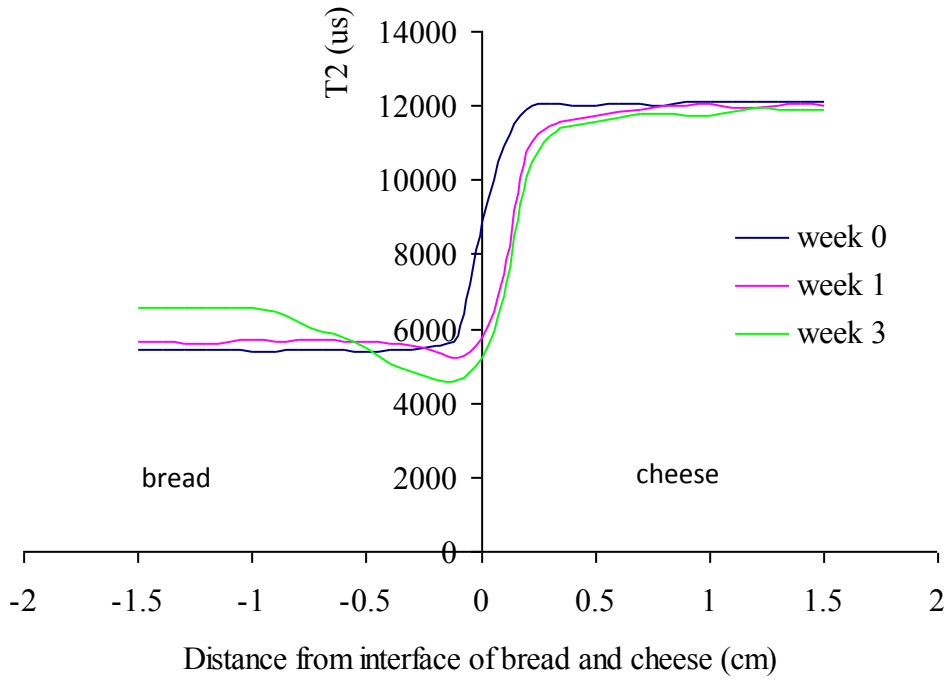

Figure 2.2.5.1. Longitudinal distribution of T2 for a binary system of 0%lipid-bread and cheese

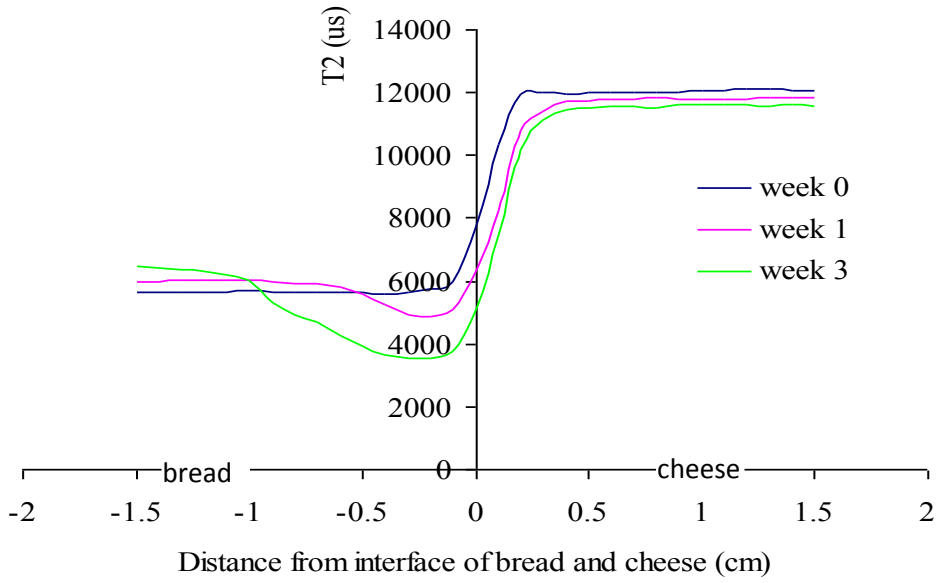

Figure 2.2.5.2. Longitudinal distribution of T2 for a binary system of 5%lipid-bread and cheese

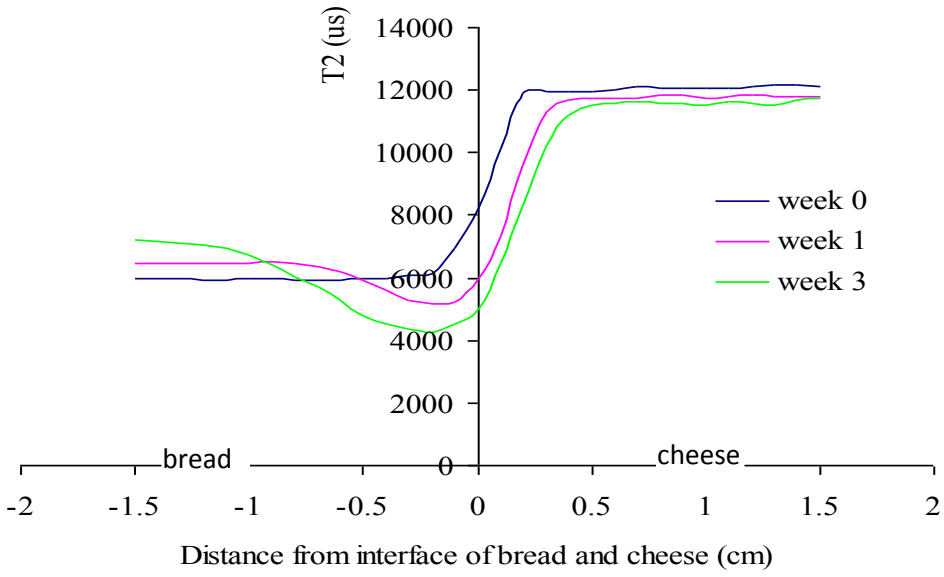

Figure 2.2.5.3. Longitudinal distribution of T2 for a binary system of 10%lipid-

bread and cheese

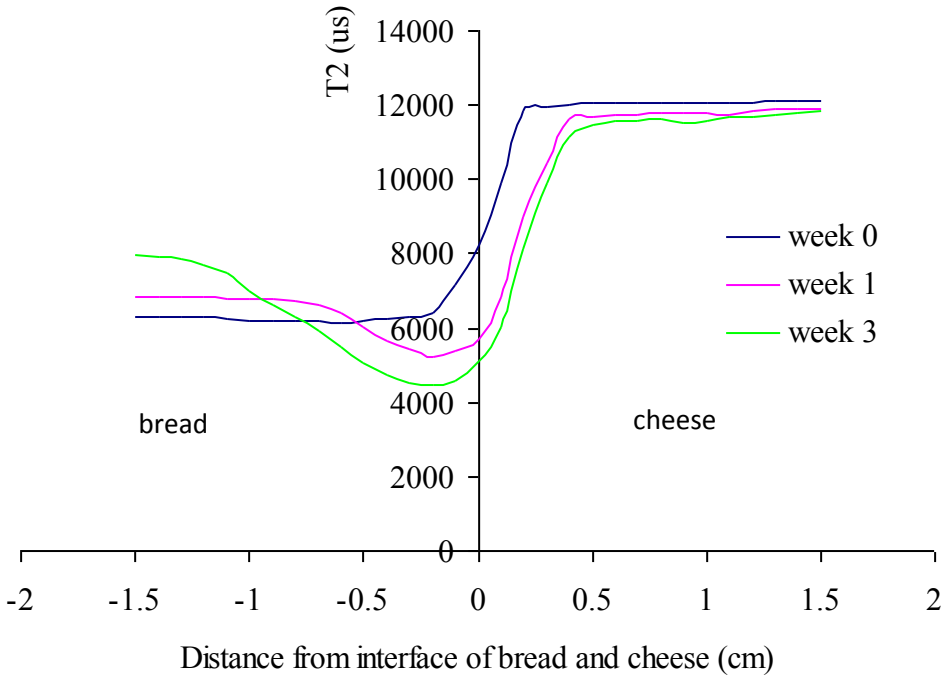

Figure 2.2.5.4. Longitudinal distribution of T2 for a binary system of 15%lipid-bread and cheese

The data in Figures 2.2.5.1 to 2.2.5.4 are rearranged into Figures 2.2.5.5 to 2.2.5.7, which show the longitudinal distribution of T_2 values for several assemblies of various bread samples with cheese at identical storage times. At Week 0 for initial bread samples, Figure 2.2.5.5 shows that the bread with higher lipid contents have slightly higher T_2 values for the flour bread samples. Figures 2.2.5.6 and 2.2.5.7 show that during the three-week storage the T_2 values in bread parts containing higher lipid contents were

higher for the bread of 5, 10 and 15% lipid, while the bread without lipid exhibited different pattern. T_2 values in cheese parts were also observed at different storage times.

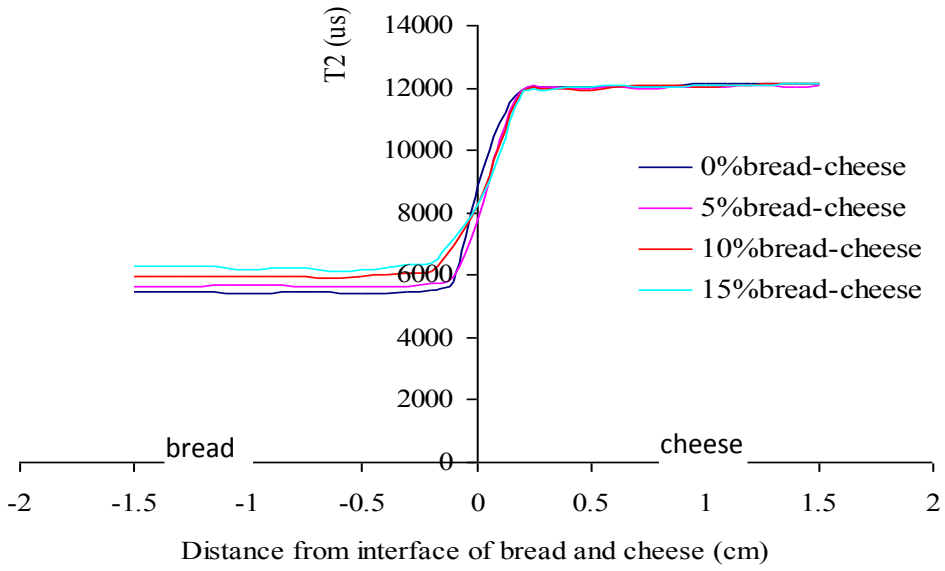

Figure 2.2.5.5. Longitudinal distribution of T2 for a binary system of 15%lipid-bread and cheese. Longitudinal distribution of T2 for binary systems of bread and cheese at week 0

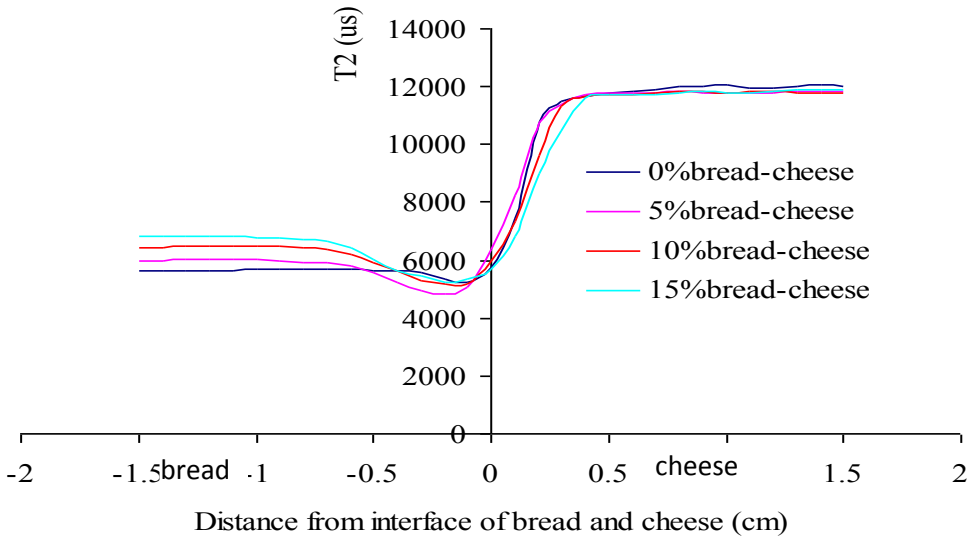

Figure 2.2.5.6. Longitudinal distribution of T2 for binary systems of bread and cheese at week 1

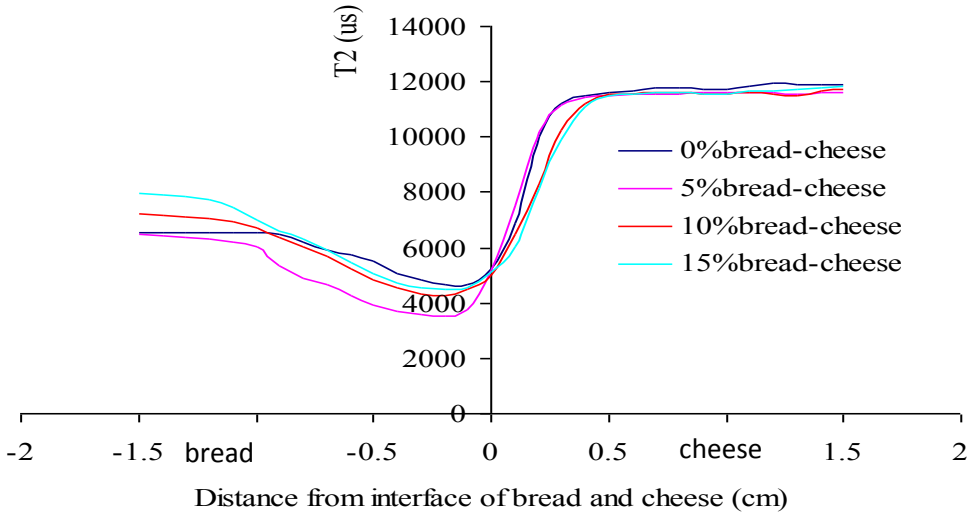

Figure 2.2.5.7. Longitudinal distribution of T2 for binary systems of bread and cheese at week 3

The data in Figures 2.2.5.1 to 2.2.5.4 were used to calculate the differences in the average T_2 values for the identical slices along the direction perpendicular to the interface between Week 1 and 0, and Week 3 and 1. The distributions of the differences are shown in Figures 2.2.5.8 and 2.2.5.9. Figure 2.2.5.8 shows a dramatic negative change in T_2 values between Week 1 and 0 within a – 0.2 to 0.2 cm range around the interface. Figure 2.2.5.9 shows the dramatic change shifted left to around – 0.5 cm and became broad between Week 1 and 3. This dramatic change indicates at the position most of the migrating water became structural water, and the active sites were fully occupied, and less free water was present there.

The formation of the structural water continued to move to the bread parts away from the interface with longer storage time. Figures 2.2.5.8 and 2.2.5.9 also exhibits that the T_2 change around the interface is much larger between Week 1 and 0 than those between Week 3 and 1. The T_2 positive change at the end of the bread parts was far away the interface and increased from Week 1 to Week 3, which indicates the motion of free water present in the bread. The T_2 small negative change in cheese during the 3-week storage appears to remain stable.

Figure 2.2.5.8 shows that during Week 1 the T_2 negative change around the interface increase in the order of the binary systems of 5, 10 and 15% lipid bread, while from Week 1 to Week 3 the converse change trends was observed in Figure 2.2.5.9. This means the systems with higher lipid contents have slow water diffusion.

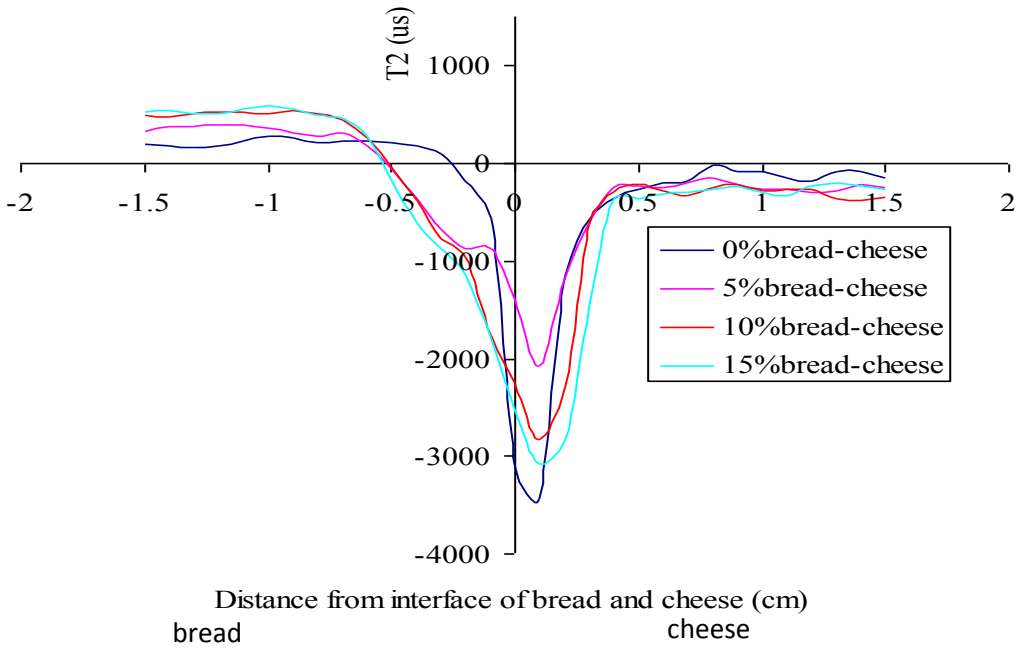

Figure 2.2.5.8. Longitudinal distribution of difference in T2 between Week 1 and 0 for binary systems of bread and cheese

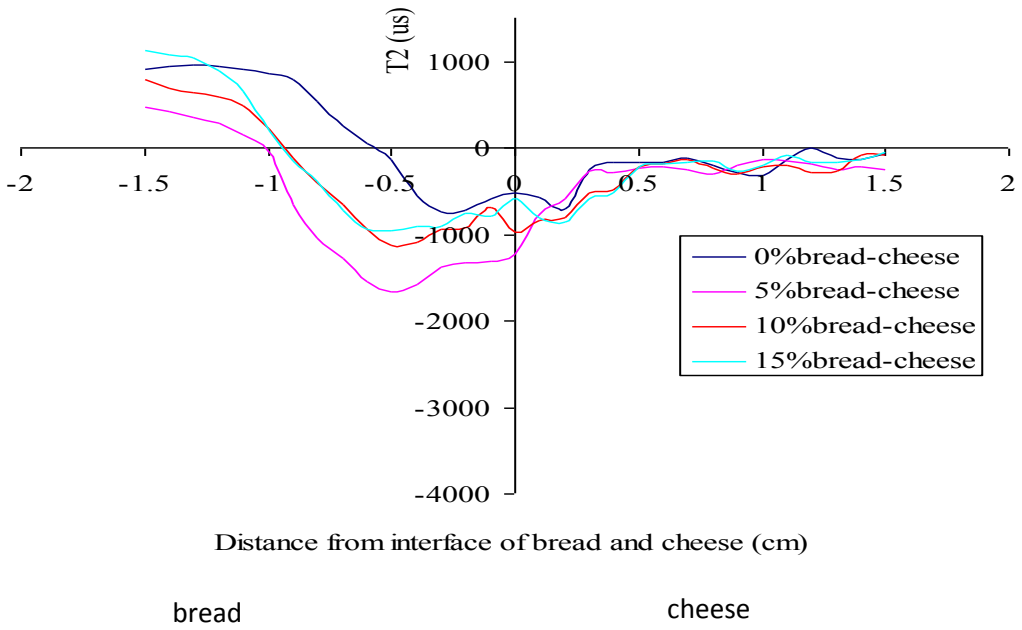

Figure 2.2.5.9. Longitudinal distribution of difference in T2 between Week 3 and 1 for binary systems of bread and cheese

In conclusion, advanced MRI technique can be applied to investigate water diffusion between two phases of bread and cheese. The T_2 mapping or distribution approach can be used to monitor the migration of water from cheese to bread. Based upon the hypothesis of transition point, some water migrated faster in the bread containing higher lipid.

CHAPTER 3 ADATATION OF ADVANCED NMR TECHNIQUES ON DRX2 FOR FOOD AND NON-FOOD APPLICATIONS

Frequent measurements of moisture contents of materials and products are always required in many food processes. Moisture analysis methods have to be able to yield correct results within a time frame set by the process and quality management scheme. Therefore it would be desirable that the methods be performed automatically and possibly allow continuous monitoring of the moisture content of the materials or products during processes and storage. The Karl Fisher titration method is by far the most important and effective direct method of this kind, and is often used for calibration of other indirect techniques. Results from the Karl Fisher method often serve as a reference. However, the Karl Fisher method requires that all water be in contact with the reagents directly to react with them. To achieve this, it is sometimes necessary to take additional steps to liberate all the water in the sample. NMR method can be considered as a method which utilizes the physical characteristics of water molecules in response to physical influence such as electromagnetic radiation. Such method is extremely rapid (within seconds), and often require little sample preparation. Some of them are ideal for on-line processes. Therefore NMR method has decisive advantages compared to other methods.

Protons are the most common “probe” nuclei used in NMR and MRI experiments. The proton density of proton-containing compounds can be quantified by using NMR and

MRI. Because the proton density is proportional to the concentration of the proton-containing compounds, it is possible to quantitatively determine the concentration of these proton-containing compounds via NMR and MRI techniques. The relaxation behavior of a nucleus is influenced by the environment in which it is embedded. A proton in a water molecule relaxes differently from the one in a carbohydrate, a lipid, or a protein molecule. Spin-spin relaxation technique is often used in determination of proton intensity in foods and biological materials. It can be seen that water and carbohydrate or protein protons usually have distinguished $T2$ for most of the foods and biological materials. It is therefore not difficult to differentiate water protons from protons in carbohydrates and proteins. However, lipids can present a serious problem in this technique because the $T2$ of water protons is often not very far away from that of lipid protons. In many cases, it is also necessary to quantify the lipid content while determining the moisture content, giving rise to the need for simultaneous determination of moisture and fat contents (Brosio, et al. 1982; Gambhir and Agarwala 1985; Mitchekk, et al. 1991).

One simple and practical approach is to relate the amplitude or integral of the FID curve to the amount of water in the sample. Since the amplitude and integral are proportional to the proton density, they can be used to determine water content if only water varies in the sample. This method requires a calibration curve or equation, which is a linear plot of amplitude or integral of the FID curve against moisture content. To determine the moisture content of an unknown sample, the amplitude or integral is

measured from the FID curve, and translated into moisture content using the linear calibration curve or equation.

Water content has been a universal parameter in relation to biological, chemical and physiochemical reactions, apparently because of its straightforward meaning and ease of determination. However, water exists in different states in bioploymers such as foods and biological materials. It is thought that water molecules in different states function differently. Therefore it appears that it is helpful to quantify the amount of each fraction of water in a certain state or of a certain mobility, and analyze the relationship between the fractions of water and the chemical or physical phenomena of interest. NMR is such a technique that is capable of differentiating among water molecules of different mobility (Fullerton and Cameron 1988). In addition to this capability, NMR, unlike other methods for moisture content determination, is a nondestructive and fast technique.

Both diffusion of water and diffusion of solutes in water are important phenomena, which are part of the metabolic activities of biological materials, and occur during the processing and storage of food products. Diffusion of water and diffusion of solutes through water play an important role in creating favorable conditions for reactants to physically come together, allowing a particular reaction to occur. Many chemical and enzymatic reactions are considered diffusion-controlled. Many food processing techniques involve removal or absorption of water. Undesirable migration of water in foods and drugs during storage may cause serious shelf life problems. Understanding how water moves during these processes is viable to the design and control of these

processes. NMR techniques may be used to demonstrate the relationships between moisture migration and the mobility of water. The combination of these two techniques will permit more accurate mathematical models for water migration to be established and instrumentally validated.

The **objective** of this NMR work is to develop techniques for the evaluation of properties of water in foods of low moisture contents. In this part of the study, three pulse sequences, namely FID (free induction decay), CPMG (Carr-Purcell-Meiboom-Gill), and INVREC (Inverse recovery) were adapted on the DRX2 large horizontal bore MRI system and validated using model foods. The application of these sequences in the studies of several food systems is then demonstrated.

3.1. NMR Techniques Development and Validation

3.1.1. Pulse sequence development

Three commonly used pulse sequences, namely FID (free induction decay), CPMG (Carr, Purcell, Meiboom, and Gill), INVREC (inversion recovery) were installed and customized on the Maran DRX2 low field MRI system described in 2.1.1. The sequences are illustrated in Figures 3.1.1a-c. FID and CPMG are for analysis of spin-spin relaxation times (T2) and INVERC for analysis of spin-lattice relaxation time (T1). All the parameters were tuned to provide desirable signal to noise ratio.

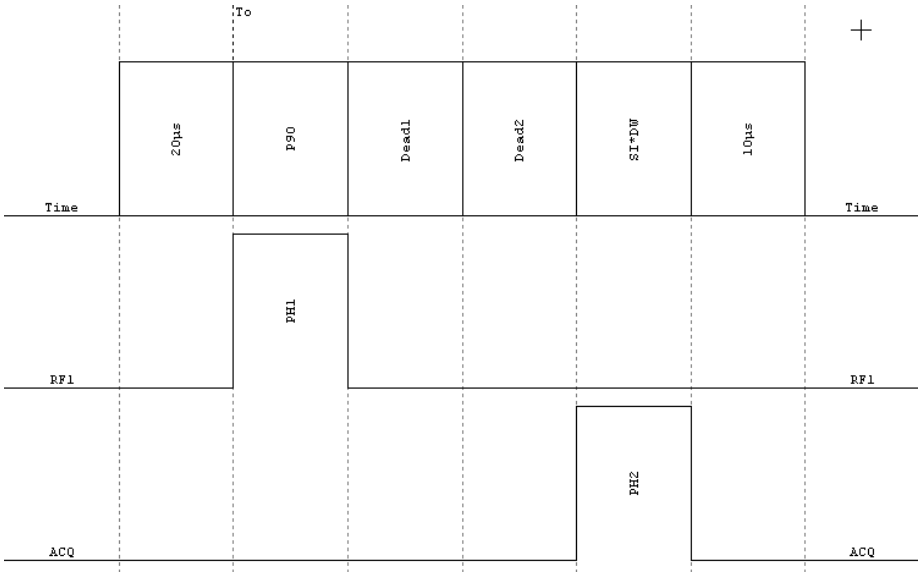

Figure 3.1.1a. FID sequence diagram

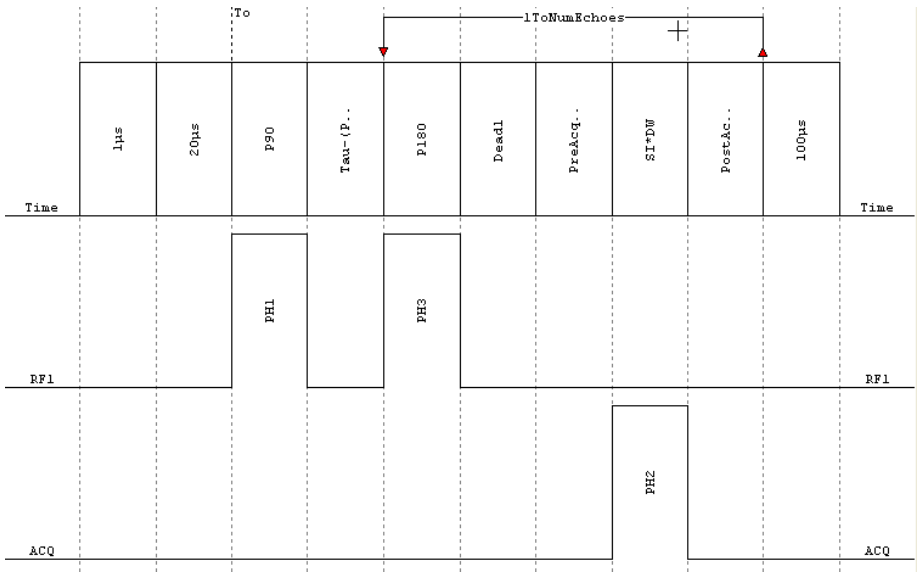

Figure 3.1.1b. CPMG sequence diagram

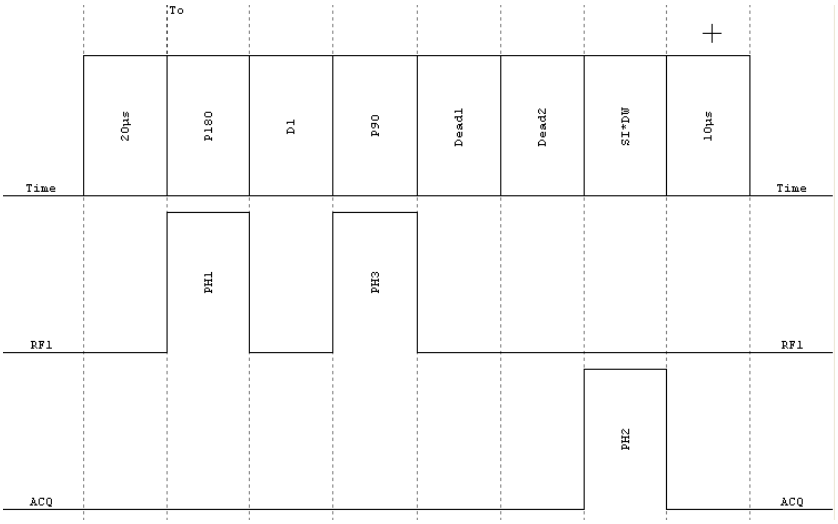

Figure 3.1.1c. INVREC sequence diagram

3.1.2. Validation of moisture content measurement technique

Flour dough samples with different moisture contents (Table 3.1) were prepared to establish the calibration curve. A test flour dough sample with 35 g water/100g dough.

Table 3.1. Sample specifications

Flour dough Samples	Moisture content (g water/100g dough)

F-1	20
F-2	30
F-3	40
F-4	50
Test	35

We analyzed the four calibration samples using FID sequence and obtained the amplitudes. The plot of FID amplitudes and FID integral were plotted against moisture content to give the calibration curves shown in Figure 3.1.1d. and 3.1.1e. We then analyzed the test sample (35g water/100g dough) using the same sequence and parameters, and checked the moisture content against the calibration curves. from the FID amplitude based calibration curve gave 32g water/100g dough while the FID integral based calibration curve gave 31g water/100g dough. Therefore, the FID technique provides a good estimation of moisture content of the flour dough.

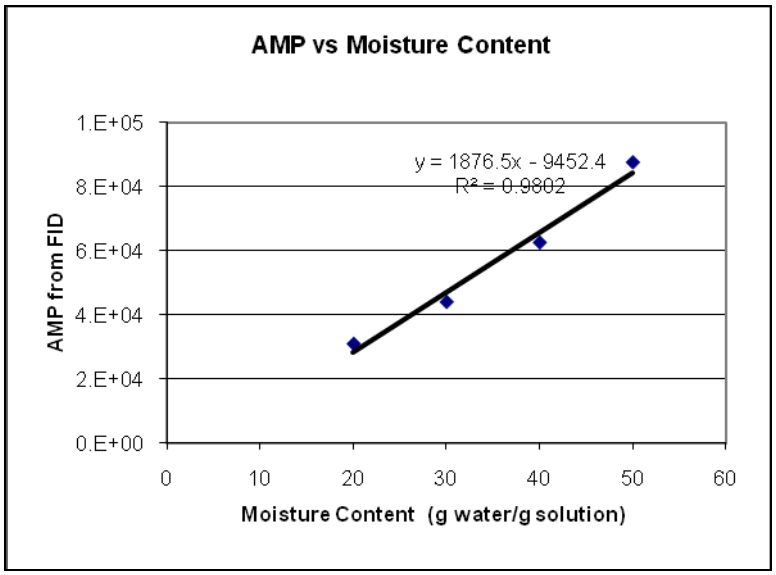

Figure 3.1.1d. Calibration curve of FID amplitude value vs. moisture content

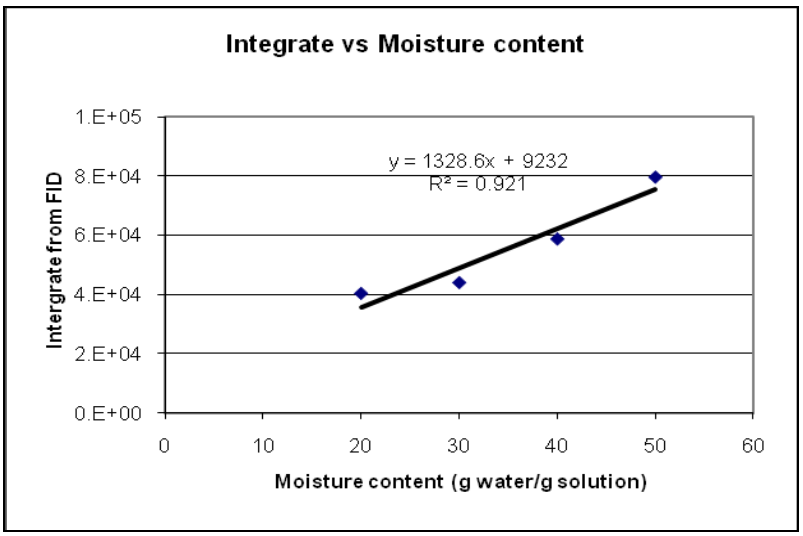

Figure 3.1.1e. Calibration curve of FID integrate value vs. moisture content.

3.1.3. Validation of relaxation time distribution analysis techniques

In addition to the four flour dough samples used above, glucose solution samples with different moisture contents (40%, 45% and 50%) were also prepared. The dough samples and glucose samples were analyzed with the adapted FID, CPMG, INVREC pulse sequences. The data obtained from the NMR experiments were processed using single component model, multi-component discrete model, and continuous distribution model to obtain T2*, T2 and T1 parameters. T2* characterizes the relaxation in an inhomogeneous magnetic field. FID curves were fitted using a single-component exponential function as follows:

$$S(t) = A\exp(-t/T_2^*) \tag{3.1}$$

where S is the NMR signal intensity at signal decay time t, A is the amplitude, and T_2* is the transverse relaxation time constant of protons in the sample. CPMG curves were fitted using a two-component exponential function as follows:

$$S(t) = A_{21}\exp(-t/T_{21}) + A_{22}\exp(-t/T_{22}) \tag{3.2}$$

where S is the NMR signal intensity at signal decay time t, A_{21} and A_{22} are the amplitudes, T_{21} is the short component of the transverse relaxation time constant of protons in the sample and T_{22} is the long component of transverse relaxation time constant of protons in the sample. Inverse-recovery curves were fitted using:

$$S(t) = A(1 - 2e^{-\frac{t}{T1}}) \quad (3.3)$$

where S is the NMR signal intensity at signal decay time t, A is the amplitude, and T_1 is the longitudinal relaxation time constants of protons in the sample. A continuous fitting model was also used to analyze the continuous distribution of relaxation time parameters.

Figure 3.2.1a-d showed the results from calculation from Equation 3.1 and 3.2. Figure 3.2.2a-b showed the results from calculation from Equation 3.3. From these figures (Figures 3.2.1- 3.2.2), we noticed that water content was closely related to NMR parameter distributions in this low magnetic field. And such relationship is very clear. As moisture content increases, color bars shift to the right side of the figures (Figures 3.2.1a-d) for discrete figures while color peaks also shift to the right side of the figures (Figures 3.2.2a-b) for continuous figures. In other words, larger water content always leads to a higher T2 values which can be related to higher water mobility.

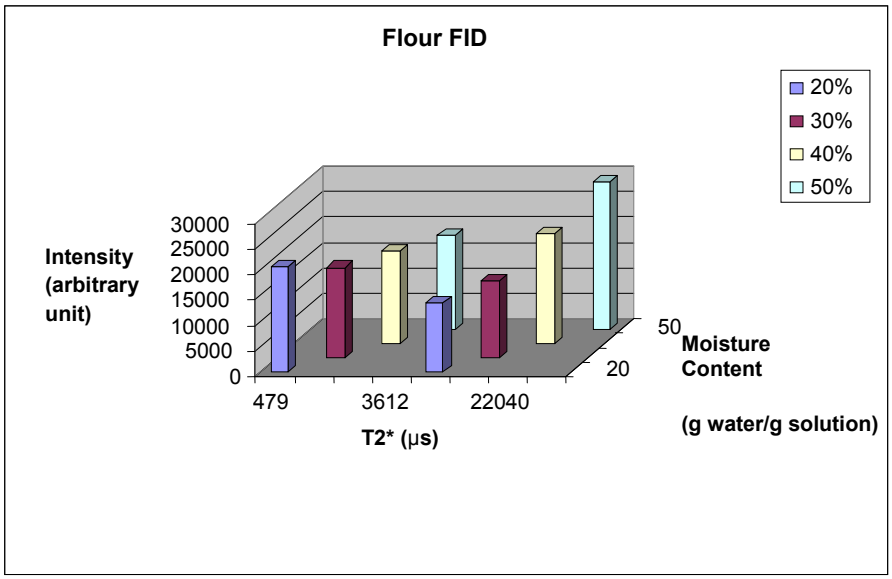

Figure 3.2.1a. T2* distribution for flour with different moisture contents.

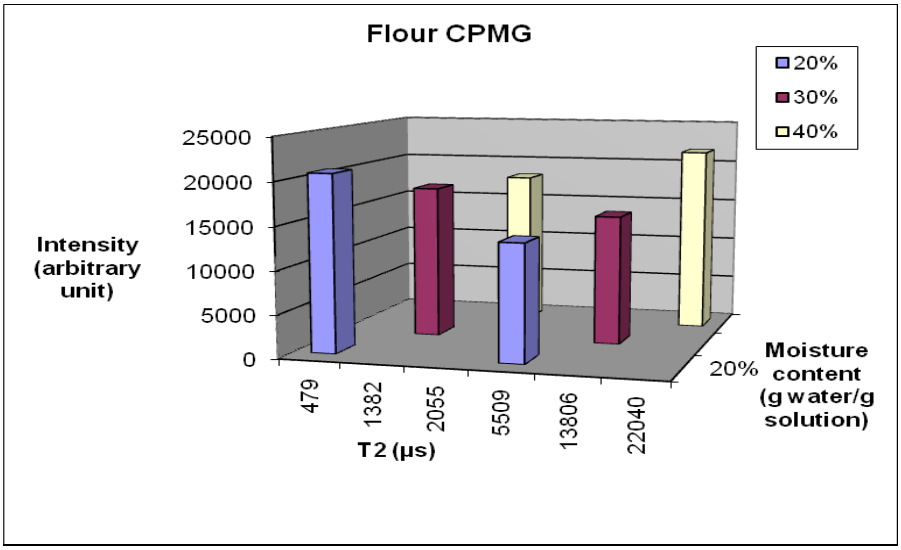

Figure 3.2.1b. T2 distribution for flour with different moisture contents.

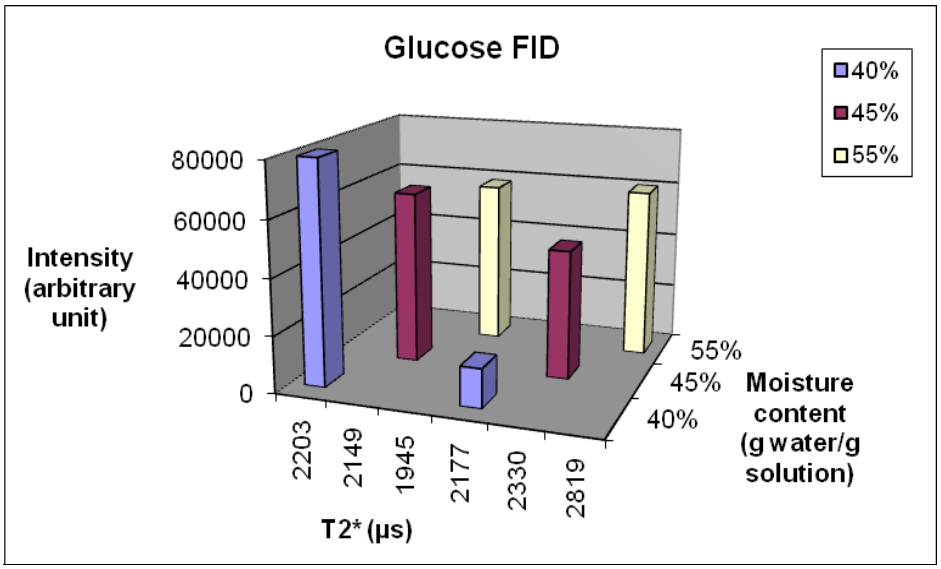

Figure 3.2.1c. T2* distribution for glucose with different moisture contents.

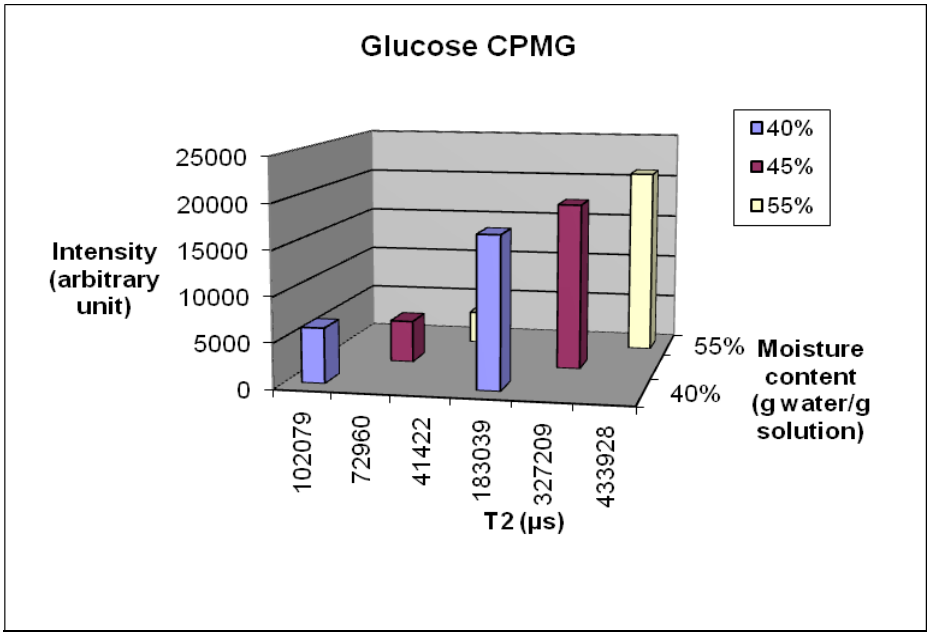

Figure 3.2.1d. T2 distribution for glucose with different moisture contents.

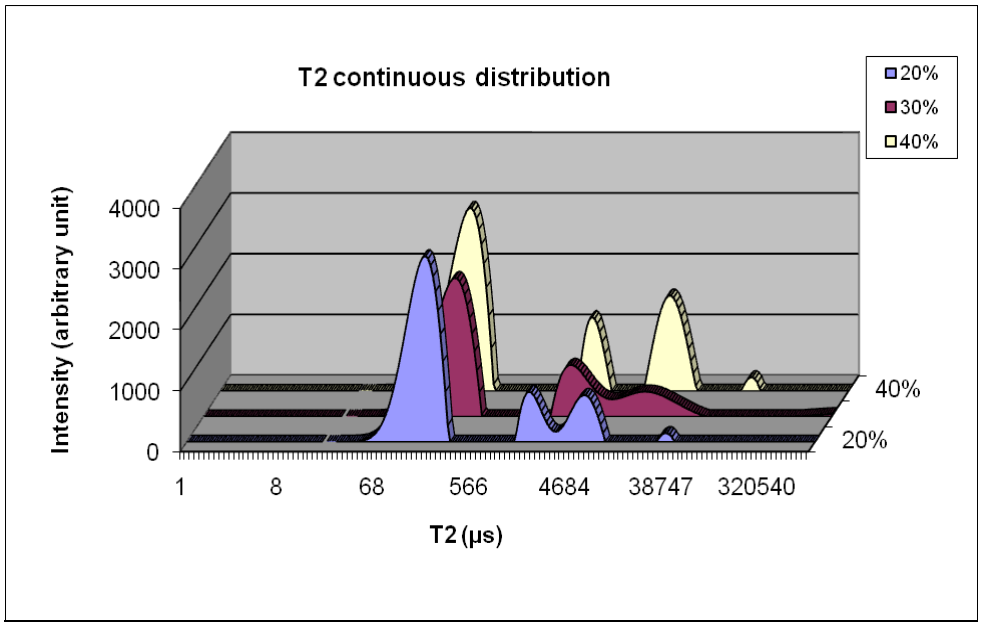

Figure 3.2.2a. T2 continuous distribution for flour with different moisture contents.

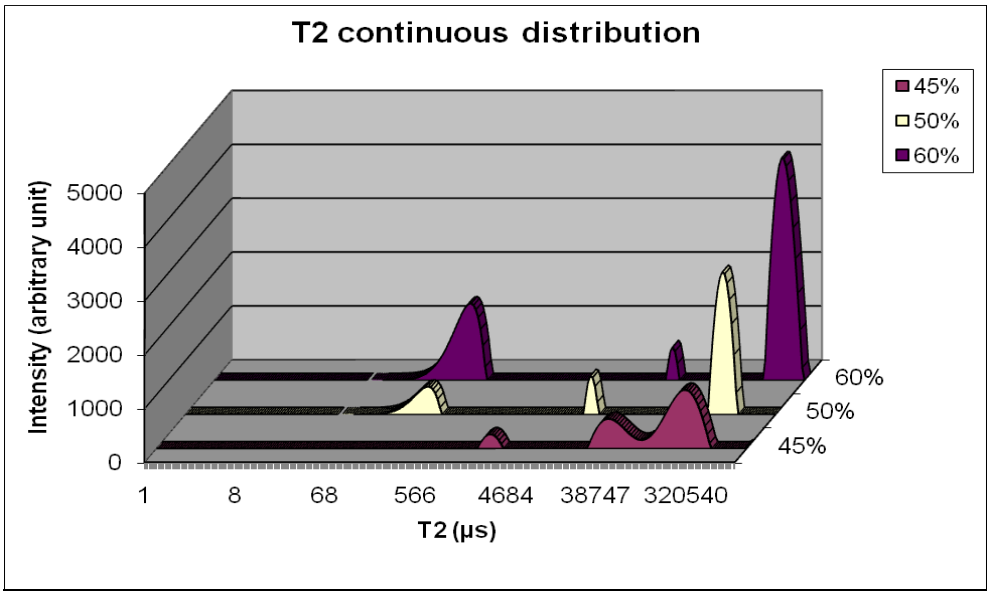

Figure 3.2.2b. T2 continuous distribution for glucose with different moisture contents.

3.2. Application of the NMR Technique in Food Research

3.2.1 Study of properties of water in sandwiches subjected to different processes

Samples

Sandwiches from major food processing company generally consist of two major compartments, crust and filling. Three sandwich samples identified as Control, Leaky, and Soggy were the subject of this study. The leaky ones became soggy over time.

The objective of this preliminary study was to use NMR/MRI technique to monitor the change in water content, mobility and distribution in these three samples. The T1, T2, and T2* values were measured to illustrate the changes in quantity and mobility of water

which interacted with other filling materials. The spatial moisture distributions were presented by the proton intensity images acquired using MRI.

One piece of each of the three samples, identified as control, leaky and soggy, was sealed in plastic wrap and used for the NMR and MRI experiments.

NMR Tests

NMR and MRI experiments were conducted at 25°C using an MRI system with an 12.9 MHz permanent magnet. FID, CPMG and INVREC sequences were used to measure T2*, T2 and T1 values, respectively. Three pieces of sandwiches, one each type, were piled together and MRI 3D images of matrix 64*64*64 were obtained using a 3D spin echo sequence.

Data processing

The NMR relaxation parameter values were calculated from the raw data using software WINFIT. The continuous distributions of these parameters were obtained using software WINDXP. The 3D images were constructed using software IDL 5.6RI advanced image. The moisture distributions were presented by Matlab software.

Results and Discussion

Tables 3.2 and 3.3 show the NMR relaxation data obtained from the crusts and fillings of the samples, respectively. Figures 3.3.1-3.3.3 show the continuous distribution from the same samples. Since it was difficult to obtain crusts free of fillings, precautions should be taken when analyzing data from crusts. Relaxation times (T2*, T21, and T22) indicate the mobility. The longer the relaxation time, the higher the mobility is. The intensity (A2*, A21, and A22) are proportional to the quantity of water or other proton-containing molecules.

The crust of the control sample had a very low T2* compared with those of Leaky and Soggy, which is in agreement with the firm texture of the control sample. The higher A2* for the crust of the control sample suggests that the control sample may firmly keep the tightly bound water molecules, or the hydrogen bound help to keep the structure together. On the other hand, the leaky and soggy samples may somewhat disintegrate probably due to gaining moisture from the fillings, and the disintegrated structure would allow moisture to escape from crust to the environment. It appears that the leaky and soggy samples were more fragile than the control, probably due to loss of moisture content in the later stage. Meanwhile, from Figure 3.3.1-3.3.3, I also found out that the T2 distribution of leaky and soggy samples is a little more complicated than the control sample and have more peaks appeared in the distribution figures, meaning that structural changes were happened to the leaky and soggy samples resulting in the change of the moisture distribution.

With regard to more mobile water in the crust characterized by T21, T22, A21 and A22, it appears that the control sample was able to hold up more water than the leaky and soggy. This may be again due to escape of moisture from the disintegrated crusts to the environment. We hypothesize that in the earlier stage (before the crusts disintegrated) the crusts of leaky and soggy may have higher moisture content than the control.

For the fillings, it was found that the control sample had higher bound water (A2*) than the leaky and soggy samples. However, the picture of the more mobile water (A21 and A22) is less clear. The water in leaky sample seems to have literally leaked to the crust while the mobile water in the soggy sample remains high.

The differences observed could be attributed to a number of reasons, e.g.,

(1) different formulation of the fillings

(2) the imhomogeneity of the fillings

Further work may involve observation of the changes in MRI and NMR properties during storage.

Table 3.2. NMR properties of sandwich crusts.

NMR Parameters	**Control**	**Leaky**	**Soggy**
T2 (μs)*	603	878	1010
*A2**	9877	5839	4562
T21 (μs)	1127	1599	1177

T22 (μs)	59085	67171	54852
A21	1793 (86%)	1280 (85%)	1330 (89%)
A22	288 (14%)	225 (15%)	166 (11%)
A21+A22	2082	1506	1496

Table 3.3. NMR properties of sandwich fillings.

NMR Parameters	**Control**	**Leaky**	**Soggy**
T2 (μs)*	2687	2668	2256
*A2**	7538	7072	5313
T21 (μs)	2564	1129	2569
T22 (μs)	23945	13503	37186
A21	545 (10%)	301 (8%)	447 (6%)
A22	5093 (90%)	3601 (92%)	6483 (94%)
A21+A22	5639	3903	6930

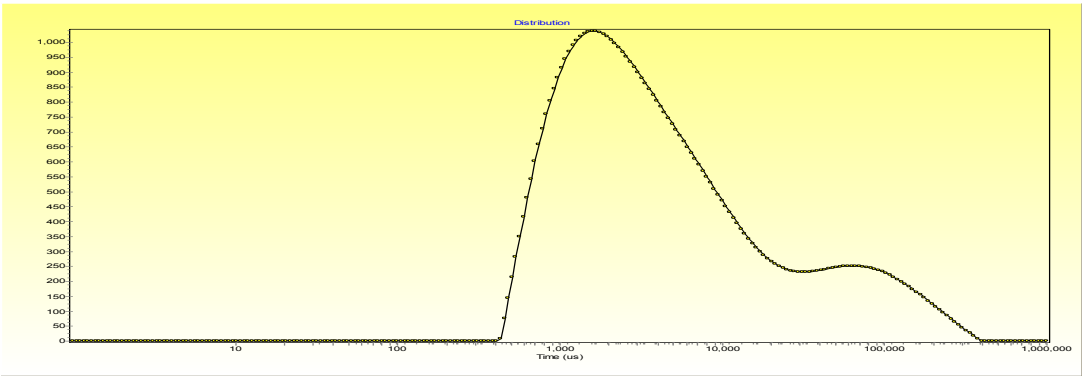

Figure 3.3.1. Continuous distribution of T2 from CPMG test. Sample: control.

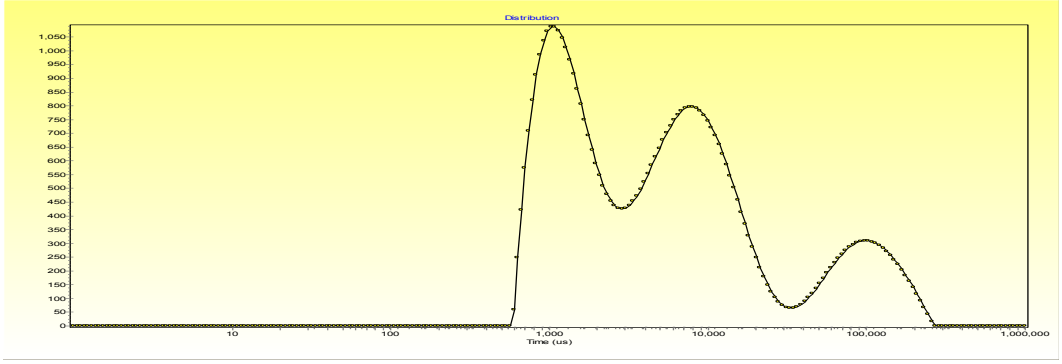

Figure 3.3.2. Continuous distribution of T2 from CPMG test. Sample: leaky.

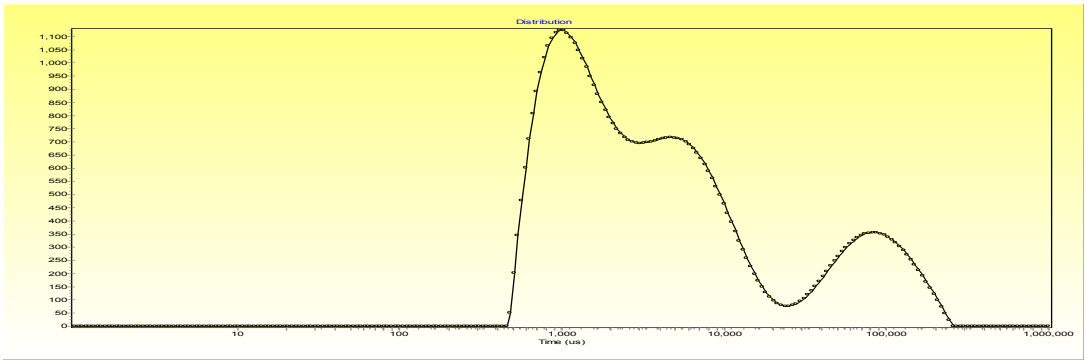

Figure 3.3.3. Continuous distribution of T2 from CPMG test. Sample: soggy.

3.2.2 Relationship between diffusion and relaxation properties of water in beans

Samples

Three groups of different types of beans from local food processing company were used as samples and prepared for NMR tests. They were denoted as A (green beans), B (yellow beans) and C beans. Green beans and Yellow beans had similar sizes, while C beans were much larger than the other 2 types of beans. There were four individual beans in each group. Each group of beans was soaked in water at 25°C. The A and B group were taken for tests before soaking and every hour after soaking for 7 hours. The C group was taken for tests before soaking (0h) and 0.5-hour, 1-hour, 2-hour, 4-hour, 6-hour, 8-hour, 10-hour, 24-hour after soaking. The samples were returned to the soaking process after testing.

NMR Tests and Data processing

NMR experiments were conducted at 25°C using a MRI system with an 12.9 MHz permanent magnet. FID, CPMG and INVREC sequences were used to measure T2*, T2

and T1 values, respectively. The NMR relaxation parameter values were calculated from the raw data using software WINFIT.

Results and Discussion

Tables 3.4 summarizes the relaxation times (T2*, T2, T1) for different samples obtained through discrete model fitting. Figures 3.3.4-3.3.7 show the relaxation time changes during soaking process for each sample type.

Table 3.4. Relaxation times - FID T2*, CPMG T2, amplitude (A2) and T1 as a function of time in different samples

	T2*(μs)	T21(μs)	A21(%)	T22(μs)	A22(%)	T1(ms)
Green_0h	248	333	91%	1843	9%	33
Green_1h	253	367	90%	3011	10%	35
Green_2h	267	395	85%	5200	15%	42
Green_3h	1428	500	83%	14102	17%	47
Green_4h	1752	530	81%	15948	19%	49
Green_5h	2259	543	79%	17213	21%	50
Green_6h	2588	526	78%	18035	22%	54
Green_7h	2744	535	77%	18866	23%	57

Yellow_0h	275	328	92%	1920	8%	33
Yellow_1h	349	329	90%	2704	10%	39
Yellow_2h	586	365	87%	3700	13%	42
Yellow_3h	1284	429	86%	7000	14%	44
Yellow_4h	1631	416	85%	8623	15%	46
Yellow_5h	1815	436	84%	9807	16%	48
Yellow_6h	1955	443	83%	10261	17%	50
Yellow_7h	2500	530	82%	11207	18%	51
C_0h	248	337	91%	1970	9%	34
C_0.5h	269	343	89%	2113	11%	/
C_1h	298	346	86%	3231	14%	37
C_2h	1187	531	83%	14075	17%	44
C_4h	2706	540	76%	16693	24%	48
C_6h	3800	574	72%	19690	28%	54
C_8h	3679	584	70%	21139	30%	57
C_10h	4313	580	69%	22236	31%	58
C_24h	6007	603	68%	23908	32%	60

Before samples were soaked in water, all three samples had similar T2* values in the range of 240-280 microseconds with Yellow beans having the highest T2*. After samples were soaked in water, T2* values started to increase because water diffused into

beans. During the first 1 to 2 hours, T2* increased gradually for Yellow beans, slowly for C beans and much more slowly for Green beans, shown from Figure 3.3.4 and 3.3.5. After soaking for more than 2 hours, T2* had a similar increasing trend for Yellow beans (Figure 3.3.4), but increased sharply for Green beans and increased more obviously for C beans (Figure 3.3.5). This may due to different microstructures of different types of beans, leading different hydration behavior. From Table 3.4 and Figure 3.3.4, we could both see that T2* values after 2 hours for Green beans surpassed Yellow beans. This indicates that although Yellow bean had a faster hydration process in the first 2 hours, Green beans tended to absorb more water later on. From Table 3.4 and Figure 3.3.4, we found that after 3 hours, C beans had the largest T2* values. This may due to the much larger sizes of C beans, leading much larger surface areas for water to diffuse in more easily.

From CPMG data (Table3.4) and Figure 3.3.6-3.3.7, we found similar increasing trends of T22 values for the 3 types of beans as their respective T2* values. But T22 values for Green beans were all the way larger than Yellow beans. This might due to that when water kept diffusing into beans, Green beans tended to have more highly mobilized water than Yellow beans. We may speculate that more water would gather near the skin for Green bean, which had weaker attraction, but water may more easily went into the inner part of Yellow beans, which had stronger attraction.

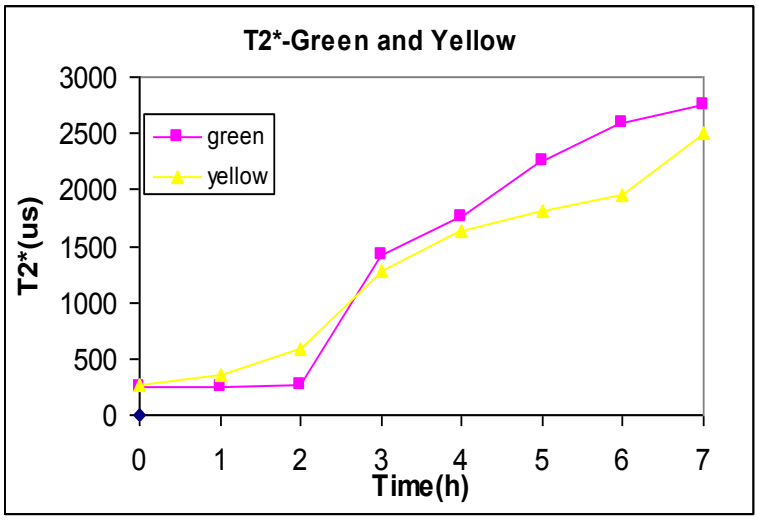

Figure 3.3.4. Change in relaxation time T2* for Yellow and Green beans at different times

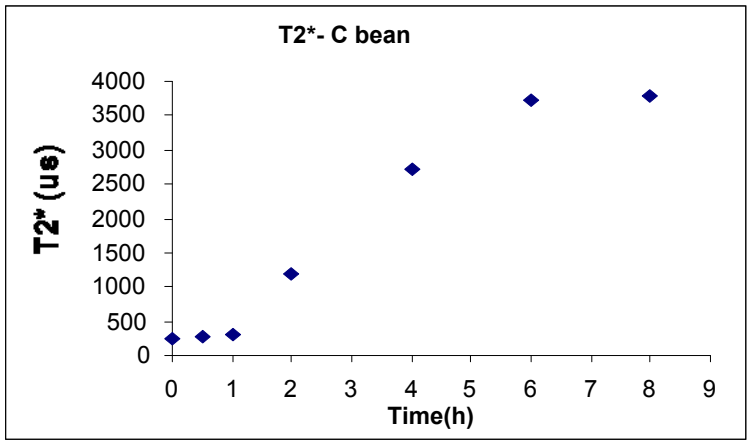

Figure 3.3.5. Change in relaxation time T2* for C beans at different times

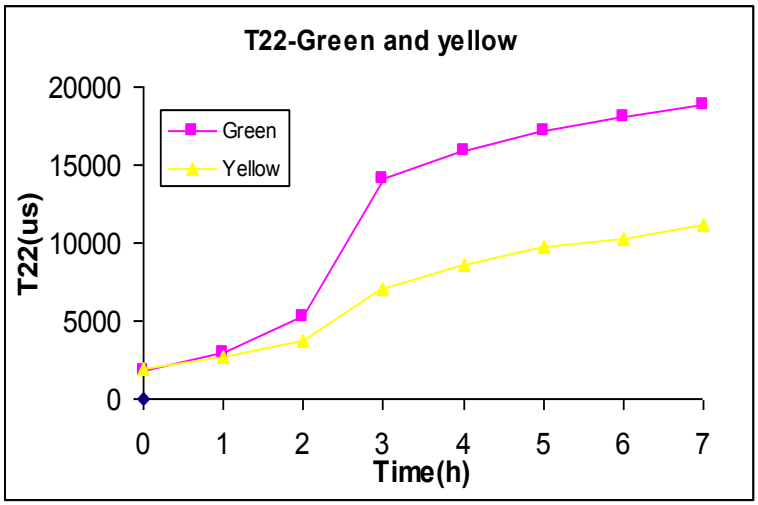

Figure 3.3.6. Change in relaxation time T22 for Yellow and Green beans at different times

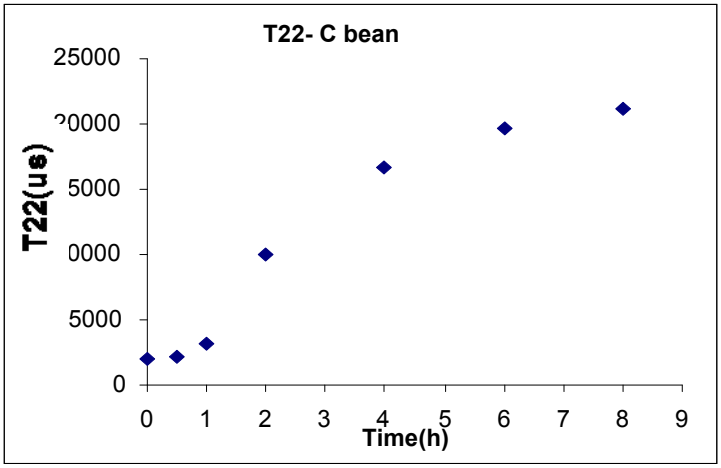

Figure 3.3.7. Change in relaxation time T22 for C beans at different times.

CHAPTER 4 NMR STATE DIAGRAMS

As discussed earlier that NMR state diagram is a useful tool for categorizing ingredients based on their physiochemical properties as measured by NMR relaxometry techniques, this chapter will be designated to the adaption of the techniques on the DRX2 machine and application of the adapted techniques in the studies of food and non-food materials.

4.1. Methodology

4.1.1. Hardware modification

To obtain an NMR state diagram for an ingredient, the relaxation times of the ingredient at different temperatures will be determined, which will require the MRI machine to be functional over a range of temperatures. To attain and maintain a set temperature, a temperature control system must be developed and incorporated into the MRI machine for the analysis. The DRX machine has a built-in temperature system consisting of an Omron temperature controller and a Luxtron750 optic fiber temperature sensor with an accuracy of ±0.1°C, as shown in Figure 4.2.1. In my research, I designed and constructed a temperature control system for DRX2 machine. This temperature control system consists of a heating/cooling element and control device operated through computer. Temperatures can be maintained at set temperature ± 0.1°C. Necessary insulation was provided

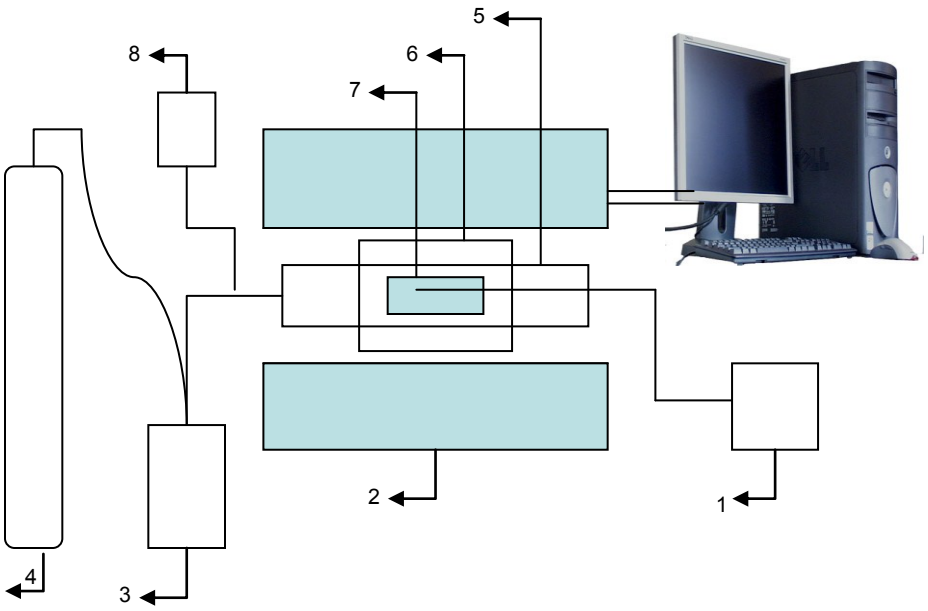

1. Luxtron750 optic fiber sensor; 2. Low field permanent magnet; 3. Liquid nitrogen container; 4. Nitrogen gas cylinder; 5. Sealed vessel; 6. NMR testing probe; 7. Sample with glass bottle; 8. Temperature controller.

Figure 4.2.1. Schematic of MRI system for determination of NMR state diagram.

MRI experiments were conducted at 35°C using an MRI system with a 21.4 MHz permanent magnet. Several pellets were imaged together using a matrix of 64*64*64 by a SPRITE3D sequence (Li et al., 2008).

4.1.2. Sample preparations

Two sets of samples were used in this study. They were protein bars and their ingredients, and flour pellets.

Ingredients and making of protein bars

The purpose of this study was to evaluate the textural properties of protein bars as a function of physiochemical properties of the key ingredients determined with the NMR state diagram techniques. The key ingredients for the protein bars included powdered proteins and syrups. It was hypothesized that screening of the ingredients using NMR state diagram help select ingredients for the formulation of protein bars with desirable textural properties.

Six powdered proteins {SUPRO® 313 (Solae), SUPRO® 320 (Solae), SUPRO® 430 (Solae), calcium caseinate (Farbest Foods), whey protein isolate (WPI) (Glanbia), and milk protein isolate (MPI, Kerry Ingredients)} were selected for analysis and entered into a 2^{nd} degree simplex lattice mixture design. All proteins were used in duplicate at 100% levels and in singular in all possible 50/50 blends of proteins, resulting in 27 total combinations. Protein blends were created using a V-blender (Paterson Kelly Model C445220, Troy, Ohio). Three syrup blends {sugar syrup (SS) (50.4% 63DE corn syrup, 41.25% high fructose corn syrup, 8.35% glycerine), polyol syrup (PS) (35% glycerine, 35% maltitol, 20% polydextrose, 10% sorbitol), and reduced-sugar "blend" syrup (BS) (50% SS + 50% PS)}were created using the Hobart mixer (Model H-600, Troy, Ohio). Both syrups were used in duplicate at 100% level and in singular for the reduced-sugar

blend syrup, resulting in five total syrups. Aliquots of all proteins and all syrups were removed for use in NMR analyses, with the remainder used to make food bars.

The protein d bars were made using all 27 powdered proteins in all three syrup models (SS, PS, BS) using a 30% protein chocolate bar formulation, resulting in 81 distinct bar formulas. Each batch was made on bench top scale using a Hobart mixer (Model A120, Troy, Ohio) and evaluated for water activity (Decagon AQUA Lab Series 3TE, Pullman, Washington), bar integrity, and stickiness immediately after processing. Bar integrity was scored on a 10-point scale (1 = most crumbly, 5 = ideal texture, 10 = most fluid), and stickiness was scored on a 5-point scale (1 = most sticky, 5 = least sticky). After processing, bars were packaged in oxygen-barrier opaque pouches (Ampac, Cincinnati, OH), heat-sealed, and placed in accelerated storage (90°F). Bars were removed after 1, 7, 14, 28, and 42 days of storage for texture analysis testing using the TAxT2i (Texture Technologies Corp, Scarsdale, NY), with day 42 corresponding to 12 months of ambient storage.

Flour pellets

The objective of this study was to find out the differences in the moisture distributions of sample pellets as a function of three factors: location of the plants,

additive level and flour type by using state diagram method. Results from other NMR tests and MRI tests were used to confirm the state diagram results.

Six types of sample pellets were tested in this study, shown in Table 4.6.

Table 4.6. Sample labels

Sample ID	Location	Additive Level	Flour Type
Cntrl	N	0	Y
A	N	2	Z1
B	N	3	Z1
Control	P	0	Y
D	P	2	W
C	P	2	Z2

4.1.3. NMR and MRI Experiments

NMR state diagram measurements were conducted on DRX and DRX2 systems. Samples (approximately 12 grams of protein powders or 20 ml of syrups) were put in a glass bottle of size/cap 27*55mm. The glass bottle was placed into a sealed testing vessel positioned at the center of the NMR probe. Each sample was scanned from –35°C to

50°C at an average temperature scan rate of 0.6°C/minute. Free-induction-decay (FID) sequence, performed with a 90° pulse length of 28 μs, 256 data points and 0.6 s repetition time for each scan, and 16 scan repetitions, was used to measure T_2* values. Carr-Purcell-Meiboom-Gill (CPMG) sequence, performed with a 90° pulse length of 35 μs, time between 90 and 180 pulses of 150 μs, 1 s repetition time for each scan and 8 scan repetitions, was used to measure T_2 values. The number of echoes for CPMG sequence varied from 64 to 1024, depending on the temperature, with higher temperatures having a larger number of echoes. T_2* values were plotted against temperature to produce NMR state diagrams (T_2* vs. temperature curves) (Li et al., 2008).

The data obtained from the NMR experiments were fitted into Equations 2.2 and 2.4 in Chapter 2.

4.2. Results and Discussion

4.2.1. Protein Bars

Firmness Change

The effectiveness of the mixture design was analyzed in Minitab, with R-squared ranging from 95.69% (SS) to 99.83% (BS). The food bars made covered the entire range of both the stickiness and the bar integrity scales. None of the duplicate samples were considered significantly different from their counterparts ($p<0.05$), so replicate data for

proteins and syrups was pooled and averaged. In general, bars made with sugar syrup had a crumblier bar integrity (BI $\leq$ 5), while bars made with the polyol or the reduced-sugar blend syrup had a more fluid bar integrity (BI $\geq$ 5). Bar integrity and stickiness are important factors for determining which bars can be manufactured on a larger scale, with bars that are too crumbly, too fluid, or too sticky being unprocessible.

As anticipated, the food bars hardened over the course of accelerated storage, with the rate and extent of hardening dependent upon the syrup base and proteins used. Like Lin *et al.* 2006, bar hardening was a non-linear process. To linearize the curves, double log plots were created using Equations 4.3 and 4.4, the results of which are shown in Table 4.1. Some proteins had hardening rates that were more dependent on syrup base than others. For example, the hardening rate constant for WPI in sugar syrup was 0.06, which corresponds to an increase of about 6.85 g of force per day. When WPI was used in the reduced-sugar blend syrup, the hardening rate constant increased to 0.73, corresponding to an increase of more than 176 g of force per day. On the other hand, the hardening rate constant for SUPRO® 313 was approximately the same for each syrup base used. Typical acceptance levels for bar hardness range from less than 1500 g of force to no more than 2000 g of force. When texture measurements exceed 2000 g, sensory hedonic overall liking scores decrease substantially.

$$ln(H_t) = ln(H_0) + kln(t), \text{ or} \tag{4.3}$$

$$H_t = H_0\, t^k \tag{4.4}$$

where H_0 is the initial hardness, H_t is the hardness at time t, and k is a rate constant.

Table 4.1. Regression results for determination of hardening rate over the course of accelerated storage.

	SS			PS			BS		
Protein	Initial hardness H_0 (g)	Hardening rate (k)	R^2	Initial hardness H_0 (g)	Hardening rate (k)	R^2	Initial hardness H_0 (g)	Hardening rate (k)	R^2
CaCas	300.19	-0.09	0.64	207.93	0.50	0.98	81.47	0.54	0.93
CaCas+MPI	117.10	-0.02	0.08	22.80	0.45	0.92	29.48	0.10	0.85
CaCas+WPI	393.35	0.23	0.69	80.27	0.21	0.93	285.30	0.25	0.95
MPI	30.45	-0.14	0.92	11.39	0.37	0.79	10.79	0.10	0.89
MPI+WPI	147.99	0.00	0.00	849.89	0.12	0.80	55.05	0.30	0.83
SUPRO®313	1050.22	0.32	0.75	137.25	0.38	0.88	297.72	0.36	0.85
SUPRO® 313+CaCas	354.63	0.07	0.53	29.06	0.47	0.97	48.92	0.33	0.95
SUPRO®313+MPI	148.81	0.11	0.79	21.57	0.46	0.96	34.88	0.36	0.85
SUPRO® 313+SUPRO®320	637.18	0.18	0.96	71.56	0.73	0.84	150.53	0.61	0.97
SUPRO® 313+SUPRO®430	308.85	0.46	0.98	56.43	0.59	0.88	108.98	0.57	0.93
SUPRO®313+WPI	723.74	0.36	0.91	256.63	0.23	0.84	374.43	0.45	0.93
SUPRO®320	969.94	0.20	0.69	1507.64	0.44	0.89	553.05	0.77	0.90

SUPRO® 320+CaCas	400.02	0.14	0.88	988.19	0.30	0.85	375.59	0.64	0.79
SUPRO®320+MPI	122.27	0.03	0.31	86.75	0.68	0.93	71.96	0.76	0.97
SUPRO® 320+SUPRO®430	416.61	0.31	0.99	468.53	0.52	0.87	186.97	0.94	0.82
SUPRO®320+WPI	1051.87	0.05	0.55	224.73	0.21	0.77	255.19	0.55	0.91
SUPRO® 430+CaCas	171.21	0.31	0.95	82.54	0.72	0.92	70.92	0.67	0.94
SUPRO®430+MPI	50.41	0.17	0.93	24.28	0.49	0.88	23.22	0.39	0.89
SUPRO®430+WPI	636.09	0.17	0.69	156.24	0.17	0.88	207.60	0.59	0.91
SUPRO®431	266.79	0.37	0.94	113.04	0.73	0.86	103.13	0.95	0.75
WPI	1399.09	0.05	0.34	314.81	0.15	0.47	460.23	0.76	0.95

While certain proteins may appear to have performed well in a bar because the bars had a slow rate of hardening or a soft texture at the end of the shelf life, many of these bars would not have been initially processible. For example, when MPI was used in the polyol bar, the bars were very soft at the end of the shelf-life, but addition of MPI correlated strongly with unacceptable bar integrity ($p < 0.05$). On the other hand, some proteins appeared to make bars that were quite hard, but smaller concentrations of these proteins can make the dough easier to work with and increase processibility. For example, SUPRO® 320 used in the polyol or reduced-sugar blend syrup bases created bars that were hard at the end of the shelf-life, yet addition of this protein correlated

strongly with ideal stickiness ($p < 0.05$) and desired bar integrity ($p < 0.05$) in both of those syrup models, suggesting that smaller concentrations of SUPRO® 320 can help overall performance in polyol and reduced-sugar blend syrup formulations.

To see the entire protein performance picture, bar integrity, stickiness, bar hardening rate, and bar hardness at the end of accelerated storage must be examined simultaneously. Protein performance was examined for all 3-way combinations of proteins in each syrup model using overlaid contour plots and was found to be a strong function of the syrup type ($R^2 = 92.33\%$). Figures 4.2.2a and 4.2.2b show two of these plots, both representing the sugar syrup base. The white regions of these plots encompass all combinations (2- or 3-way) of proteins that will make a bar that will be processible on a large scale and will also have acceptable texture at the end of the shelf-life. Although none of the soy proteins should be used at 100% levels in sugar syrup, the majority of 2- and 3-way combinations of the soy proteins will produce acceptable bars. Calcium caseinate and MPI can only be used in limited quantities in the sugar syrup model and must be used in combination with WPI to make an all-dairy bar that is processible. Some 2-way blends of proteins exhibited synergistic effects, meaning bars made with a blend of 2 proteins were softer at the end of accelerated storage than bars made with either protein at 100% level. One example of synergistic proteins, SUPRO® 313 and Calcium caseinate in polyol syrup-based bars, is shown in Figure 4.2.3. Other synergistic combinations are discussed later.

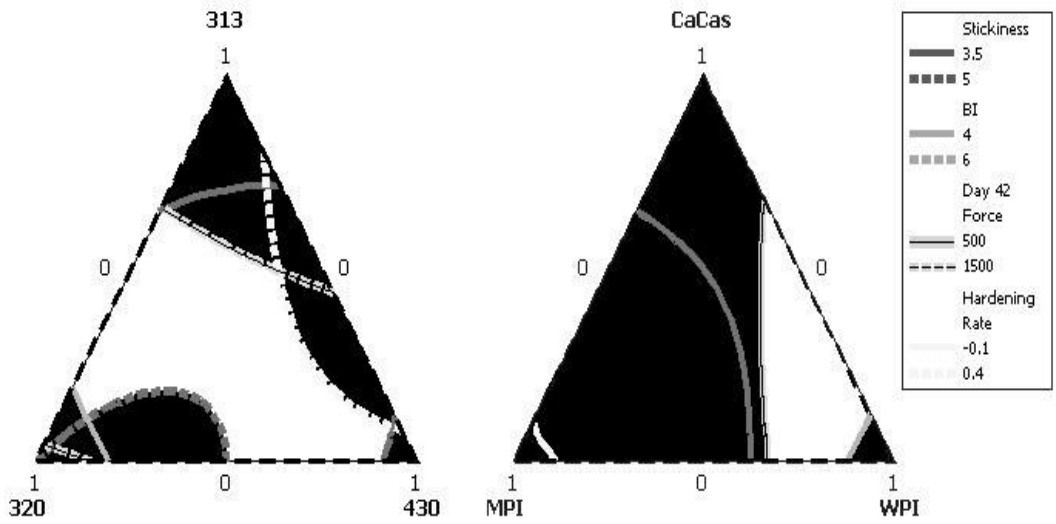

Figure 4.2.2 a - b. Overlaid contour plots showing the 2- and 3-way combinations (white regions) of all (a) soy and (b) dairy proteins that result in acceptable stickiness (score 3.5 – 5.0), bar integrity (score 4 – 6), and texture (Accelerated storage texture 500g – 1500g, Hardening Rate -0.1 – 0.4) in the sugar syrup bar model.

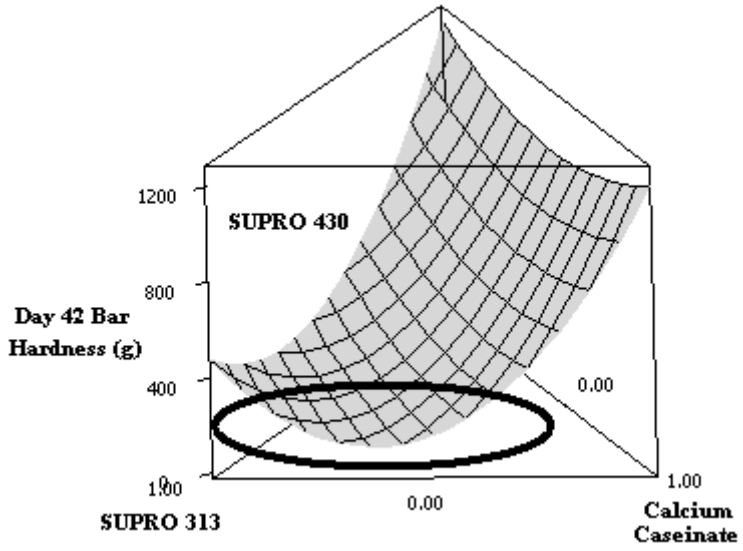

Figure 4.2.3. In combination, SUPRO® 313 and Calcium Caseinate have a synergistic softening effect in bars made using a polyol syrup model. Many other synergistic combinations of proteins were found in this study.

NMR State Diagrams

A NMR state diagram was created for each syrup and for each protein, the identities of which were unknown to the lab group until all data collection and analysis (including categorizing) was complete. Differences in significant features of the temperature- T_2* curves for the proteins, similar to those discussed by Chung *et al.* 2001, are included in Table 4.2. Transition temperatures were found for some, but not all, of the protein samples. The slopes for the before-transition phase (k_{BT}) and for the post-

transition phase (k_{PT}) of the curves were used to place the proteins into categories. The proteins that did not have transition temperatures were categorized based on the slope of the entire curve. The powdered proteins fell into all four of the categories developed by Chung *et al.* 2003, as detailed in Table 4.3, the NMR state diagram curves of which are shown in Figure 4.2.4. All replicate samples were placed blindly into the same groups. Samples of 100% soy proteins were placed into Type C or Type D, while 100% dairy proteins fell into Type A, Type B, or Type C. Type A proteins would be predicted to be the least stable proteins, undergoing changes even at low temperatures, while Type B proteins are predicted to be moderately stable, undergoing changes after the transition point (Lin *et al.* 2006). Type D proteins are predicted to be the most stable, undergoing very few changes, regardless of temperature.

Table 4.2. Significant features of NMR state diagram curves for powdered proteins.

Protein Type	T_{trans}	k_{BT}	k_{PT}
A	Yes	> 0.15	> 0.0
B	Yes	≤ 0.15	> 0.0
C	No	≥ 0.10	≥ 0.10
D	No	< 0.10	< 0.10

Table 4.3. Distinguishing parameters for powdered proteins, taken from the NMR state diagrams shown in Figure 4.2.4.

Protein Type	Proteins Used	Transition Temperature (°C)	k_{BT} (μs/°C)	k_{PT} (μs/°C)
A	MPI	2.5	0.24	1.48
	CaCas+MPI	10	0.35	2.39
	CaCas	22.5	0.37	2.57
	SUPRO® 430+CaCas	30	0.22	1.02
	SUPRO® 320+MPI	35	0.32	1.96
B	MPI+WPI	15	0.02	0.60
	CaCas+WPI	25	0.08	0.73
	SUPRO® 430+MPI	25	0.13	0.84
	SUPRO® 320+CaCas	25	0.15	0.72
	SUPRO® 313+CaCas	35	0.04	1.28
C	WPI	------	0.10	0.10
	SUPRO® 320+WPI	------	0.13	0.13
	SUPRO® 320	------	0.13	0.13
D	SUPRO® 313+WPI	------	0.01	0.01
	SUPRO® 313+SUPRO® 430	------	0.02	0.02
	SUPRO® 430	------	0.03	0.03

SUPRO® 313	------	0.05	0.05
SUPRO® 320+SUPRO® 430	------	0.05	0.05
SUPRO® 313+SUPRO® 320	------	0.07	0.07
SUPRO® 430+WPI	------	0.08	0.08

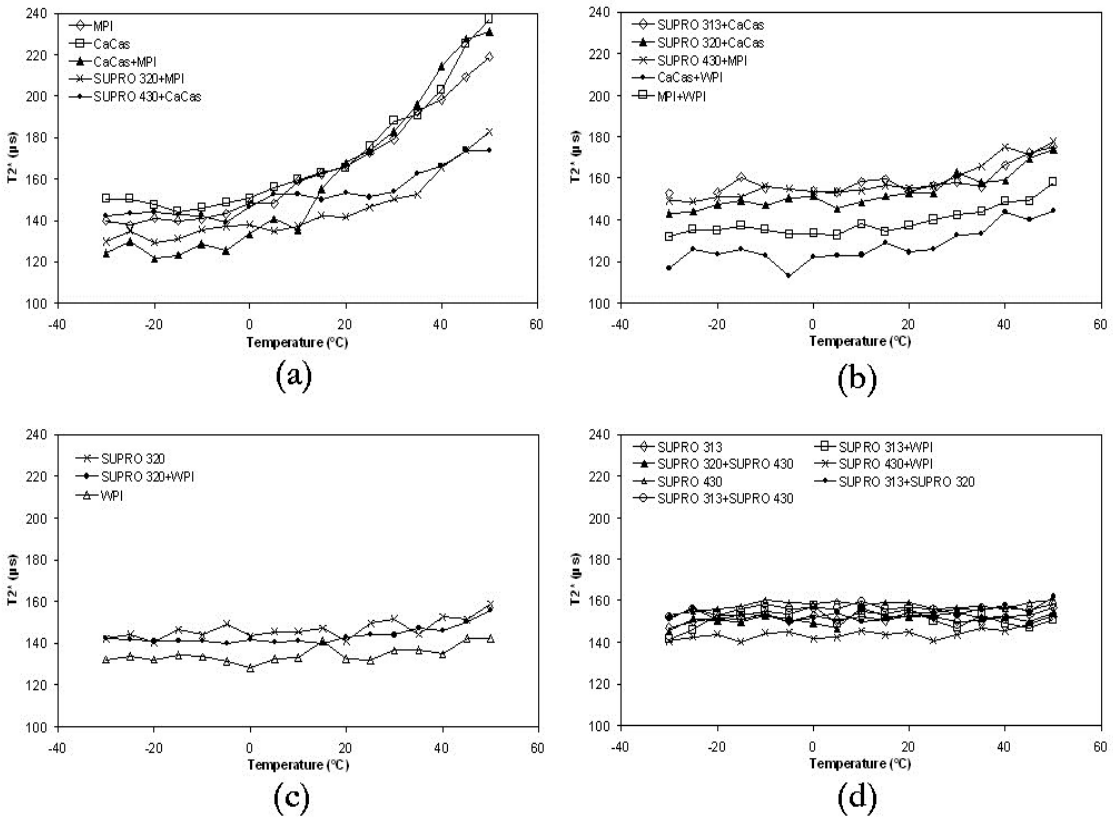

Figure 4.2.4 NMR state diagrams showing changes in T_2* as a function of temperature for powdered proteins separated by type (A, B, C, and D).

Relationships between NMR relaxometric properties and Textural properties

Protein Type Versus Bar Texture

NMR was used to classify proteins into types (A, B, C, and D) based on the shape of their individual NMR state diagram curves. To look at the effect of protein type on performance of these proteins in food bars, correlation matrices were developed. Strong correlations were seen between protein type and both hardening rate and day 42 hardness of bars made using the sugar syrup model (R^2 = 79%, 90% respectively, $p < 0.05$). In the PS and BS models, protein type correlated with bar integrity (R^2 = 76%, 54% respectively, $p < 0.05$). "State of water" measurements were also run on the samples to determine values for T_1, T_2, and T_2* of the proteins at room temperature (20°C). The average values of T_2 at 20°C correlated well with protein type (R^2 =98%, $p < 0.05$), so proteins that were classified as more stable (Type D) over the entire temperature range studied had higher values for T_2. In the context of high protein food bars, higher values of T_2 for proteins were thought to have been associated with a softer bar texture (Lin *et al.* 2006), but this study found that not to be true. Instead, higher values of T_2 for proteins indicated the bars were harder at the end of storage, but had more ideal dough stickiness and bar integrity, regardless of syrup model base used.

In the polyol syrup model, bars made with Type A proteins hardened the most rapidly, yet, in the sugar syrup model, the opposite was true, with Type A proteins creating bars which hardened the slowest. These differences were also apparent when the

average values of T_2 and T_2*, recorded at room temperature, were compared, as shown in Figure 4.2.5. When the powdered proteins were analyzed, Type A proteins had the highest values of T_2*, yet the lowest values of T_2.

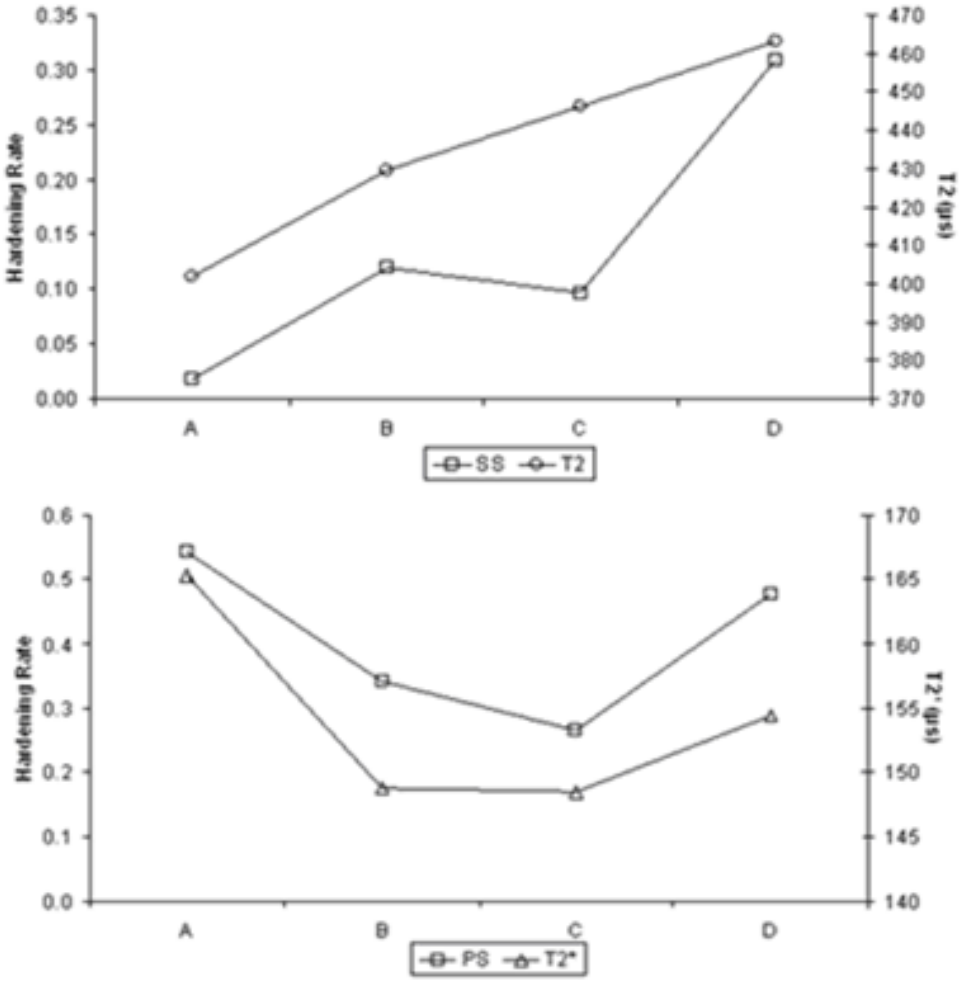

Figure 4.2.5. Changes in hardening rate of food bars made with Type A proteins in a sugar syrup based-formula (top) and in a polyol syrup-based formula (bottom) mirror values for T_2 and T_2*, respectively, measured at 20 °C.

Syrup Mobility vs. Bar Texture

For the syrup samples, average values of T_{21}, T_{22}, T_2*, and T_1 recorded at 20°C increased with increasing moisture content, as well as increasing concentration of polyols (SS<BS<PS). The state diagrams for syrup samples are shown in Figure 4.2.6, and key bar and syrup parameters are listed in Table 4.4. Initial and final (42 days at 90°F) water activity values for the bars were averaged by syrup type and means were compared using two sample t-tests. Initial water activity values were not significantly different from one another, but differences in final water activity were apparent. Water activity values for bars made using the sugar syrup base were increasing slightly, but not significantly ($p > 0.05$). Bars made using the polyol syrup base had the highest increase in water activity over time, with bars made using the reduced-sugar blend syrup base exhibiting intermediate water activity increases.

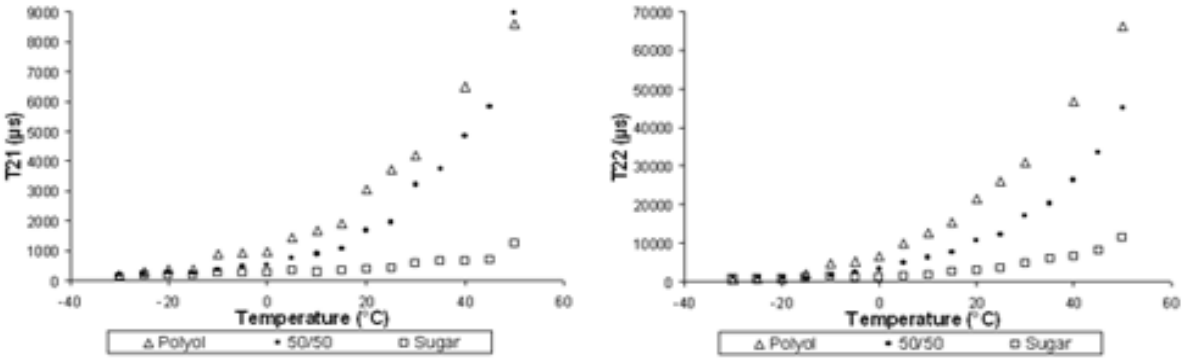

Figure 4.2.6. NMR state diagrams showing changes in T_{21} (short component) and T_{22} (long component) with respect to temperature for polyol, reduced-sugar blend, and sugar syrups.

Table 4.4. NMR state diagram parameters for each syrup studied.

[1] Means in rows and in columns containing the same letters are not significantly different from one another ($p > 0.05$).

				Short component			**Long component**		
Syrup	**Initial bar a_w**	**Final bar a_w**	**Tg (°C)**	**T_{21} at 20°C (µs)**	**$K_{before\ Tg}$ (µs/°C)**	**$K_{post\ Tg}$ (µs/°C)**	**T_{22} at 20°C (µs)**	**$K_{before\ Tg}$ (µs/°C)**	**$K_{post\ Tg}$ (µs/°C)**
Sugar	0.518 **a** [1]	0.531 **a**	10	438	5	38	2992	16	243
Blend	0.509 **a**	0.543 **b**	15	1681	20	203	10659	142	1009
Polyol	0.519 **a**	0.563 **c**	15	2670	36	199	19697	314	1463

Lin *et al.* 2006 found that samples having NMR state diagram curves with large differences in values of T_2 over time created less stable food products than samples having little to no differences in values of T_2 over time. Based on Lin *et al.* 2006,

predictions could be made about the three syrups used in the study as a result of their NMR state diagram shape. The syrups were predicted to differ in stability, with polyol syrup being the least stable, blend syrup being moderately stable, and sugar syrup being the most stable. Those predictions were valid in that bars made with sugar syrup had greater initial hardness than bars made with either polyol or reduced sugar blend syrup, but, over time, the sugar syrup bars hardened the slowest and to a lesser extent than bars made with polyol or blend syrup. Additionally, bars made with sugar syrup had no significant changes in water activity over storage, while polyol-containing bars had significant increases. Although an increase in water activity may suggest the bars are getting softer over time, that was not the case. Instead, it appears that, initially, more water is available to act as a plasticizer in polyol-containing bars, but over time this water is becoming "free water," leading to an elevated rate of bar hardening and explaining the increase in water activity. It is also possible that some of the low molecular weight polyols in the syrups are initially acting as plasticizers. Over time, these polyols could lose this plasticizing capability and have greater interactions with the proteins in the bar, possibly strengthening hydrophobic interactions of the protein molecules (Gekko 1981), and leading to a firmer texture.

Differences in NMR state diagram shape may also explain the variety of bar texture when syrup type is altered, but protein type remained the same. For example, bars made with SUPRO® 320 (Type C) in the sugar syrup had bar integrity of 3 (moderately too crumbly), yet in a polyol or reduced-sugar blend syrup, bar integrity was

ideal. The other Type C proteins also had the best bar integrity in polyol or reduced-sugar blend syrup. On the other hand, bars made with MPI (Type A) in the sugar syrup model had ideal bar integrity, yet in the polyol or reduced-sugar blend syrup, bar integrity was at the absolute maximum (extremely too fluid). All other Type A proteins, as well as Type B proteins, functioned well in sugar syrup also, with none having acceptable bar integrity in either polyol-containing syrup. Type D proteins functioned well in all three syrup models, perhaps because these proteins were considered the most stable. Understanding which individual proteins or protein blends work best in combination with each syrup type is crucial for extending the shelf-life of nutrition bars.

Protein Synergy and T_2*

Synergistic softening effects were seen in bars for particular blends of proteins in specific syrup models. The example given previously (Figure 4.2.3) showed the synergistic softening effect of a blend of SUPRO® 313 and calcium caseinate in a polyol-based bar. When values for T_2*, measured at 20°C, were compared for 100% SUPRO® 313 (Type D protein), 100% calcium caseinate (Type A protein), and a 50/50 blend of those two proteins (Type B protein), this synergy was seen again, as shown in Figure 4.2.7, where the changes in T_2* mirrored the changes in day 42 polyol-based bar hardness. Table 4.5 summarizes the synergistic combinations of proteins by syrup model, noting the protein type of each. Synergistic effects were seen only when Type C or Type D proteins were present. Type A or Type B proteins in combination with a Type C or

Type D protein could exhibit synergy, but no Type A or Type B protein showed synergy in the absence of a Type C or Type D protein. It is also important to note the synergy of soy and dairy proteins in food bars. Out of the 10 total syrup-dependent synergistic blends of proteins, 8 were composed of one soy protein and one dairy protein. The exact mechanism to explain this soy-dairy synergy, or, more generally, the hardening of high protein food bars over time, remains unclear.

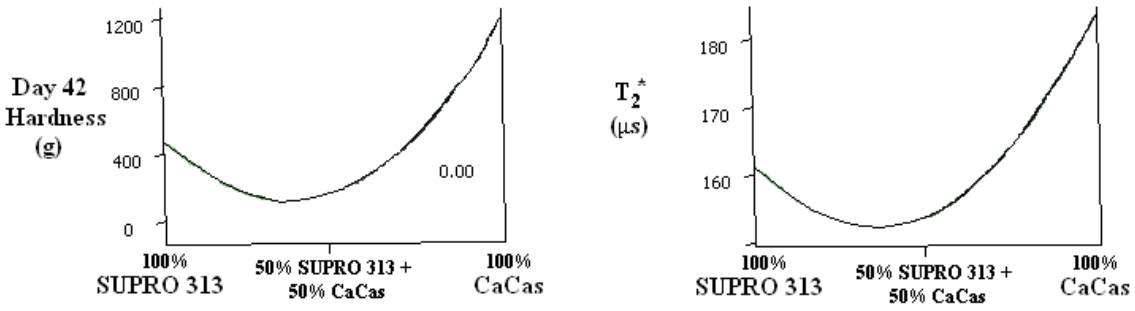

Figure 4.2.7. Synergistic lowering of T_2*, measured at 20°C, for blends of SUPRO® 313 and calcium caseinate mirror the synergistic softening effect of blending the same proteins in a polyol syrup-based bar.

Table 4.5. Combinations of proteins that exhibited synergistic softening effects in the three bar models studied.

SUGAR SYRUP		POLYOL SYRUP		BLEND SYRUP	
1	2	1	2	1	2
SUPRO 313 **(D)**	CaCas **(A)**	SUPRO 320 **(C)**	WPI **(C)**	SUPRO 313 **(D)**	CaCas **(A)**
SUPRO 313 **(D)**	SUPRO 320 **(C)**	SUPRO 430 **(D)**	CaCas **(A)**	SUPRO 313 **(D)**	SUPRO 430 **(D)**
SUPRO 320 **(C)**	WPI **(C)**	SUPRO 430 **(D)**	WPI **(C)**	SUPRO 320 **(C)**	WPI **(C)**
				SUPRO 430 **(D)**	WPI **(C)**

Summary on protein bar study

NMR is a useful tool for predicting protein functionality in sugar-, polyol-, and reduced-sugar blend syrup based food bars. NMR state diagrams can be used to categorize proteins in order to make predictions about protein performance in nutrition bars. While hardening of high protein food bars during storage is inevitable, understanding interactions between proteins and syrups can slow the bar hardening process. Use of Type C and Type D proteins, which are capable of delivering synergistic softening effects, can allow for the formulation of more stable food bars. In addition, exploiting the synergistic effects of protein blends, particularly the synergy between soy and dairy proteins, can lead to more rapid formulation optimization as well as overall cost savings. Future research is necessary to better understand the molecular interactions among syrups, proteins, and water which lead to bar hardening (Li et al., 2008).

4.2.2 Flour Pellets

State diagram analysis

As we know, T2 value is a good indicator of water mobility and state diagrams show clearly how T2 changes as temperature increases. All state diagrams are shown in Fig.4.2.8. Tg (transition temperature points), Kbt (slope before Tg) and Kpt (slope after Tg) values calculated from individual state diagram curve are shown in Table 4.7. Generally speaking, greater differences between T_g and storage temperatures above T_g or larger slope values are expected to be associated with more rapid sample quality changes. Some major observations are: 1) Pellet Cntrl has the smallest Tg value and largest Kpt value than the other pellet types, which indicate that such controlled pellets may suffer more rapid quality changes, such as rapid moisture diffusion, during storage time. On the other hand, it may also suggest that pellets with the additive or different flour types may be relatively more stable and have less moisture diffusion during storage time. 2) By comparing pellet A and B, we find that Tg value increases and Kpt value decreases as additive level increases, which indicate that larger amount of additive may be capable for enhancing the stability of pellet quality and also prevent moisture diffusion more efficiently. We can also see such trend by comparing controlled samples with other pellet types since controlled samples have no additive. 3) As for the location difference, we find that generally pellets from location M have relatively larger Kpt values than pellets from location P. And pellets from location M also have relatively larger T2* values above Tg as we can see from the positions of these state diagram curves. Since larger T2 values always indicate higher water mobility and a more mobile system, pellet Cntrl and pellet A may be more susceptible to quality changes. 4) By comparing pellet C and D, we can see that pellet C has larger Tg value and smaller Kpt, which indicate that C may be more

stable than D. Since the only difference of these two pellet type is their flour component, which may also suggest that flour D may lead to less quality changes and less moisture diffusion than flour Z2.

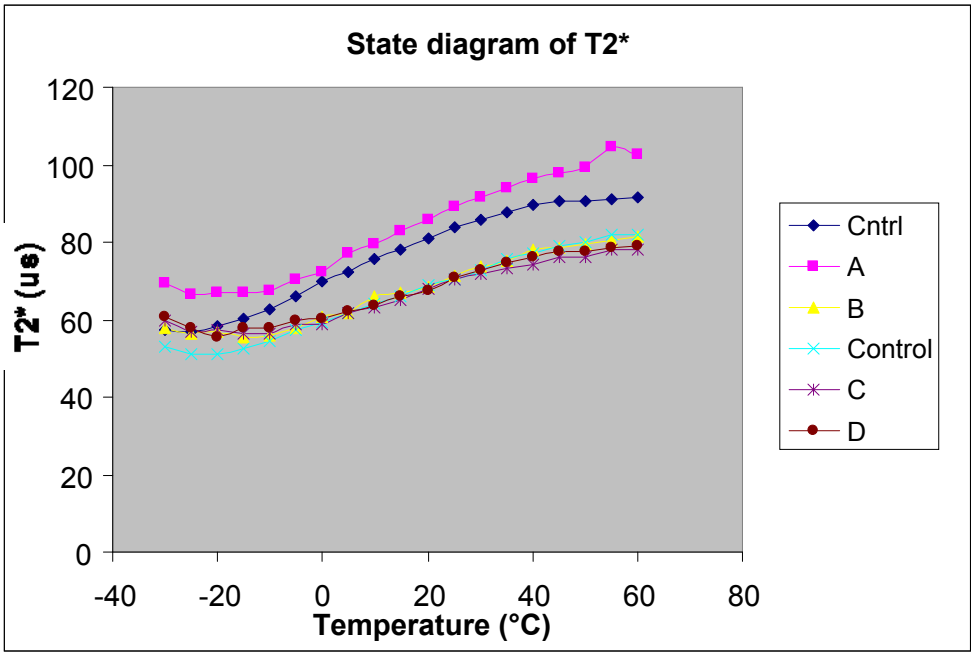

Figure 4.2.8. T2 state diagrams of all pellet types

Table 4.7. Tg, Kbt, Kpt values of all pellet types

	Tg (°C)	Kbt	Kpt
Cntrl	-23	0.08	0.53
A	-16	-0.07	0.50
B	-10	-0.09	0.44
Control	-17	-0.06	0.45
C	-12	-0.15	0.35

D	-6	-0.02	0.33

Confirmation by NMR test results

The moisture content data and NMR relaxation times are shown in Table 4.8 and Table 4.9. We can see that NMR results agree with previous moisture content data and previous state diagram results. Two controlled pellet types have relatively higher moisture contents than the other four types and pellet Cntrl has the highest moisture content (10.5%) among all pellet types. We can also find such MC difference in Table 4.8 that pellet Cntrl has the longest T22 values and largest A22 proportions which indicates a larger fraction of more free water component in such pellet type. And pellet B& A have larger T22 values (including T21 and T22 values) than pellet C*D which also agree with their moisture content values. Therefore, from these NMR results, we may suggest that pellets from location P with higher additive level appear to be more stable, may have less moisture diffusion and quality changes than the other pellet types.

Table 4.8. Moisture contents

	Moisture Content
Cntrl	10.5%
B	8.8%

A	8.6%
Control	9.7%
C	9.4%
D	9.6%

Table 4.9. NMR relaxation times

	T2*(μs)	T21(μs)	T22(μs)	A21	A22	T1(ms)
Cntrl	91	826	83444	11%	89%	78
B	73	442	73507	14%	86%	77
A	86	496	72902	15%	85%	71
Control	72	439	76465	12%	88%	81
C	70	426	70255	17%	83%	77
D	71	440	71766	16%	84%	80

Confirmation by MRI test results

Five pellets were put together due to size of the testing probe. Both controlled pellets have generally stronger signals than the other four pellets. Images are shown in Figure.4.2.9-16. We found that the MRI results agreed with previous NMR state diagram analysis. Stronger signal intensity always represents higher proton density and a more

mobile water state, indicating a higher possibility to be unstable. From these MRI figures, we can see that pellet Cntrl has the strongest signal intensity which indicates that such controlled pellets may suffer more rapid quality changes, such as rapid moisture diffusion. A has stronger intensity than B which agrees with their Tg and Kpt relationship as well. Pellet Control has the stronger signal intensity than C and D. The difference between C and D is not as apparent as the difference between B and A, which also can be found from the position of their individual state diagram curve that C curve and D curve always overlap with each other from Figure 4.2.8.

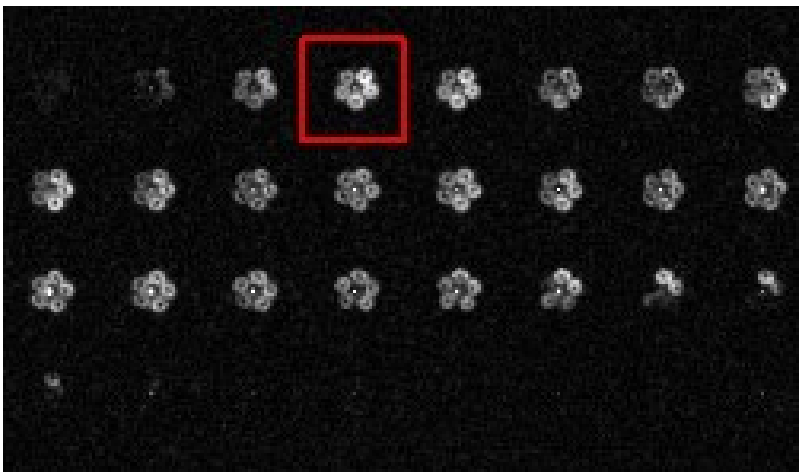

Figure 4.2.9. Sample array of MRI slice images with five pellets put together

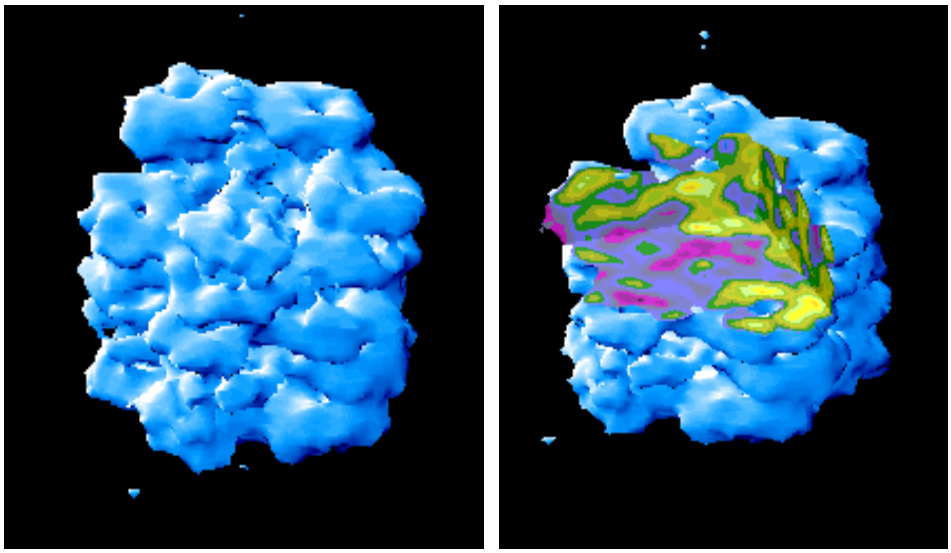

Figure 4.2.10. and 11. Sample 3D MRI image of five pellets put together

Low intensity High intensity

Figure 4.2.12. Color bar

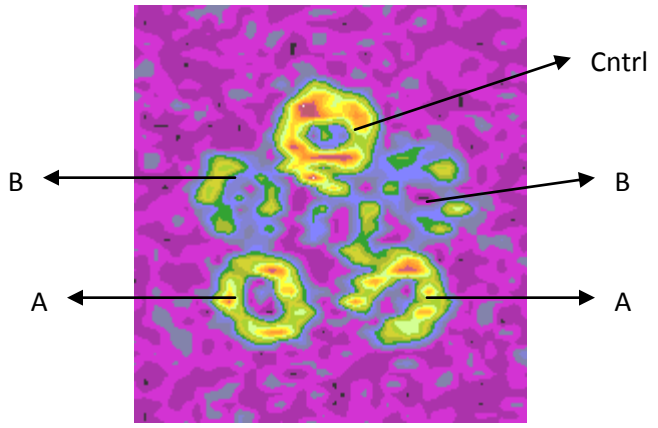

Figure 4.2.13. Slice image of pellet Cntrl, B & A, as we can see Cntrl has the strongest signal intensity and A has stronger intensity than B

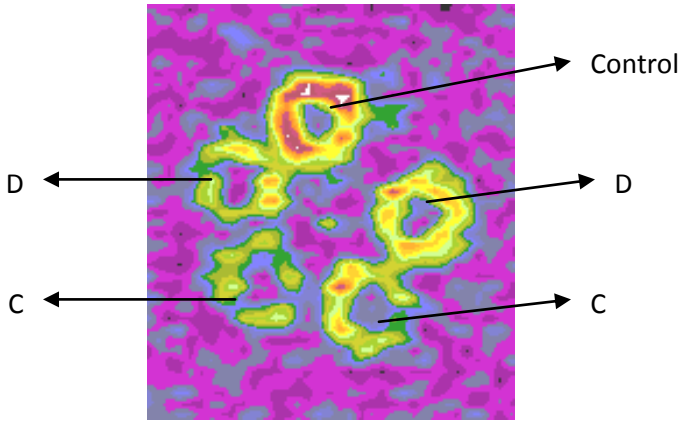

Figure 4.2.14. Slice image of pellet Control, C & D, as we can see pellet Control still has the strongest signal intensity and D has slightly stronger intensity than C. The difference between C and D is not as apparent as the difference between B and A.

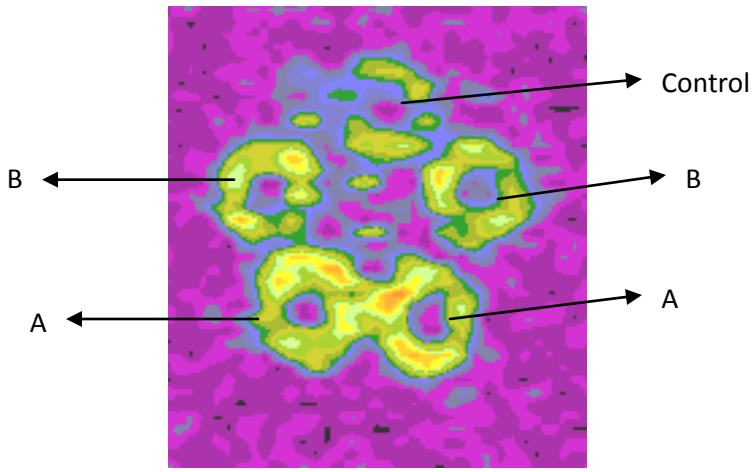

Figure 4.2.15. Slice image of pellet Control, B & A, as we can see pellet Control has relatively weaker signal intensity than the other two pellet types and A still has stronger intensity than B, same as shown in Figure 4.2.13.

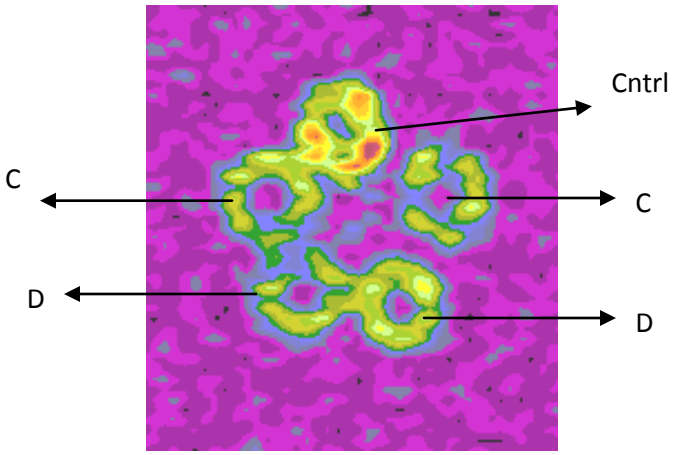

Figure 4.2.16. Slice image of pellet Cntrl, C & D, as we can see pellet Cntrl still has the strongest signal intensity but The difference between C and D is not as apparent as the difference between B and A, same as shown in Figure 4.2.14.

CHAPTER 5. SUMMARY AND FUTURE STUDY

5.1 Summary and conclusions

Nuclear magnetic resonance techniques, including nuclear magnetic imaging (MRI) and nuclear magnetic resonance (NMR) relaxometry are increasingly gaining interest and acceptance by food scientists and engineers. These techniques are being used to study moisture and fat content, water mobility, distribution of water, fat, and temperature in foods. They are also used to determine freezing front and viscosity of foods. A unique advantage of NMR techniques is their non-invasive and non-destructive nature, making analysis quick and reliable. MRI work in the food area is primarily conducted using expensive and hard to operate large MRI systems. Most food companies, especially small companies, are not willing to use or cannot afford to purchase such large systems. Therefore, developing small systems specifically for food samples is an urgent need. NMR relaxometry has been used by food scientists for decades. However, only recently food scientists began to realize that the technique has more to offer. Research on the relationship between NMR relaxation times and physiochemical properties of foods is emerging.

A suite of techniques were developed for the acquisition of reliable data and high quality images using low field MRI machines. Advanced pulse sequences were adapted

to our low field MRI machines for MRI imaging work and NMR relaxation work. Pulse sequences were tuned to obtain high quality images. New hardware were developed to accommodate unique samples.

New data acquisition schemes and data analysis techniques were developed for the study of food stability to obtain additional information. Models were designed for state diagrams. Coding programs were developed to calculate and analyze state diagram related parameters.

My work involved both hardware and software improvements to facilitate adaptation and implementation of advanced techniques. It is my hope that these low field MRI machines improved through my study so that they become an affordable, easy-to-operate, and relatively maintenance free analytical tool for food Research & Development and quality control labs.

5.2 Recommendations for future studies

The following suggestions are made based on my research work for future development in this area.

1. A high efficient gradient with faster switching drive should be developed for higher imaging quality.
2. A more homogeneous magnetic field should be tuned for higher imaging quality.

3. A small volume imaging probe with high and linear gradient should be developed for food samples.
4. More replicates need to be made to confirm some effects on food processing experiments.

REFERENCES

Bertram, H.C., Wiking, L., Nielsen, JH. 2005. Direct measurement of phase transition in milk fat during cooling of cream – a low field NMR approach. International Dairy Journal 15 (2005) 1056-1063.

Both, M., Schultze, J., Reuter, M. 2005. Fast T1-and T2-weighted pulmonary MRimaging in patients with bronchial carcinoma. European Journal of Radiology 53(3) 478-488.

Brosio, E., Conti, F., Lintas, C. and Sykora, S. 1978. Moisture determination in starch-rich food products by pulsed nuclear magnetic resonance. J. Fd. Technol. 13:107.

Buera MP,KarelM. 1995. Effect of physical changes on the rates of nonenzymic browning and related reactions. Food Chem 52(2):167–73.

Charlton, A. 2010. The food sector and nuclear magnetic resonance spectroscopy: a 10 year overview. New Food 1:9-12.

Chambers, J., McKevitt, N. J., Scdamore, K. A. and Bowman, C. E. 1989. Non-destructive determination of the moisture content of individual wheat grains by nuclear magnetic resonance. J. Sci. Food Agric. 49:211.

Clark, C.J., Hockings, P.D., Joyce, D.C., Mazucco, R.A. 1997. Application of magnetic resonance imaging to pre- and post- harvest studies of fruits and vegetables. Postharvest Viology and Technology 11(1997) 1-21.

Clark, C.J. and MacFall, J.S. 2003. Quantative magnetic resonance imaging of Fuyu persimmon fruit during development and ripening. Magnetic Resonance Imaging 21(2003) 679-685.

Constantinesco, A., Choquet, P., Cauffet, G.1997. Low field dedicated and desktop magnetic resonsnce imaging system for agriculture and food applications. Magnetic Resonance in Chemistry, Col 35, S69-S75 (1997).

Deka, K., Macmilan, M.B., Ouriadov, A.V. 2005. Quantitative density profiling with pure phase encoding and a dedicated 1D gradient. Journal of Magnetic Resonance 178 (1) 25-32.

Di Dola, A. and Brosio, E. 1983. Bound and free water determination by pulsed nuclear magnetic resonance. J. Fd. Technol. 18:125.

Divakar, S. 1998. Nuclear magnetic resonance spectroscopy in food applications: a critical appraisal. Journal of Food Science & Technology, India 35(6):469-481.

Emid, S. and Cryghton, JHN. 1985. High resolution NMR imaging in solids. Physica B&C. 128(1): 81-83.

Epstein, C.L., and Magland, J. 2006. A novel technique for imaging with inhomogeneous fields. Journal of Magnetic Resonance 183 (2) 183-192.

Espinosa, M.G., Sosa, M., et al. 2006. Blackberry (Rubus spp.): a PH-dependent oral contrast medium for gastrointestinal tract images by magnetic resonance imaging. Magnetic Resonance Imaging 24(2) 195-200.

Fang, ZJ, Hoepfel, D. andWinter, K. 2001. Application of Single Point Imaging (SPI) to solid state materials. Magnetic Resonance Imaging 19(3-4) 501-503.

Galed, G., Fernandez-Valle, ME, Martinez, A. 2004. Application of MRI to monitor the process of ripenging and decay in cirtus treated with chitosan solutions. Magnetic Resonance Imaging 22(1) 127-137.

Ghosh, PK, Jayas, DS, Gruwel, MLH and White, NDG. 2006. Magnetic resonance image analysis to explain moisture movement during wheat drying. Transactions of the ASABE 49(4):1181-1191.

Ghosh, PK, Jayas, DS, Gruwel, MLH and White, NDG. 2007. A magnetic resonance imaging study of wheat drying kinetics. Biosystems Engineering 97(2):189-199.

Goetz, C., Breton, E., Choquet, P. 2008. SPECT low field MRI system for small animal imaging. The Journal of Nuclear Medicine. Vol 49. No.1 Jan.2008.

Goloshevsky, A.G., Walton, J.H., Shutov, M.V. 2005. Development of low field nuclear magnetic resonance microcoils. Review of Scientific Intstruments 76, 024101 (2005).

Gonzalez, J.J., Calle, R.C. Bobroff, S. 2001. Detection and monitoring of internal browning development in Fuji apples using MRI. Postharvest Biology and Technology 22 (2) 179-188.

Goodman, B.A., Billiamson, B. and Chudek, J.A. 1992. Nuclear magnetic resonance micro-imaging of raspberry fruit: further studies on the origin of the image. New Phytologist Vol. 122, No.3. pp 529-535.

Granizo DP., Reuhs, BL and Stroshine R. 2007. Evaluating the solubility of powdered food ingredients using dynamic nuclear magnetic resonance relaxometry. LWT 40 (1) 36-42.

Grimault, S., Lucas, T., and Quellec S. 2004. Quantitative measurement of temperature by proton resonance frequency shift at low field: a general method to correct non-linear spatial and temproal phase deformations. Journal of Magnetic Resonance 170 (1) 79-97.

Gruwel, MLH, Latta, P. , and Volotovskyy V. 2004. Magnetic Resonance Imaging of Seeds by Use of Single Point Acquisition. J. Agric. Food Chem. 52(16): 4979-4983.

Guojonsdottir, M, Belton, PS., Webb GA. 2009. Magnetic resonance in food science. Challenges in a changing world. RSC Publishing: Cambridge

Haacke, E.M, Brown, R.W., Thompson, M., and Venkatesan, M.1999. Magnetic resonance imaging, physical principles and sequence design. John Wiley & Sons, Inc: New York.

Hahn, E. L. 1950. Spin echoes. Phys. Rev. 80:580.

Hartley, I. D., Kamke, F. A. and Peemoeller, H. 1994. Absolute moisture content determination of aspen wood below the fiber saturation point using pulsed NMR. Holzforschung 48(6):474.

Hernandez-Sanchez, N., Hills, B.P., and Barreiro P. 2007. An NMR study on internal browning in pears. Postharvest Biology and Technology 44 (3) 260-270.

Hills, B. P. 1991. Multinuclear NMR studies of water in solutions of simple carbohydrates. I. Proton and deuterium relaxation. Molec. Phys. 72:1099.

Hills, B. 1995. Food processing: an MRI perspective. Trends in Food Science & Technology 6(4):111-117.

Kakalis, L., Baianu, I. C. and Kumosinski, T. F. 1990. Oxygen-17 and proton nuclear magnetic relaxation measurements of soy protein hydration and protein-protein interactions in solution. J. Agric. Food Chem. 38:639.

Kegler, C., Seton, HC, and Hutchison, JMS. 2007. Prepolarized fast spin echo pulse sequence for low field MRI. Magnetic Resonance in Medicine 57(6): 1180-1184.

Kilcast D, Subramaniam P. 2000. The stability and shelf-life of food. Cambridge, U.K.:

Woodhead Publishing.

Kuo, M.I., Anderson, M.E., and Gunasekaran. 2003. Determination effects of freezing on pasta filata and non-pasta filata mozzzarella cheeses by nuclear magnetic resonance imaging. J.Dairy Sci. 86(8): 2525-2536.

Lai, H. S. and Schmidt, S. J. 1990. Lactose crystallization in skim-milk powder observed by hydrodynamic equilibria, scanning electron microscopy and 2H nuclear magnetic resonance. J. Food Sci. 55:995.

Lai, H. S. and Schmidt, S. J. 1990. Water mobility and crystallization action of lactose-water systems by oxygen-17 and carbon-13 NMR. J. Food Sci. 55:1435.

Lai, H.M. and Schmidt, S. J. 1993. Mobility of water in various sugar-water systems as studied by oxygen-17 NMR. Food Chemistry 46:55.Lammertyn, J., Dresselaers, T., Hecje, P.V. 2003. MRI and X-ray CT study of spatial distribution of core breakdown in Conference pears. Magnetic Resonance Imaging 21 (7) 805-815.

Levine, H. and Slade, L. 1991. A food polymer science approach to structure-property relationships in aqueous food systems: non-equilibrium behavior of carbohydrate-water systems. In Water relationships in foods — advances in the 1980s and trends in the 1990s. H. Levine and L. Slade, ed. New York, Plenum Press. pp. 29.

Lee, J.K., Choi, H.Y., and Lee S.W. 2000. Usefulness of T1-weighted image with fast inversion recovery technique in intracranual lesions comparison with T1-weighted spoin echo image. Journal of Clinical Imaging 24(5)263-269.

Li, Tao and Mirowitz Scott, A. 2003. Fast T2-weighted MR imgaing: impact of variation in pulse sequence parameters on image quality and artifacts. Magnetic Resonance Imaging 21 (7) 745-753.

Li, Y, Szlachetka, K, Chen, P. 2008. Ingredient Characterization and Hardening of High-Protein Food Bars: an NMR State Diagram Approach. Cereal Chemistry 85(6):780–786.

Lin, X., Ruan, R., Chen, P., Chung, M., Ye, X., Yang, T., Doona, C. and Wagner, T. 2006. "NMR state diagram concept." Journal of Food Science. 71(9): 136-45;

McEntyre, E, Ruan, R and Fulcher, RG. 1998. A comparision of water absorption patterns in two barley cultivars. Cereal Chemistry 75(6): 792-795.

Melhem, ER, Jara, H, and Yucel, EK. 1996. Multislice T1-weighted hybrid RARE in CNS imaging: Assessment of magnetization transfer effects and artifacts. Journal of Magnetic Resonance Imaging. 6(6): 903-908.

Micklander, E., Peshlov B., and Purslow, P. 2002. NMR-cooking: monitoring the changes in meat during cooking by low field H-NMR. Trends in Food Science & Technology 13 (9-10) 341-346.

Mora-Gutierrez, A. and Gaianu, I. C. 1989. 1H NMR relaxation and viscosity measurements on solutions and suspensions of carbohydrates and starch from corn: the investigation of carbohydrates hydration and stereochemical and aggregation effects in relations to 17O and 13C NMR data for carbohydrate solutions. J. Agric. Food Chem. 37:1459.

Nanassy, A. J. 1973. Use of wide line NMR for measurement of moisture content in wood. Wood Sci. 5(3):187.

Nanassy, A. J. 1976. True dry-mass and moisture content of wood by NMR. Wood Sci. 9(2):104.

Nguyen, TA, Dresselaers, T., and Verboven, P. 2006. Finite element modeling and MRI validation of 3D transient water profiles in pears during postharvest storage. Journal of the Science of Food and Agriculture. 86(5):745-756.

Noel TR, Ring SG, Whittam MA. 1990. Glass transitions in low-moisture foods. Trends Food Sci Technol 1:62–7.

Pui Margaret, H., and Fok Elizabeth, C.M. 1995. MR imaging if the brain: comparison of gradient echo and spin echo pulse sequence. Asian Association of Radiology Congress, Jan.1995.

Rahman, MS.2006. State diagram of foods: Its potential use in food processing and product stability. Trends in Food Science and Technology. 17(3): 129-141.

Ramos-Cabrer, P, Duynhoven, JPMv, Timmer, H and Nicolay K. 2006. Monitoring of moisture redistribution in multicomponent food systems by use of magnetic resonance imaging. Journal of Agricultural & Food Chemistry 54(3):672-677.

Regier, M, Hardy, EH, Knoerzer, K, Leeb, CV and Schuchmann, HP. 2007. Determination of structural and transport properties of cereal products by optical scanning, magnetic resonance imaging and Monte Carlo simulations. Journal of Food Engineering 81(2):485-491.

Renou, J. P., Briguet, A., Gatellier, P. and Kopp, J. 1987. Technical note: determination of fat and water ratios in meat products by high resolution NMR at 9.6 MHz. International J. Fd. Sci. Technol. 22:169.

Richardson, S. J., Baianu, I. C. and Steinberg, M. P. 1986. Mobility of water in wheat flour suspensions as studied by proton and oxygen-17 nuclear magnetic resonance. J. Agric. Food Chem. 34:17.

Richardson, S. J., Baianu, I. C. and Steinberg, M. P. 1987. Mobility of water in sucrose solutions determined by deuterium and oxygen-17 nuclear magnetic resonance. J. Food Sci. 52:806.

Rocha, AJ, Oliverira, ASB, and Fonseca, RB. 2004. Detection of corticospinal tract compromise in amyotrophic lateral sclerosis with brain MRI: relevance of the T1-weighted spin echo magnetization transfer contrast sequence. AJNR Am J Neuroradiol 25(9): 1509-1515.

Roos Y. 1995a. Characterization of food polymers using state diagrams. J Food Eng 24:339–60.

Roos, YH, Karel, M and Kokini, JL. 1996. Glass transitions in low moisture and frozen foods: Effect on shelf life and quality. Food Technol. 50(11):95-108.

Ruan, R and Chen, PL. 1998. Water in food and biological materials: A nuclear magnetic resonance approach.Technomic Publishing Inc: Lancaster.

Ruan, RS., Schmidt, AS and Litchfield, JB. 1989. Nondestructive measurement of transient moisture profiles and the moisture diffusion coefficient in potato during drying and absorption by nuclear magnetic resonance imaging. AICHE International Summer Meeting. Philadelphia, PA. Paper No. 10(d).

Schmalbrock, P., Chakeres, DW., Monroe, JW. 1999. Assessment of Internal Auditory Canal Tumors: A comparison of contrast-enhanced T1-weighted and steady state T2 weighted gradient echo MR imaging. AJNR Am J Neuriradiol 20: 1207-1213.

Schmidt, SJ and Lai, H. 1990. Use of NMR and MRI to study water relations in foods. In: Lavine, H. & Slade, L., editors. Water relationships in foods. New York: Plenum Press. p. 405-452.

Schmidt, S. J. and Lai, H. 1991. Use of NMR and MRI to study water relations in foods. In Water relationships in foods. H. Lavine and L. Slade, ed. New York, Plenum Press. pp. 405.

Schrader, GW, Litchfield, JB and Schmidt, SJ. 1992. Magnetic resonance imaging applications in the food industry. Food Technology 46(12):77-83.

Sharp, A. R., Riggin, M. T. and Kaiser, R. 1979. Determination of moisture content of wood by pulsed nuclear magnetic resonance. Wood and Fiber 10(2):74.

Shyh-Shin, H, Yu-Che, C, Chen, C, Huu-Sheng, L and Ta-Te, L. 2009. Magnetic resonance imaging and analyses of tempering processes in rice kernels. Journal of Cereal Science 50(1):36-42.

Simoneau, C, McCarthy, MJ and German, JB. 1993. Magnetic resonance imaging and spectroscopy for food systems. Food Research International 26(5):387-398.

Slade, L., Levine, H.,Ievolella, J., et al. 1993. The glassy state phenomenon in applications for the food industry. Journal of Science of Food and Agriculture. 63(2): 133-176.

Stark, D. D. and Bradley, W. G. 1989. Magnetic resonance imaging. St. Louis, USA, The C.V. Company.

Thybo, A.K., Anderson, H.J., and Karlsson A.H.2003. Low field NMR relaxation and NMR imaging as tools in differentiation between potato sample and determination of dry matter content in potatoes. Lebensm-Wiss U-Technol. 36 (3) 315-322.

Tollner, E. W. and Hung, Y. C. 1992. Low resolution pulse magnetic resonance for measuring moisture in selected grains and kernels. J. Agric. Engng. Res. 53:195.

Yi-Lin, C and Hsi-Mei, L. 2004. Water status of two gelatin gels during storage as determined by magnetic resonance imaging. Journal of Food & Drug Analysis 12(3):221-227.

Appendix

Main listing of T2 mapping programs:

```
%for each element, if >threshhold, set it to 0, otherwise keep it

%off: level if signal is greater than off, if off_flag=1

%off_flag: remove signal if off_flag=0%folder: folder name containing several folders named  as T1000, ..., which

%contains several slices named s08,s12, ... saved from IDL as txt files.

function [TauOut, outImage]=T2mappingV3(folder, threshhold, off_level, off_flag, isShowResult)

%clear all;

close all;

if nargin <1

   error('input: at least one as folder');

end

if ischar(folder)~=1

   error('first parameter should be a string as a folder name');

end
```

```
        %%import data in txt files; %[row,colum,slice,Tau]= imagesMultiTau

[imagesMultiTau,Tau,slicesNames]=importT2images(folder);



        %% label slices for corresponding slice T2 mapping

sliceLabel=sliceLabels(slicesNames);

%sliceFigNames=sliceNames('slice plot:_Tau=', Tau, sliceLabel);

        %%[m,n]=sliceFigNames,  m=Tau, n=slice#



%surf4D(imagesMultiTau, sliceFigNames);   %cannot show too many figures

%surf4D(imagesMultiTau, sliceFigNames,sliceNum);



if nargin ==1

            %%check threshhold and display slices

    checkTh=T2checkThreshhold(imagesMultiTau,Tau,sliceLabel);



    TauOut=Tau;
```

```
    outImage=imagesMultiTau;

    return;

end



%%remove threshhold

cut4D=cutThreshhold(threshhold,imagesMultiTau, folder);

% sliceFigNames=sliceNames('slice(remove noise):_Tau=', Tau, sliceLabel);

% surf4D(cut4D, sliceFigNames,sliceNum);



[row,column,page,D4]=size(cut4D);

    for i=1:D4

        figureName=strcat('image at Tau=', int2str(Tau(i)));

        figure('name',figureName);

        showMultiSlices(cut4D(:,:,:,i));

    end
```

```
%if p~=q
   %error('only one image, no T2 mapping')
 %end
      %%calculate T2 mapping values
T2map3D=T2MapMultiTau(cut4D,off_level,off_flag, Tau, folder);
      %%display T2 mapping slice one by one

 [T2mean,T2std]=meanStd(T2map3D)

figure('name','T2 mapping 2D surface for each slice');
showSurfSlices(T2map3D, sliceLabel);

figure('name','T2 mapping for each slice');
showMultiSlices(T2map3D,sliceLabel);

if nargin==5
```

```
    if strcmp(isShowResult,'showAll')==1
        surf3DT2(sliceLabel, T2map3D);
    end
end


    % %average 1D rpofile
    % %output the data into a file
    % %'showYes'=display plot; 'showNo'=not display
    % %T2av1Dcolumn: row=slice, column=1D T2 values
T2av1Dcolumn = T2av1Dprofile_3D(folder,T2map3D, 'column', isShowResult, sliceLabel);
figure('name', strcat('T2 mapping average1Dprofile along', ' column'));
showMulti1Dprofiles(T2av1Dcolumn, sliceLabel);


T2av1Drow = T2av1Dprofile_3D(folder,T2map3D, 'row', isShowResult, sliceLabel);
figure('name', strcat('T2 mapping average1Dprofile along', ' row'));
```

```
showMulti1Dprofiles(T2av1Drow, sliceLabel);


      %%histogram for all T2 values calculated from a whole sample
 figureName=strcat('Histogram for 3D T2 mapping');
    figure('name',figureName);
hist3DT2=hist4D(T2map3D,folder, off_flag);
%mean and deviation


%outp=Tau;
%outp=hhist;
%outp=T2map3D;
%outp=sliceLabel;
%outp=slicesNames;
%outp=hist3DT2;
%TauOut=T2av1Drow;
TauOut=T2map3D;
```

```
outImage=cut4D;

 return;
```